# Fabrication and manipulation of non-wetting surfaces and drops: From super liquid-repellency and the Leidenfrost effect to liquid marbles

## Dissertation

## zur Erlangung des Grades

## „Doktor der Naturwissenschaften”

## im Promotionsfach Chemie

**Fachbereich Chemie, Pharmazie und Geowissenschaften**

**der Johannes Gutenberg-Universität**

**in Mainz**

**Maxime Paven**

geboren in Brest, Frankreich

Mainz, November 2016

Die vorliegende Arbeit wurde von Oktober 2013 bis November 2016 unter der Betreuung von [n.a. in online version] am Max-Planck-Institut für Polymerforschung in Mainz angefertigt.

Tag der Prüfung: 14. Dezember 2016

Dekan: [n.a. in online version]

1. Berichterstatter: [n.a. in online version]

2. Berichterstatter: [n.a. in online version]

# Table of content

# Abstract

Controlling wetting, i.e. how drops interact and spread on surfaces, is of interest from a fundamental, physicochemical point of view and has relevance in many industrial processes like printing and spray coating. A great deal of attention is dedicated to the situation where drops ball up on a surface to minimize any contact between both. The reduced contact area results in a comparatively low adhesion force between the surface and the drop. Under certain conditions the lateral adhesion forces become so small, that drops easily move over the surface. A high drop mobility on a given surface is appealing for numerous applications, e.g. self-cleaning surfaces or the use of drops as microreactors. The non-wetting behavior results from entrapment of air pockets between drops and the surface. The entrapment of air pockets between both is either due to surface properties of the substrate, like in the case of super liquid-repellent surfaces and the Leidenfrost effect, or due to surface properties of the drop, like in the case of liquid marbles. In the presented thesis, I introduce the fundamentals, discuss state of the art research and challenges, and finally present contributions in all three fields.

Super liquid-repellent surfaces rely on surface chemistry and, most importantly, on a nano- to micrometer-sized surface texture which stabilizes the air pockets between drop and substrate. However, surface textures on this size scale have low wear resistance what hampers the practical breakthrough of super liquid-repellent surfaces so far. Much attention is thus dedicated improving the mechanical strength of super liquid-repellent surfaces, but consistent approaches to quantify the mechanical durability of such surfaces are missing. Ultimately, a consistent test protocol requires force-sensitive indentation measurements to obtain quantitative results. Here, I investigate the mechanical properties of candle soot-templated super liquid-repellent surfaces. First off, the influence of the soot collection height on the wetting properties of the surface is explored. Then, I investigate the role of the reaction parameters on the mechanical properties of the candle soot-based test system. Therefore, force-sensitive measurements using colloidal indenters mounted to a scanning probe microscope are conducted. Comparison of these results to wetting experiments allows the careful balance of mechanical strength against repellency.

In the Leidenfrost state, a drop hovers on a hot plate due to steady evaporation of the liquid. This creates an air cushion between both, drop and surface, and prevents any contact between them. The Leidenfrost effect is only observed if the surface temperature of the substrate exceeds the boiling point of the liquid by a lower, critical value before the drop comes close to it. Otherwise, surface and drop contact and the drop quickly evaporates. Whereas this is known, it was shown recently that drops on a superhydrophobic surface can enter a Leidenfrost-like state, starting from ambient conditions by a continuous decrease of the surrounding pressure. The surface texture restricts the vapor flow of the evaporating water drop which leads to an upward force. This results in the drop to jump from the substrate and continuously bounce at increasingly higher heights. In my thesis, I show that not only a pressure-

time gradient but also a temperature-time gradient can lead to a similar effect. In particular, jumping and bouncing is observed even on smooth hot substrates for elastic hydrogel balls containing more than 90 wt% water. This study connects controlled heat transfer to drop bouncing depending on the drop elasticity.

Liquid marbles are powder encapsulated drops. In contrast to the two aforementioned approaches, the non-wettability of liquid marbles is a drop, not a substrate property. The particle powder shell of liquid marbles is porous and entraps air pockets. The shell prevents the inner liquid from wetting the substrate and affords high mobility both, on solid and liquid substrates. In terms of applications, they serve as flexible, microliter sized reservoirs to carry analytes and reactants. The movement of these reservoirs is under investigation to prepare drop delivery systems which are controllable in space and time. If necessary, the inner liquid can be released to initiate a reaction or analysis. In this thesis, I introduce photo-thermally responsive liquid marbles. Such liquid marbles can be propelled over the air-water interface to a desired place at a given timing. Propulsion of the liquid marble is generated by shining light on the shell material. The light is converted into heat and the heat dissipates into the water leading to a heat gradient on the water surface close to the liquid marble. This in turn causes a Marangoni flow on the water surface, pushing the liquid marble forward. The inner liquid can be on-demand released by an external stimulus.

In conclusion, contributions in all three fields are presented leading to mechanically optimized super liquid-repellent surfaces and two strategies were exploited to move and manipulate drops using the Leidenfrost effect and liquid marbles.

# Zusammenfassung

Das Benetzungsverhalten von Tropfen kontrollieren zu können ist sowohl aus physikalisch-chemischer Sicht als auch für eine Vielzahl industrieller Prozesse, wie etwa die Sprühlackierung, von Relevanz. Dabei spielt vor allem die Wechselwirkung von Tropfen mit einer Oberfläche und welche Wölbung sie dabei annehmen eine entscheidende Rolle. Ein besonderes Augenmerk liegt dabei auf Tropfen, die nahezu sphärisch sind und somit ihren Kontakt mit der Oberfläche minimieren. Die Haftkraft der Tropfen an die Oberfläche wird dadurch deutlich reduziert. In einigen Fällen kann das dazu führen, dass die Tropfen sich leicht von der Oberfläche lösen lassen und über sie hinweg gleiten können. Auf diesem Effekt basierend wurden vielversprechende Anwendungen vorgeschlagen, z. B. selbstreinigende Oberflächen oder die Verwendung von Tropfen als Mikroreaktoren. Das geringe Benetzungsvermögen der Tropfen beruht auf Luftpolstern, die sich zwischen Tropfen und Oberfläche befinden. Diese Luftpolster resultieren entweder aus oberflächen- oder aus tropfenspezifischen Eigenschaften. Ersteres ist der Fall für super-flüssigkeits-abweisende Oberflächen und den Leidenfrost-Effekt, Zweiteres für flüssige Murmeln. Die vorgelegte Dissertation erläutert die grundlegenden Konzepte dieser drei Herangehensweisen, geht auf aktuelle Forschungsentwicklungen ein und präsentiert eigene Forschungsbeiträge auf allen drei Gebieten.

Ein Schlüsselelement super-flüssigkeitsabweisender Oberflächen sind Oberflächenstrukturen im Nano- bis Mikrometerbereich. Diese Strukturen sind allerdings empfindlich gegenüber mechanischer Beanspruchung, was deren großflächigen Einsatz bisher erschwert. Daher gibt es zahlreiche Bestrebungen, mechanisch verstärkte Oberflächen herzustellen. Die Charakterisierung der mechanischen Eigenschaften solcher Oberflächen ist allerdings nicht vereinheitlicht. Die mechanischen Eigenschaften werden üblicherweise mittels qualitativer Tests untersucht, wie etwa der Scheuertest. Nicht zuletzt sollten aber auch quantitative, d. h. kraft-sensitive Messungen durchgeführt werden, um einen Vergleich von Materialeigenschaften zu ermöglichen. In diesem Sinne untersuche ich die mechanischen Eigenschaften eines Kerzenruß-basierten Testsystems für super-flüssigkeitsabweisende Oberflächen. Zunächst wird der Einfluss der Berußungs-position innerhalb der Kerzenflamme auf die Benetzungseigenschaften evaluiert. Anschließend wird die Rolle der Reaktionsparameter auf die mechanische Stabilität beleuchtet. Dazu verwende ich Rasterkraftmikroskopie und als Eindringkörper wird ein Silikamikropartikel gewählt. Die Ergebnisse der Messungen werden mit dem Benetzungsverhalten der jeweiligen Oberflächen in Beziehung gesetzt, wodurch beides, mechanische Stabilität und Benetzungsverhalten, gegeneinander abgewogen werden können.

Beim Leidenfrost-Effekt gleitet ein Tropfen kontaktlos über eine heiße Oberfläche. Die Temperatur der Oberfläche muss ausreichend hoch sein, bevor der Tropfen aufgebracht wird, damit eine rasche, primäre Verdampfung des Tropfens stattfinden kann und der Tropfen auf dem generierten Dampfpolster gleitet. Ist die Temperatur zu gering, kann es passieren, dass der Tropfen die heiße Oberfläche berührt und

zügig verdampft. Kürzlich konnte gezeigt werden, dass Tropfen, die sich auf einer wasserabweisenden Oberfläche befinden, auch von Umgebungsbedingungen ausgehend in einen Leidenfrost-ähnlichen Zustand übergehen können. Der Umgebungsdruck wird dabei sukzessiv vermindert; was die Verdunstungsrate des Wassertropfens beschleunigt. Der enstehende Wasserdampf kann durch die Oberflächenstruktur umgelenkt werden, was zu einer aufwärtsgerichteten Kraft führt. Der Tropfen löst sich daraufhin von der Oberfläche und beginnt graduell höher und höher zu springen. In meiner Dissertation zeige ich, dass nicht nur eine Druckänderung, sondern auch eine Temperaturänderung der Oberfläche zu einem ähnlichen Effekt führen kann. Unter anderem werden tropfenähnliche Hydrogele verwendet, die nahezu nur aus Wasser bestehen (>90 Gew%). Es wird gezeigt, dass Hydrogeltropfen durch einen Temperaturgradienten von flachen Oberflächen gelöst werden und danach kontinuierlich springen können. Diese Beobachtung setzt die kontrollierte Wärmeübertragung in Zusammenhang mit dem Springen von Tropfen und beleuchtet dabei die Rolle der Tropfenform und Elastizität.

Bei flüssigen Murmeln handelt es sich um Tropfen, die mit Pulverteilchen ummantelt sind. Die Teilchenschale der flüssigen Murmeln ist porös und schließt Luftpolster ein. Diese Luftpolster verhindern, dass die innere Flüssigkeit mit dem Substrat in Berührung kommt. Im Gegensatz zu den beiden obigen Herangehensweisen sind die nicht benetzenden Eigenschaften nun an den Tropfen gebunden und nicht an das Substrat. Das führt dazu, dass flüssige Murmeln sowohl über feste als auch flüssige Substrate bewegt werden können. Studien zeigen, dass flüssige Murmeln vielversprechende Kandidaten sind, um effizient Flüssigkeitsmengen im Mikroliterbereich zu bewegen und anschließend an einem gezielten Ort wieder freizusetzen. Die nichtinvasive, ferngesteuerte Bewegung solcher flüssigen Murmeln ist dabei von großem Interesse. Um flüssige Murmeln gezielt und nichtinvasiv bewegen zu können, habe ich flüssige Murmeln hergestellt, deren Schalenmaterial Licht in Wärme umwandelt. Platziert man solche flüssigen Murmeln auf die Wasser-Luft Grenzfläche, so kann man durch Lichteinstrahlung einen Hitze-basierten Marangoni Fluss auf der Grenzfläche erzeugen. Dieser schiebt die flüssige Murmel zügig in die entgegengesetzte Richtung der Lichteinstrahlung. Dieser Effekt kann durch die Kontrolle der Einstrahlung zeitlich wie auch räumlich koordiniert werden. Es wird ebenfalls gezeigt, wie die innere Flüssigkeit durch äußere Einflüsse gezielt freigesetzt werden kann, um eine Reaktion auszulösen.

Zusammenfassend konnten mittels Oberflächenindentation mechanisch ausbalancierte, super-flüssigkeitsabweisende Oberflächen erhalten werden. Außerdem wurden der Leidenfrost-Effekt und flüssige Murmeln genutzt, um gezielt die Bewegung von Tropfen zu manipulieren.

# 1 Introduction

From our daily life, it is clear that drops can wet and adhere to solid surfaces. This is e.g. the case for raindrops impacting a window: Initially, the drops stick to the window. Neighboring drops coalesce to puddles and finally slide off when gravitational forces dominate the lateral adhesion forces of the drops. In general, the drops slide off at high inclination angles and/or comparably high drop volumes (few hundreds µl to ml), leaving a water trail behind them. Interestingly, few cases can be found where drops behave differently, i.e. they do not wet the surface of the substrate but rather move like liquid spheres over them. The presented work deals with three approaches to yield such non-wetting surfaces and drops: i) Super liquid-repellency, ii) the Leidenfrost effect and iii) liquid marbles. **Figure 1** summarizes the three different approaches to reduce the adhesion between the surface of a substrate and drops. The approaches all rely on entrapment of air between both, substrate and drop:

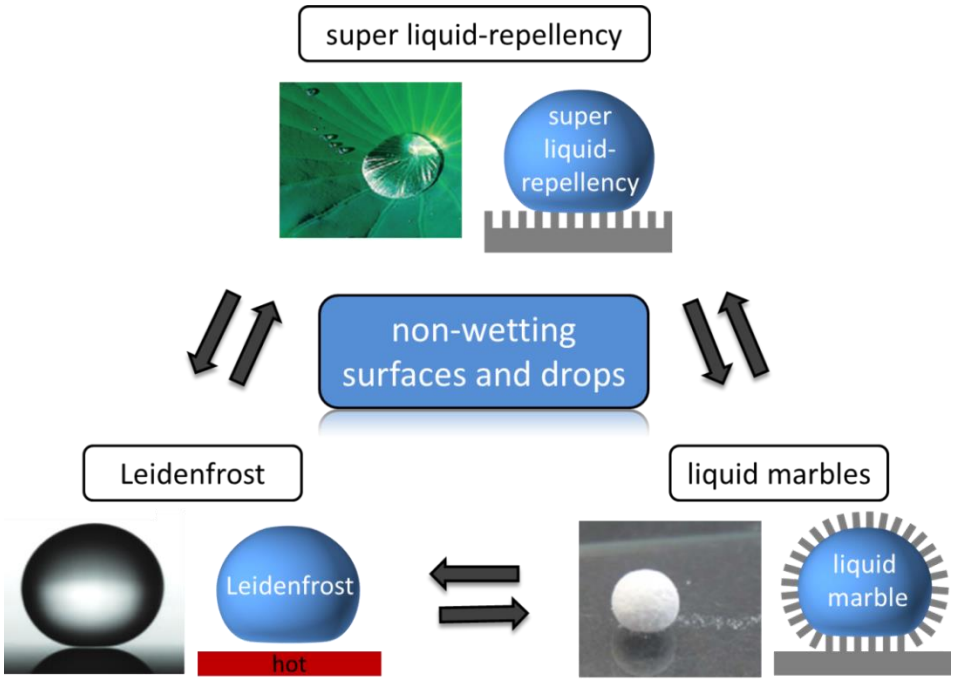


**Figure 1**: Approaches towards non-wetting surfaces and drops by entrapping air between drop and substrate: Super liquid-repellency, the Leidenfrost effect and liquid marbles. An experimental image (left) and a schematic drawing (right) is shown for each approach. In part adapted from Ref[1, 2] (with permission of The Royal Society of Chemistry) and Ref[3] (adapted with permission, Copyright (2010) American Chemical Society).

Drops dispensed on **super liquid-repellent surfaces** have high contact angles and easily roll-off at low inclination angles. Amongst others, this can be observed on the lotus leave which was also name giving for the so-called lotus or self-cleaning effect.[4, 5] In contrast to a normal surface (**Figure 2**a), a drop rolls down a super liquid-repellent surface and collects any dust and dirt on its way without leaving any visible trail of liquid behind (Figure 2b).

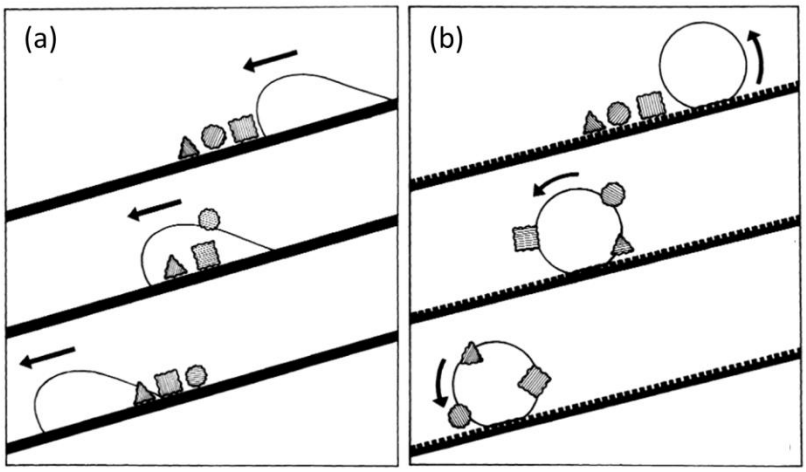


**Figure 2**: The Lotus effect. a) A drop slides off a smooth surface. Dirt particles along its way are redistributed on the surface. b) Drops roll-off a super liquid-repellent surface. Dirt is taken up by the drop and removed from the surface. Reprinted with permission from Ref[5].

The principle behind super liquid-repellency is the presence of air cushions between drop and substrate: Though the drop seems to make firm contact with the surface macroscopically, it is suspended on only a few, generally hydrophobic, nm-µm sized surface protrusions.[6-8] Consequently, the solid-liquid interaction is reduced by the air pockets and the surface tension of the liquid dominates the drop shape. The drop balls up like a sphere and a high contact angle at the three-phase contact line between surface, drop and air is formed. The air pockets also reduce the lateral adhesion force between drop and surface. This means that such drops readily start to move over the surface, even if only a small external force is applied to the drop. Surfaces which repel water at inclination angles of 10° and less and have high contact angles of more than 150° are called superhydrophobic. If a surface repels both, water and low surface tension liquids, like oils, it is superamphiphobic. The term super liquid-repellency groups up both, superhydrophobicity and superamphiphobicity.

Similarly to the lotus leave, water drops can skate on a hot pan. On a sufficiently hot surface, a continuous water vapor film is formed under a drop, which prevents the drop from contacting the surface. This is known as the **Leidenfrost effect.**[1, 9-11] The lateral adhesion becomes negligible and the drop moves almost frictionless over the surface.

In both aforementioned cases, the peculiarities of the surface provide the non-wetting properties and the low adhesion between drop and surface. The drop can also alter its wetting properties by “shielding” itself with hydrophobic particles. In nature, this can be observed when rain falls on hydrophobic soils: Initially, the water drops do not infiltrate the ground but are rather wrapped up by the soil. The hydrophobic soil particles adhere to the air-water interface and encapsulate the drops leading to so-called **liquid marbles**.[12-16] The particle shell is porous and efficiently entraps air pockets. This prevents that the inner liquid contacts the substrate. Consequently, liquid marbles have a low adhesion to solid and even liquid substrates.

Each approach entraps air pockets between substrates and drops in a different way, but all result in a non-wetting behavior between both. Using these approaches, drops in the order of µl to ml can be manipulated to achieve specific goals which can, for example, be transport, reaction, or analysis of the liquid.

The presented work addresses specific questions in all three fields of research. Prior to this, topical parallels and differences between super liquid-repellency, the Leidenfrost effect and liquid marbles are highlighted. Furthermore, fundamental principles, the state of research and challenges of the respective fields are presented in the associated subchapters.

## 1.1 Conceptual similarities and differences in super liquid-repellency, the Leidenfrost effect and liquid marbles

Though different on the first glance, super liquid-repellent surfaces, the Leidenfrost effect and liquid marbles are connected by the principle to entrap air cushions between a drop and the surface of a substrate which was recently highlighted by McHale and Newton.[16] In all three cases, a comparatively small normal and lateral adhesion force between drop and surface is observed. The normal force corresponds to the force required to detach the drop from the surface in a vertical direction, whereas the lateral adhesion force is the force required to make the drop move in a horizontal direction over the surface. External forces can e.g. be gravity acting on a drop: On a tilted surface, a drop starts to move if the gravitational force exceeds the lateral adhesion force $F_{La}$. $F_{La}$ depends on the surface tension of the liquid $\gamma_{lv}$, and on the drop geometry right before the drop moves, i.e. the contact angle $\theta_{adv}$ on the advancing side and $\theta_{rec}$ on the receding side. Furthermore, $F_{La}$ also depends on the drop contour $R$ which takes shape and length of the three-phase contact line into account:[17, 18]

$$F_{La} = \gamma_{lv} R k (\cos\theta_{rec} - \cos\theta_{adv}) \qquad \text{(eq. 1.1)}$$

$k$ is an experimental fit factor to consolidate theory and experimental data. It accounts for surface inhomogeneities, e.g. when drops pin to small surface defects. $F_{La}$ decreases with decreasing contour factor, i.e. becomes smaller if the contact line between solid and liquid is broken and parts of it are replaced e.g. by a liquid-air interaction instead. $F_{La}$ is also reduced if $\cos\theta_{rec} - \cos\theta_{adv}$ becomes small. In a strict sense, eq. 1.1 applies only for drops in direct contact with a solid. Still, one can argue that super liquid-repellent surfaces diminish the contour factor $R$ by breaking up the three-phase contact line due the air cushions. Furthermore $\cos\theta_{rec} - \cos\theta_{adv}$ is comperatively small because the surface texture is coated with a low surface compound. In this sense, both lead to a small $F_{La}$, what is in accordance with experimental observations. Eq. 1.1 can be also conceptually extended to describe the low lateral adhesion of drops in the Leidenfrost state and liquid marbles: $\cos\theta_{rec} - \cos\theta_{adv}$ is almost negligible for drops in the Leidenfrost state and $R = 0$ for liquid marbles because the liquid does not touch the solid substrate anymore.

The similarity of the three approaches can be underlined by conceptual conversion of one approach into the other which is shown in the following:

i) In the case of super liquid-repellent surfaces, the air cushions between drop and substrate are created by surface texturing of low energy materials: The drops rest on the asperities and entrap air cushions in-between drop, asperities and substrate. This is schematically shown in **Figure 3**a, for a pillar decorated superhydrophobic surface:

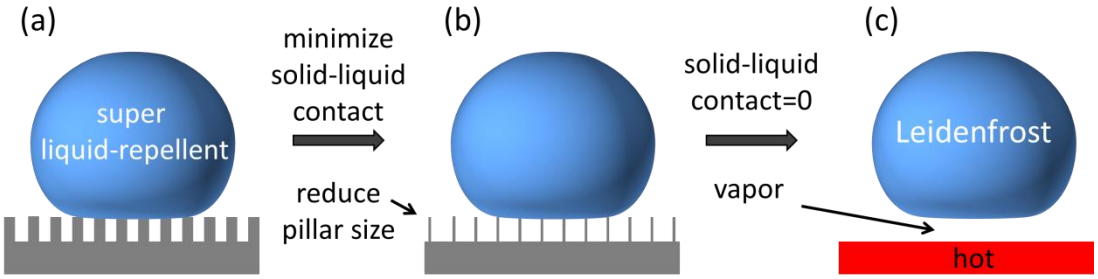


**Figure 3**: Connection between super liquid-repellency and Leidenfrost: a) A drop rests on a pillar decorated superhydrophobic surface and entraps air. b) The solid-liquid contact is reduced by shrinking the diameter of the pillars. c) A drop levitates on its vapor cushion on a hot surface without touching any surface features (Leidenfrost state). The solid-liquid contact is zero.

Super liquid-repellent surfaces are connected to the Leidenfrost effect by imagining that the size of the air pockets is constantly increased while the diameter of the pillars is steadily decreased (Figure 3b). The pillars are not existent anymore when the pillar diameter reaches zero. At this point, the drop hangs in mid-air on a continuous air cushion. This is precisely the case for a drop in the Leidenfrost state on a hot surface: It levitates on a cushion of its own vapor without touching any surface features. This results in a zero solid-liquid interaction (Figure 3c).

ii) A similar analogy can be drawn between super liquid-repellent surfaces and liquid marbles (**Figure 4**). The shape of a drop contacting a surface results from different factors like temperature, gravity and the way it is deposited. The shape particularly depends on the surface tension of the respective interfaces, i.e. solid-air $\gamma_{sa}$, solid-liquid $\gamma_{sl}$ and liquid-air $\gamma_{la}$. The liquid-air surface tension $\gamma_{la}$ strives to reduce the overall energy by making the drop ball shaped. This results in a finite force acting on the three-phase contact line, trying to pull up the

substrate. In the case of super liquid-repellent surfaces this force is exerted on the asperities of the surface which contact the drop. Ideally, the asperities are strongly connected to the rigid substrate and withstand this stress (Figure 4a). In a different case, the asperities detached from the substrate either by a force exceeding the yield stress or due to an artificial detachment mechanism (Figure 4b). Interestingly, a drop in contact with the detached asperities does not spread on the substrate but the asperities rather attach to the drop interface and wrap it up (Figure 4c).

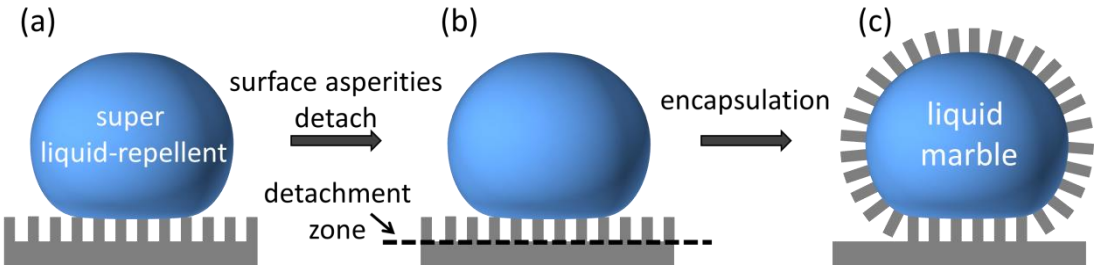


**Figure 4**: Connection between super liquid-repellency and liquid marbles: a) A drop sits on a pillar decorated superhydrophobic surface and entraps air. b) Pillars detach from the substrate. c) Pillars assemble around the drop and shield it from the substrate (liquid marble).

In this analogy, the asperities become the shell of a liquid marble. The particle can be seen as a mobile, super liquid-repellent layer coating the water drop. Depending on the kind of adsorbed particles the shell can be densely packed, e.g. with a monolayer of monodisperse nanoparticles, or be very porous, e.g. if a multilayer of µm to mm sized flocs attach to the drop. Anyhow, air is entrapped in between the particles reducing lateral adhesion and granting non-wettability between the inner liquid and the substrate.

iii) In the case of the Leidenfrost effect, the air layer under a drop is continuous, whereas it is discontinuous in the case of liquid marbles due to the adsorbed particles (**Figure 5**a and c). Practically, air pockets not only prevent wetting but also shield the drops thermally: The vapor layer and the air pockets are thermally insulating and efficiently suppresses the heat transfer between substrate and drop. This leads to unexpectedly long live times of drops in the Leidenfrost state and liquid marbles on hot surfaces. This similarity between Leidenfrost drops and liquid marbles was e.g. demonstrated by Aberle et al.[19], where graphite coated liquid marbles and water drops both had similar lifetimes

of more than one minute on a 465 °C hot surface. This allows drawing a connection between the Leidenfrost state and liquid marbles, which can be allegorized by a liquid marble sitting on a hot surface (Figure 5b). The interface between a liquid marble and a substrate can be considered as a composite particle-air layer consisting of spacer particles and air pockets. The particle-air layer prevents wetting and suppresses heat exchange between the hot substrate and the drop, just like a pure vapor cushion does in the Leidenfrost state. Removal of the spacer particles from a hot liquid marble and replacement by air in Figure 5b directly leads to a drop in the Leidenfrost state:

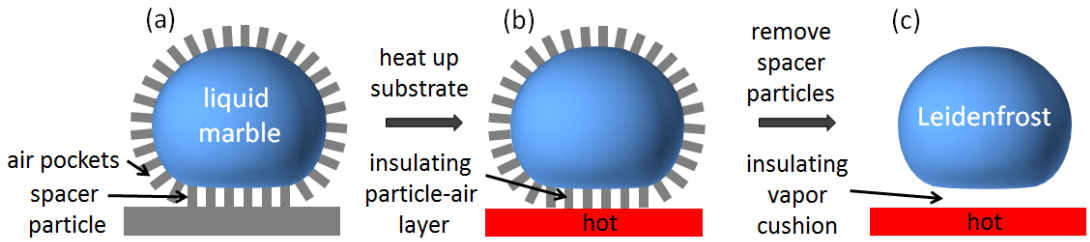


**Figure 5**: Connection between the Leidenfrost state and liquid marbles: a) Liquid marble shielded by air pockets and spacer particles b) The composite particle-air layer thermally insulates the liquid marble from a hot surface. c) Spacer particles are removed and the drop floats on an air cushion. In the Leidenfrost state, the air cushion is supplied by evaporation of the liquid.

Whereas Leidenfrost drops are restricted to high surface temperatures, liquid marbles and super liquid-repellent surfaces also work under moderate temperatures. The lateral drop adhesion and thus lateral mobility differ between all three approaches due to fundamental differences in the drop-surface interaction.[16] Drops on super liquid-repellent surfaces directly interact with the surface of the substrate. Leidenfrost drops only indirectly interact with the hot substrate due to the continuous vapor cushion. Liquid marbles are intermediate in their interaction mode: The particles adhere to the drop and a solid-solid interaction takes place upon lateral movement of the drop. The interaction is indirect because the particles mainly adhere to the drop and not the surface. Leidenfrost drops show the highest mobility because friction arises only from viscous losses in the vapor flow. The lateral adhesion of super liquid repellent surfaces and liquid marbles very much depends on the individual details of the studied system. In the case of super liquid-repellent surfaces and liquid marbles these specific details are, amongst others, the specific surface texture, powder

size and shape, and the respective surface tensions involved. Further details about each approach can be found in the following subchapters.

## 1.2 Super liquid-repellency

### 1.2.1 Wetting of smooth and rigid surfaces

Wetting deals with the contact between three phases of which at least two are fluid, i.e. gaseous or liquid.[20, 21] In particular, the wetting behavior between drops (few µl) and solid substrates in air affects many domains, ranging from efficient cooling up to self-cleaning surfaces. The measured, apparent contact angle $\theta_{app}$ describes the wettability of the surface. $\theta_{app}$ is obtained from the drop shape and is measured at the three-phase contact line, where liquid, surface and air meet.[22] Theoretically, Thomas Young was the first to discuss the wetting behavior of perfectly flat and smooth surfaces under thermodynamic equilibrium in 1805.[23] The Young contact angle $\theta_E$ depends on the surface tensions acting at the three-phase contact line, i.e. the solid-air ($\gamma_{sa}$), the solid-liquid ($\gamma_{sl}$) and the liquid-air surface tensions ($\gamma_{la}$) (**Figure 6**). Gravity, pinning and other inhomogeneities are neglected. In that sense $\theta_E$ can be seen as an idealized material contact angle which is inherent to the combination of drop and surface material.

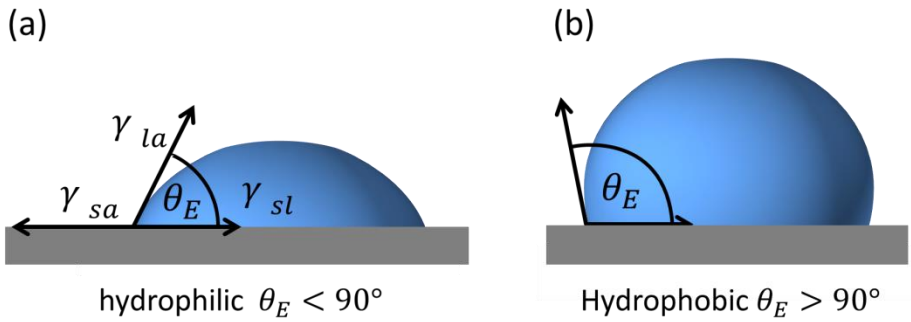


**Figure 6**: Scheme of a drop resting on a surface. The Young contact angle $\theta_E$ is determined at the three-phase contact line of liquid, surface and air.

In equilibrium, the horizontal components of the surface tensions are equal. This leads to the Young equation:

$$\gamma_{\mathrm{la}}\cos(\theta_E) = (\gamma_{\mathrm{sa}} - \gamma_{\mathrm{sl}}) \qquad \text{(eq. 1.2)}$$

The drop either spreads completely or forms a finite contact angle. Two further cases can be distinguished if a finite contact angle is formed: i) The surface tension of the solid-air surface is higher than that of the solid-liquid interface, i.e. $\gamma_{\mathrm{sa}} - \gamma_{\mathrm{sl}}$ is positive and $\theta_E < 90°$. In this case, wetting of the surface is preferred

and the surface is called hydrophilic (Figure 6a). ii) The opposite is true and $\gamma_{sa} < \gamma_{sl}$. The solid-air interface is energetically preferred over the solid-liquid interface which leads to $\theta_E > 90°$. Such a surface is called hydrophobic (Figure 6b). $\theta_E$ can reach a maximum value of $120°$ on a flat surface.[24] $\theta_E$ can be tuned by chemical surface modification. This works especially well for water as reference solvent. Protic and polar surface groups, like hydroxy or carboxy groups, generally lead to hydrophilic surfaces. Hydrophobic surfaces are obtained by alkylation or fluorination of the respective surface. If the surface is the same but different liquids are used, $\theta_E$ decreases with decreasing liquid-air surface tension $\gamma_{la}$. Typically, low surface tension liquids, like many organic solvents, form a Young contact angle $\theta_E < 90°$ on common materials.

### 1.2.2 **Contact angle hysteresis**

The Young equation predicts exactly one contact angle $\theta_E$ for a given drop-surface combination. Experimentally, this is not true and a distribution of contact angles is measured if several drops are dispensed and measured on the same material under the same conditions. Several factors neglected by Young influence the measured apparent contact angle $\theta_{app}$. In particular, real surfaces are not perfectly flat and smooth, but are sprinkled with chemical and topological inhomogeneities. The three-phase contact line of drops can be pinned and hindered to move on by a locally different adhesion force or topological unevenness which need to be overcome. Pinning leads to a deviation from $\theta_E$ and can increase the sliding angle.[21, 25] Pinning can experimentally be studied if a drop is inflated and deflated on such a non-perfect surface using a goniometer. The contact angle first increases when the drop is inflated, while the contact line is initially in rest. When the contact angle reaches an upper threshold value, the contact line starts to move. The contact angle just before the contact line advances is called the advancing contact angle $\theta_{adv}$. Likewise, the contact angle first decreases, when the drop volume is decreased until the contact line moves. The contact angle before the contact line recedes is called the receding contact angle $\theta_{rec}$. $\theta_{adv}$ is always larger than $\theta_{rec}$. The theoretical equilibrium contact angle $\theta_E$ is somewhere between $\theta_{adv}$ and $\theta_{rec}$. The difference between both,

$\theta_{adv} - \theta_{rec}$, is called contact angle hysteresis (CAH). Schematically, the process of contact line pinning is shown in **Figure 7** for a drop moving over a small surface unevenness.[21]

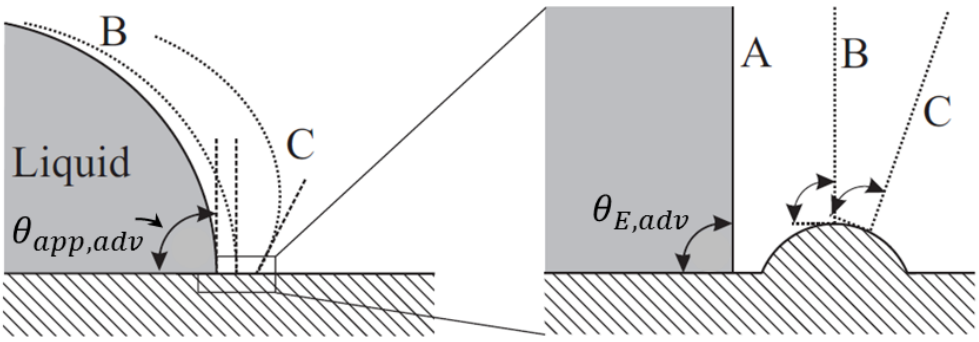


**Figure 7**: A drop advances on a surface with a small unevenness. A to C denote the different stages of the advancing process. Left: Macroscopic view of the drop indicating the change in $\theta_{app}$. Right: Zoomed-in view of the contact line encountering the surface unevenness. From Ref[21]. Adapted with permission from John Wiley and Sons.

A to C represent different stages of the advancing contact line. In A the contact line continuously advances with a material advancing contact angle of $\theta_{E,adv} = 90°$. Initially, $\theta_{app,adv} = \theta_{E,adv} = 90°$ at the three-phase contact line. The contact line needs to follow the shape of the surface unevenness to move on. During this, the material advancing contact angle will remain constant, i.e. $\theta_{E,adv} = 90°$. The contact line quickly moves forward to point B once the unevenness is reached. This process goes quickly because the curvature of the liquid interface points inward for the three-phase contact line to climb up the unevenness what is energetically unfavorable. On the maximum point (B), the contact line fulfills again $\theta_{app,adv} = \theta_{E,adv} = 90°$. To move down, the contact line again needs to follow the shape of the unevenness. This time, climbing down leads to an outward pointing curvature of the liquid to sustain $\theta_{E,\ adv} = 90°$. In this case, $\theta_{app,adv}$ is larger than 90° and the drop is pinned. The drop is depinned if $\theta_{app,adv} = \theta_{E,adv} = 90°$ is true again and the unevenness is overcome.

### 1.2.3 **Wetting of rough surfaces: The Wenzel and Cassie-Baxter states**

Surface texture, i.e. surface roughness, can have a tremendous impact on $\theta_{app}$ and can make it differ strongly from $\theta_E$ on a smooth surface.[7, 26] Surface textures

on the nm-µm scale have the strongest impact. Depending on the specific topography of the surface texture, the surface chemistry and the surface tension of the liquid, different scenarios can be observed.

In the so-called Wenzel state, a drop strictly follows the contour of the surface texture and the contact area between drop and substrate is fully wetted (**Figure 8**a).[27] In the so-called Cassie-Baxter, or just Cassie state, drops rest on the top faces of the surface texture and the air is entrapped underneath the drop (Figure 8b).[28]

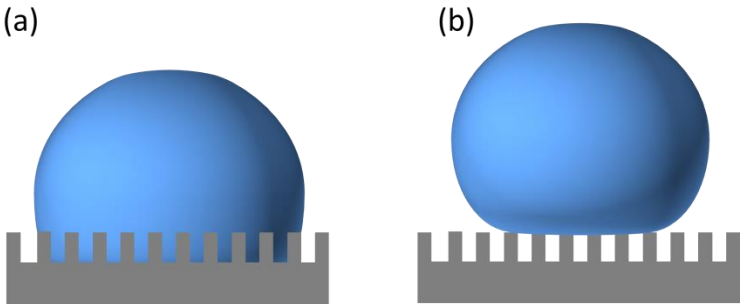


**Figure 8**: a) The Wenzel state and b) the Cassie state.

The surface roughness is defined by $r$ and is the real contact area divided by the projected, 2-dimensional surface area. For a perfectly flat surface $r$=1 and for a real surface $r$>1. If a surface is moderately rough, the drop is in the Wenzel state. According to Wenzel, the contact angle $\theta_w$ is amplified by the surface roughness:

$$\cos(\theta_w) = \mathrm{r} \cdot \cos(\theta_E) \qquad \text{(eq. 1.3)}$$

On a hydrophobic surface $\theta_w > \theta_E > 90^o$, while on a hydrophilic surface $\theta_w < \theta_E < 90^o$.

If a drop is deposited on very rough hydrophobic surfaces it might rather be in the Cassie state, i.e. contacting only the top of the surface texture. In this case, the drop forms a composite liquid-solid and liquid-air contact area. The Cassie-Baxter equation considers a universal approach where a drop contacts a chemically heterogeneous surface.[28] Assuming a two component contact area, which consists of solid and air, one can calculate $\theta_C$ using the liquid-solid fraction $\Phi_{sl}$ and $\theta_E$:

$$\cos(\theta_C) = -1 + \Phi_{sl}\big(1 + \cos(\theta_E)\big) \qquad \text{(eq. 1.4)}$$

For $\Phi_{SL} = 1$ the surface is flat and $\theta_C = \theta_E$. For $\Phi_{sl} = 0$, the contact angle is 180° and the drop floats over the surface. Though impossible for super liquid-repellent surfaces, this is realized in case of the Leidenfrost effect. Consequently, $\theta_C$ can be mathematically increased by reducing $\Phi_{sl}$. Practically, this only works up to a critical value until the Cassie state becomes unstable.

Whereas air pockets between surface and drop are necessary for super liquid-repellency, the Wenzel and Cassie-Baxter equations cannot be used to predict contact angles for practical surfaces and to confirm if a surface is super liquid-repellent or not. Both equations are derived based on energy minimization and neglect contact angle hysteresis and pinning. They also do not consider dynamic contact angles, i.e. $\theta_{adv}$, $\theta_{rec}$ and roll-off angles. The equations also do not give any information on lateral adhesion forces. These are all essential aspects of super liquid-repellent surfaces. Moreover, the Cassie state corresponds to a local energy minimum in the energy landscape, whereas the Wenzel state is lowest in energy. The Cassie state is thus metastable and an irreversible transition to the Wenzel state can occur.[29] Once trapped in the Wenzel state, a drop can only go back to the Cassie state if external energy is provided.[30] The stability of the Cassie state depends on various points, e.g. on the shape of the surface texture, surface chemistry, surface tension of the liquid and the drop size. The stability also depends on external conditions like temperature and vibrations. All these aspects determine the stability of the Cassie state and affect the critical pressure a liquid can exert on a surface texture before it sags into the structure and wets the substrate. This critical pressure, where a liquid starts to sag-in, is the so-called impalement pressure and will be discussed in more detail in chapter 1.2.7.[31]

Even though the Wenzel and Cassie-Baxter equations are of limited use to determine if a surface will be super liquid-repellent or not, they highlight that surface texturing is a key parameter for the preparation of such surfaces.

### 1.2.4 **Superhydrophobic surfaces**

Superhydrophobic surfaces repel water at inclination angles of 10° and less and have apparent contact angles of more than 150°.

Numerous examples of such surfaces can be found in nature, e.g. various plant leaves, exoskeletons of certain insects like the water strider, or feathers and furs of animals.[3, 8, 32] Most of these superhydrophobic surfaces exhibit a hierarchal surface roughness on two length scales: For example, electron microscopy images of a water strider leg and a lotus leave reveal that both have a primary surface structure in the micrometer range which is again decorated with surface textures on the nm scale (**Figure 9**).

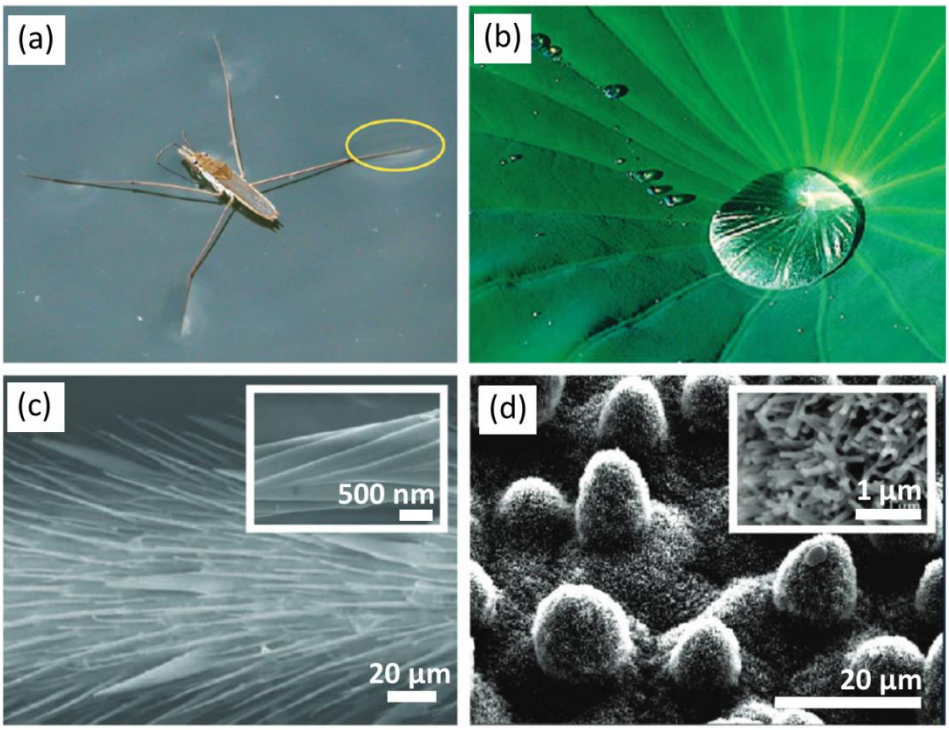


**Figure 9**: Examples of natural superhydrophobic surfaces. a) The legs of a water strider and b) the lotus leaf. Both surfaces have a hierarchical structure on two length scales. c) and d) are electron microscopy images of a) and b). The water strider legs consist of micrometer-sized setae c) covered with nano grooves (inset, scale bar: 200 nm). d) Lotus leaf showing microprotrusions covered with nanometer-sized wax crystals (inset). Reprinted with permission from Ref[3]. Copyright 2010 American Chemical Society.

The nanoscale roughness provides an additional wetting barrier and increases the stability of the Cassie state.[33] Fabrication techniques of superhydrophobic

surfaces are highlighted together with superamphiphobic surfaces in chapter 1.2.8.

### 1.2.5 **How drops move on superhydrophobic surfaces**

If a drop in the Cassie state readily moves or not, depends on the lateral adhesion forces which are connected to the movement of the three-phase contact line. This again is connected to pinning and depinning events between the surface and the liquid. Understanding and controlling the pinning and depinning dynamics is of practical relevance to improve and tune super liquid-repellent surfaces. The pinning and depinning events typically take place at a length scale of tenths to hundreds of µm and can thus not be well resolved using optical cameras. Over the last years, laser scanning confocal microscopy (LSCM) turned out to be a versatile technique to study dynamic wetting processes. LSCM relies on an inverted laser which scans a drop sitting on a thin and transparent (glass) slide point by point.[29, 34] The reflection of the laser beam is recorded and, if applicable, the fluorescence of an excited dye. Typical scan sizes are in the order of hundreds of µm and the resolution of one pixel is up to 500 nm (lateral) and 200 nm (horizontal). Images can be recorded as time evolution to visualize dynamic wetting processes. The wettability of the glass substrates can be varied by chemical treatment and surface texturing. In **Figure 10**, an LSCM is used to observe the contact area of a drop sitting on an array of micropillars.[34] Micropillars of different geometries can be readily prepared by lithography and are a well-established model system to study wetting. The micropillars shown in Figure 10 are superhydrophobic, i.e. water drops have high static contact angles and roll-off at less than 10° (Figure 10b). In Figure 10c, a vertical cross section of the three-phase contact line imaged by LSCM is shown.

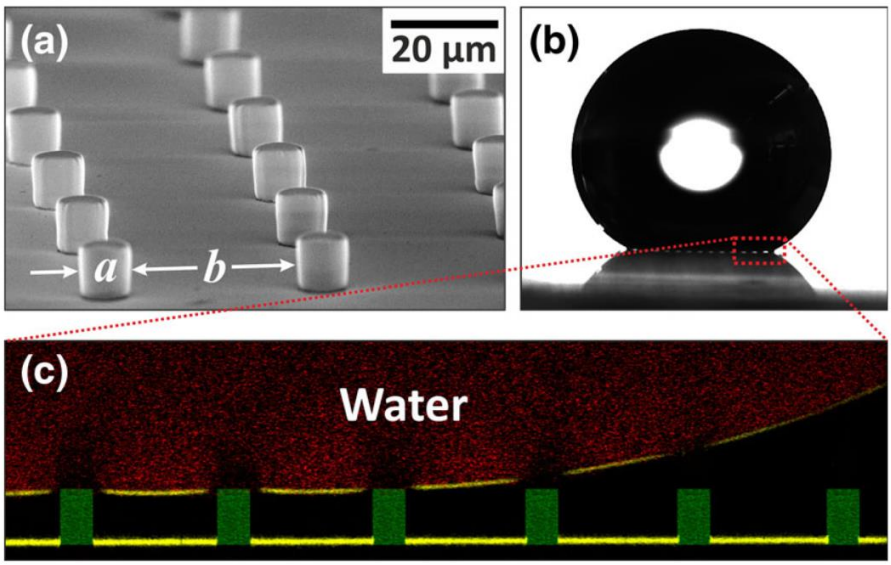


**Figure 10**: a): Scanning electron microscopy image of an array of cylindrical, hydrophobized micropillars ($a = 10\ \mu m, b = 30\ \mu m, height = 15\ \mu m$). b) Video image of a 2 mm high water drop sitting on the micropillar surface. c) Vertical LSCM image of a water drop (dyed with Alexa Fluor 488) on the micropillar surface shown in a) and b). The water drop is shown in red, the refraction from the interfaces are shown in yellow. The position of the pillars are known from the raw data. The green pillars are artificial and were added via image post processing to achieve a better readability. Figure 10 adapted with permission from Ref[34]. Copyrighted by the American Physical Society.

Whereas it is poorly distinguishable from Figure 10b if there are air cushions below the drop, the Cassie state can be clearly confirmed by LSCM in Figure 10c. Furthermore, the dynamic responses of the three-phase contact line can be observed when the drop overcomes lateral adhesion and leaps into motion: Schellenberger et al. tilted the LSCM and visualized the advancing and receding contact angle of drops on superhydrophobic pillar surfaces.[34] **Figure 11** shows a series of snapshots of the advancing (Figure 11a) and receding contact line (Figure 11b). Their study shows that the movement of drops on superhydrophobic surfaces is discontinuous due to contact line pinning to the pillars: When the drop started to move, the contact line gradually bent down until it touched the next pillar (Figure 11a, 29.74 s).

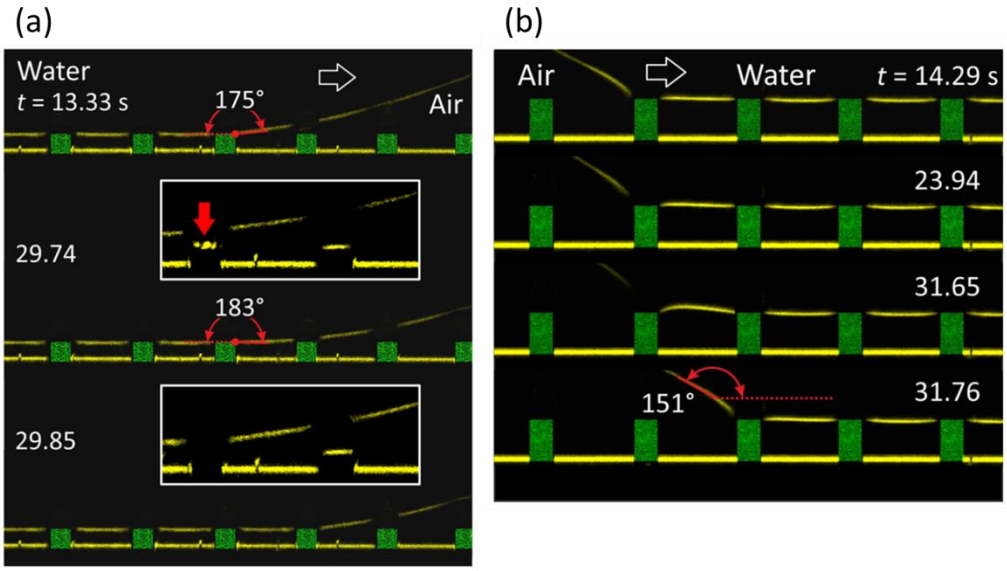


**Figure 11**: Waterfronts a) advancing and b) receding on a superhydrophobic micropillar surface inclined by 9°. (a) At t=13.33 s the waterfront touches the third pillar from the left and gradually bends down toward the fourth pillar. The image at t=29.74 s shows the waterfront just before touchdown. The inset shows the refraction at the pillar top face, indicating that it is not wetted yet. At t=29.85 s the waterfront touches down on the fourth pillar and no refraction of the pillar top face can be seen anymore in the inset. This confirms wetting of the pillar. b) The receding contact angle distorts from t=14.29 s until t=31.65 s. At t= 31.65 s the contact line detaches from the second pillar and jumps one pillar further. The measured receding contact angle is indicated by the red lines at t= 31.65 s. Pillar geometries: a) $a = 10\,\mu m, b = 30\,\mu m, height = 10\,\mu m$; b) $a = 10\,\mu m, b = 30\,\mu m, height = 16\,\mu m$. Figure 10 adapted with permission from Ref[34]. Copyrighted by the American Physical Society.

Once in contact, the pillar was immediately fully wetted and the contact line jumped forward. Similarly, the liquid pulled on the last pillar at the rear side of the drop. The liquid detached from the pillar when the surface tension of the liquid pulled strongly enough to overcome the adhesion force to the respective pillar. In this context, it was confirmed that the advancing contact angles reach values of 180° and more on superhydrophobic surfaces before touchdown on the next pillar. This implies that the advancing contact angle, and consequently the contact angle hysteresis CAH, is not a suitable measure of super liquid-repellency. In contrast, the receding contact angles measured by LSCM were in good agreement with goniometer measurements and give a measure of the drop adhesion and thus mobility. Hence, receding contact angles and roll-off angles are more useful to determine if a surface is super liquid-repellent or not.

### 1.2.6 **Superamphiphobic surfaces**

Most superhydrophobic surfaces are wetted by low surface tension liquids. Surfaces which repel both, water and low surface tension liquids, are superamphiphobic. Superamphiphobic surfaces are promising for various applications, amongst others to retard corrosion of metals and slow down biofouling.[35-38]

Superhydrophobicity is readily achieved by coating a simple surface texture with a low surface tension compound. In contrast, superamphiphobic surfaces are much more challenging to design and prepare. This comes from the fact that water has a surface tension which is about three times higher than those of many organic solvents (72.8 mN/m for water, compared to e.g. 27.5 mN/m for n-hexadecane at room temperature). The term superamphiphobicity is yet not strictly defined. Similarly to superhydrophobic surfaces, “oil drops” have high apparent contact angles (150° and more) and roll-off below an inclination angle of 10°. Therefore, it is important to report the specific liquids a surface repels and which not. It is also important to report the time elapsed between the deposition of the drop and the measurement of the contact angles. Generally, contact angles are measured less than a few minutes after the deposition of the drop. It was shown recently, that drops can impale a surface texture over time, especially if the surface tension of the liquid is low.[39] Common reference solvents are diiodomethane (50.8 mN/m), rapeseed oil (~33 mN/m) and hexadecane (27.5 mN/m). Ideally, superamphiphobicity is confirmed with liquids, which have a surface tension of $\gamma_{la}$< 30 mN/m. In some studies this is not the case and calling such surfaces “superamphiphobic” is questionable.

According to the Young equation (eq. 1.2), water forms a material contact angle of $\theta_E > 90^o$ on a flat, hydrophobic surface if the surface tension of the solid is less than ~20 mN/m.[40] This is true e.g. for Teflon which has a solid-air surface tension of ~18.5 mN/m. For most alkanes ($\gamma_{la}$~20-30 mN/m), the surface tension of the solid needs to be ~6 mN/m to yield $\theta_E > 90^o$. This is hardly feasible and flat surfaces are generally oleophilic towards alkanes and other low surface tension liquids, i.e. have contact angles $\theta_E < 90^o$. Consequently, a simple, hydrophobic surface texture can readily lead to water drops in the Cassie state, but low surface tension liquids generally end up in the Wenzel state.

However, this can be circumvented by the fabrication of surface textures which have overhangs. Overhangs are surface features which bear out of the central chunk of the surface asperity. They can act as an energy barrier for the drop and prevent impalement of the liquid into the coating, even in the case of low surface tension liquids. The presence of overhangs can thus lead to metastable superamphiphobic surfaces even though the material is intrinsically oleophilic.[41-46] As an example, Tuteja et al. prepared a periodical array of reentrant pillars, so-called microhoodoos, by stepwise etching of silicon (**Figure 12**a).[47]

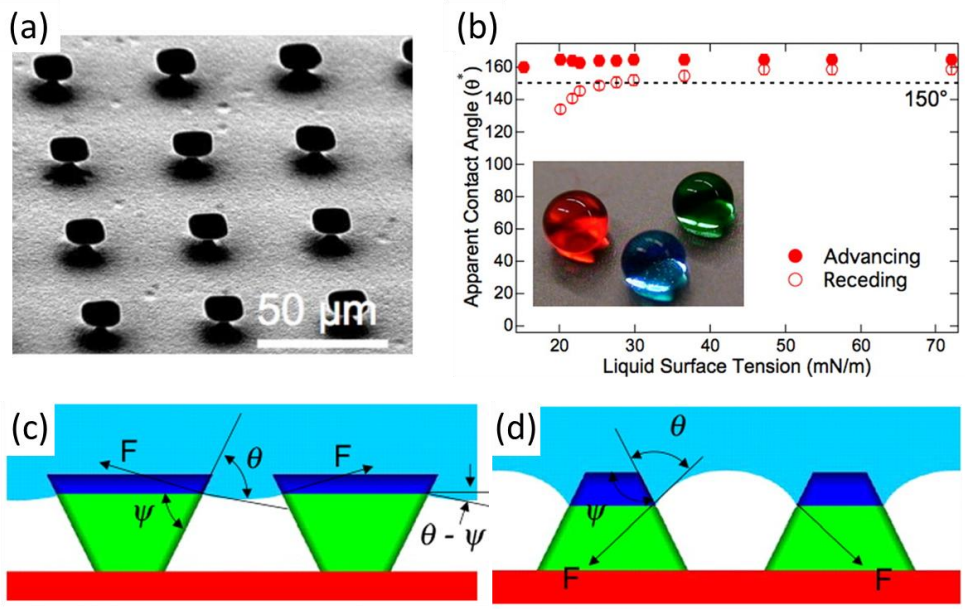


**Figure 12** a) SEM image of an array of "microhoodoos" prepared by stepwise etching of silicon. b) Apparent advancing and receding contact angles on hydrophobized microhoodoos. Inset: Drops of heptane (red), methanol (green) and water (blue) are repelled from an array of microhoodoos. c) and d) show schematic diagrams illustrating the role of the geometrical angle $\Psi$ on the curvature of the liquid-air interface, while $\theta_E$ is the same in both cases. From Ref[47]. Copyright 2008 National Academy of Sciences.

After hydrophobization, the microhoodoos repelled even heptane and methanol (Figure 12b). Figure 12c and d show a liquid interface resting on different surface textures. The material contact angle $\theta_E$ and the local geometrical angle of the specific texture $\Psi$ are shown. The three-phase contact line can be pinned to an overhang if $\theta_E$ is equal or higher than $\Psi$. In this case, the net force of the liquid-air interface is directed upwards towards the top of the texture (Figure 12c). In this case, a local energy minimum of the interfacial free energy is obtained which

allows the metastable pinning of the three-phase contact line at the overhang preventing wetting of the substrate. If the opposite $\theta_E < \Psi$ is true, the liquid will be pulled downward, resulting in complete wetting of the substrate (Figure 12d). Surface textures having overhangs where $\Psi < 90°$ is hence a key element to obtain superamphiphobic surfaces.[30, 47] Recently, the importance of surface morphology over surface chemistry was impressively demonstrated by Liu and Kim.[48] They revisited the design of the microhoodoos and added an additional, vertical overhang to the rim of the hoodoos (**Figure 13**).

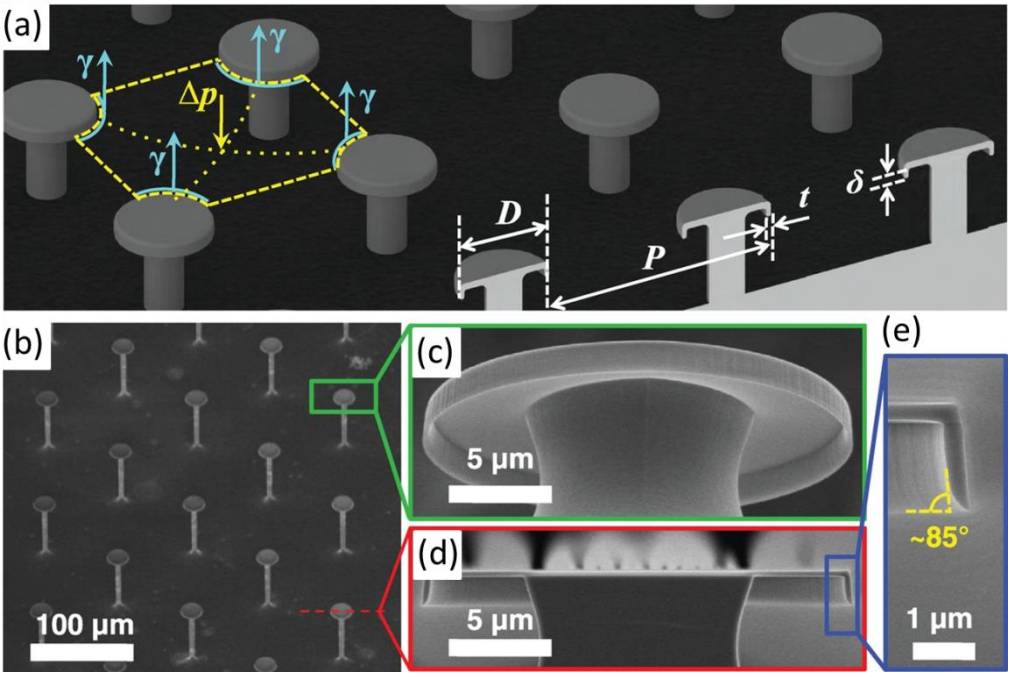


**Figure 13**: a): Schematic picture of double reentrant microhoodoos having vertical overhangs. D is the post diameter (D~20 µm), P the center to center distance (P=100 µm), $\delta$ and t are the length and thickness over the vertical overhang, respectively (t~300 nm and $\delta$=1.5 µm. b) Top view SEM of double reentrant microhoodoos. c) Bottom angle and d) cross-sectional view of a post. e) Cross-sectional image of a vertical overhang. From Ref[48]. Reprinted with permission from AAAS.

The vertical rim provides an additional stability of the Cassie state because the contact angle of the liquid at the rim is close to 0° and the surface tension has a component pointing upwards to the bulk liquid. Water, several oils and even fluorinated solvents with a surface tension as low as 10 mN/m were efficiently repelled. Most surprisingly, this was even the case if the microhoodoo surface

was not chemically hydrophobized beforehand which shows the tremendous impact of the surface texture.

### 1.2.7 **Design parameters of super liquid-repellent surfaces**

Several theoretical studies consider the role of surface texture, in particular the shape of single asperities, on the specific properties of super liquid-repellent surfaces. These properties can e.g. be dynamic contact angles, the mechanical strength of the asperities and hence durability of the coating or the impalement pressure. To tune these properties, it is important to understand how they interplay with shape, size and spacing of the surface texture. Depending on the surface of interest, different geometrical models and parameters can be considered, e.g. microhoodoos and similar systems[30, 42, 45] or individual fibers as part of a fabric[49].In a different case, super liquid-repellent surfaces were modeled as pillars consisting of stacked, connected spheres.[31, 43] This model serves well for surfaces which were prepared by assembly of colloids (**Figure 14**, see chapter 1.2.8 for details about preparation of super liquid-repellent surfaces):

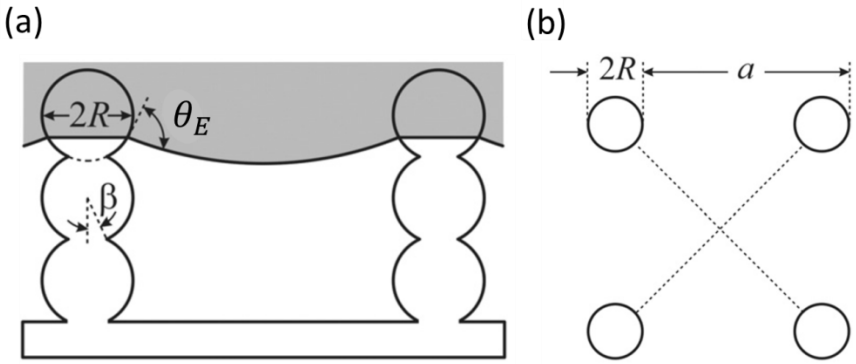


**Figure 14**: Idealized model of a super liquid-repellent layer based on pillars of stacked, connected spheres. Side view (left) and top view (right). The grey shaded area represents a liquid. Reprinted from Ref[31]. Copyright 2015, with permission from Elsevier.

The liquid is pinned at the upmost spheres of the pillars. The pillars are formed of N vertically stacked spheres of same radius R. The spheres are connected by solid bridges with a connection angle $\beta$. $a$ is the pitch distance between the pillars.

An important aspect of super liquid-repellent surfaces is the mentioned impalement pressure (chapter 1.2.3). Practical examples, where the impalement pressure is relevant, are e.g. water repellent textiles or membranes. Here, the membranes have to withstand the pressure exerted by a liquid without breakthrough of the liquid to the other side of the membrane. Instead of a fiber model, the aforementioned model based on a stack of sintered spheres is further discussed because it has more practical relevance in the context of this thesis (**Figure 15**).

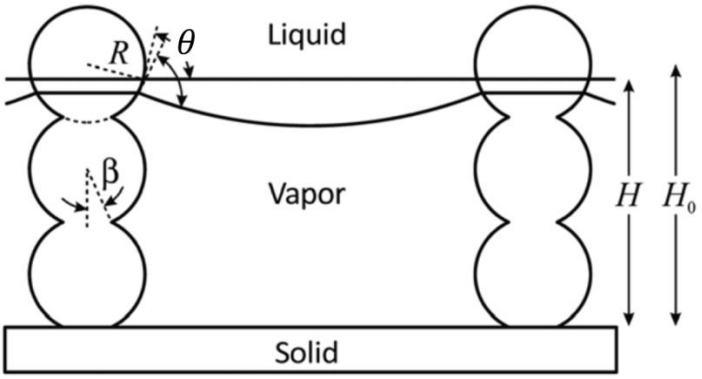


**Figure 15**: Schematic impalement of a model system for super liquid-repellent surfaces based on pillars of stacked, connected spheres. The liquid-air interface sags down with increasing pressure of the liquid. Adapted from Ref[43] with permission of The Royal Society of Chemistry.

In equilibrium, the liquid-air interface is nearly planar and pinned at $\theta_E$ to the uppermost spheres of the pillars at a height $H_0$ which is equal to $H_0 = (2N-1)Rcos(\beta)$. The liquid-air interface starts to sag down when the pressure of the liquid increases. At a given pressure the reduced height $H$ is given by $H = (2N-1)Rcos(\beta) - Rcos(\theta_E)$. The liquid wets the substrate at a critical impalement pressure. The critical impalement pressure is given by the Laplace equation, which relates the mean curvature to the pressure difference P between the liquid and the air phase, depending on the interfacial tension of the liquid:

$$P = \frac{4}{\sqrt{2}}\frac{\gamma}{a} \qquad \text{(eq. 1.5)}$$

To increase the value of the critical impalement pressure, the distance of the pillars should be as narrowly spaced as possible and the pillars should be taller than $H > \frac{a}{\sqrt{2}}$.

The Cassie-Baxter equation, in turn, suggests minimizing the solid-liquid fraction $\Phi_{sl}$ to obtain high apparent contact angles values. Preferentially, the pillar distance $a$ is as big as possible while the particle radius $R$ is as small as possible.

In contrast, the pillar structure shows an increasing vertical stress resistance with increasing $R$ and $\beta$ as well as with decreasing $a$. The critical vertical stress $\sigma_{vp}$ for yielding a pillar is given as:

$$\sigma_{vp} = \frac{\sigma_y \pi (R sin\beta)^2}{a^2} \qquad \text{(eq. 1.6)}$$

Here, $\sigma_y$ is the yield stress of the pillar bulk material. For example, for $R = 50\ \mathrm{nm}$, $a = 1,\ \beta = 30°$ and $\sigma_y = 6.5\ \mathrm{GPa}$ (for a silica pillar), the critical vertical stress $\sigma_{vp}$ is 13 MPa.[43, 50]

However, increasing R and decreasing $a$ to maximize the mechanical strength is in direct contrast to the aforementioned minimization of $\Phi_{sl}$ to achieve high static contact angles $\theta_{app}$. This contradiction shows that both aspects, i.e. high static contact angles $\theta_{app}$ and a high vertical stress resistance $\sigma_{vp}$, cannot be optimized simultaneously, but need to be balanced against each other.

### 1.2.8 **Fabrication of super liquid-repellent surfaces**

Numerous studies present approaches to fabricate super liquid-repellent surfaces. Especially, superhydrophobic surfaces found in nature, like various plant leaves or insect skins, fueled the preparation of artificial, biomimetic superhydrophobic surfaces. More and more studies are also reported on the fabrication of superamphiphobic surfaces, even though they are more challenging to prepare because surface textures with overhangs are required.

Superhydrophobic and superamphiphobic surfaces can be fabricated by different techniques, e.g. templating, sol-gel chemistry, layer-by-layer deposition, bottom-up fabrication, phase separation of polymer/solvent or polymer/polymer mixtures, plasma treatment of polymer surfaces, surface etching, chemical vapor deposition, anodic oxidation of substrates, and electrochemical deposition.[51-57] Summarizing details and specialties about each technique is beyond the scope of this work, but comprehensive reviews are cited above. Two examples are shown

in the following based on bottom up and templating on rigid surfaces and sol-gel chemistry on textiles.

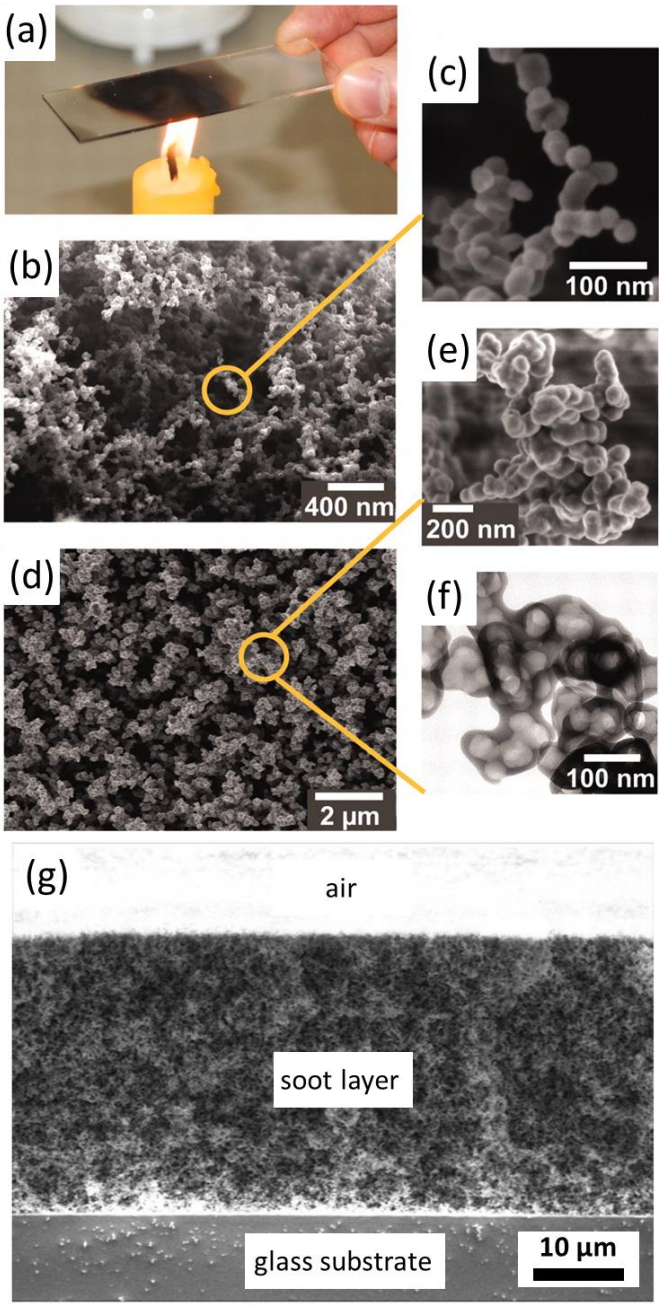


**Figure 16**: a) Soot collection. b) SEM of the highly porous soot network deposited on the glass slide. c) SEM of a chain of almost spherical carbon spheres. d) SEM of the soot network coated with a silica shell after chemical vapor deposition. e) SEM of a silica cluster after carbon removal at 600 °C. f) TEM of a silica cluster after carbon removal. g) Cross-section of the silica-stabilized soot network shown in d. From Ref[46]. Reprinted with permission from AAAS.

The first example, which is also relevant for this work, is based on thermal deposition of nanoparticles to prepare a robust model system for superamphiphobic surfaces.[46] The other example shows the fabrication of superamphiphobic textiles which can be used as membranes and functional clothing.[49, 58, 59]

Soot can be collected on a fire resistant substrate like glass or steel by holding it into the flame of a candle (**Figure 16**a).[46] A soot layer is gradually built up from the substrate with increasing deposition time and can reach a thickness of 2 to several tenths of µm. Soot consists of loosely connected carbon particles with a size of 30 to 50 nm in diameter. The particles are loosely connected by van der Waals forces and form a fractal-like, highly porous network with numerous overhangs (Figure 16b and c). The soot network is used as a template and coated with silica from the gas phase via chemical vapor deposition of tetraethoxysilane. The silica adopts the shape of the soot network and keeps it, even after sintering of the specimen at 600 °C (Figure 16d-f). The carbon interior, in contrast, is completely combusted by the sintering step as shown in the TEM image in Figure 16f, and almost transparent surfaces are obtained. At this stage, the samples are superhydrophilic and become superamphiphobic after deposition of a semi-fluorinated silane.

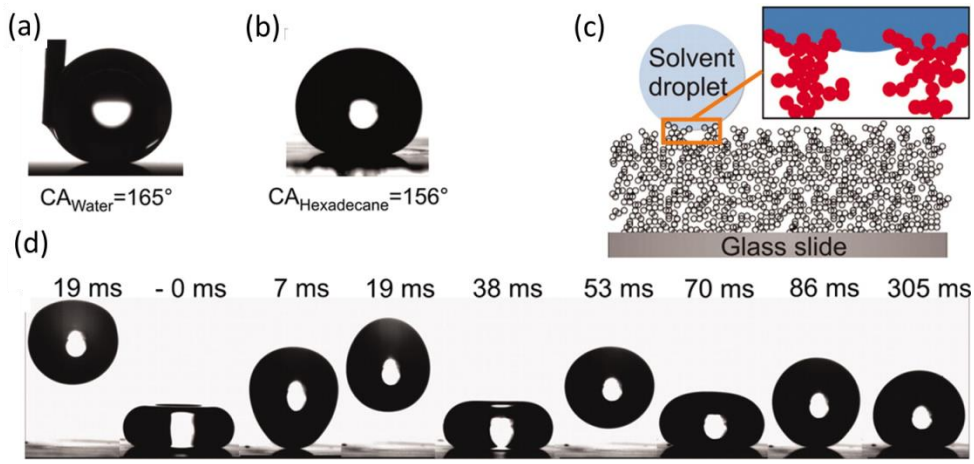


**Figure 17**: a) Water and b) hexadecane on a candle-soot based super-amphiphobic surface. The contact angles are $CA_{water}=165^{o}$ and $CA_{hexadecane}=156^{o}$, respectively. c) Schematic drawing of a drop resting on overhanging silica structures. d) Snapshots of a 5 µl hexadecane drop impacting and bouncing on a superamphiphobic surface. From Ref[46]. Reprinted with permission from AAAS.

Water and hexadecane have apparent contact angles of 165±1° and 156±1° and are repelled at tilting angles of 2±1° and 5±1°, respectively (**Figure 17**a and b).[46] Drops of low surface tension liquids falling from a certain height are efficiently reflected, like hexadecane in Figure 17d.[46, 60]

The structure of the candle soot hence provides multiple overhangs which need to be overcome before the substrate is fully wetted (Figure 17c). This makes candle soot-templated surfaces an efficient and simple strategy to fabricate superamphiphobic surfaces.

Textiles offer a couple of advantages as substrates for the fabrication of super liquid-repellent coatings. They can be easily made super liquid-repellent by surface functionalization and by adding further levels of hierarchal structures using sol-gel chemistry.[49, 59] The structure of textiles is composed of numerous interwoven fibers and textiles are thus intrinsically rough. Also, the shape of a fiber acts as an overhang perpendicular to its prolongation. The interwoven structure withstands mechanical stress well and most of the surface stress is dissipated into the topmost fibers. Consequently, nanoparticles or other nanostructures deposited on the textiles, to increase the repellency, can be shielded to a certain degree. Especially nanostructures in between the fibers are exposed to a much lower stress. Leng et al., for example, prepared multiscale rough superamphiphobic textiles by adding a layer of micro and nanoparticles on cotton textiles using sol-gel chemistry (**Figure. 18**).[59] First, the textiles were decorated with a layer of larger silica particles (diameter of 800 nm). The particles were created in-situ by hydrolysis and condensation of tetraethoxysilane (Stöber reaction). After their adhesion to the textile, the particles were covalently bonded by subsequent hydrolysis of silicon tetrachloride. In the next step, the surface of the nanoparticle decorated textile was functionalized with (3-aminopropyl)-triethoxysilane (APS). The surface of the textile became positively charged due to the APS treatment. Negatively charged silica nanoparticles (diameter of about 160 nm) attached to the textile by electrostatic interaction. The textile was finally hydrophobized with a fluorosilane. Leng et al. found that the nanoparticles were essential to repel hexadecane efficiently.

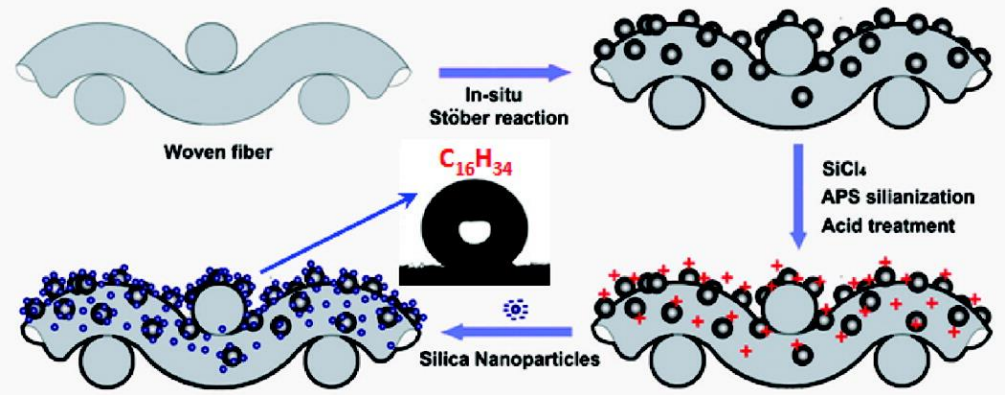


**Figure. 18**: Scheme illustrating the coating process used by Leng et al. to obtain multiscale rough superamphiphobic cotton textiles by adsorption and functionalization of silica particles using sol-gel chemistry. Reprinted with permission from Ref[59]. Copyright 2009 American Chemical Society.

### 1.2.9 **Challenges and opportunities of super liquid-repellent surfaces**

Despite the promising applications of superhydrophobic and super-amphiphobic surfaces, a widespread use in consumer products is not observed yet. The major reason is that under real conditions such surfaces seldom retain super liquid-repellent for a long time. Amongst others, surfaces degrade or alter their properties due to abrasive wear, UV exposure, chemical reaction, acidic and basic corrosion, solvent contamination and biofilm deposition. One of the severest stresses for super liquid-repellent surfaces is wear abrasion because it breaks the surface texture. [61-66] Surface textures are especially prone to wear because a vertical or a shear stress is not equally distributed over the entire surface area $A_0$, like in the case of a flat surface. The stress is rather distributed over the top faces of the surface texture, which directly contact the abradant. As a result, the real contact area $A$ between abradant and surface is greatly reduced and the stress acting on the surface texture is much higher than the stress acting on a flat surface instead. Once a critical stress is exceeded, individual asperities of the surface texture fatigue and break. Broken asperities reduce the surface roughness and hydrophilic spots on the surface can be revealed. Both increase the lateral adhesion of drops which is connected to a decrease of super liquid-repellency. This concept is allegorized in **Figure 19** where a drop does not roll-off a superhydrophobic surface after its abrasion:

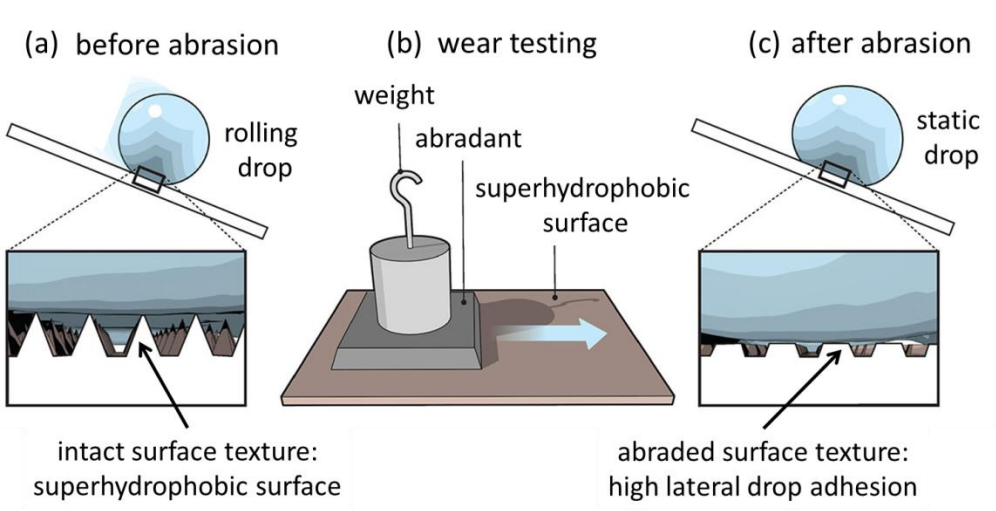


**Figure 19**: a) Superhydrophobic surface before applying stress. Drops easily roll-off. b) Stress is applied to the surface by pushing a sand paper loaded with a specific weight. c) The top parts of the asperities are damaged by abrasion and a drop does not roll-off anymore. From Ref[61]. Adapted with permission from AAAS.

Accordingly, tuning the mechanical durability of the surface and the strength of the asperities for a given application is one of the key aspects towards consumer products with super liquid-repellent properties. However, measuring and comparing mechanical quantities, an essential part of the tuning process of such coatings, is not trivial. The mechanical durability results from the interplay of several minute details: Geometry and density of the asperities, material properties in terms of elasticity and hardness, and the thickness of the coating. This complex interplay and versatility leads to surfaces spanning a broad range in terms of mechanical durability. This also hinders the adoption of a unique and generalized testing procedure to evaluate the mechanical strength and durability of super liquid-repellent surfaces.

Consequently, various tests can be found in the literature to evaluate the mechanical durability and strength of super liquid-repellent coatings. They can be separated into two categories which are qualitative (i) and quantitative (ii) tests.

(a)

Recommendations for primary mechanical durability tests.

| Durability test | Method | Apparatus | Desired performance |
|---|---|---|---|
| Adhesion | ASTM D3359 | Blade for scratching and high adhesion strength tape (e.g. 3 M™ 250) | 5B (all squares should remain intact) |
| Abrasion (smoothing, soft/mild abradant) | Linear abrasion | Taber CS-5 abradant, crocking cloth or common textiles | Low CAH after 10's of cycles with applied pressure > 10 kPa |
| Abrasion (smoothing, hard/resilient abradant) | Linear abrasion | Rubber-type abradant (e.g. Taber CS-10F) | Low CAH after 10's of cycles with applied pressure > 10 kPa |
| Abrasion (scratching, vitrified abradant) | Linear abrasion | Vitrified abradant (e.g. Taber H-18 or sandpaper with varying grade | Low CAH after 10's of cycles with applied pressure > 10 kPa |
| Finger Rub (with and without glove) | Linear rubbing | No apparatus needed | No material removed to |

(b)

Recommendations for Secondary Mechanical Durability Tests.

| Methods | Sample Applications | Apparatus | Desired Performance |
|---|---|---|---|
| Sand impact | Outdoor applications in dusty environment | Sand container with regulated particle delivery system | Low CAH after 40–50 g of particles delivered from >20 cm height within 5 min |
| Drop impact | Outdoor applications in general | Water drop dispenser with adjustable height | Low CAH after thousands of drops impacting with velocity > 1 m/s |
| Jet/spray impact | Outdoor applications in rainy environment | Jet dispenser or spray nozzles supplied with adjustable pressure | Low CAH with >25 kPa pressure with exposure time > 30 min |
| Ultrasound baths or rotary slurry test | Underwater | Ultrasonic cleaner and particles dispersed in water | Low CAH after several hours of treatment |

**Figure 20**: Overview of qualitative mechanical durability tests to test super liquid-repellent surfaces. Reprinted from Ref[66]. Copyright 2016, with permission from Elsevier.

(i) Qualitative tests impose a certain mechanical stress to a sample and its effect, e.g. fatigue, delamination and fracturing, and are judged according to the test criteria. Most importantly, the dynamic wetting behavior needs to be confirmed before and after the test to detect an eventual break-down of super liquid-repellency. This is of course only possible if the size of the abraded area is large enough to deposit drops. Additionally, depending on the length scale of the surface damage, the zone of impact can be visualized by optical images, scanning electron microscopy or scanning probe microscopy. Milionis et al. recently reviewed qualitative durability tests used for superhydrophobic surfaces and further subdivided them into primary and secondary mechanical durability tests (**Figure 20**).[66] The primary tests focus on the adhesion strength of the coating to the substrate and its abrasion resilience: Adhesion of the coating can be tested by performing (cross) cuts on the surface and then peel off a piece of adhesive tape glued to the respective area (ASTM D3359/ ISO 2409). A controlled shear stress can be performed by linear abrasion, using different abrasion materials and different loads (similarly to ASTM D2486). The secondary mechanical durability tests mimic outdoor situations. For example, a certain amount of sand is dropped on a surface over a specific time (ASTM D968) or the surface is exposed to a water jet at a certain pressure. A third category is also proposed and its layout is flexible, depending on the requirements of a specific application. For example, if the super liquid-repellent surface should be durable against scratches, it can be tested by scratching it with pencils of different hardness (ASTM D3363/ ISO 15184). Momentarily, linear abrasion using sandpaper (as shown in Figure 19) is one of the most popular techniques to quantify the mechanical durability. Unfortunately, a comparison of mechanical durability between relevant studies is hampered because the testing conditions are not standardized and differ between the studies. Parameters which should be agreed on in the future are e.g. grit size of the sandpaper, applied load, traveled distance, cycles of abrasion. Certainly, the advantages of qualitative tests are that they are application oriented, simple, quick and low priced. Such tests do not work well anymore if mechanically similar samples are investigated. This can happen, especially if a new coating is developed and the influence of single parameters on the coating durability needs to be judged. Furthermore, no material properties and other details, e.g. about the breaking mechanism, can be

obtained from quantitative tests. This is only possible with force sensitive measurements:

(ii) Quantitative tests are force sensitive and measure the displacement into a sample as function of imposed force. A schematic force displacement curve of a spherical probe indenting a plane surface is shown in **Figure 21**:

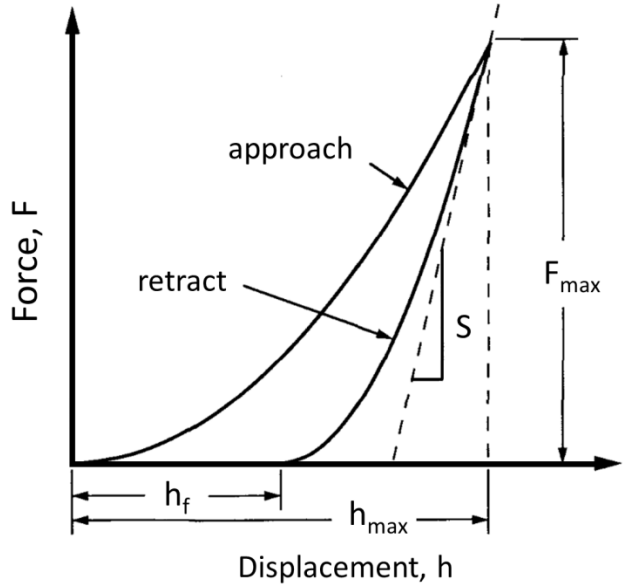


**Figure 21**: Force versus displacement curve of a probe indenting a flat surface. Adapted from Ref[67].

In a typical indentation experiment, the probe approaches the sample up to a maximum indentation depth $h_{max}$ where a force $F_{max}$ is reached. The probe then retracts and reaches a final indentation depth $h_f \leq h_{max}$ where the contact to the surface is lost if adhesion is not significant. If $h_f < h_{max}$, a residual indent will be found on the surface.

How to analyze force-displacement curves based on different contact models is explained in more detail in the appendix, chapter 7.1. There, it becomes clear that obtaining quantitative values from indentation experiments on super liquid-repellent surfaces is appealing but not trivial. The surfaces are extremely rough and in many cases the surface asperities have a random shape. Often, the asperities do not respond elastically, but break at low yield stresses which complicates the analysis. Ideally, the surfaces are probed with a high nominal contact area to average over many asperities and to get an averaged mechanical response. Preferentially, the indentation depth does not exceed the coating

thickness by more than 10% to neglect substrate effects. Also, the surface needs to be probed with a high sensitivity due to the fragility of the surface asperities. Whereas nanoindentation offers a high nominal contact area, generally $mm^2$ to few $\mu m^2$ in diameter, its sensitivity is in the range of mN down to few hundreds and tenths of nN. Scanning probe microscopy, on the other hand, provides high sensitivity (down to fN), but the contact area is typically in the order of a few $nm^2$ or even less. Advantages of both, i.e. high contact area and high sensitivity, can be obtained by replacing the sharp tip on an SPM by a µm-sized colloid.[68, 69] Using such colloidal probes might be a way to precisely resolve the influence of reactants and reaction parameters on the mechanical properties, which allows tuning surfaces in terms of mechanical strength and balance their reaction parameters against their wettability.

## 1.3 The Leidenfrost effect

Similarly to super liquid-repellent surfaces, drops on a hot surface produce a vapor cushion which prevents contact and wetting of the substrate.[1, 9, 10] Already in 1756, Johann Gottlob Leidenfrost observed this effect when he placed a drop on a hot spoon. He placed a candle behind the drop and realized that a thin vapor gap between drop and spoon exists.[11] A similar situation to the experiment of Leidenfrost is shown in **Figure 22**a, where a drop is placed on a 300 °C hot polished aluminum plate. The magnified image shows that there is a thin vapor cushion between both, drop and substrate.[1] Drops of different sizes can levitate under these conditions. Figure 22a shows a small, almost spherical drop with a small contact area, whereas a large puddle, flattened by gravity, having a large contact area is shown in Figure 22b. Biance et al. found that the upper limit of stable water Leidenfrost drops is about 2 cm in diameter.[10]

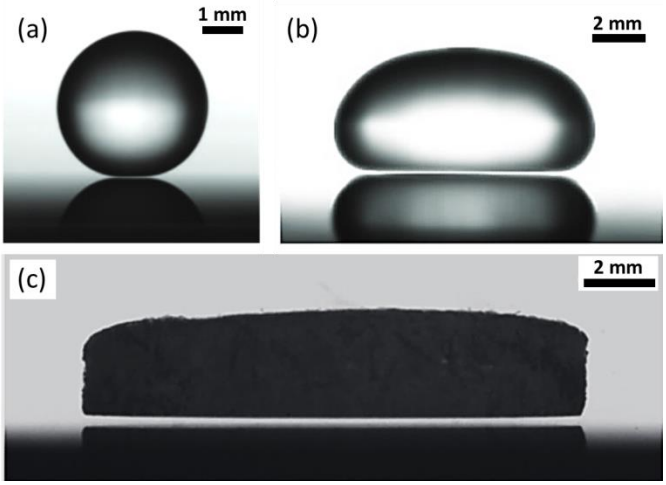


**Figure 22**: Levitating water drops a) and b) and dry ice c). The substrate is a 300 °C hot polished aluminum plate. Adapted From Ref[1].

They also investigated the thickness of the vapor layer by diffraction of a laser beam at the vapor gap. From the diffraction pattern, they found that the thickness of the vapor cushion is in the order of 100 µm. Solid objects can also float on hot surfaces if the solid sublimates under the chosen conditions. On the 300 °C hot aluminum plate, for example, a piece of dry ice (frozen carbon dioxide, sublimation temperature =-78 °C) generates sufficient vapor to float at about the same height above the substrate as the water drops do (Figure 22c).[70]

### 1.3.1 **Features of boiling and the lifetime of drops**

For a drop to enter the Leidenfrost regime, the temperature difference between substrate and boiling point of the drop needs to be large enough to sustain a constant vapor production. The lower critical value for this temperature difference depends on the boiling or sublimation point of the liquid or object and can be obtained from the respective boiling or sublimation curves. **Figure 23** exemplarily shows the boiling curve of water as function of heat flux against the surface superheat $\Delta T$.[71, 72]

$$\Delta T = T_{sur} - T_{sat} \qquad \text{(eq. 1.7)}$$

Here, $T_{sur}$ is the surface temperature and $T_{sat}$ is the saturation temperature of the liquid, i.e. the maximum temperature of the liquid before it evaporates. Until about $\Delta T \sim 10\,°C$ heat is efficiently transferred from the wall to the liquid. The heat causes the formation of single vapor bubbles at the surface. These small bubbles can promote convection between surface-near warm water and cooler bulk water. At higher $\Delta T$ the heat flux increases and bubbles start to rise. The number of bubbles increases with increasing $\Delta T$ and heat flux. This regime is called nucleate boiling. At a certain $\Delta T$ value, a critical heat flux is achieved which indicates that a critical percentage of the solid-liquid interfacial contact area turned into a solid-gas interfacial area due to strong bubble nucleation. The bubbles act as an insulator between surface and water and decrease the efficiency of the heat flux. With increasing $\Delta T$, boiling enters an unstable regime which is also called transition boiling. Though $\Delta T$ increases thereafter, the heat flux decreases because the insulating solid-gas interfacial area grows. At a certain $\Delta T$ value, for water about $\Delta T \sim 50\,°C$, the heat flux reaches a local minimum and a continuous vapor film establishes between surface and liquid. From this point on, called the Leidenfrost temperature $T_L$, the liquid is in the film boiling regime and the liquid hovers on a vapor cushion. Film boiling is maintained upon further heating accompanied by an increase in heat flux which accelerates evaporation of the liquid.[1, 72, 73]

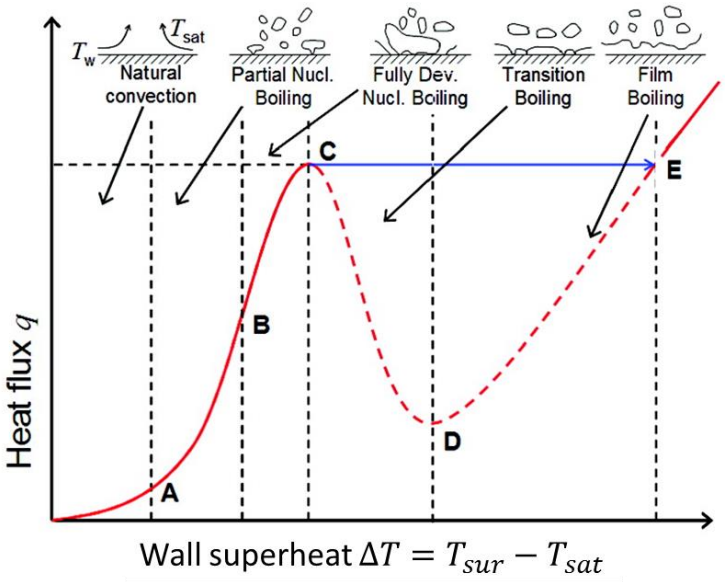


**Figure 23**: Boiling curve of water as function of heat flux $q$ against the surface superheat $\Delta T$. Adapted with permission from Ref[71]. Copyright 2009 American Chemical Society.

Likewise, the lifetime of a drop until its evaporation $\tau_s$ can be measured as function of $T_{sur}$ (**Figure 24**). For example, Biance et al. investigated $\tau_s$ of drops on a flat, heatable aluminium plate as function of the surface temperature.[10]

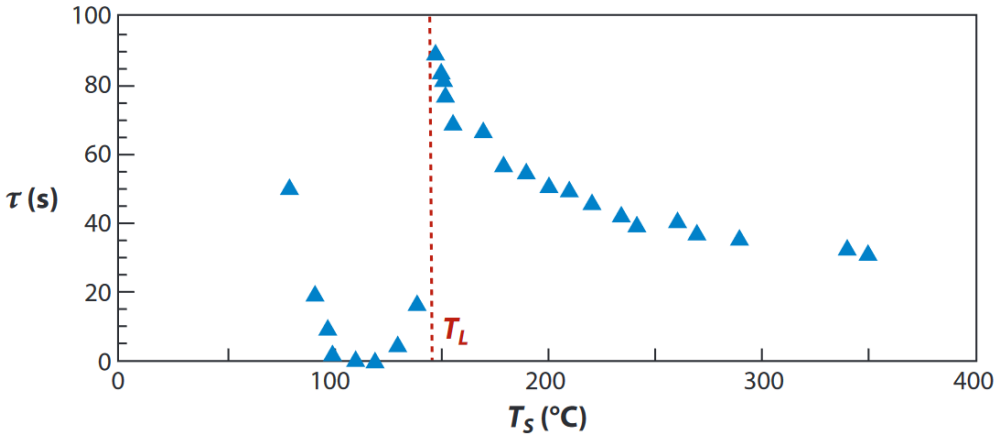


**Figure 24**: Life-time $\tau_s$ of drops until they fully evaporate as function of the surface temperature of a polished aluminium plate. The drops initially have a radius $r = 1\ mm$. From Ref[1].

At room temperature, the drop spreads and forms a finite contact angle on the aluminum plate. Upon heating, $\tau_s$ decreases until a minimum of $\tau_s \leq 1\ s$ is reached at $T_{sur}$ slightly above 100 °C. At this point, violent boiling of the drop occurs. At $T_{sur} = T_L$, for water about 150 °C, a sudden jump in $\tau_s$ is observed and drops exist for more than 1 minute. At the same time, the drop changes its shape.

It becomes ball-like and a thin vapor film underneath the drop becomes visible. The sharp increase in $\tau_s$ corresponds to a change from the transition boiling regime to the film boiling regime, in which a drop is in the Leidenfrost state. A further temperature increase leads to a decrease of $\tau_s$. Overall, it is remarkable that drops exist for more than 30 s at temperatures of about 350 °C. The extended life-time of Leidenfrost drops impressively demonstrate the insulating properties of the vapor cushion between drop and surface.

### 1.3.2 **Lateral and vertical movement of drops and objects exploiting the Leidenfrost phenomenon**

The vapor flow underneath a Leidenfrost drop is isotropic when the drop is placed on a flat, hot surface. The flow distribution can be manipulated when the surface is anisotropically textured instead. The vapor flow can be rectified leading to propulsion of drops, as demonstrated by Linke et al. They developed a hydrophobic ratchet having a teeth depth $a$ and a teeth distance $\lambda$ (**Figure 25**).[1, 74]

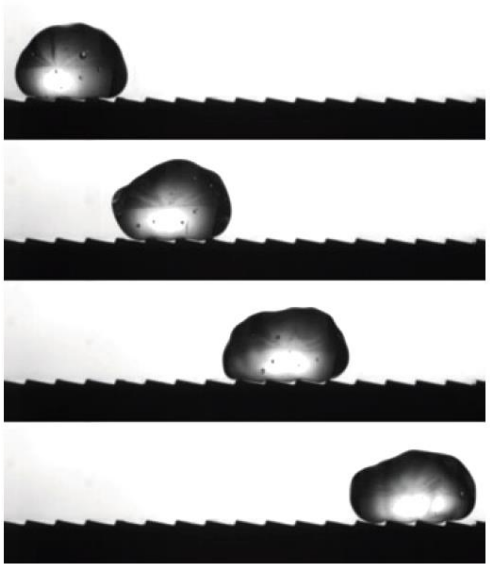

**Figure 25**: Image sequence of a drop ($r = 2\,mm$) placed on a ratchet. For $T > T_L$, a drop propels forward. The ratchet has a teeth depth $a = 0.2\,mm$ and a teeth length $\lambda = 1.5\,mm$. The time elapsed between the images is 40 ms. From Ref[1].

The propulsion mechanism is attributed to an anisotropic gas flow exerting viscous forces between drop and surface, what drags the drop forward.[74, 75] The

maximum velocity Linke et al. achieved on such a ratchet is about 10 cm/s, even though the forces acting on drops in the Leidenfrost state are in the order of ten µN. This means, that the drop velocity nearly corresponds to the velocity of the water vapor ejection from the drop itself, underlining the low friction forces acting on drops in the Leidenfrost state.[1] Similarly, solid objects like dry ice and camphor crystals were propelled on ratchets.[76]

Changing from the lateral to the vertical motion of drops, the Leidenfrost effect also plays an important role if drops impinge a hot surface. Technically, this is important for spray cooling of hot work pieces.[77] Depending on the temperature of the surface, the kinetic energy and the size of the drop, different scenarios can be distinguished:[78]

i) The drop boils upon contact (contact boiling).

ii) At $T_{sur} > T_L$ the drop spreads out but there is a vapor film between drop and surface which prevents contact and allows the drop to bounce back (gentle film boiling).

iii) The drop does both, i) and ii): Tiny drops are ejected when the drop spreads out on its vapor cushion (spraying film boiling).

In the case of ii) and iii), the drop can rebound several times after the initial reflection from the surface. This is similar to drop impact on super liquid-repellent surfaces.[1, 78-80]

Lee and Song showed that the rebound dynamics at a certain temperature can be tuned by surface texturing.[81] They compared the behavior of water drops impinging a smooth hydrophobic surface and a specially textured hydrophobic surface, both heated to 140 °C. The textured surface consisted of a periodic array of holes (**Figure 26**a and b). The drops were dropped from low heights, i.e. they had low initial kinetic energy at impact. The smooth hydrophobic surface was initially wetted by the impinging water drop and the drops had an apparent contact angle of about 100°. After more than 2 s the drops showed an apparent contact angle of about 160° and had an overall lifetime of more than 30 s, proving that they entered the Leidenfrost state.

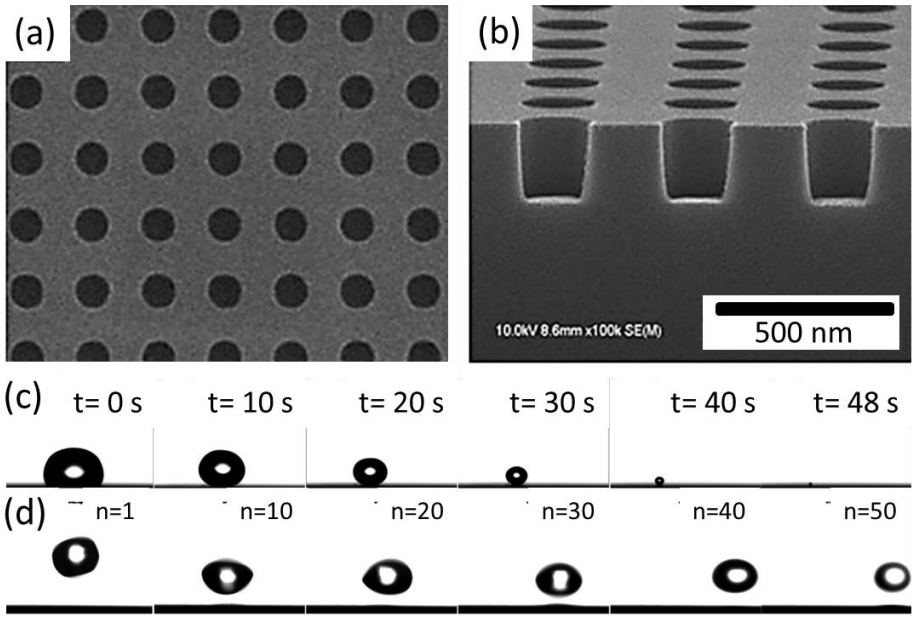


**Figure 26**: Dynamic behavior of water drops in contact with smooth and textured surfaces, both having 140 °C. a) and b) show electron microscopy images of the textured surface, a periodic array of holes. c) and d) show time sequences of optical images for a drop contacting c) a smooth hydrophobic surface and d) a textured hydrophobic surface. Reprinted from Ref[81], with the permission of AIP Publishing.

In contrast, water drops did not wet the textured surface in Figure 26d, but are reflected and bounced repeatedly for more than 50 times at low energy dissipation. This was attributed to an overpressure build up underneath the drop due to water evaporation. This resulted in an upward force, partially compensating for the energy losses due to drop deformation and adhesion.

Schutzius et al. showed that drops can spontaneously start to bounce without having any initial kinetic energy.[82] More precisely, the drops were in rest on a superhydrophobic surface. The ambient pressure was quickly reduced at a rate of 0.1 bar/s down to 0.01 bar. The drops started to vibrate and finally bounced repeatedly when the pressure was decreased (**Figure 27**). The jump height successively increased up to a few mm for a drop with a radius of about 1 mm. This effect results from: i) the low liquid-solid adhesion between drop and surface, ii) from overpressure generated below the drop resulting from its fast vaporization, which is analogue to the Leidenfrost effect, iii) the surface roughness which confines the vapor flow and supports the pressure build up.

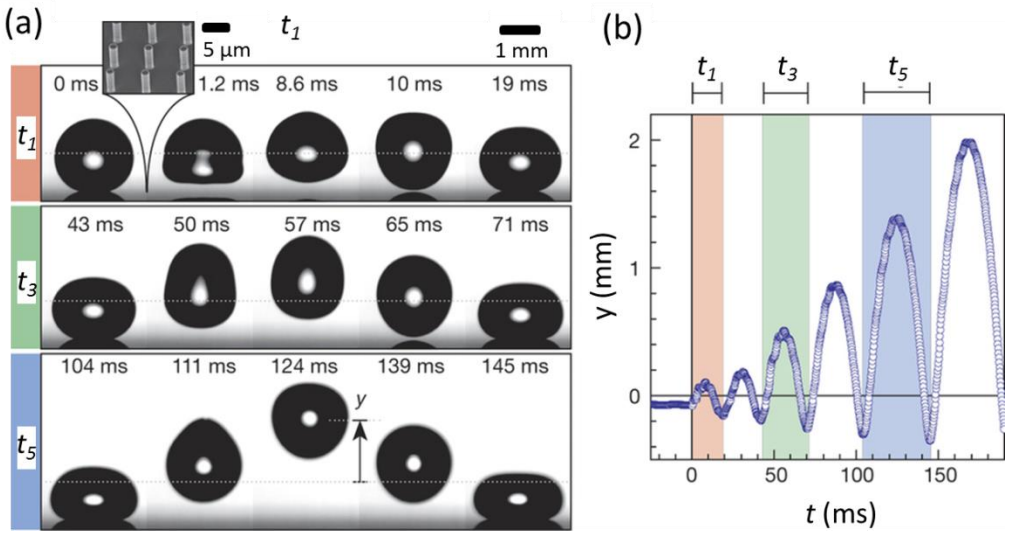


**Figure 27**: Spontaneous drop bouncing by reducing ambient pressure: a) Image sequence of a drop ($r \approx 1\,mm$) initially in rest which starts to bounce. Inset: SEM of the superhydrophobic pillar array. b) Bounce heights of the drop shown in a) as function of time. Reprinted by permission from Macmillan Publishers Ltd: Nature[82], copyright 2015.

### 1.3.3 **Challenges and opportunities in drop and object manipulation using transition and film boiling**

Momentarily, repeated, long-lasting bouncing of drops, starting from either a stationary state or upon contacting a hot surface at low kinetic energy, seems to rely on structured surfaces. This comes from mainly three prerequisites: i) high initial contact angles before jumping, ii) a low solid-liquid adhesion between drop and surface and iii) a confined, rectified vapor flow between drop and surface which leads to an upward force. Hydrogels are water-infused polymeric networks and consist of up to 99 wt% water.[83] Spherical hydrogel balls are consequently similar to balled up water drops on super liquid-repellent surfaces in terms of solid-liquid contact area and shape. This allows investigating if jumping off and repeated bouncing is necessarily due to a specific surface texture or if it is more strongly connected to the drop shape and properties than expected. In other words, is it possible to make spherical hydrogel balls jump from and bounce on a smooth surface if the temperature of the surface is ramped up from room temperature to above $T_L$? This approach allows decoupling surface texture from the jumping and bouncing mechanism.

Heat induced jumping from the surface and repeated bouncing of water and hydrogel balls is potentially interesting for two aspects: i) The hydrogel balls can also be seen as shape-stable, elastic solids. From this point of view, making hydrogel balls jump from and bounce on smooth surfaces conceptually connects to the idea to overcome the adhesion force between two solids by heating. ii) Repeated bouncing of water drops on surfaces can be a strategy to clean them. The dirt particles attach to the drops when they impinge the surface and are removed together with the drops when they bounce off. A spontaneous, heat-initiated jumping from the surface of drops could efficiently entrain particles with even higher adhesion forces to the surface which might not be taken up solely by bouncing drops.

## 1.4 Liquid marbles

In some cases, particles efficiently stabilize fluid-fluid interfaces. This happens if the adsorption of the particles to the interface is energetically more favorable than a complete immersion in one or the other phase. Depending on the fluids and the hydrophilicity or hydrophobicity of the particles, different kind of particle-stabilized interfaces can be obtained (**Figure 28**).[84, 85] Two popular examples are Pickering emulsions (liquid-in-liquid)[86] and water-in-air emulsions, so-called dry water.

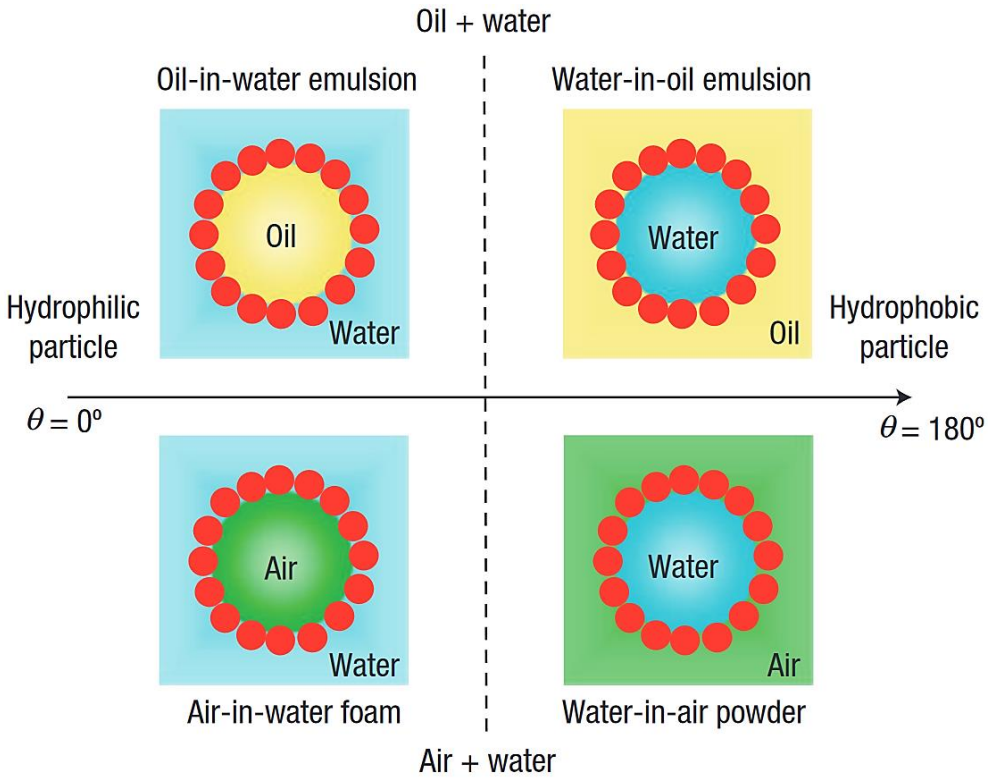


**Figure 28**: Overview of particle stabilized fluid-fluid interfaces. Left part: hydrophilic particles stabilize oil and air in water. Right part: hydrophobic particles stabilize water in oil and air. Reprinted by permission from Macmillan Publishers Ltd: Nature Materials[85], copyright 2006.

The adsorption of particles to the interface is favored if the energy of the entire system is lower in the mixed state than it was for the individual components before mixing. This is illustrated in **Figure 29** for the adsorption of a single particle to a drop of water: In this simplified image, a particle sticks out of the drop by a distance $d = r(1 - \cos(\theta_E))$. The change in surface free energy upon adsorption is based on the replacement of a circular, cap shaped part of the particle's solid-air interfacial area $A_{sa}$ by a solid-liquid interfacial area $A_{sl}$ of the same size, i.e. $A_{sa} = A_{sl}$.

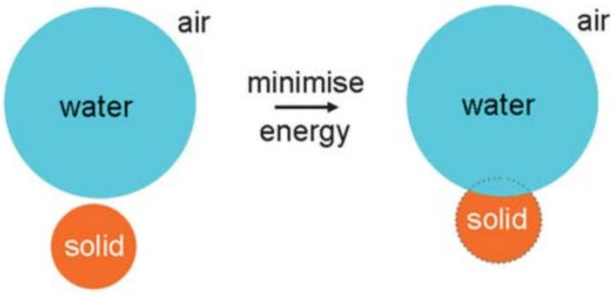


**Figure 29**: Illustration of a particle adsorbing to the liquid-air interface of a drop. Adsorption leads to a reduction of the free surface energy of the particle-drop system. Adapted from Ref[15] with permission of The Royal Society of Chemistry.

In parallel, a part of the liquid-air interfacial area of the drop $A_{la}$ is replaced by a liquid-particle interaction. The adsorption of the particle is energetically favored if the change in net free surface energy $\Delta_f$ is negative:[15]

$$\Delta_f = A_{sa}(\gamma_{sl} - \gamma_{sa}) - A_{la}\gamma_{la} < 0 \qquad \text{(eq. 1.8)}$$

Here, $\gamma_{sl}$, $\gamma_{sa}$ and $\gamma_{la}$ are again the solid-liquid, solid-air and liquid-air interfacial tensions, respectively. Insertion of Young's equation in the form $-\gamma_{la}\cos(\theta_E) = \gamma_{sl} - \gamma_{sa}$ and subsequent rearrangement leads to:

$$\Delta_f = -A_{SA}\gamma_{LA}\left(\cos(\theta_E) + \frac{A_{LA}}{A_{SA}}\right) \qquad \text{(eq. 1.9)}$$

For spherical particles the ratio of the interfacial areas is given as:

$$\frac{A_{LA}}{A_{SA}} = \frac{1-\cos(\theta_E)}{2} \qquad \text{(eq. 1.10)}$$

Eq. 1.10 is always positive for $0° < \theta_E < 180°$ and $\Delta_f$ in eq. 1.9 is consequently negative. This means that for $0° < \theta_E < 180°$ particle adsorption is always energetically favored. For both extreme cases, i.e. $\theta_E = 0°$ and $\theta_E = 180°$, no stable adsorption is possible. For $\theta_E = 0°$, the particle is completely engulfed by the liquid, and for $\theta_E = 180°$, $\Delta_f = 0$ and no energy is gained by adsorption of the particle. The adsorption energy reaches its highest value for $\theta_E = 90°$.[13, 15]

In this sense, liquid marbles are millimetric to centimetric particle-stabilized drops in air. They can be easily prepared by rolling a liquid on a powder bed of suitable particles for about a minute. This leads to a densely packed shell of particles around the drop. The procedure is schematically shown in **Figure 30**. The shell can consist of a monolayer or multilayers of particles. This depends on the

surface tension of the liquid, morphology and size of the particles or flocs. Particles in the first layer are more strongly bound to the drop due to a strong solid-liquid interaction. Particles in the outer layers generally interact less well with the liquid and mainly attach to other particles by van der Waals interaction. Thus, particles in the outer layers eventually detach from liquid marbles when they are moved over a substrate.

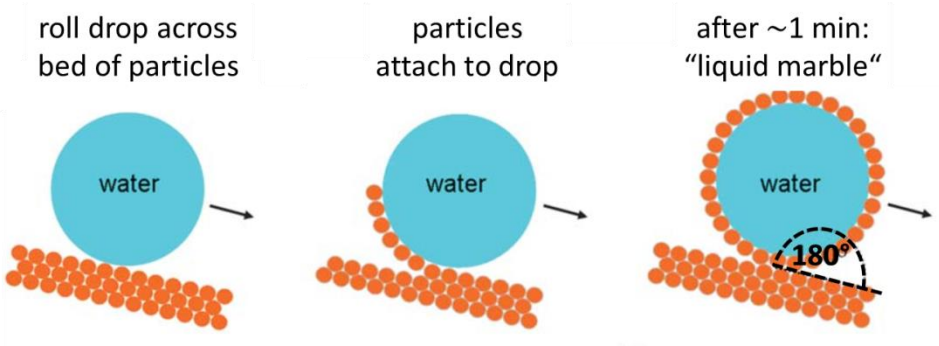


**Figure 30**: Preparation of liquid marbles by rolling a water drop over a bed of particles which adsorbed to the interface. Adapted from Ref[15] with permission of The Royal Society of Chemistry.

The particle shell of liquid marbles is remarkably robust to mechanical stress. Therefore, they can be transferred, e.g. by a spoon, to a different substrate after their preparation.[12, 13, 16] In nature, galling aphids rely on a similar strategy for waste disposal: The aphids live in small plant dwellings and secrete honeydew. To remove the unwanted honeydew from their dwellings, the aphids encapsulate the dew with wax particles. The aphids then push these liquid marbles out of their dwelling.[87, 88]

Thus, the encapsulated liquid is efficiently shielded from the substrate and the liquid inside the liquid marble forms contact angles close to 180°. The encapsulation efficiently lowers the adhesion force between the liquid and the substrate resulting in a high mobility of liquid marbles.[14, 16] This is conceptually similar to drops on super liquid-repellent surfaces and drops in the Leidenfrost state.[16] What is different is that the non-wetting properties are attached to the drop and are part of it until the liquid marble breaks. This allows placing liquid marbles on various substrates, which are intrinsically not super liquid-repellent or hot. Liquid marbles can even be placed on liquid interfaces. Depending on the wetting properties of the powder not only water but also many non-polar and

functional liquids can be encapsulated (**Figure 31**a).[89, 90] Xue et al. demonstrated the encapsulation of liquids spanning surface tensions from 72.8 mN/m (water) down to 21.6 mN/m (octane).[90] Some liquid marbles can even float on water and hexadecane (Figure 31b).

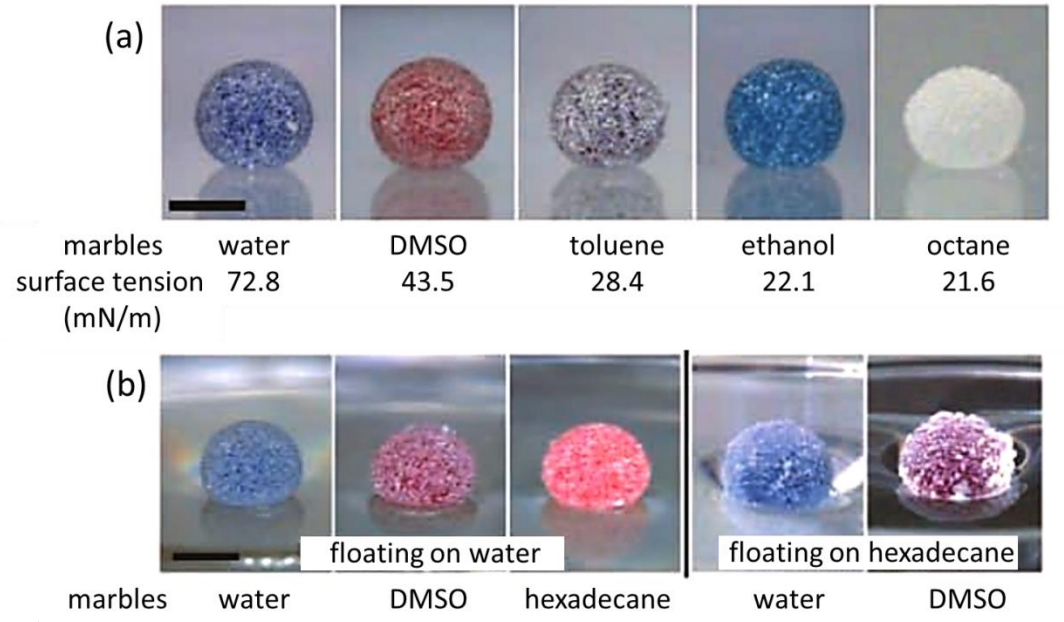


**Figure 31**: a) Different liquids (dyed, 3 µl) encapsulated by a fluorinated decyl polyhedral oligomeric silsesquioxane (FD-POSS) forming liquid marbles. The surface tension decreases from left to right. b) Different liquid marbles floating on either water (left) or hexadecane (right). Scale bar: 1 mm. From Ref[90]. Adapted with permission from John Wiley and Sons.

### 1.4.1 **Manipulation and application of liquid marbles**

Liquid marbles can be used for the loss-free transport of drops. At a given place and time, liquid marbles can be broken by an external stimulus to release the inner liquid. The movement of liquid marbles can be achieved by different schemes and methods, e.g. electromagnetically, mechanically or by other means like pH or temperature changes.[13, 89, 91] An overview of the different schemes and methods to manipulate liquid marbles is given in **Figure 32**.

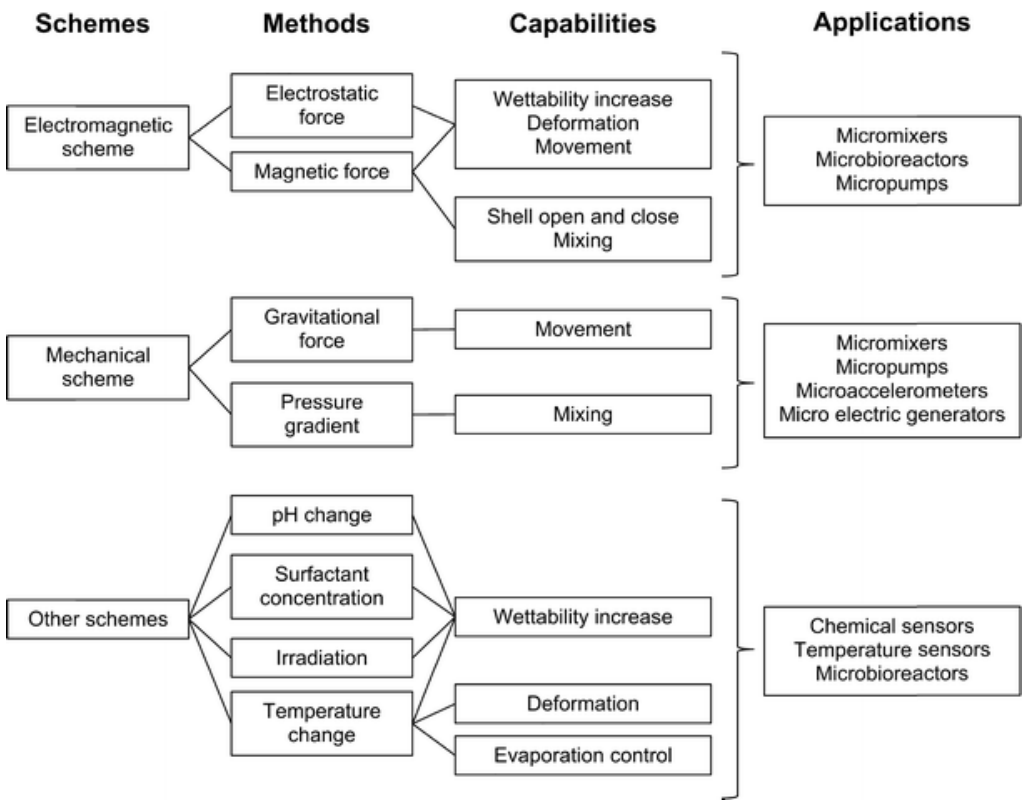


**Figure 32**: Overview of different schemes to manipulate liquid marbles. Each scheme consists of several methods, capabilities and their potential applications. From Ref[89]. With permission of Springer.

In this context, the term manipulating involves movement, release and also functional applications of liquid marbles, which will be discussed in the following. The most common way to move and manipulate liquid marbles without directly contacting them is to use magnetic forces.[90, 92-94] For this method, magnetic particles need to be either part of the shell material or part of the liquid. The magnetic field declines with $\frac{1}{r^2}$ and the magnet is typically at a distance of a few mm to cm away from the liquid marbles. A magnetic marble resting on a solid or on a liquid interface can be rolled or moved over it if a magnet is brought close as shown in **Figure 33**. Liquid marbles cannot only move laterally, but also vertically, e.g. by electrostatic forces.[13] Furthermore, they can also sink and rise vertically in water. Chu et al. prepared chloroform filled, photo-thermally active liquid marbles.

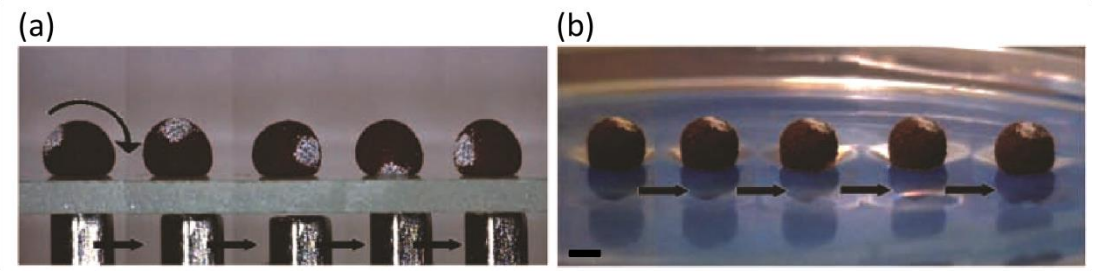


**Figure 33**: Magnet-induced motion of liquid marbles (7 µl). The shell consists of a blend made of fluorinated decyl polyhedral oligomeric silsesquioxane (FD-POSS) and hydrophobic $Fe_3O_4$. The white stained area is pure FD-POSS. The liquid marble a) rolls on a solid and b) drifts on a liquid interface. Scale bar: 1 mm. From Ref[90]. Adapted with permission from John Wiley and Sons.

Placed in a water bath, the liquid marbles sunk due to the higher density of chloroform compared to water. Irradiation of the photo-thermally active shell converted light into heat and caused some of the chloroform to evaporate inside the liquid marble. This provided enough buoyancy for the liquid marble to rise vertically. When the light-based heat supply stopped, the chloroform condensed again and the liquid marble sunk.[95]

Once liquid marbles are at a desired, specific place, the inner liquid can be released by an external stimulus. This can be achieved using mechanical pressure, pH, light, temperature or other stimuli. [92, 96-103] For some stimuli, e.g. pH, the encapsulating powder needs to be special designed. The shell material needs to change its wettability if it is exposed to the specific stimulus. This causes instability of the liquid marbles leading to their spontaneous disintegration.

In terms of potential applications, liquid marbles can serve as miniaturized chemical reactors. For example, they can be used as gas sensors.[104] The surrounding gas can diffuse through the porous shell and interact with an encapsulated indicator (**Figure 34**). Floating liquid marbles can thus be used to probe the pH of the air-water interface they float on. Such microreactors are also interesting to process small amounts of expensive or delicate reactants and substances. The reactants can be mixed either by magnetically forced coalescence of two liquid marbles or by slightly opening the shell of a liquid marble using a magnet and adding the reactants stepwise to the

microreactor.[90-94] After the reaction, the liquid marbles can be analyzed by spectroscopy or other analytical tools.[90]

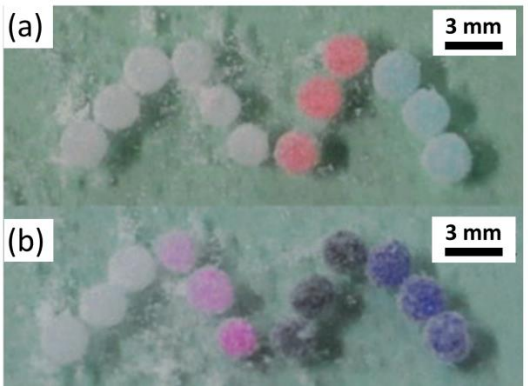


**Figure 34**: Gas sensing liquid marbles. Four groups of three liquid marbles each containing water, phenolphthalein, $CoCl_2$ and $CuCl_2$ solutions (left to right) are shown. a) Before exposure to ammonia gas, b) after exposure to ammonia gas. The colors of the liquid marbles containing an indicator changed. Adapted from Ref[104] with permission of The Royal Society of Chemistry.

Miao et al. exploited the interplay between the powder shell and the liquid (**Figure 35**). They prepared a catalytically active powder shell from perfluorodecanethiol-grafted silver nanowires. Encapsulated drops of methylene blue were successfully reduced in a redox reaction in the presence of sodium borohydride ($NaBH_4$).[105]

Sheng et al. focused on the chemical modification of the particles encapsulating the liquid. They obtained polydopamine-coated Janus particles by encapsulation of a basic dopamine solution with silica particles.[106] The percentage of surface coating could be controlled by the addition of a surfactant and the polydopamine-coated part could be further functionalized.[106]

Liquid marbles were also used for biological and diagnostic assays. Cells[107] and aerobic microorganisms[108] were cultured and investigated. Arbatan and co-workers were able to conduct blood grouping of human blood by using “blood marbles”[109] and the potential of liquid marble-based DNA/RNA/protein microarrays[16] is under discussion.

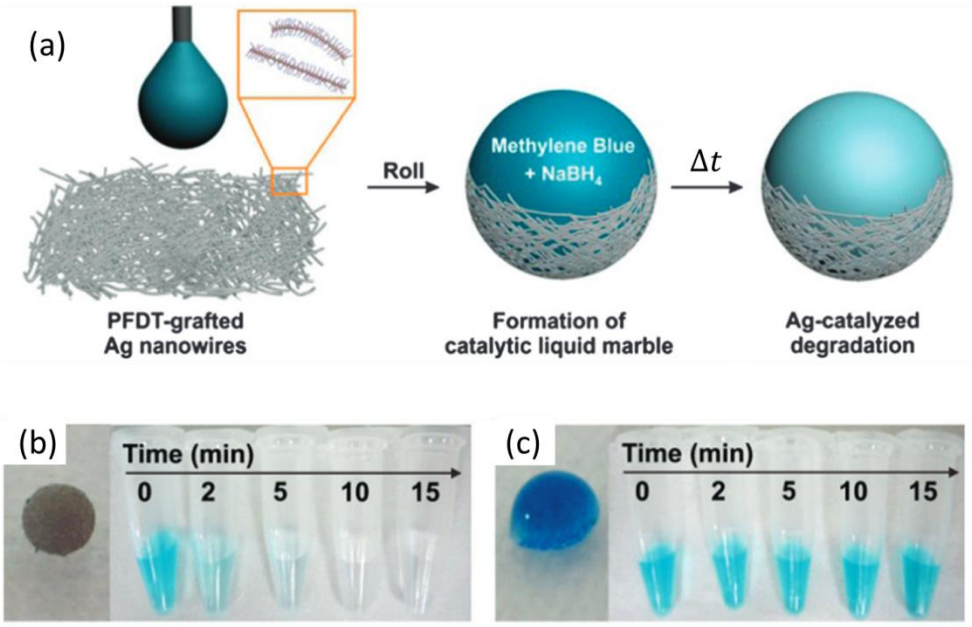


**Figure 35**: Catalytic liquid marbles. a) Schematic of a solution of methylene blue and sodium borohydride being encapsulated by hydrophobized silver nanowires. b) The solution inside the catalytic liquid marble is shown after different incubation times. The solution changes from blue to transparent due to the successive reduction of methylene blue. c) Control experiment: The solution is incubated for the same time intervals like b), but no silver wires are present. Within the same time interval, the color of the solution does not change to transparent. From Ref[105]. Published by The Royal Society of Chemistry.

### 1.4.2 **Challenges and opportunities of liquid marbles**

The above mentioned examples show how versatile millimetric marbles are and how precisely they can be manipulated in terms of movement and release of the inner liquid. Their capability to serve as microreactors and sensors arouse strong interest over the last years, but practical implementation is slow. One of the major reasons for the reluctant adoption of liquid marbles in any practical implementation is that the preparation, use and analysis of liquid marbles are delicate and time-consuming. Automated setups, e.g. for liquid marble cell-culturing or blood typing, would be a significant step forward in terms of a broader applicability. One of the challenges hereby is the precise control and handling of individual liquid marbles in time and space. Though convenient, magnet-induced movement lacks spatial selectivity to manipulate several liquid marbles independently due to the $\frac{1}{r^2}$ dependency of magnetic fields. If neighboring liquid

marbles are too close to each other and within reach of the magnetic field they might also be manipulated unintentionally. This results in a minimum distance between liquid marbles for a precise, individually manipulation using magnets and also negatively affects the dimension of a potential, practical setup. A spatially more precise and selective technique to move liquid marbles in time and space could contribute to make such a platform more practical in future.

## 1.5 Aim of the thesis

Super liquid-repellent surfaces, the Leidenfrost effect and liquid marbles have in common that the adhesion between surface and drop is strongly reduced by entrapped air pockets between both. Based on this common ground, this thesis presents individual contributions which focus on current demands and developments in the respective fields.

First off, I want to investigate if force sensitive measurements can be used to quantify the mechanical properties of super liquid-repellent surfaces. This allows obtaining intrinsic material properties like the effective elastic modulus in contrast to qualitative tests, e.g. linear abrasion. The measurements are performed using a colloidal indenter mounted to a scanning probe microscope (SPM). This combines benefits from nanoindentation and scanning probe microscopy, i.e. a large contact area can be probed with a high sensitivity. This is required for most super liquid-repellent surfaces because they are inherently rough and fragile. The technique is tested on candle soot-based super liquid-repellent surfaces. In a first study, the influence of the sooting height is investigated with respect to the position of the substrate in the flame by comparing the wetting properties of the respective surfaces obtained from different heights. In a second study, the role of the fabrication parameters on the mechanical properties is investigated. The results are compared to systematic wetting measurements to balance the mechanical strength of the coating against its repellency. Eventually, this technique turns out to be a valuable, complementary test to characterize the mechanical properties of super liquid-repellent surfaces.

Then I want to investigate if continuous heating of a surface can be used to overcome the adhesion between drop-like hydrogel balls and a smooth surface. Ideally, the hydrogel balls spontaneously jump from and bounce repeatedly thereafter due to fast vaporization of the water on and in the gel. This connects to a recent observation, where water drops on superhydrophobic surfaces started to jump when the surrounding pressure was reduced. Here, shape-stable hydrogel drops with high water content are used instead of pure water drops, which makes using a superhydrophobic surface redundant to provide high contact angles and a smooth surface can be used instead. This allows decoupling the jumping mechanism from the surface texture. Jumping from the surface and repeated

bouncing are further investigated as a function of hydrogel elasticity. This connects the controlled heat transfer between smooth surfaces and drops to drop bouncing based on fast water evaporation.

Finally, I want to investigate how to control the movement and release of liquid marbles - powder encapsulated drops - in space and time. The movement is important to transport the inner liquid to a certain location, where a reaction or analysis can then be triggered by a controlled release of the inner liquid. Inspired by the stenus beetle and the soap boat, I want to prepare photo-thermally responsive liquid marbles which can convert light into heat. If the liquid marble sits on an air-water interface, the heat can lead to propulsion of the liquid marble based on a heat-induced surface tension flow (Marangoni effect). This allows the liquid marble to move to a desired place and its content can then be released by a stimulus. Furthermore, I want to investigate if such light-driven liquid marbles can be used as towing engines to push objects floating at the air-water interface, similar to ants lifting a cargo. I will conduct this project as a visiting scientist in the group of Assoc. Prof. Syuji Fuji (Osaka Institute of Technology in Osaka, Japan) and in close cooperation with Assoc. Prof. Hiroyuki Mayama (Asahikawa Medical University, Japan).

Hence, these contributions support recent developments in the mechanical refinement of super liquid-repellent surfaces and demonstrate new strategies for the manipulation of drops using the Leidenfrost effect and liquid marbles.

## 1.6 References


[1] Quere, D. Leidenfrost Dynamics. In *Annual Review of Fluid Mechanics, Vol 45*, Davis, S. H.; Moin, P., Eds., 2013; Vol. 45, pp 197-215.

[2] Dupin, D.; Thompson, K. L.; Armes, S. P. Preparation of stimulus-responsive liquid marbles using a polyacid-stabilised polystyrene latex. *Soft Matter* **2011,** *7* (15), 6797-6800.

[3] Su, Y. W.; Ji, B. H.; Huang, Y.; Hwang, K. C. Nature's Design of Hierarchical Superhydrophobic Surfaces of a Water Strider for Low Adhesion and Low-Energy Dissipation. *Langmuir* **2010,** *26* (24), 18926-18937.

[4] Shirtcliffe, N. J.; McHale, G.; Atherton, S.; Newton, M. I. An introduction to superhydrophobicity. *Advances in Colloid and Interface Science* **2010,** *161* (1-2), 124-138.

[5] Barthlott, W.; Neinhuis, C. Purity of the sacred lotus, or escape from contamination in biological surfaces. *Planta* **1997,** *202* (1), 1-8.

[6] Feng, X. J.; Jiang, L. Design and creation of superwetting/antiwetting surfaces. *Advanced Materials* **2006,** *18* (23), 3063-3078.

[7] Quere, D. Wetting and roughness. In *Annual Review of Materials Research*, 2008; Vol. 38, pp 71-99.

[8] Bhushan, B.; Jung, Y. C. Natural and biomimetic artificial surfaces for superhydrophobicity, self-cleaning, low adhesion, and drag reduction. *Progress in Materials Science* **2011,** *56* (1), 1-108.

[9] Gottfried, B. S.; Lee, C. J.; Bell, K. J. The leidenfrost phenomenon: film boiling of liquid droplets on a flat plate. *International Journal of Heat and Mass Transfer* **1966,** *9* (11), 1167-1188.

[10] Biance, A.-L.; Clanet, C.; Quéré, D. Leidenfrost drops. *Physics of Fluids* **2003,** *15* (6), 1632-1637.

[11] Leidenfrost, J. G. *De Aquae Communis Nonnullis Qualitatibus Tractatus*: Duisburg: Ovenius, 1756a.

[12] Aussillous, P.; Quere, D. Liquid marbles. *Nature* **2001,** *411* (6840), 924-927.

[13] Aussillous, P.; Quéré, D. Properties of liquid marbles. *Proceedings of the Royal Society of London A: Mathematical, Physical and Engineering Sciences* **2006,** *462* (2067), 973-999.

[14] Bormashenko, E. New insights into liquid marbles. *Soft Matter* **2012,** *8* (43), 11018-11021.

[15] McHale, G.; Newton, M. I. Liquid marbles: principles and applications. *Soft Matter* **2011,** *7* (12), 5473-5481.

[16] McHale, G.; Newton, M. I. Liquid marbles: topical context within soft matter and recent progress. *Soft Matter* **2015,** *11* (13), 2530-2546.

[17] ElSherbini, A. I.; Jacobi, A. M. Retention forces and contact angles for critical liquid drops on non-horizontal surfaces. *Journal of Colloid and Interface Science* **2006,** *299* (2), 841-849.

[18] Antonini, C.; Carmona, F. J.; Pierce, E.; Marengo, M.; Amirfazli, A. General Methodology for Evaluating the Adhesion Force of Drops and Bubbles on Solid Surfaces. *Langmuir* **2009,** *25* (11), 6143-6154.

[19] Aberle, C.; Lewis, M.; Yu, G.; Lei, N.; Xu, J. Liquid marbles as thermally robust droplets: coating-assisted Leidenfrost-like effect. *Soft Matter* **2011,** *7* (24), 11314-11318.

[20] de Gennes, P.-G. B.-W., Françoise; Quéré, David *Capillarity and Wetting Phenomena*; Springer New York: New York, 2004.

[21] Butt, H. J.; Graf, K.; Kappl, M. *Physics and Chemistry of Interfaces*; WILEY-VCH Verlag GmbH & Co. KGaA: Weinheim, 2006.

[22] Winkels, K. G.; Peters, I. R.; Evangelista, F.; Riepen, M.; Daerr, A.; Limat, L.; Snoeijer, J. H. Receding contact lines: From sliding drops to immersion lithography. *The European Physical Journal Special Topics* **2011,** *192* (1), 195-205.

[23] Young, T. An Essay on the Cohesion of Fluids. *Philosophical Transactions Royal Society London* **1805,** *95*, 65-87.

[24] Blossey, R. Self-cleaning surfaces [mdash] virtual realities. *Nat Mater* **2003,** *2* (5), 301-306.

[25] Degennes, P. G. Wetting - Statics and Dynamics. *Reviews of Modern Physics* **1985,** *57* (3), 827-863.

[26] Su, B.; Tian, Y.; Jiang, L. Bioinspired Interfaces with Superwettability: From Materials to Chemistry. *Journal of the American Chemical Society* **2016,** *138* (6), 1727-1748.

[27] Wenzel, R. N. Resistance of solid surfaces to wetting by water. *Industrial and Engineering Chemistry* **1936,** *28*, 988-994.

[28] Cassie, A. B. D.; Baxter, S. Wettability of porous surfaces. *T Faraday Soc* **1944,** *40*, 0546-0550.

[29] Papadopoulos, P.; Mammen, L.; Deng, X.; Vollmer, D.; Butt, H. J. How superhydrophobicity breaks down. *PNAS* **2013,** *110* (9), 3254–3258.

[30] Nosonovsky, M. Multiscale Roughness and Stability of Superhydrophobic Biomimetic Interfaces. *Langmuir* **2007,** *23* (6), 3157-3161.

[31] Butt, H.-J.; Vollmer, D.; Papadopoulos, P. Super liquid-repellent layers: The smaller the better. *Advances in Colloid and Interface Science* **2015,** *222*, 104-109.

[32] Neinhuis, C.; Barthlott, W. Characterization and distribution of water-repellent, self-cleaning plant surfaces. *Annals of Botany* **1997,** *79* (6), 667-677.

[33] Mammen, L.; Bley, K.; Papadopoulos, P.; Schellenberger, F.; Encinas, N.; Butt, H.-J.; Weiss, C. K.; Vollmer, D. Functional superhydrophobic surfaces made of Janus micropillars. *Soft Matter* **2015,** *11* (3), 506-515.

[34] Schellenberger, F.; Encinas, N.; Vollmer, D.; Butt, H.-J. How Water Advances on Superhydrophobic Surfaces. *Physical Review Letters* **2016,** *116* (9), 096101.

[35] Pan, S.; Kota, A. K.; Mabry, J. M.; Tuteja, A. Superomniphobic Surfaces for Effective Chemical Shielding. *Journal of the American Chemical Society* **2013,** *135* (2), 578-581.

[36] Privett, B. J.; Youn, J.; Hong, S. A.; Lee, J.; Han, J.; Shin, J. H.; Schoenfisch, M. H. Antibacterial Fluorinated Silica Colloid Superhydrophobic Surfaces. *Langmuir* **2011,** *27* (15), 9597-9601.

[37] Paven, M.; Papadopoulos, P.; Schöttler, S.; Deng, X.; Mailänder, V.; Vollmer, D.; Butt, H.-J. Super liquid-repellent gas membranes for carbon dioxide capture and heart–lung machines. *Nat Commun* **2013,** *4*.

[38] Efimenko, K.; Finlay, J.; Callow, M. E.; Callow, J. A.; Genzer, J. Development and Testing of Hierarchically Wrinkled Coatings for Marine Antifouling. *ACS Applied Materials & Interfaces* **2009,** *1* (5), 1031-1040.

[39] Papadopoulos, P.; Vollmer, D.; Butt, H. J. Long-Term Repellency of Liquids by Superoleophobic Surfaces. *Physical Review Letters* **2016,** *117* (4).

[40] Cao, L.; Price, T. P.; Weiss, M.; Gao, D. Super Water- and Oil-Repellent Surfaces on Intrinsically Hydrophilic and Oleophilic Porous Silicon Films. *Langmuir* **2008,** *24* (5), 1640-1643.

[41] Herminghaus, S. Roughness-induced non-wetting. *EPL (Europhysics Letters)* **2000,** *52* (2), 165.

[42] Tuteja, A.; Choi, W.; Ma, M. L.; Mabry, J. M.; Mazzella, S. A.; Rutledge, G. C.; McKinley, G. H.; Cohen, R. E. Designing superoleophobic surfaces. *Science* **2007,** *318* (5856), 1618-1622.

[43] Butt, H. J.; Semprebon, C.; Papadopoulos, P.; Vollmer, D.; Brinkmann, M.; Ciccotti, M. Design principles for superamphiphobic surfaces. *Soft Matter* **2013,** *9* (2), 418-428.

[44] Chen, W.; Fadeev, A. Y.; Hsieh, M. C.; Oner, D.; Youngblood, J.; McCarthy, T. J. Ultrahydrophobic and ultralyophobic surfaces: Some comments and examples. *Langmuir* **1999,** *15* (10), 3395-3399.

[45] Tuteja, A.; Choi, W.; McKinley, G. H.; Cohen, R. E.; Rubner, M. F. Design Parameters for Superhydrophobicity and Superoleophobicity. *MRS Bulletin* **2008,** *33* (08), 752-758.

[46] Deng, X.; Mammen, L.; Butt, H. J.; Vollmer, D. Candle Soot as a Template for a Transparent Robust Superamphiphobic Coating. *Science* **2012,** *335* (6064), 67-70.

[47] Tuteja, A.; Choi, W.; Mabry, J. M.; McKinley, G. H.; Cohen, R. E. Robust omniphobic surfaces. *Proceedings of the National Academy of Sciences* **2008,** *105* (47), 18200-18205.

[48] Liu, T. Y.; Kim, C. J. Turning a surface superrepellent even to completely wetting liquids. *Science* **2014,** *346* (6213), 1096-1100.

[49] Choi, W.; Tuteja, A.; Chhatre, S.; Mabry, J. M.; Cohen, R. E.; McKinley, G. H. Fabrics with Tunable Oleophobicity. *Advanced Materials* **2009,** *21* (21), 2190-+.

[50] Lacroix, R.; Kermouche, G.; Teisseire, J.; Barthel, E. Plastic deformation and residual stresses in amorphous silica pillars under uniaxial loading. *Acta Materialia* **2012,** *60* (15), 5555-5566.

[51] Celia, E.; Darmanin, T.; Taffin de Givenchy, E.; Amigoni, S.; Guittard, F. Recent advances in designing superhydrophobic surfaces. *Journal of Colloid and Interface Science* **2013,** *402*, 1-18.

[52] Wang, S.; Liu, K.; Yao, X.; Jiang, L. Bioinspired Surfaces with Superwettability: New Insight on Theory, Design, and Applications. *Chemical Reviews* **2015,** *115* (16), 8230-8293.

[53] Ma, M.; Hill, R. M. Superhydrophobic surfaces. *Current Opinion in Colloid & Interface Science* **2006,** *11* (4), 193-202.

[54] Roach, P.; Shirtcliffe, N. J.; Newton, M. I. Progess in superhydrophobic surface development. *Soft Matter* **2008,** *4* (2), 224-240.

[55] Chu, Z.; Seeger, S. Superamphiphobic surfaces. *Chemical Society Reviews* **2014,** *43* (8), 2784-2798.

[56] Guo, Z.; Liu, W.; Su, B.-L. Superhydrophobic surfaces: From natural to biomimetic to functional. *Journal of Colloid and Interface Science* **2011,** *353* (2), 335-355.

[57] Wen, Q. Y.; Guo, Z. G. Recent Advances in the Fabrication of Superhydrophobic Surfaces. *Chemistry Letters* **2016,** *45* (10), 1134-1149.

[58] Zhou, H.; Wang, H. X.; Niu, H. T.; Fang, J.; Zhao, Y.; Lin, T. Superstrong, Chemically Stable, Superamphiphobic Fabrics from Particle-Free Polymer Coatings. *Advanced Materials Interfaces* **2015,** *2* (6).

[59] Leng, B.; Shao, Z.; de With, G.; Ming, W. Superoleophobic Cotton Textiles. *Langmuir* **2009,** *25* (4), 2456-2460.

[60] Deng, X.; Schellenberger, F.; Papadopoulos, P.; Vollmer, D.; Butt, H.-J. Liquid Drops Impacting Superamphiphobic Coatings. *Langmuir* **2013,** *29* (25), 7847-7856.

[61] Tian, X.; Verho, T.; Ras, R. H. A. Moving superhydrophobic surfaces toward real-world applications. *Science* **2016,** *352* (6282), 142-143.

[62] Paven, M.; Mammen, L.; Vollmer, D. CHAPTER 8 Challenges and Opportunities of Superhydrophobic/Superamphiphobic Coatings in Real Applications. In *Smart Materials for Advanced Environmental Applications*; The Royal Society of Chemistry, 2016, pp 209-243.

[63] Xue, C.-H.; Ma, J.-Z. Long-lived superhydrophobic surfaces. *Journal of Materials Chemistry A* **2013,** *1* (13), 4146-4161.

[64] Verho, T.; Bower, C.; Andrew, P.; Franssila, S.; Ikkala, O.; Ras, R. H. A. Mechanically Durable Superhydrophobic Surfaces. *Advanced Materials* **2011,** *23* (5), 673-678.

[65] Dyett, B. P.; Wu, A. H.; Lamb, R. N. Mechanical Stability of Surface Architecture—Consequences for Superhydrophobicity. *ACS Applied Materials & Interfaces* **2014,** *6* (21), 18380-18394.

[66] Milionis, A.; Loth, E.; Bayer, I. S. Recent advances in the mechanical durability of superhydrophobic materials. *Advances in Colloid and Interface Science* **2016,** *229*, 57-79.

[67] Oliver, W. C.; Pharr, G. M. An improved technique for determining hardness and elastic-modulus using load and displacement sensing indentation experiments. *Journal of Materials Research* **1992,** *7* (6), 1564-1583.

[68] Ducker, W. A.; Senden, T. J.; Pashley, R. M. DIRECT MEASUREMENT OF COLLOIDAL FORCES USING AN ATOMIC FORCE MICROSCOPE. *Nature* **1991,** *353* (6341), 239-241.

[69] Butt, H. J. MEASURING ELECTROSTATIC, VANDERWAALS, AND HYDRATION FORCES IN ELECTROLYTE-SOLUTIONS WITH AN ATOMIC FORCE MICROSCOPE. *Biophysical Journal* **1991,** *60* (6), 1438-1444.

[70] Lagubeau, G.; Le Merrer, M.; Clanet, C.; Quere, D. Leidenfrost on a ratchet. *Nat Phys* **2011,** *7* (5), 395-398.

[71] Chen, R.; Lu, M.-C.; Srinivasan, V.; Wang, Z.; Cho, H. H.; Majumdar, A. Nanowires for Enhanced Boiling Heat Transfer. *Nano Letters* **2009,** *9* (2), 548-553.

[72] Carey, V. P. *Liquid-vapor phase-change phenomena*; Hemisphere, New York, NY (United States): United States, 1992.

[73] Walker, J. Boiling and the leidenfrost effect. *Cleveland State University* **2010,** *1*.

[74] Linke, H.; Alemán, B. J.; Melling, L. D.; Taormina, M. J.; Francis, M. J.; Dow-Hygelund, C. C.; Narayanan, V.; Taylor, R. P.; Stout, A. Self-Propelled Leidenfrost Droplets. *Physical Review Letters* **2006,** *96* (15), 154502.

[75] Cousins, T. R.; Goldstein, R. E.; Jaworski, J. W.; Pesci, A. I. A ratchet trap for Leidenfrost drop. *Journal of Fluid Mechanics* **2012,** *696*, 215-227.

[76] Dupeux, G.; Baier, T.; Bacot, V.; Hardt, S.; Clanet, C.; Quéré, D. Self-propelling uneven Leidenfrost solids. *Physics of Fluids* **2013,** *25* (5), 051704.

[77] Kim, J. H. Spray cooling heat transfer: The state of the art. *International Journal of Heat and Fluid Flow* **2007,** *28* (4), 753-767.

[78] Tran, T.; Staat, H. J. J.; Prosperetti, A.; Sun, C.; Lohse, D. Drop Impact on Superheated Surfaces. *Physical Review Letters* **2012,** *108* (3), 036101.

[79] Callies, M.; Quere, D. On water repellency. *Soft Matter* **2005,** *1* (1), 55-61.

[80] Deng, X.; Schellenberger, F.; Papadopoulos, P.; Vollmer, D.; Butt, H. J. Liquid Drops Impacting Superamphiphobic Coatings. *Langmuir* **2013,** *29* (25), 7847-7856.

[81] Lee, D. J.; Song, Y. S. Anomalous water drop bouncing on a nanotextured surface by the Leidenfrost levitation. *Applied Physics Letters* **2016,** *108* (20).

[82] Schutzius, T. M.; Jung, S.; Maitra, T.; Graeber, G.; Köhme, M.; Poulikakos, D. Spontaneous droplet trampolining on rigid superhydrophobic surfaces. *Nature* **2015,** *527* (7576), 82-85.

[83] Appel, E. A.; Loh, X. J.; Jones, S. T.; Biedermann, F.; Dreiss, C. A.; Scherman, O. A. Ultrahigh-Water-Content Supramolecular Hydrogels Exhibiting Multistimuli Responsiveness. *Journal of the American Chemical Society* **2012,** *134* (28), 11767-11773.

[84] Fujii, S.; Mochizuki, M.; Aono, K.; Hamasaki, S.; Murakami, R.; Nakamura, Y. pH-Responsive Aqueous Foams Stabilized by Hairy Latex Particles. *Langmuir* **2011,** *27* (21), 12902-12909.

[85] Binks, B. P.; Murakami, R. Phase inversion of particle-stabilized materials from foams to dry water. *Nat Mater* **2006,** *5* (11), 865-869.

[86] Pickering, S. U. CXCVI.-Emulsions. *Journal of the Chemical Society, Transactions* **1907,** *91* (0), 2001-2021.

[87] Benton, T. G.; Foster, W. A. Altruistic Housekeeping in a Social Aphid. *Proceedings of the Royal Society of London B: Biological Sciences* **1992,** *247* (1320), 199-202.

[88] Kutsukake, M.; Meng, X.-Y.; Katayama, N.; Nikoh, N.; Shibao, H.; Fukatsu, T. An insect-induced novel plant phenotype for sustaining social life in a closed system. *Nat Commun* **2012,** *3*, 1187.

[89] Ooi, C. H.; Nguyen, N.-T. Manipulation of liquid marbles. *Microfluidics and Nanofluidics* **2015,** *19* (3), 483-495.

[90] Xue, Y.; Wang, H.; Zhao, Y.; Dai, L.; Feng, L.; Wang, X.; Lin, T. Magnetic Liquid Marbles: A “Precise” Miniature Reactor. *Advanced Materials* **2010,** *22* (43), 4814-4818.

[91] Newton, M. I.; Herbertson, D. L.; Elliott, S. J.; Shirtcliffe, N. J.; McHale, G. Electrowetting of liquid marbles. *Journal of Physics D: Applied Physics* **2007,** *40* (1), 20.

[92] Zhang, L.; Cha, D.; Wang, P. Remotely Controllable Liquid Marbles. *Advanced Materials* **2012,** *24* (35), 4756-4760.

[93] Tippkötter, N.; Al-Kaidy, H.; Wollny, S.; Ulber, R. Functionalized Magnetizable Particles for Downstream Processing in Single-Use Systems. *Chemie Ingenieur Technik* **2013,** *85* (1-2), 76-86.

[94] Zhao, Y.; Fang, J.; Wang, H.; Wang, X.; Lin, T. Magnetic Liquid Marbles: Manipulation of Liquid Droplets Using Highly Hydrophobic Fe3O4 Nanoparticles. *Advanced Materials* **2010,** *22* (6), 707-710.

[95] Chu, Y.; Liu, F.; Qin, L.; Pan, Q. Remote manipulation of a microdroplet in water by near infrared laser. *ACS Applied Materials & Interfaces* **2015**.

[96] Fujii, S.; Sawada, S.; Nakayama, S.; Kappl, M.; Ueno, K.; Shitajima, K.; Butt, H. J.; Nakamura, Y. Pressure-sensitive adhesive powder. *Materials Horizons* **2016,** *3* (1), 47-52.

[97] Dupin, D.; Armes, S. P.; Fujii, S. Stimulus-Responsive Liquid Marbles. *Journal of the American Chemical Society* **2009,** *131* (15), 5386-5387.

[98] Fujii, S.; Kameyama, S.; Armes, S. P.; Dupin, D.; Suzaki, M.; Nakamura, Y. pH-responsive liquid marbles stabilized with poly(2-vinylpyridine) particles. *Soft Matter* **2010,** *6* (3), 635-640.

[99] Fujii, S.; Aono, K.; Suzaki, M.; Hamasaki, S.; Yusa, S.-i.; Nakamura, Y. pH-Responsive Hairy Particles Synthesized by Dispersion Polymerization with a Macroinitiator as an Inistab and Their Use as a Gas-Sensitive Liquid Marble Stabilizer. *Macromolecules* **2012,** *45* (6), 2863-2873.

[100] Xu, Z.; Zhao, Y.; Dai, L.; Lin, T. Multi-Responsive Janus Liquid Marbles: The Effect of Temperature and Acidic/Basic Vapors. *Particle & Particle Systems Characterization* **2014,** *31* (8), 839-842.

[101] Yusa, S.-i.; Morihara, M.; Nakai, K.; Fujii, S.; Nakamura, Y.; Maruyama, A.; Shimada, N. Thermo-responsive liquid marbles. *Polym J* **2014,** *46* (3), 145-148.

[102] Nakai, K.; Nakagawa, H.; Kuroda, K.; Fujii, S.; Nakamura, Y.; Yusa, S.-i. Near-infrared-responsive Liquid Marbles Stabilized with Carbon Nanotubes. *Chemistry Letters* **2013,** *42* (7), 719-721.

[103] Nakai, K.; Fujii, S.; Nakamura, Y.; Yusa, S.-i. Ultraviolet-light-responsive Liquid Marbles. *Chemistry Letters* **2013,** *42* (6), 586-588.

[104] Tian, J.; Arbatan, T.; Li, X.; Shen, W. Liquid marble for gas sensing. *Chemical Communications* **2010,** *46* (26), 4734-4736.

[105] Miao, Y.-E.; Lee, H. K.; Chew, W. S.; Phang, I. Y.; Liu, T.; Ling, X. Y. Catalytic liquid marbles: Ag nanowire-based miniature reactors for highly efficient degradation of methylene blue. *Chemical Communications* **2014,** *50* (44), 5923-5926.

[106] Sheng, Y.; Sun, G.; Ngai, T. Dopamine Polymerization in Liquid Marbles: A General Route to Janus Particle Synthesis. *Langmuir* **2016,** *32* (13), 3122-3129.

[107] Arbatan, T.; Al-Abboodi, A.; Sarvi, F.; Chan, P. P. Y.; Shen, W. Tumor Inside a Pearl Drop. *Advanced Healthcare Materials* **2012,** *1* (4), 467-469.

[108] Tian, J.; Fu, N.; Chen, X. D.; Shen, W. Respirable liquid marble for the cultivation of microorganisms. *Colloids and Surfaces B: Biointerfaces* **2013,** *106*, 187-190.

[109] Arbatan, T.; Li, L.; Tian, J.; Shen, W. Liquid Marbles as Micro-bioreactors for Rapid Blood Typing. *Advanced Healthcare Materials* **2012,** *1* (1), 80-83.

[110] Persson, B. N. J. Contact mechanics for randomly rough surfaces. *Surface Science Reports* **2006,** *61* (4), 201-227.

[111] Barthel, E. Adhesive elastic contacts: JKR and more. *Journal of Physics D: Applied Physics* **2008,** *41* (16), 163001.

[112] Hertz, H. Ueber die Berührung fester elastischer Körper. In *Journal für die reine und angewandte Mathematik* 1882, pp 156-171.

[113] Johnson, K. L.; Kendall, K.; Roberts, A. D. Surface Energy and the Contact of Elastic Solids. *Proceedings of the Royal Society of London. A. Mathematical and Physical Sciences* **1971,** *324* (1558), 301-313.

[114] Derjaguin, B. V.; Muller, V. M.; Toporov, Y. P. Effect of contact deformations on the adhesion of particles. *Journal of Colloid and Interface Science* **1975,** *53* (2), 314-326.

[115] Muller, V. M.; Derjaguin, B. V.; Toporov, Y. P. On two methods of calculation of the force of sticking of an elastic sphere to a rigid plane. *Colloids and Surfaces* **1983,** *7* (3), 251-259.

[116] Greenwood, J. A.; Williamson, J. B. P. Contact of Nominally Flat Surfaces. *Proceedings of the Royal Society of London A: Mathematical, Physical and Engineering Sciences* **1966,** *295* (1442), 300-319.

[117] Fuller, K. N. G.; Tabor, D. The Effect of Surface Roughness on the Adhesion of Elastic Solids. *Proceedings of the Royal Society of London. A. Mathematical and Physical Sciences* **1975,** *345* (1642), 327-342.

[118] Bush, A. W.; Gibson, R. D.; Thomas, T. R. The elastic contact of a rough surface. *Wear* **1975,** *35* (1), 87-111.

[119] Bush, A.; Gibson, R.; Keogh, G. The limit of elastic deformation in the contact of rough surfaces. *Mechanics Research Communications* **1976,** *3* (3), 169-174.

[120] Persson, B. N. J. Theory of rubber friction and contact mechanics. *The Journal of Chemical Physics* **2001,** *115* (8), 3840-3861.

# 2 Optimization of superamphiphobic layers based on candle soot

*Maxime Paven, Periklis Papadopoulos, Lena Mammen, Xu Deng, Hermann Sachdev, Doris Vollmer*, Hans-Jürgen Butt**

Max Planck Institute for Polymer Research, Ackermannweg 10, D-55128, Mainz, Germany. Email: butt@mpip-mainz.mpg.de, vollmerd@mpip-mainz.mpg.de

Reprinted from *Pure Appl. Chem.* **2014**; 86 (2): 87–96.



Keywords: Cassie state; roughness; superhydrophobicity; super-omniphobicity; Wenzel state; wetting

## 2.1 Abstract:

Liquid repellent layers can be fabricated by coating a fractal-like layer of candle soot particles with a silicon oxide layer, combusting the soot at 600°C and subsequently silanizing with perfluoroalkylsilanes. Drops of different liquids deposited on these so-called "superamphiphobic" layers easily roll off thanks to the low liquid-solid adhesion. The lower value of the surface tension of liquids that can be repelled depends on details of the processing. Here, we analyze the influence of the soot deposition duration and height with respect to the flame on the structure and wetting properties of the superamphiphobic layer. The mean diameter of the soot particles depends on the distance from the wick. Close to the wick, the average diameter of the particles varies between 30 – 50 nm as demonstrated by scanning electron microscopy. Close to the top of the flame the particles size decreases to 10 – 20 nm. By measuring the mass of superamphiphobic layers and their thickness by laser scanning confocal microscopy in reflection mode, we could determine that the average porosity is

0.91. The height-dependent structural differences affect the apparent contact and roll-off angles. Lowest contact angles are measured when soot is deposited close to the wick due to wax that is not completely burnt, smearing out the required overhanging structures. The small particle size close to the top of the flame also reduces contact angles, again due to decreasing size of overhangs. Sooting in the middle of the flame led to optimal liquid repellency. Furthermore, for sooting times longer than 45 s the properties of the layer did not change with sooting time, verifying the self-similarity of the layer.

## 2.2 Introduction

Superamphiphobic layers repel water and oils.[1-2] Tilting a superamphiphobic surface by less than 10 degrees is enough to allow droplets to roll-off. Superamphiphobic layers are “self-cleaning”, which means that water, soap solutions and oil drops are able to remove dust and contaminants while rolling off the surface. Superamphiphobic layers can serve as almost contact-free substrates for many liquids and solutions.

In general, the wetting behavior of a surface can be characterized by the value of the contact angle of a liquid droplet deposited on it. The liquid may spread completely or form a finite contact angle Θ. For a smooth, homogeneous surface, the contact angle of a liquid droplet on a solid surface in thermodynamic equilibrium can be calculated theoretically by Young’s equation.[3]

$$\gamma_{\mathrm{lv}}\cos(\Theta_E) = \left(\gamma_{\mathrm{sv}} - \gamma_{\mathrm{sl}}\right) \qquad \text{(eq. 2.1)}$$

Here, $\gamma_{LV}$, $\gamma_{SV}$ and $\gamma_{SL}$ are the liquid-vapour, solid-vapour, and solid-liquid surface tensions, respectively. If the surface tension of the solid-air interface is higher than that of the solid-liquid interface ($\gamma_{SV} > \gamma_{SL}$), the right side of the Young equation is positive. As a consequence, cosΘ is also positive, corresponding to a contact angle between 0 and 90°; the surface is lyophilic. When the right side of the Young equation is negative ($\gamma_{SV} < \gamma_{SL}$), cosΘ is negative; this corresponds to a contact angle higher than 90°and the surface is lyophobic. In the case of smooth surfaces, the highest contact angle observed for a water drop is about 120° on fluorinated materials.

To reach higher apparent contact angle, the surface needs to be textured. For textured surfaces, the apparent contact angle can exceed 150°, if the texture leads to an entrapment of air.[4] On such composite surfaces the drop partially sits on air pockets. The situation, where the drop sits to a significant degree on air, is called the Cassie-state.[5] In addition to the high apparent contact angle, the drop rolls off at small tilting angles. A surface is called super-repellent with respect to a certain liquid if the liquid forms an apparent contact angle above 150° and a drop rolls off at a tilting angle below 10°.[6-8]

No naturally occurring flat surface is known to show a contact angle greater than 90° for organic liquids. Few synthetic superamphiphobic surfaces have been reported[9-16], as they are considerably more difficult to create than superhydrophobic surfaces. Tuteja et al. proved that careful design of the topography of a surface allows constructing surfaces with a contact angle for hexadecane close to 160°, although the flat surface was oleophilic.[2] Composite surfaces with convex small-scale roughness and overhanging structures can provide a sufficient energy barrier to prevent complete impalement of the liquid.[17-19] When the liquid impales a superamphiphobic layer and the entrapped air is displaced is called the Wenzel state.[20] Superamphiphobicity is lost in the Wenzel state and only exists in the Cassie state.

Lately we developed a facile method to fabricate transparent superamphiphobic layers by using candle soot as a template.[21] Soot is well-known for its good water-repellency.[22-23] This procedure is applicable to a whole variety of different substrates, which can be heated to 600°C such as glass plates, metal pieces and meshes. In this manuscript, we show that the size and shape of deposited soot can be tuned by the soot deposition procedure. Large aggregates are formed close to the wick, whereas small particles are deposited if the substrate is placed close to the top of the candle flame. Size and shape of the particles change the level of liquid repellency of the layer.

## 2.3 Materials and methods

**Chemicals**. All chemicals were used without further purification: Ammonia (25% in water, Fluka, Germany), tetraethoxysilane (TEOS, 98%, Acros Organics,

Belgium), absolute ethanol (>99,8%, Sigma-Aldrich, Germany) and trichloro(1H,1H,2H,2H-perfluorooctyl)silane (97%, Sigma Aldrich, Germany). Milli-Q water was obtained from a Millipore purification system operating at 18.2 MΩ cm. The glass slides, Menzel GmbH, Germany and silicon wafers (Si-Mat, Germany) taken as a substrate for the superamphiphobic layers were cleaned with a Hellmanex II solution (Hellma GmbH).

**Characterization methods**. The morphology of the soot particles and the layer were characterized by scanning electron microscopy (SEM, low voltage LEO 1530 Gemini, Germany, and SU8000, Hitachi, Japan). The samples were prepared on a silicon wafer and investigated without further treatment. The thickness of the layer and its topography were determined by laser scanning confocal microscopy (LSCM, Leica, TCS SP5 II – STED CW).[24] Static contact angles and roll-off angles were measured in the sessile drop configuration (Dataphysics OCA35, Data Physics Instruments GmbH, Germany). Contact and roll-off angles were measured at six positions after depositing a 6 µl water droplet on the surface, removing the needle and tilting the stage at a speed of 1.3°/s. Simultaneously the shape of the droplet was recorded. Increasing the speed by one order of magnitude or droplet volume by a factor of two did not change the tilting angle within experimental accuracy. The chemical composition of the layer was investigated using a confocal Raman microscope (Bruker, Senterra).

**Sooting of samples**. Preparation of superamphiphobic layers (**Figure 1**) starts with sooting.[21,25] Silicon wafers or glass slides (2 x 2 $cm^2$, Menzel) were used as substrates. The substrates were cleaned with Hellmanex II solution prior to usage. The samples were coated with an automated sooting machine, which could hold and move the substrate. The horizontal range of the linear sooting movement was 18 cm and a full cycle took 1.4 s. The velocity followed a sinusoidal profile to reduce vibrations close to reversal of direction.

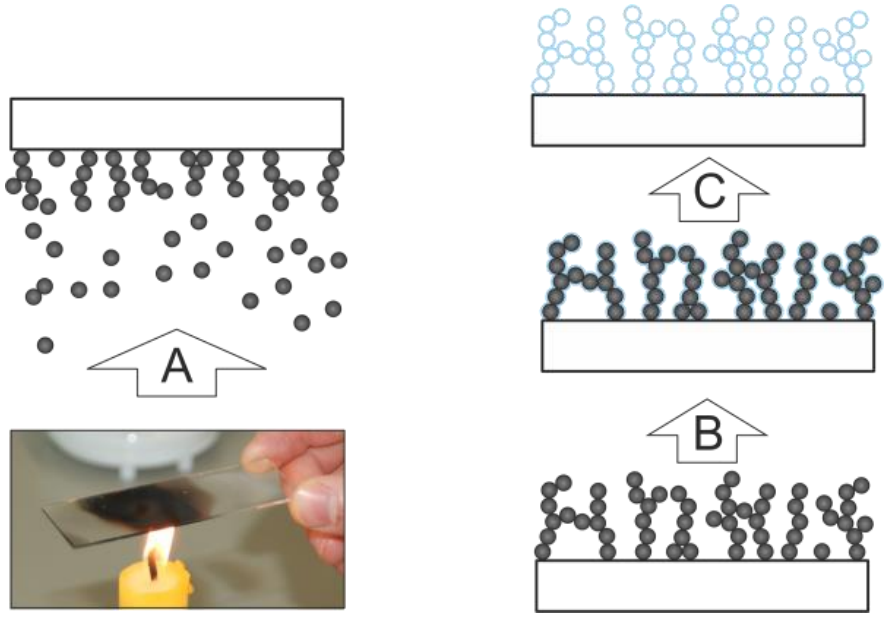


**Figure 1**: Schematic of the fabrication of superamphiphobic surfaces. A) deposition of soot. B) Chemical vapor deposition of tetraethoxysilane coats the soot with a silica shell. C) Combustion of the soot renders the surface transparent.

The range of the sooting movement exceeded the size of the substrates by a factor of 9. Therefore, the velocity of the substrate was almost constant while sooting. The distance of the substrate from the candle wick was fixed during deposition and could be varied between 0 – 3 cm.

**Chemical vapor deposition (CVD) of tetraethoxysilane (TEOS).** Soot coated samples were transferred to a desiccator and two snap cap vials with a diameter of 2.4 cm and a volume of 30 ml were placed next to the samples. One snap cap vial was filled with 3 ml ammonium hydroxide aqueous solution and the other vial with 3 ml TEOS. The desiccator was sealed and vacuum was applied for ≈30 s (250 mbar). The vacuum was slowly released by opening the desiccator valve up to the point where a faint hissing could be noticed. The pressure in the desiccator reached 1 atm after 1 min. CVD was carried out for 24 h, if not stated otherwise. Similar to a Stöber reaction, silica is formed by hydrolysis and condensation of TEOS catalyzed by ammonia. Samples were directly used after preparation.

**Combustion.** CVD-coated samples were heated for 2 hours at 600°C becoming nearly transparent.

**Hydrophobization**. After combustion the samples were coated with trichloro(1H,1H,2H,2H-perfluorooctyl)silane. Again, samples were transferred to a desiccator and a snap cap vial with a diameter of 2.4 cm and a volume of 30 ml was filled with 100 µl trichloro(1H,1H,2H,2H-perfluorooctyl)silane and placed next to the samples. The desiccator was sealed and vacuum was applied until the pressure reached a value of 200 mbar (1 min). The vacuum was released after 3-4 hours. To remove the excess of not chemically bound trichloro(1H,1H,2H,2H-perfluorooctyl)silane, the samples were placed in an oven at 60°C and 200 mbar for 2 hours.

The properties of the superamphiphobic layer depend on details of the sooting procedure as well as on the period of CVD of TEOS. Both influence the nanoscale structure, which plays an important role for the superamphiphobic character of the sample. Therefore, sooting parameters play a crucial role for the density, mechanical strength and superamphiphobicity of these surfaces. Variation of sooting height and time permits to tune the structure of the soot template.

## 2.4 Results

### 2.4.1 **Deposited soot mass**

In order to explore the influence of soot deposition parameters we designed an automated sooting device, which permits varying the distance of the candle wick to the substrate, $h_i$. To compare different flames, we use the relative sooting height $R_i = h_i / H$ in the following. Here, $H$ denotes the height of the flame (**Figure 2**). To explore the mass of deposed soot with regard to the different sooting heights and times, glass substrates with a dimension of 2 x 2 $cm^2$ were coated using the automated sooting device. We measured the mass of the glass substrate before and after sooting. The soot mass deposited increases linearly with sooting time although the error is large for low sooting times and for substrates that were positioned just above the wick, for $R$ = 0.25 (**Figure 3**). The gas flow may inhibit effective and homogenous absorption of soot particles onto the glass. The maximal deposition rate is obtained at $R$ = 0.45. Close to the top of

the flame, $R$ = 0.92, the amount of deposited soot per unit of time decreases again, likely due to partial combustion of the soot particles.

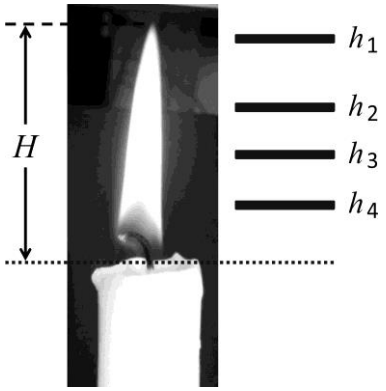


**Figure 2**: Image of a candle flame. The black solid lines denote the positions of the substrate (glass slide or silicon wafer). The different sooting heights, $h_i$, were measured with respect to the wick, dotted line. In most cases, the flame height was $H \approx 3$ cm. This corresponds to relative sooting heights: $R_1$ = 0.92, $R_2$ = 0.64, $R_3$ = 0.45, and $R_4$ = 0.26 from top to bottom.

To gain more insight into the size and shape of the deposited particles we investigated the surface of the layer by scanning electron microscopy (**Figure 4**). Close to the top of the flame, $R$ = 0.92, the particles are almost spherical but they are too small to be clearly resolved.

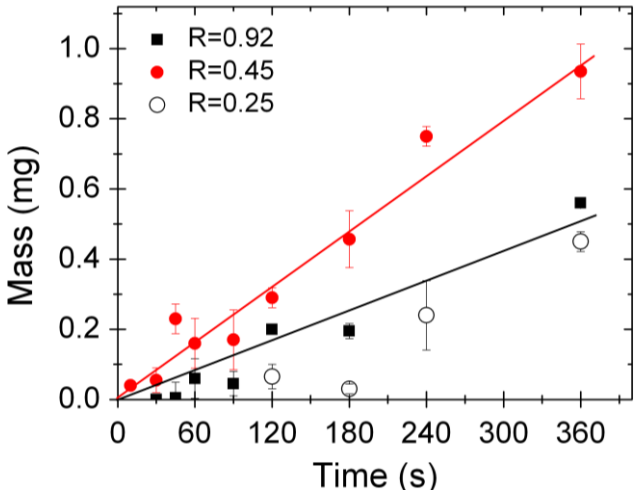


**Figure 3**: Deposited soot mass on a 2 x 2 cm$^2$ glass slide for different sooting times and heights. Each data point represents the arithmetic mean of two or three independent measurements. The solid lines are guides to the eye.

The particles with a diameter of 10 to 20 nm (Figure 4a) assemble in particles strands varying in length, orientation, and shape. The strands form a highly

porous fractal-like network (Figure 4b). Close to the wick, $R$ = 0.25, the particles are larger and less spherical (Figure 4c, **Figure 5**a).

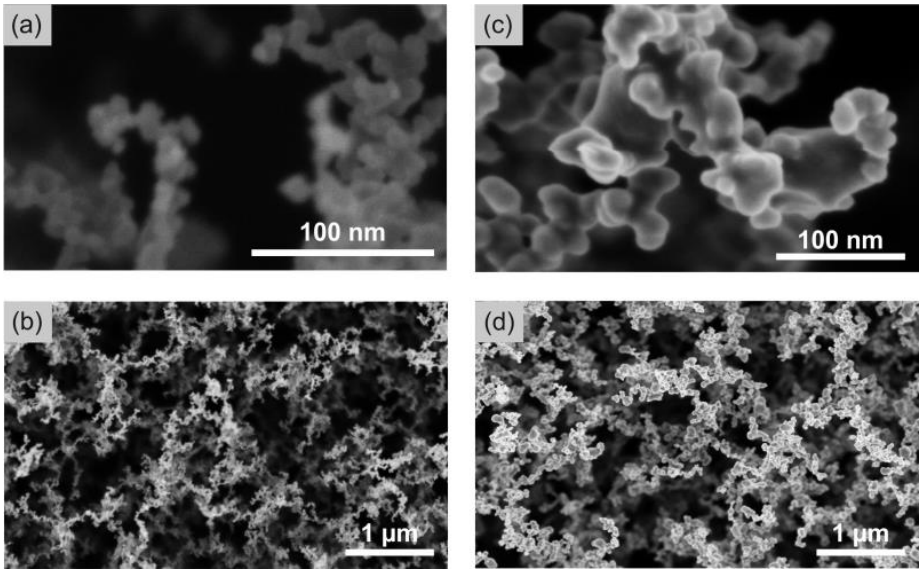


**Figure 4**: Dependence of the size and shape of the soot particles on the sooting height. The substrates were sooted for 20 s. Images a) and b) were taken at $R$ = 0.92. Images c) and d) were taken $R$ = 0.25.

High magnification SEM shows that aggregates are formed which seem to consist of several isolated particles. It is possible that the wax is not fully burned, causing that neighboring particles are embedded in a layer of evaporated wax. At lower magnification, the denser network still appears fractal-like (Figure 4d). To check whether incompletely burned wax is the reason for the formation of aggregates, we heated the deposited soot in a vacuum oven for 3 h at 200 °C.

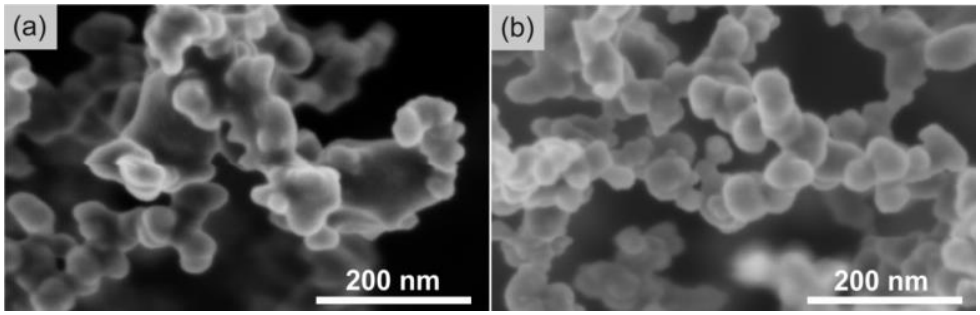


**Figure 5:** SEM images showing the morphology of soot deposited at low sooting height, $R$ = 0.25. a) Image was taken directly after depositing soot for 20 s. b) Image was taken after heating the soot coated substrate for 3h at 200 °C in a vacuum oven.

At this temperature, wax evaporates slowly. After heating, the irregularly shaped aggregates are shown to consist of almost spherical soot particles (Figure 5b). The size of the particles varied between 30 and 50 nm. Thus, close to the wick evaporated wax can lead to cluster formation, whereas close to the top of the flame combustion causes smaller particle sizes.

### 2.4.2 **Network structure for different sooting times**

To test whether the morphology of the network depends on the sooting time, different sooting times between 20 s and 3 min were explored. Neither the topography of the layer nor the size and shape of the particles changed with the sooting time, as indicated by SEM images taken at different magnifications (**Figure 6**). This supports the self-similarity of the layer. Therefore, the final properties of the layer should be independent on the sooting time in agreement with our previous findings.

For the time-dependent measurements, we select samples coated at a middle height ($R$ = 0.64). The samples shown in Figure 6 were not heated before the SEM images were taken.

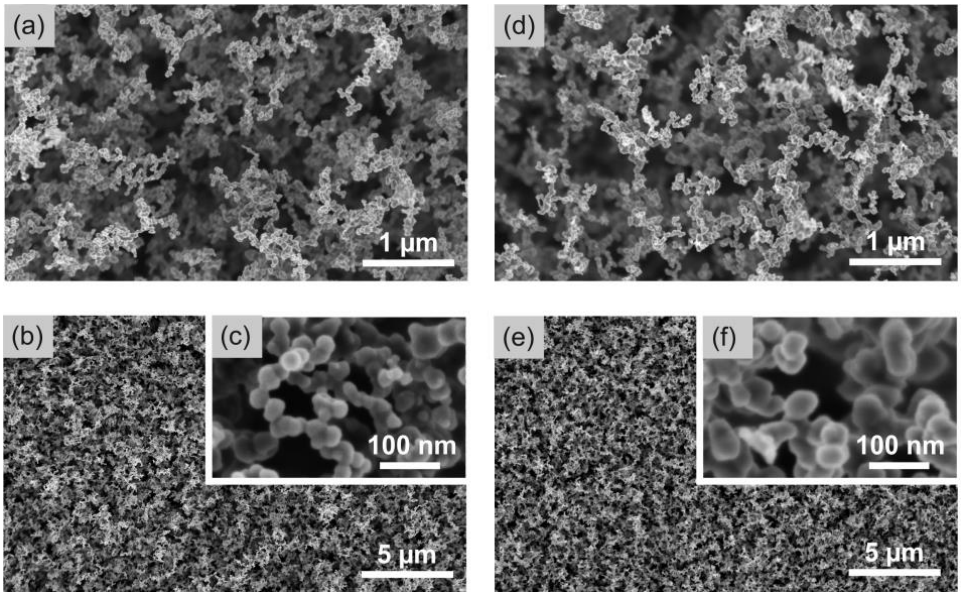


**Figure 6:** SEM images showing the dependence of the morphology and particle size on sooting time and magnification, $R$ = 0.64. a) to c) the substrates were sooted for 20 s. d) to f) the substrates were sooted for 120 s.

The high-resolution SEM images show that the particle aggregates are made up of almost spherical carbon beads, having a size of 40 ±10 nm, i.e. still much larger than those close to the top of the flame. At this height, hardly any wax could be resolved, implying that at this height the wax already burned completely (Figure 6c and 6f). This renders heat treatment of the samples before usage unnecessary.

### 2.4.3 **Analyzing soot composition by Raman spectroscopy**

The soot particles are only connected by weak physical bonds. Therefore, the fractal-like structure is fragile. To improve its mechanical stability we developed a technique to coat the soot particles with a silica shell. However, for a good chemical bonding of TEOS to the soot surface, a surface functionalization with hydroxyl groups would be beneficial. Raman spectroscopy was used as a non-destructive tool to verify the presence of hydroxyl groups. We deposited a thick layer of soot (> 100 µm) on a platinum substrate to ensure that the substrate does not contribute to the Raman signal. For comparison, we measured the spectrum of pure soot (**Figure 7**, black line) and the soot layer after CVD of TEOS (Figure 7, red line). Since the preparation of the soot took place in air, the soot samples can chemically be described as $C_xH_yO_z$, with x>>y,z. Rather pure, unordered carbons with different $sp^2/sp^3$ ratio gives usually rise to various intense D- and G- bands in the spectra with almost no or only broad, unstructured contributions in the range of 2500-3500cm$^{-1}$ where C-H stretching vibrations are expected.

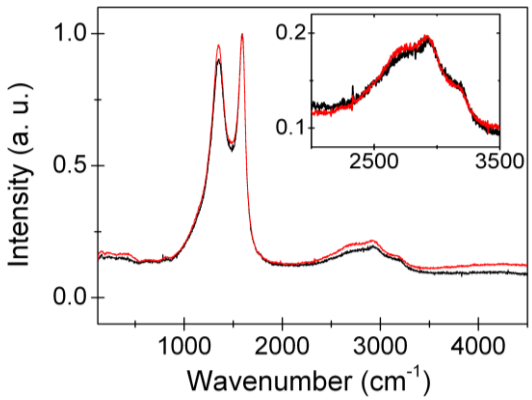


**Figure 7:** Raman spectrum of soot (black line) and silica-coated soot (red line). The spectra proof the hydrophilicity of the soot surface, due to the presence of OH-groups. Sooting height: R ≈ 0.64. Laser excitation: 488 nm.

Highly ordered (few layer) graphene or graphitic materials lead to well resolved D, G, D´, D+D´´, 2D, D+D´and 2D´contributions, the last four also located in the above-mentioned region.[26-28] Since ternary $C_xH_yO_z$ materials still have significant amounts of aliphatic and aromatic CH- bonds and also C-OH- bonds (of weak Raman activity) in the same region, the Raman modes of weakly crystalline carbonaceous materials, such as soot, can reveal significant contributions of these moieties in this region. In that case, the features resulting from highly crystalline graphene structures can be excluded if broad D and G band structures are present.

For both samples, the Raman spectrum shows a broad D-peak at 1360 $cm^{-1}$ and G-peak at 1560 $cm^{-1}$ indicating a weakly ordered carbonaceous material. In addition, in the range from $\tilde{\nu}$= 2700 to 3300 $cm^{-1}$ it is possible to assign the modes according to the above described arguments for an extremely weak ordered carbon material also to originate from superposition of symmetric and anti-symmetric aliphatic C-H stretches ($\tilde{\nu}$ = 2800-2950 $cm^{-1}$), aromatic C-H stretches ($\tilde{\nu} \geq$3000 $cm^{-1}$) and O-H stretches ($\tilde{\nu} \approx$ 3300 $cm^{-1}$, broad). The latter broad peak suggests hydroxyl groups on the soot surface, enabling an ammonia catalyzed nucleophilic condensation of TEOS on the surface in order to form an enveloping silica network.

A treatment of the sooted samples before or after TEOS CVD in a water vapor or oxygen containing plasma can further enhance the number of OH binding states (and also of CH- and $CH_2$ groups in the case of water) at the surface of the carbon soot.

### 2.4.4 **Thickness of porous silica**

Coating the soot particle network with silicon oxide keeps the network intact. To measure the thickness of the layer we coated the soot deposited on glass substrates with silica and combusted the carbon at 600°C. This renders the black layer almost transparent. The transparency decreases with increasing thickness of the layer. Up to a few tens of micrometers, the thickness of the layer can be measured by confocal microscopy in reflection mode. Although the layer is largely transparent, a minor part of the light is reflected at the silica-air interfaces

(**Figure 8**). The thickness of the layer is measured at different positions of the glass plate. Near the rim of the plate (0 mm), no superamphiphobic layer was visible. The black line shows the reflection of the light at the upper surface of the glass plate (Figure 8a, inverted intensity scale). The reflectivity curve of the glass-air interface is almost symmetric, with a width given by the diffraction limit of confocal microscopy (Figure 8b, black line). When looking at the superamphiphobic layer 5 and 10 mm away from the rim toward the center of the glass substrate the peak is followed by a plateau. Light is also reflected up to 10 µm above the glass-air interface (Figure 8b, red line).

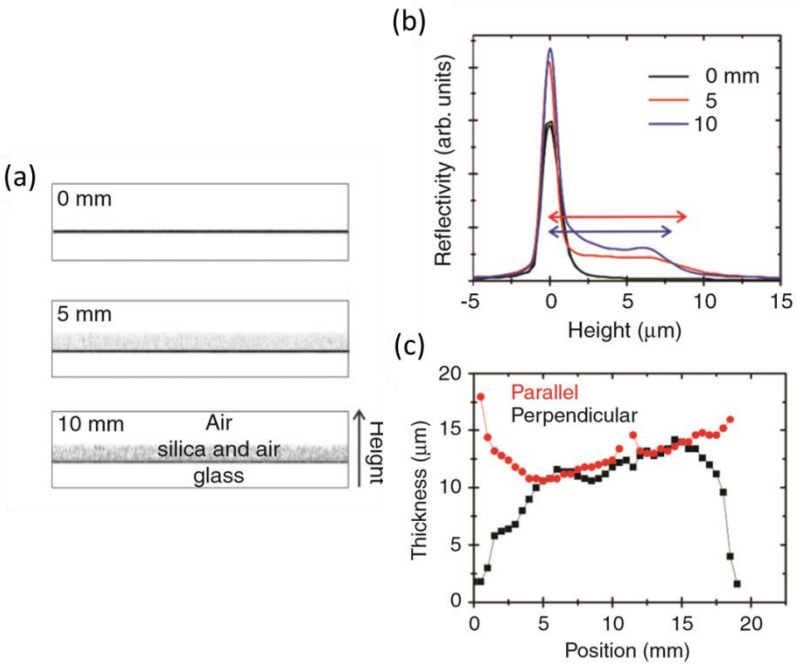


**Figure 8:** a): Vertical cross-sectional confocal images of the reflectivity along the sample measured at different distances from the rim of the glass slide. Image width: 180 µm. b) Average reflectivity as a function of height measured at different positions of a glass plate; size: 20 × 20 mm$^2$. The sharp reflection at $z$ = 0 results from the glass-silica interface. The "plateau" for higher $z$ results from light scattered by the porous silica network. Local variations of the layer thickness cause that the reflectivity is smeared out. Therefore, we used the inflection point to measure the thickness of the layer, red and blue arrow. c) The thickness of the silica layer parallel (red data points) and perpendicular (black data points) to the sooting direction. This glass plate was sooted for 30 s at $R$ = 0.45, treated for 48 h with CVD of TEOS and the soot was subsequently combusted.

Further above the glass surface, the reflectivity decreases strongly, pointing towards the absence of material that can reflect light. From the end of the plateau, we estimated the layer thickness (Figure 8b, red arrow). Further experiments showed that the thickness of the layer hardly varies parallel to the sooting direction (Figure 8c, red data points). Perpendicular to the sooting direction it is maximally close to the center and decreases when approaching the edges (Figure 8c, black data points). The fluctuations of the layer thickness in the "plateau" region arise from local inhomogeneities of the deposition of soot. These inhomogeneities are caused by turbulences in the gas stream carrying the soot particles.

### 2.4.5 **Porosity of the layer**

To estimate the mean density of the superamphiphobic layer, the volume and the mass need to be known. The volume of the layer can be estimated from the thickness of the layer (Figure 8c). Furthermore, the mass of the layer was measured after sooting for well-defined periods, as well as after CVD of TEOS, combustion of soot and fluorination. This yields for the average density of soot, $\rho_{soot}$ = 0.072 ± 0.02 g/cm$^3$ (**Figure 9**).

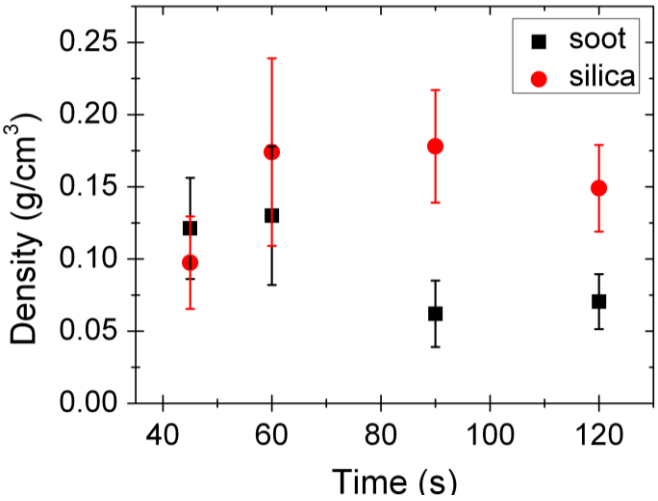


**Figure 9.** Dependence of the density of the soot layer (squares) and of the hollow silica layer after fluorination (circles) on sooting time. Before combustion, the soot was exposed to CVD of TEOS for 48 h. $R$ = 0.45.

Although 48 h of CVD of TEOS slightly smears out the overhanging structures, a thicker silica shell increases the accuracy of the measurements of the tiny

masses. The density of the fluorinated hollow silica network is larger, likely due to the high density of silica, $\rho_{SiO2}$ = 0.14 ± 0.03 g/cm$^3$. Note that $\rho_{SiO2}$ depends on the period of CVD of TEOS. Within experimental accuracy, the density does not vary with sooting time, in agreement with the independence of the morphology on time (Figure 6). Assuming a density of the pure soot (amorphous carbon) of 2.0 g/cm$^3$ and that of amorphous silicon oxide of 2.5 g/cm$^3$ the porosity of the superamphiphobic layer is 0.96 and 0.94, respectively. For the silicon oxide, we should also consider that the value includes the hollow space which has previously been filled by the soot. This space is not available to the liquid. If we only ask for the available porosity, this hollow space needs to be taken into account. The available porosity is given by adding the porosity of the soot and that of the silicon oxide to a final value of 0.91.

### 2.4.6 **Contact angle and roll-off angles**

To transform the hydrophilic silicon oxide layer into a superamphiphobic layer its surface was coated by CVD with trichloro(perfluorooctyl)silane. The contact and roll-off angle of the final superamphiphobic layer did not change within experimental accuracy when the period of CVD was decreased to 1 h. The apparent contact angle slightly decreased and the roll-off angle increased when the soot was not combusted. Still, the layer can resist wetting of liquids with low surface tension such as hexadecane.

**Contact angle measurements.** Water was not suitable to reliably measure contact and roll-off angles since; the contact angles were too large and drops immediately rolled off. Therefore *n*-hexadecane was used to characterize all samples. The surface tension of hexadecane is 27.5 mN/m. It shows a contact angle of 64 ±1° on a flat fluorinated surface. Highest contact angles and lowest roll off angles were achieved with $R$ = 0.45 and sooting times longer than 45 s (**Figure 10**).

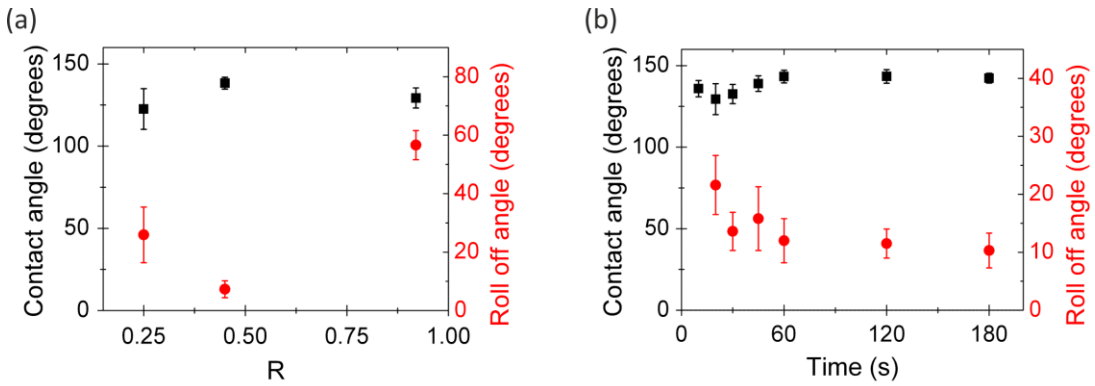


**Figure 10**: a) Dependence of the contact and roll-off angles of hexadecane on the sooting height, $R$. b) Variation of the contact angle and roll off angle with sooting time. Relative sooting height: $R$ = 0.45. The error is the standard deviation of 6 independent measurements. Drop volume: 6 µL.

Samples with sooting times of 45 s or less suffer from pinning effects of hexadecane, especially for low sooting times. Likely, the layer was so thin that the drop can impale the layer. Removal of the drop can cause the removal of the topmost part of the layer.

## 2.5 Conclusions

The size of the soot particles depends on the sooting height. Close to the wick the particles are enveloped by a layer of wax, which can be removed by heating in vacuum. The average particle size varies between 30 and 50 nm. Close to the top of the flame the particles size decreases to 10 – 20 nm as confirmed by scanning electron microscopy. Coating the particles with a silica shell is possible due to the presence of hydroxyl groups on the outside of the soot particles. Raman spectroscopy also reveals that both the soot and the silica shell are amorphous. Combustion of the soot renders the superamphiphobic layer transparent. The thickness of the layer can be measured by LSCM in reflection mode. The average mass density of soot is 0.07 g/cm$^3$, proving a high porosity of the soot layer of 0.96. The contact and roll-off angles depend on the initial sooting position, because of the variation in particle size and due to the formation of wax coated particle aggregates. Sooting in the middle of the flame led to layers with best liquid repellency. These results might promote industrial-scale applications of superamphiphobic coatings based on soot.

## 2.6 Acknowledgments

M.P. synthesized the candle-soot templated surfaces and characterized the samples gravimetrically and by contact angle measurement. L.M. and X.D. took SEM images. H.S. analyzed the soot samples using Raman spectroscopy. H.-J. B. and D.V. had the idea for the project and organized it. M.P., D.V. and H.-J. B. wrote the manuscript. All authors discussed the results and edited the manuscript.

We are grateful to S. Geiter, G. Glasser and G. Schäfer for technical support. We acknowledge financial support from the Deutsche Forschungsgemeinschaft via SPP 1273 (D.V.), SPP 1420 (H.J.B.).

## 2.7 References

[1] Xie, Q. D.; Xu, J.; Feng, L.; Jiang, L.; Tang, W. H.; Luo, X. D.; Han, C. C. *Advanced Materials* **2004**, *16*, 302.

[2] Tuteja, A.; Choi, W.; Ma, M. L.; Mabry, J. M.; Mazzella, S. A.; Rutledge, G. C.; McKinley, G. H.; Cohen, R. E. *Science* **2007**, *318*, 1618.

[3] Young, T. *Phil. Trans. Roy. Soc. London* **1805**, *95*, 65.

[4] Oner, D.; McCarthy, T. J. *Langmuir* **2000**, *16*, 7777.

[5] Cassie, A. B. D.; Baxter, S. *Trans. Faraday Soc.* **1944**, *40*, 0546.

[6] Quere, D. *Rep. Prog. Phys.* **2005**, *68*, 2495.

[7] Feng, L.; Li, S. H.; Li, Y. S.; Li, H. J.; Zhang, L. J.; Zhai, J.; Song, Y. L.; Liu, B. Q.; Jiang, L.; Zhu, D. B. *Advanced Materials* **2002**, *14*, 1857.

[8] Dorrer, C.; Ruhe, J. *Soft Matter* **2009**, *5*, 51.

[9] Shibuichi, S.; Yamamoto, T.; Onda, T.; Tsujii, K. *J. Colloid Interface Sci.* **1998**, *208*, 287.

[10] Meng, H. F.; Wang, S. T.; Xi, J. M.; Tang, Z. Y.; Jiang, L. *J. Phys. Chem. C* **2008**, *112*, 11454.

[11] Darmanin, T.; Guittard, F. *J. Am. Chem. Soc.* **2009**, *131*, 7928.

[12] Chhatre, S. S.; Choi, W.; Tuteja, A.; Park, K. C.; Mabry, J. M.; McKinley, G. H.; Cohen, R. E. *Langmuir* **2010**, *26*, 4027.

[13] Xiong, D.; Liu, G. J.; Hong, L. Z.; Duncan, E. J. S. *Chem. Mater.* **2011**, *23*, 4357.

[14] Wong, T. S.; Kang, S. H.; Tang, S. K. Y.; Smythe, E. J.; Hatton, B. D.; Grinthal, A.; Aizenberg, J. *Nature* **2011**, *477*, 443.

[15] Artus, G. R. J.; Zimmermann, J.; Reifler, F. A.; Brewer, S. A.; Seeger, S. *Appl. Surf. Sci.* **2012**, *258*, 3835.

[16] Bellanger, H.; Darmanin, T.; De Givenchy, E. T.; Guittard, F. *RCS Adv.* **2013**, *3*, 5556.

[17] Herminghaus, S. *Europhys. Lett.* **2000**, *52*, 165.

[18] Nosonovsky, M. *Langmuir* **2007**, *23*, 3157.

[19] Butt, H. J.; Semprebon, C.; Papadopoulos, P.; Vollmer, D.; Brinkmann, M.; Ciccotti, M. *Soft Matter* **2013**, *9*, 418.

[20] Wenzel, R. N. *Industrial and Engineering Chemistry* **1936**, *28*, 988.

[21] Deng, X.; Mammen, L.; Butt, H.-J.; Vollmer, D. *Science* **2012**, *335*, 67.

[22] Callies, M.; Quere, D. *Soft Matter* **2005**, *1*, 55.

[23] Naha, S.; Sen, S.; Puri, I. K. *Carbon* **2007**, *45*, 1702.

[24] Papadopoulos, P.; Deng, X.; Vollmer, D.; Butt, H.-J. *Journal of Physics-Condensed Matter* **2012**, *24*.

[25] Arana, C. P.; Pontoni, M.; Sen, S.; Puri, I. K. *Combustion and Flame* **2004**, *138*, 362.

[26] Ferrari, A. C.; Robertson, J. *Physical Review B* **2000**, *61*, 14095.

[27] Ferrari, A. C.; Basko, D. M. *Nature Nanotechnology* **2013**, *8*, 235.

[28] Ferrari, A. C. *Solid State Communications* **2007**, *143*, 47.

# 3 Mechanical properties of highly porous super liquid-repellent surfaces

*Maxime Paven[a], Regina Fuchs[a], Taro Yakabe[b], Doris Vollmer[a], Michael Kappl[a], Akiko N. Itakura[b], and Hans-Jürgen Butt[a]**

[a] M. Paven, Dr. R. Fuchs, Prof. D. Vollmer, Dr. M. Kappl, Prof. H.-J. Butt. Max Planck Institute for Polymer Research, Ackermannweg 10, D-55128 Mainz, Germany. Email: butt@mpip-mainz.mpg.de

[b] T. Yakabe, Prof. A. Itakura. National Institute for Materials Science, 1-2-1 Sengen, Tsukuba, Ibaraki, 305-0047, Japan

Reprinted with permission from Adv. Funct. Mater. **2016**; 26 (27): 4914-4922.


Keywords: Atomic-force microscope; superamphiphobic surfaces; superhydrophobic surfaces; contact; wettability; compaction; deposition; roughness; membranes; adhesion

## 3.1 Abstract:

Surfaces with self-cleaning properties are desirable for many applications. Conceptually, super liquid-repellent surfaces are required to be highly porous on the nano- or micrometer scale, which inherently makes them mechanically weak. Optimizing the balance of mechanical strength and liquid repellency is a core aspect towards applications. However, quantitative mechanical testing of porous, super liquid-repellent surfaces is challenging due to their high surface roughness at different length scales and low stress tolerance. For this reason, mechanical testing is often performed qualitatively.

Here, the mechanical responses of soot-templated super liquid-repellent surfaces are studied qualitatively by pencil and finger scratching and quantitatively by

atomic force microscopy, colloidal probe force measurements and nanoindentation. In particular, colloidal probe force measurements cover the relevant force and length scales. The effective elastic modulus, the plastic work $W_{plastic}$ and the effective adhesive work $W_{adhesive,}$ are quantified. By combining information from force measurements with measurements of surface wetting properties, it is shown that mechanical strength can be balanced against low wettability by tuning the reaction parameters.

## 3.2 Introduction

Super liquid-repellent surfaces, or so-called superhydrophobic or superamphiphobic surfaces gained much attention[1-6] due their potential applications e.g. as self-cleaning coatings[7], membranes for gas exchange[8,9] or to suppress the formation of biofilms.[10] Liquid drops resting on these surfaces exhibit receding contact angles of more than ≈140° and easily roll-off at tilting angles lower than 10°. The excellent liquid repellency results from a low contact area of the drop with the substrate. Hereby, the drop rests on the top faces of micrometer-sized protrusions, separated from the substrate by air cushions.[11,12] The receding contact angle of the drop increases with the average distance and decreasing width of the surface protrusions. To achieve super liquid-repellency surface protrusions need to have overhangs.[13-15]

From these prerequisites, it follows that super liquid-repellent surfaces are sensitive to mechanical stress because an external force acts upon the surface protrusions and not the entire projected area. The surface protrusions break once a critical shear is exceeded.[16] As a result, the surface loses its liquid repellency.[17-19] Unfortunately, to optimize for high liquid repellency a different design for the surface morphology is required than for realizing high mechanical strength. For example, with respect to arrays of micropillars, the receding contact angle is high when choosing thin micropillars and a larger spacing between the pillars.[15] In contrast, for a good mechanical shear strength, the micropillars should be thick and narrowly spaced. Thus, for a given application the design needs to be carefully optimized and measuring the mechanical properties is an essential part of the surface improvement process.

In this work, we focus on the mechanical properties of super liquid-repellent surfaces formed by a porous network of connected particles. Such surfaces can readily be prepared by the bottom-up technique, i.e. gradually building up the surface starting from the substrate. This technique is appealing due to its simplicity, cost effectiveness and adaptability to coat large areas. The surfaces can e.g. be prepared by wet chemistry or thermal processes. Precursor solutions can contain various combinations of monomers, particles and hydrophobization agents. They can be drop, spin, dip or (electro)spray coated onto various substrates.[6, 19, 20-27] The precursor solutions can also be flame sprayed onto substrates[28, 29] or soot from the combustion of organic compounds can be collected to obtain porous layers of particles.[30, 31]

The prepared coatings, however, often suffer from low mechanical strength. The quantification and comparison of mechanical properties to improve them remains unsatisfactory. Qualitative tests e.g. the pencil hardness (ISO 15184 and ASTM D3363), (nano)wear abrasion[26, 32-35], sand (ASTM D968) or liquid jet impact[36] are fast and convenient. However, they generally only allow for a rough comparison and not for detailed insights into the surface mechanical properties. Ideally, the mechanical strength of samples is compared using quantitative properties like the effective elastic modulus, which can only be obtained by force sensitive measurements.

Here, we used complementary methods to characterize the mechanical properties of super liquid-repellent surfaces to get a comprehensive view of soot-templated surfaces. To cover different force ranges we used atomic force microscopy (AFM)[37, 38] and nanoindentation.[39] We explicitly demonstrate that force measurements with microspheres (“colloidal probe”)[40-42] instead of sharp AFM tips can be used to measure the averaged mechanical properties of soot-templated surfaces. The colloidal probe technique closes a gap of sensitivity vs. probing area and allows characterizing the mechanical properties of porous surfaces.

## 3.3 Results and discussion

Soot-templated surfaces as introduced by Deng et al.[31] served as a model system for fractal-like, highly porous super liquid-repellent surfaces (**Figure 1**a).

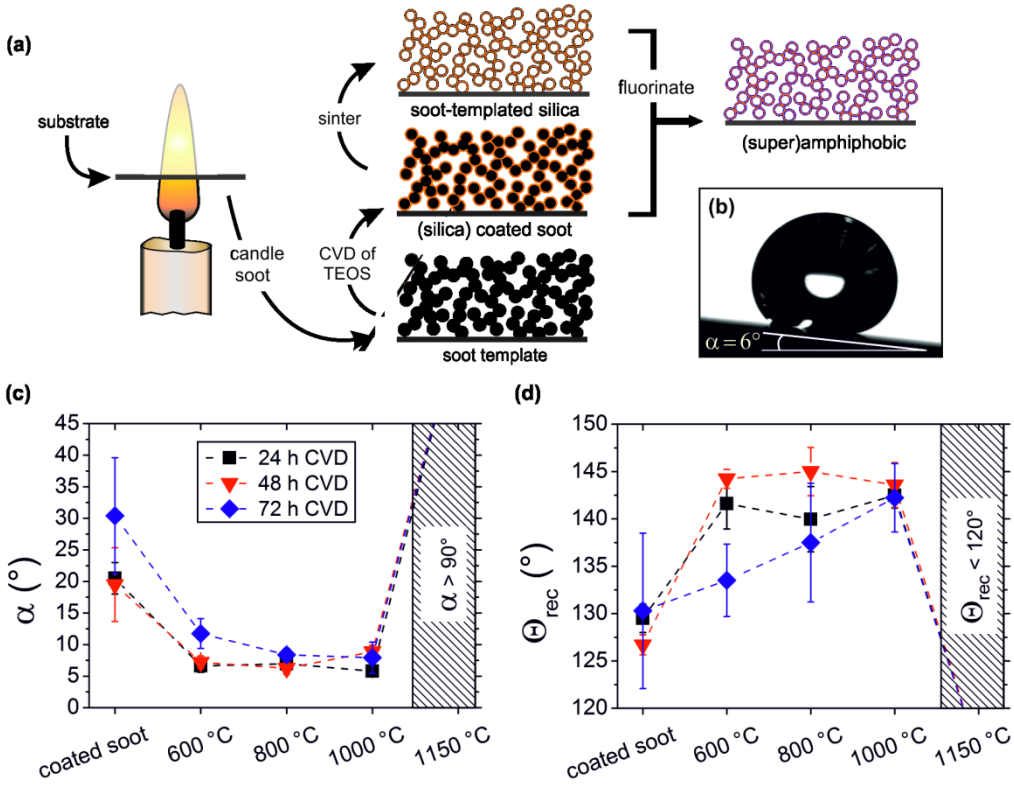


**Figure 1**: a) Scheme of sample preparation: Collection of candle soot on the substrate. Silica is deposited by chemical vapor deposition CVD of TEOS. Afterward, the coated soot was sintered at various temperatures. Deposition of a fluorosilane by CVD made the surfaces liquid repellent. b) Image of a hexadecane drop ($\gamma$=27.5 N/m, 6 µl) rolling off at 6° from a sample exposed to 24 h CVD sintered at 600 °C. c) Roll-off angles α and d) receding contact angles $\Theta_{rec}$ of hexadecane on soot-templated superamphiphobic surfaces as a function of CVD time and sintering temperature.

Soot consists of a highly porous network of carbon nanoparticles. The nanoparticles have a diameter of about 40 nm and are loosely connected by van der Waals forces. They partially assemble into agglomerates which are connected by strings of particles. The fragile network was stabilized by deposition of a silica shell using chemical vapor deposition (CVD) of tetraethyl orthosilicate (TEOS) for 24, 48 and 72 h. These samples are referred to as coated soot. The thickness of the deposited silica layer increased with CVD time and ranged from 20-35 nm, 35-71 nm and 60-100 nm for 24 h, 48 h and 72 h, respectively. The coated soot was sintered at 600 °C, 800 °C, 1000 °C or 1150 °C for 3 h. Thereby,

the carbon was completely combusted and the sintered samples are therefore referred to as soot-templated silica. Hydrophobization of coated soot and soot-templated silica with a fluorosilane led to superamphiphobic surfaces, i.e. they repelled water and oil. In the following, we investigated the influence of the sintering temperature and the time of CVD on the wetting and mechanical properties of these surfaces.

### 3.3.1 **Wetting properties**

Fluorinated coated soot and soot-templated silica surfaces (600-1000 °C) were superhydrophobic. Water drops (6 µl) rolled off at inclination angles α of 2±1°, the receding contact angles were >140°.

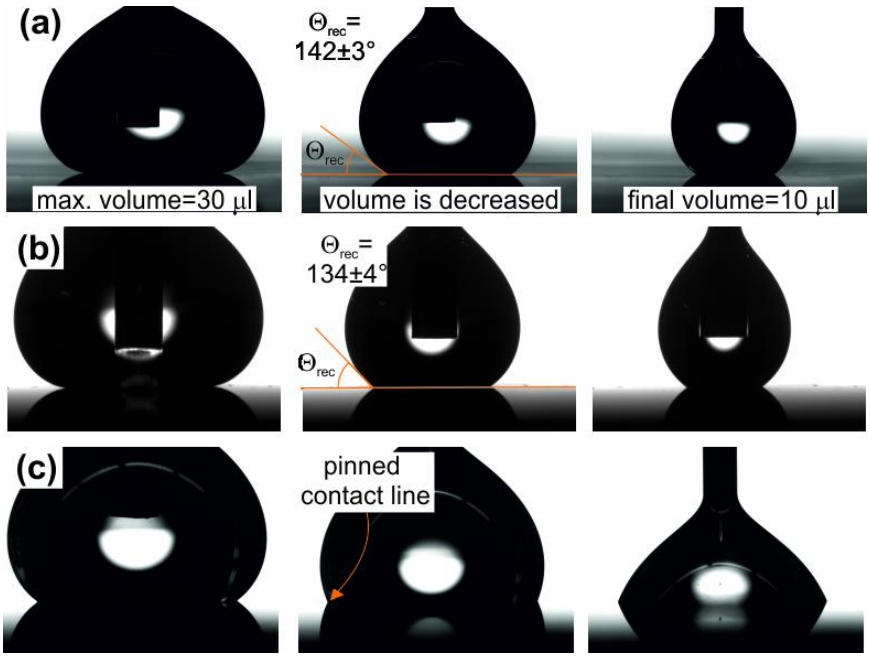


Figure S1: Snapshots of hexadecane receding on fluorinated soot-templated silica surfaces. The surfaces were exposed to a, c) 24 h and b) 72 h CVD, sintered at a, b) 600 °C or c) 1150 °C and fluorinated.

On samples sintered at 1150 °C the receding contact angles of water were also above 140° and water drops rolled off at 10±3°, 5±2° and 8±2° for CVD periods of 24 h, 48 h and 72 h, respectively. Oil repellency was tested with hexadecane (Figure 1b, Figure S1). Samples sintered at 600-1000 °C were superamphiphobic. Drops of hexadecane rolled off at tilt angles less than 10° and showed receding contact angles larger than 135° for 24 h and 48 h CVD

(Figure 1c,d). In contrast, hexadecane did not roll off on samples sintered at 1150 °C (α>90°). On coated soot, i.e. surfaces with carbon remaining inside the silica shell, the surfaces showed higher roll-off and lower receding contact angles. Potentially, hexadecane diffused through the porous silica layer and interacted with carbon. It is also possible that non-fluorinated carbon interfaces were revealed by breaking of loosely bound agglomerates due to capillary forces of deposited drops. Both can lead to an increased overall adhesion of hexadecane drops to the surface in the case of coated soot. With respect to CVD time, samples exposed longer to CVD (72 h), thus having a thicker silica shell, showed higher roll-off angles and lower receding contact angles. A comparison of TEM images of silica coated soot before and after sintering reveals that the initial overhangs, given by the soot morphology, were smoothened out by the deposited silica (Figure S2).

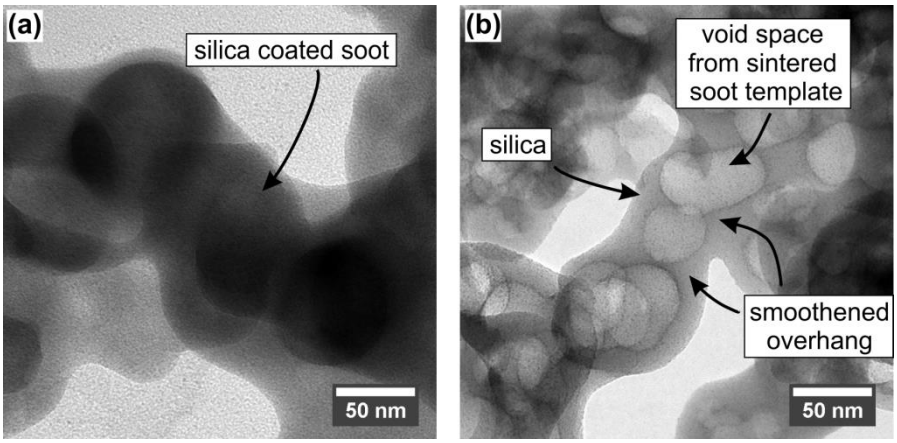


Figure S2: TEM images of candle soot coated with silica by CVD of TEOS for 72 h CVD. a) before b) after sintering at 600 °C. Arrows in b) indicate void space from sintering of the soot-template and highlight overhangs of the original template, which were smoothened by the deposited silica.

### 3.3.2 **Finger and pencil scratching**

Superhydrophobic soot-templated silica sintered at 1150 °C showed a strongly increased stability against finger scratching. Such surfaces withstood several finger scratches in contrast to superamphiphobic samples sintered below 1150 °C (Movie S1). A similar response was observed from the pencil scratch test (**Figure 2**). Samples were scratched with pencils ranging from 6H (hard) to 6B (soft) at an angle of 45° (Figure 2a).

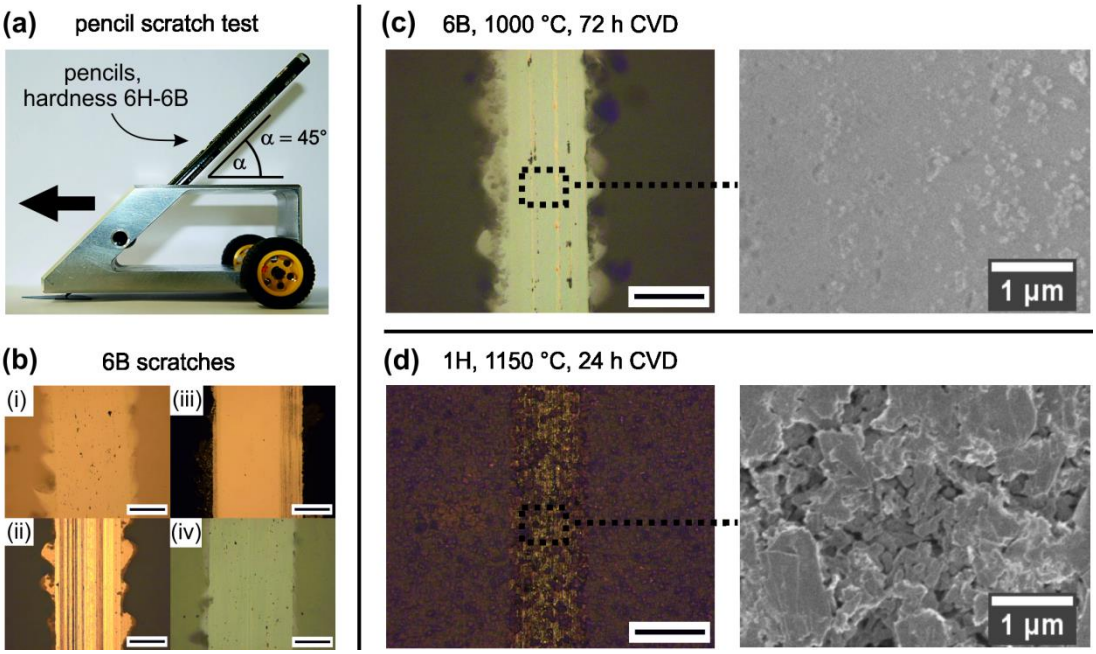


**Figure 2**: Pencil scratch test: a) pencils with a hardness ranging from 6H to 6B were pushed over soot-templated silica surfaces at an angle of 45°. b) Optical images of scratches performed by a 6B pencil. (i) 24 h, (ii) 72 h CVD of TEOS. Both samples were sintered at 600 °C. (iii) uncombusted, (iv) sintered at 1000 °C. Both samples were exposed to 24 h CVD of TEOS. c,d) optical (left) and SEM (right) images of scratches. c) 6B pencil scratch on a sample exposed to 72 h CVD, sintered at 1000 °C. d) 1H pencil scratch on a sample exposed to 24 h CVD, sintered at 1150 °C. The scale bar of the optical images is 200 µm.

The scratches were investigated by optical microscopy and SEM. Samples sintered below 1150 °C all had a gouge hardness of less than 6B, i.e. the surface was completely removed by all pencils. Figure 2b, i-iv and Figure 2c show exemplary scratches of a 6B pencil on various samples exposed to different CVD times, all sintered below 1150 °C. In contrast, samples sintered at 1150 °C had a higher tolerance to pencil scratching. The scratch hardness was found to be in the order of 1H-3H for a sample exposed for 24 h to CVD, sintered at 1150 °C (Figure 2d). SEM images of 1H scratches showed abraded lead (Figure 2d). In between the abraded lead pieces the network of the soot-templated silica could be identified and no failure of the coating was found. In contrast, 4H scratches on the same sample partially gouged the surface (Figure S3a and b, white box).

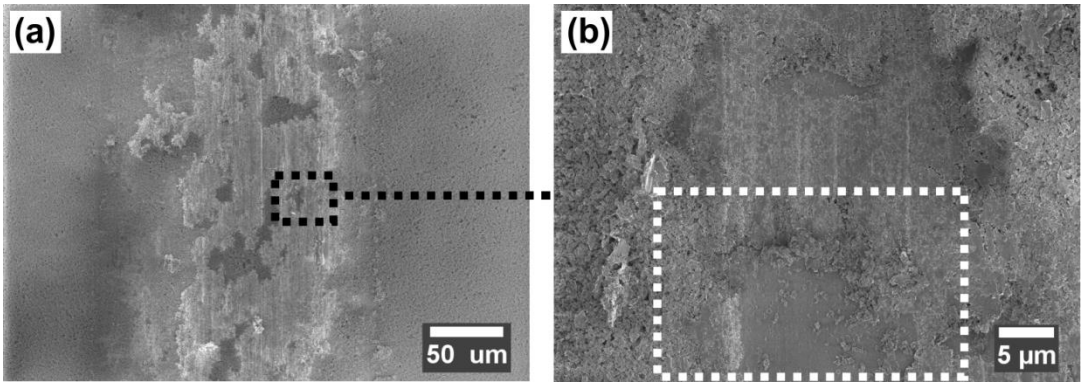


Figure S3: SEM images of samples scratched with a 4 H pencil. The sample was exposed to 24 h CVD of TEOS and sintered at 1150 °C. a) low magnification b) high magnification of scratched area. The white dashed box in b) highlights an area where the coating was partially removed by scratching.

2H and 3H scratches were in the intermediate range. This made the precise determination of the scratch hardness nontrivial. Either way, we observed a clear difference in scratch tolerance for samples sintered at and below 1150 °C.

### 3.3.3 **Morphology**

The mechanical response of a surface depends on its morphology.

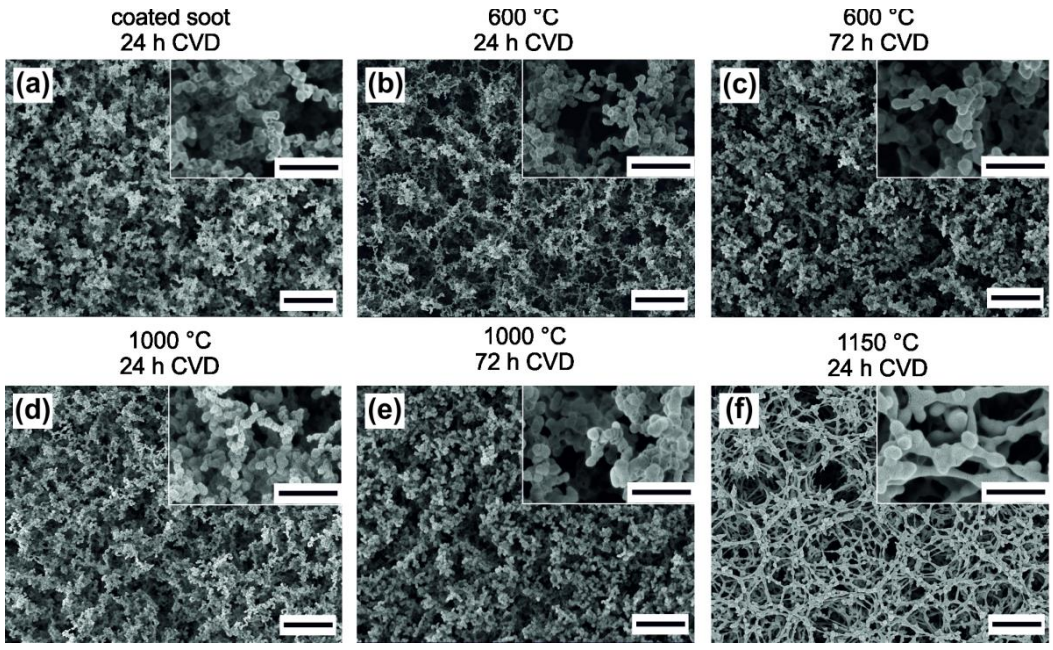


**Figure 3**: SEM images of soot-templated surfaces exposed to different periods of CVD and sintering temperatures. a) coated soot exposed to 24 h CVD. b-f) soot-templated silica sintered at b,c) 600 °C, d,e) 1000°C f) 1150 °C, respectively. b,d and f) were exposed to 24 h CVD, c,e) to 72 h CVD. The scale bars are 2 µm and 500 nm (inset).

In top view, coated soot and soot-templated silica sintered up to 1000 °C had a similar surface morphology. The size of agglomerates was in the order of 100-900 nm (**Figure 3**a-e, Figure S4 and S6).

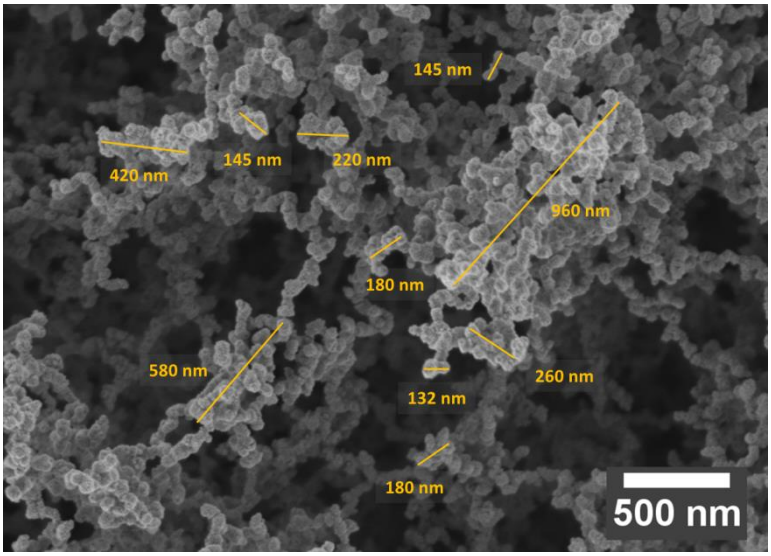


Figure S4: Exemplary determination of agglomerate size by SEM. The size of the agglomerates ranged from about 100-900 nm. The sample was exposed to CVD of TEOS for 24 h sintered at 600 °C.

The average distance between the agglomerates was around 1±0.5 µm (Figure S5).

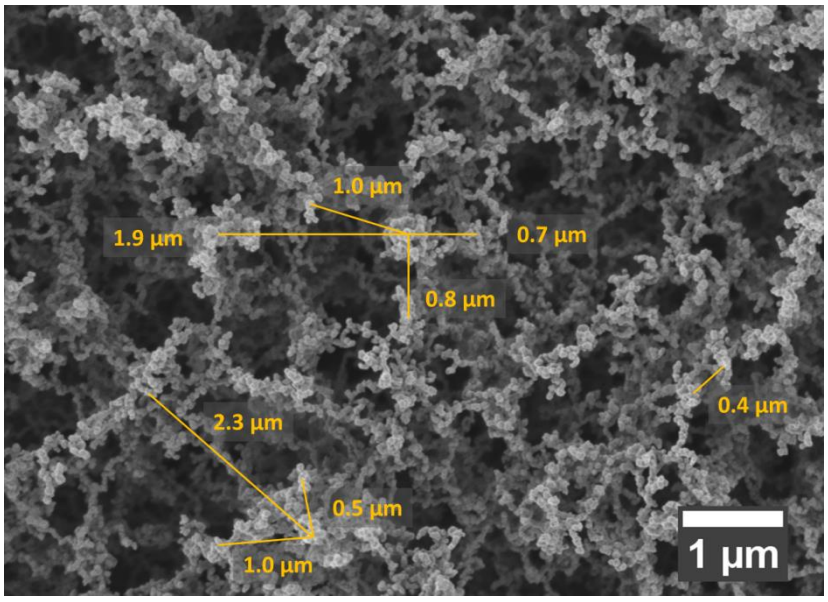


Figure S5: Exemplary determination of the average distance between agglomerate by SEM. The average distance of the agglomerates was about 1±0.5 µm. The sample was exposed to CVD of TEOS for 24 h sintered at 600 °C.

In contrast, samples sintered at 1150 °C showed a web-like morphology and the initial particle-like strings transitioned into cylinder-like strings (Figure 3f, Figure S6b and c). Though 1150 °C is well below the melting point of amorphous bulk $SiO_2$ (1713 °C), the strong temperature dependence of the viscosity of silica leads to significant viscous sintering at such temperatures.[43, 44] The viscous flow is driven by the surface tension, leading to a growth of the sinter necks by filling the menisci.[45] Hence, sintering at 1150 °C reduced the overhangs of the network by transforming particle-like strings into cylinder-like strings. The resulting surface roughness was sufficient to efficiently repel water but not hexadecane. Consequently, samples sintered at 1150 °C were superhydrophobic but not superamphiphobic.

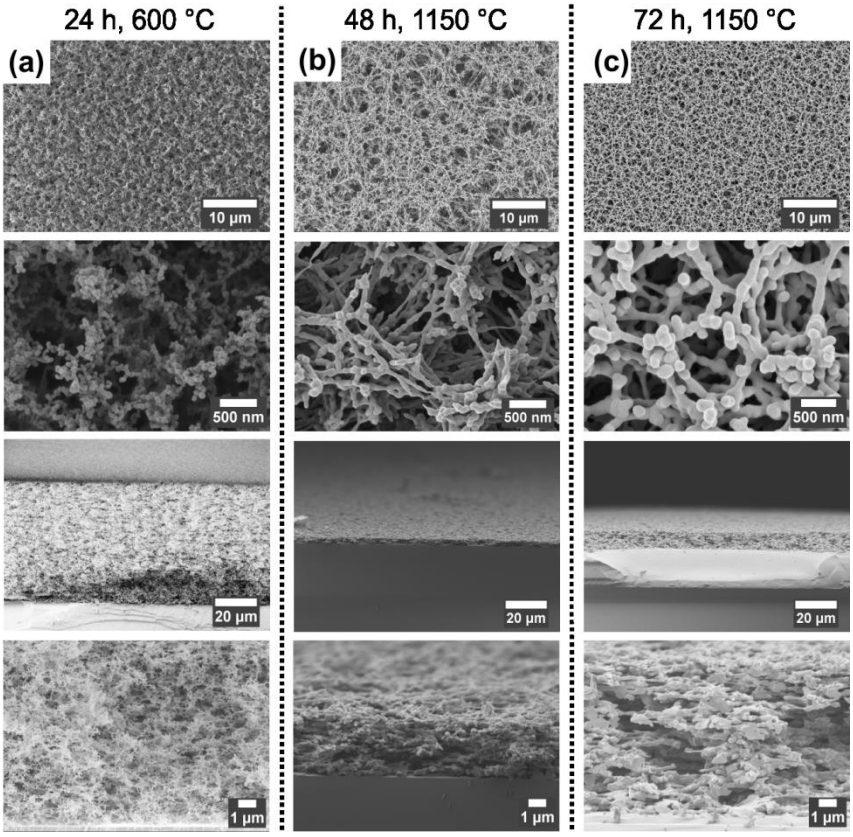


Figure S6: Top view and cross-sectional views of surfaces at different magnifications. a,b) were exposed to 24 h CVD, c) to 72 h CVD. The samples were sintered at a) 600 °C and b,c) 1150 °C, respectively. All layers had the same initial template thickness before sintering. The soot template was collected for 1 min 30 on 1.5 x 1.5 $cm^2$ silicon wafers.

Furthermore, cross-sections of samples with identical initial surface layer thickness showed that sintering at 1150 °C resulted in a pronounced compaction of surfaces layers. Surfaces treated at 600 °C, 24 h CVD, had a thickness of

62±5 µm whereas the layer thickness shrank for samples treated at 1150 °C and were found to be 4±1 µm (24 h CVD) and 9±1 µm (72 h CVD), respectively (Figure S6). The strong shrinkage reduced the network's porosity and led to increased stability.

### 3.3.4 **Nanoscale mechanical test using the atomic force microscope**

To test mechanical properties at the nanoscale we performed force measurements using an AFM. The tip radius was about 10 nm. Thus, it was much smaller than the characteristic size and distance of silica agglomerates. As an example, **Figure 4**a shows a typical force curve measured on a soot-templated silica layer after 24 h CVD and sintering at 600 °C. Force jumps of up to 10 nN were observed in the approach and about 2-5 nN in the retract curves (Figure 4a, Figure S7). The force jumps in the approach part are connected to the yield force required for the local and stepwise compression and breaking of single sintering necks. The broken and dislocated pieces stay either in contact with the protrusion or the tip, attracted by surfaces forces.[46, 47] On the scale of 100 nm these surface forces dominate over gravitational forces. These surface forces are in particular van der Waals forces. In addition, capillary forces can arise between the hydrophilic soot-templated silica and the tip. Water can condense in the gap between tip and agglomerates or strings and form a meniscus.

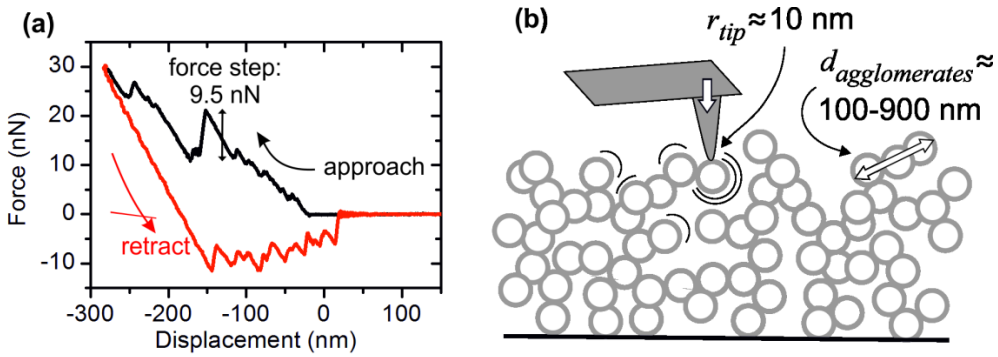


**Figure 4**: a) Force-displacement curve of a soot-templated silica surface (24 h CVD, sintered at 600 °C) indented by a sharp tip. b) Schematics illustrating the indentation process. The probe radius is about 10 nm and thus much smaller than the typical size of the agglomerates (=100-900 nm).

These surface forces cause the strong adhesion observed when retracting the tip. Jumps in the retract part are attributed to rearrangements and breaking of agglomerates and strings. These agglomerates and strings can act like a glue,

connecting the tip with the still intact parts of the superamphiphobic layer.[48] The maximum adhesion force corresponds to the main detachment event of the tip from the network. We estimate the van der Waals force of the final jump by $F = Ar_{tip}/6D^2$.

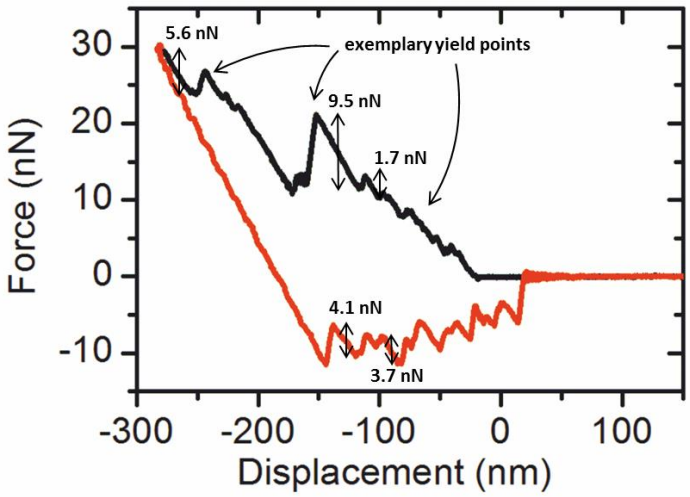


Figure S7: Exemplary force steps and yield points of a soot-templated silica surface indented by AFM. The sample was exposed to CVD of TEOS for 24 h sintered at 600 °C.

Here, *A* is the Hamaker constant (≈6×10$^{-20}$ J), $r_{tip}$ is the radius of curvature of the tip and *D* is the distance at contact (≈0.16 nm).[49] With $r_{tip}$ =10 nm we estimate a van der Waals adhesion of 4 nN. This agrees with the force measured. The height of the jumps in the approach and retract part of the force-displacement curves differed from position to position because the force was punctually applied and dissipated into the network as schematically shown **in Figure 4b.** As a conclusion, probes much smaller than the characteristic spacing between agglomerates provide information on the mechanical strength of individual agglomerates, strings and sinter necks.

### 3.3.5 **Microscale mechanical tests using colloidal probe**

For most industrial or outdoor applications of super liquid-repellent surfaces the mechanical properties on the micro and macro scale are more important, e.g. to withstand impacting rain droplets or dust particles. Therefore, we increased the indentation area by replacing the sharp AFM tip with a microsphere (“colloidal probe”) having a radius of 24 µm. The colloidal probe was approached onto the

surface until a load of 300 nN was reached to establish a defined contact with the surface, followed by a further constant approach of 200 nm. Then the probe was retracted again. This protocol allowed the investigation of superamphiphobic samples, i.e. coated soot and samples sintered up to 1000 °C.

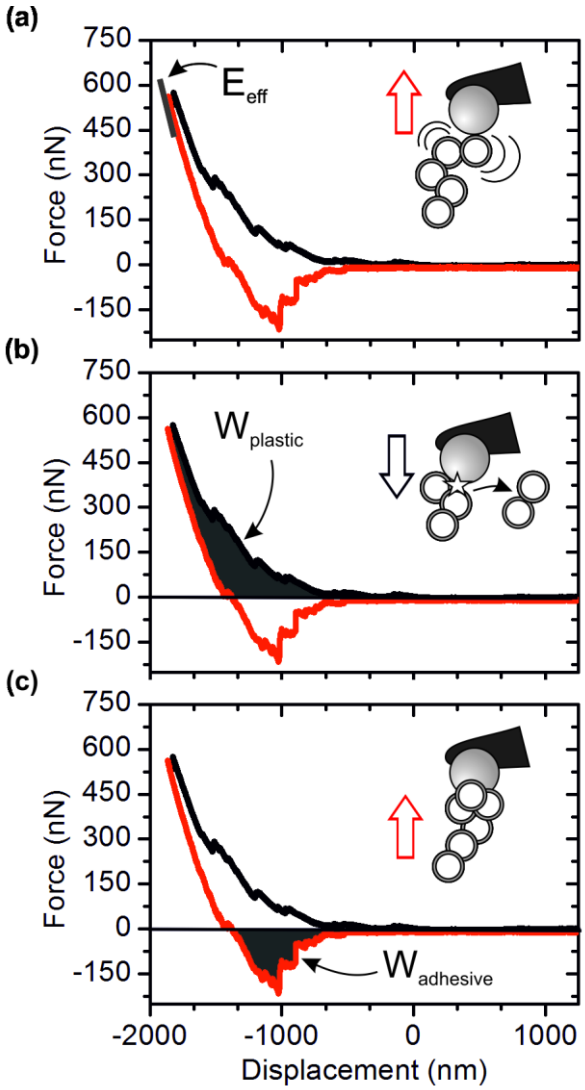


**Figure 5**: Mechanical properties extracted from typical force-displacement curves: a) effective elastic modulus $E_{eff}$, b) work of plastic deformation $W_{plastic}$ and c) effective work of adhesion, $W_{adhesive}$.

The hardness of superhydrophobic samples sintered at 1150 °C exceeded the force measurement range of the colloidal probe technique and the surfaces were therefore investigated by nanoindentation. In both cases, the indentation depth was kept below 10% of the total layer thickness to avoid substrate effects. For superamphiphobic samples, the thickness of soot-templated surfaces was chosen to be larger than 20 µm. At a typical indent of 2 µm and a probe radius of

24 µm the contact radius, calculated by the Pythagorean theorem, is 9.6 µm and thus the contact area is in the order of 290 $\mu m^2$. Consequently, the force was distributed over multiple agglomerates and strings and force-displacement curves obtained by colloidal probe indents looked smoother than force-displacement curves recorded using sharp tips (**Figure 5** and **6**). For a quantitative characterization of the mechanical properties, we defined and analyzed four parameters (Figure 5 and 6a). (1) The effective elastic modulus $E_{eff}$ is obtained from the elastic recovery upon unloading, i.e. from the slope of the onset of the retract curve. It is characteristic for the ability of the surface layer to store elastic energy upon compression. (2) The maximum indentation force $F_{max}$, that had to be applied to reach a fixed indentation depth, is related to the material hardness, i.e. its ability to withstand plastic deformation. (3) The plastic work $W_{plastic}$ and the effective adhesive work $W_{adhesive}$ are given by the integrals of the force with the x-axis on approach and retract, respectively (highlighted areas in Figure 5b and c). $W_{plastic}$ reflects the work required for plastic deformation of the sample upon approach. Work is required e.g. to break contacts between silica structures and to compress agglomerates. When retracting, work is required to break the contacts ($W_{adhesive}$), due to van der Waals interactions between the tip and the silica agglomerates that undergo rearrangement and detachment. Some agglomerates even remained attached to the probe (Figure S8).

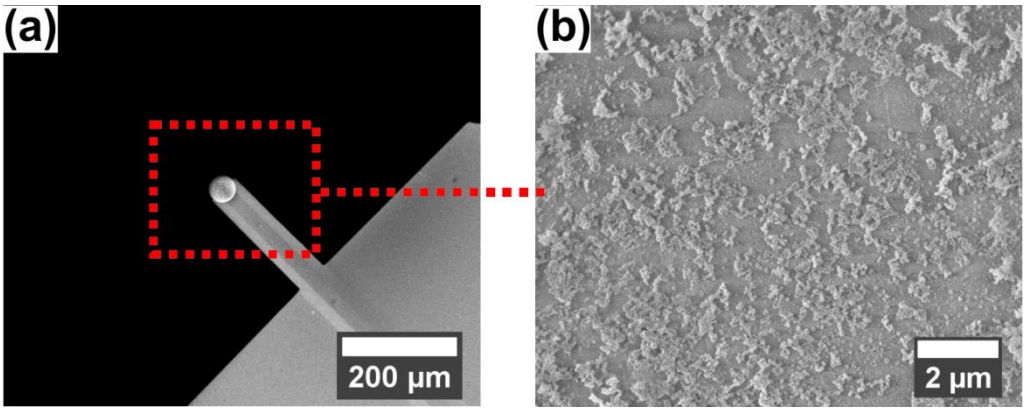


Figure S8: a) SEM images of the colloidal probe (r=24µm). b) Magnification of colloid surface. Silica agglomerates can be found on the surface after indentation of samples.

As an example, indents obtained from three different samples are compared in Figure 6. The mechanically weakest sample (Figure 6a, 24 h CVD, 600°C) was indented by almost 2 µm even at a relatively low end load of $F_{max}$=350 nN. It also

showed the lowest overall slope in the contact part. The most stable sample (Figure 6c, 24 h CVD, 1000°C) was only indented for 900 nm although the maximum force of 700 nN was much higher. Accordingly, the slope of the force curve was much steeper.

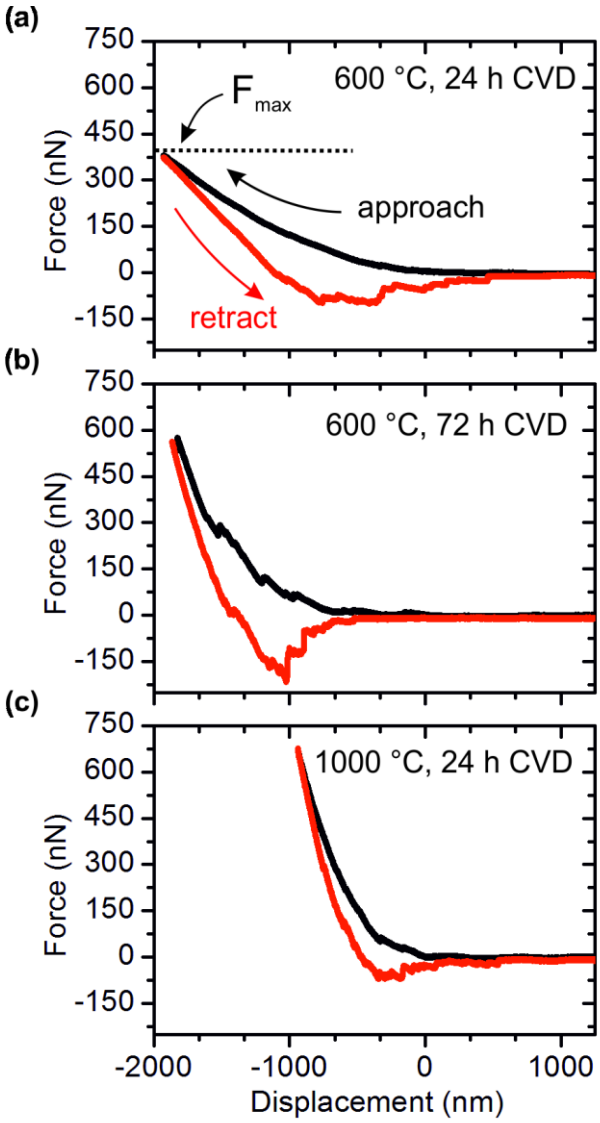


**Figure 6**: Force-displacement curves of soot-templated surfaces indented by colloidal probe (load of 300 nN followed by constant displacement of 200 nm). a-c): Representative force curves of surfaces exposed to different periods of CVD and sintering temperatures: a) and c) were exposed for 24 h, b) for 72 h to CVD of TEOS. a) and b) were sintered at 600 °C, c) was sintered at 1000 °C, respectively.

Samples treated for 72 h CVD and sintered at 600 °C showed an intermediate behavior (Figure 6b). The approach curves were smooth for 24 h CVD and sintering at 600 °C. They became less smooth exhibiting pronounced force jumps

with increasing silica thickness and sintering temperature, indicating an increase in mechanical strength. The averaged quantitative mechanical properties are shown in **Figure 7**. $E_{eff}$ and $F_{max}$ increased with the thickness of the silica shell and sintering temperature. $E_{eff}$ increased by more than an order of magnitude from 25 kPa up to 985 kPa when samples were exposed to 72 h CVD and 1000 °C sintering compared to 24 h CVD and 600 °C sintering (Figure 7a). All samples treated for 48 h or 72 h CVD had higher $E_{eff}$ than their counterparts treated for 24 h CVD. Within our experimental accuracy, $E_{eff}$ was identical for samples treated for 48 h and 72 h CVD, except when sintered at 600 °C. Coated soot showed a higher $E_{eff}$ than samples sintered at 600 °C. This is attributed to the additional elasticity provided by the encapsulated carbon template that was burned away at 600 °C.

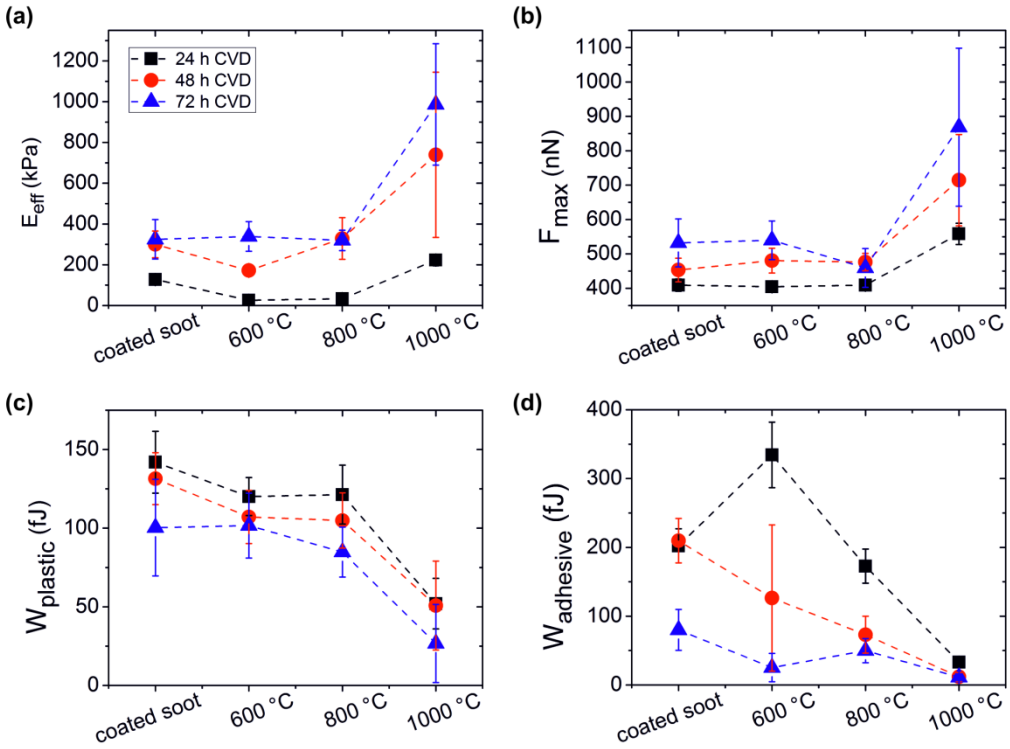


**Figure 7**: Mechanical properties of soot-templated surfaces. The black, red and blue data points represent surfaces exposed to 24 h, 48 h and 72 h of CVD, respectively. Coated soot and soot-templated silica surfaces sintered at 600 °C, 800 °C, 1000 °C were investigated, respectively. a) Effective elastic modulus $E_{eff}$, b) maximum force $F_{max}$, c) plastic work $W_{plastic}$ and d) effective adhesive work $W_{adhesive}$. The errors are the standard deviations of the respective values obtained from different force curves at different positions on multiple samples.

After 72 h CVD the silica shells were thick enough to dominate the mechanical strength and the presence or absence of the carbon template did no longer affect the mechanical properties. Correspondingly, $E_{eff}$ of coated soot and samples sintered at 600 °C or 800 °C did not differ significantly, whereas at 1000 °C $E_{eff}$ increased by a factor of more than two.

$F_{max}$ increased by a factor of more than two from 400 nN up to 900 nN for samples exposed to 72 h CVD, 1000 °C compared to 24 h CVD, 600 °C (Figure 7b). Similarly to $E_{eff}$, samples treated for 48 h and 72 h CVD showed higher Fmax than their counterparts treated for 24 h CVD. The strongest increase of $F_{max}$ was found when samples were sintered at 1000 °C. $W_{plastic}$ and $W_{adhesive}$ were in the order of hundreds of femto Joules (Figure 7c and d). $W_{plastic}$ and $W_{adhesive}$ both decreased with increasing thickness of the silica shell and sintering temperature. $W_{plastic}$ decreased by a factor greater than 4, $W_{adhesive}$ by a factor of about 30 (24 h CVD, 600 °C compared to 72 h CVD, 1000 °C). Samples sintered at 1000 °C showed a higher hardness and resisted better to the indentation. With increasing hardness, the structural differences in the network at every indentation point became more and more relevant. Consequently, the results from individual force-displacement curves showed a broader span of mechanical strength, leading to increased error bars of $E_{eff}$ and $F_{max}$ at 1000 °C.

For a given application, samples can hence be tuned for optimum repellency (hexadecane) or mechanical stability. Optimum mechanical stability at the price of slightly reduced repellency against hexadecane is achieved by exposure of samples to 72 h CVD and sinter at 1000 °C ($\Theta_{rec}$=134±4° for 72 h compared to $\Theta_{rec}$=142±3° for 48 h CVD). Optimum repellency in combination with a significant increase of $E_{eff}$ could be obtained by exposure of samples to 48 h CVD and sintering at 1000 °C. In this case, $E_{eff}$ increased by a factor of 30 from 25 kPa to 750 kPa compared to surfaces prepared by the standard procedure, i.e. 24 h CVD and sintered at 600 °C. The observed increase of stability for sintering temperatures of 1000 °C is attributed to a condensation of OH groups from the silica network combined with the initial stage of sintering, where the diameter of the sinter necks starts to increase while the overall morphology of the silica agglomerate network is only slightly changed. Therefore, the network starts to condense[50] but the overall morphology is largely preserved (Figure 3d,e). The

hardness of samples sintered at 1150 °C exceeded the force measurement range of the colloidal probe and were investigated by nanoindentation.

### 3.3.6 **Microscale mechanical tests using nanoindentation**

Nanoindentation and AFM are complementary and cover different ranges of normal forces and $E_{eff}$. from 10 MPa to more than 100 GPa. Therefore, nanoindentation was not suitable for samples sintered ≤1000 °C but it was appropriate for superhydrophobic samples sintered at 1150 °C. **Figure 8**a shows a typical force-displacement curve of a surface exposed to 72 h CVD.

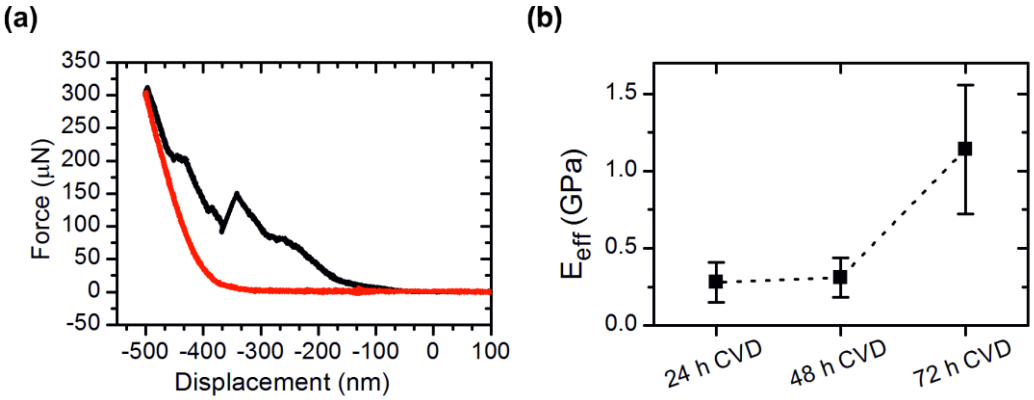


**Figure 8**: Nanoindentation of soot-templated silica surfaces sintered at 1150 °C measured with a conical diamond tip. a) Typical force-displacement curve of a surface exposed to 72 h CVD indented for 500 nm. Black curve: approach, red curve: retraction b) $E_{eff}$ of surfaces exposed to 24 h, 48 h and 72 h CVD.

Distinct force jumps in the order of several µN can be identified in the approach part, indicating a stepwise collapse of the layer. $E_{eff}$ as a function of CVD exposure time for samples sintered at 1150 °C is shown in Figure 8b. $E_{eff}$ increased by a factor of more than 3 from approximately 300 MPa to more than 1 GPa. Compared to superamphiphobic samples, $E_{eff}$ even increased by about three orders of magnitude (1 GPa for 72 h CVD, 1150 °C compared to 750 kPa for 48 h CVD, 1000 °C). Sintering at 1150 °C and the associated change in surface morphology thus led to strongly reinforced superhydrophobic samples.

## 3.4 Conclusion

For a comprehensive characterization of the mechanical strength of super liquid-repellent surfaces, different methods need to be used, because different length and force scales need to be addressed. Finger and pencil scratching of the surface can provide a first impression of its mechanical strength. Atomic force microscopy reveals the mechanical response of single agglomerates and strings, e.g. individual force steps and the yield force. Colloidal probe can be applied to obtain the averaged mechanical strength if the colloid is much larger than the distance between neighboring agglomerates. We measured three parameters, which describe the mechanical response of super liquid-repellent surfaces: The effective elastic modulus $E_{eff}$, for the elastic response, the plastic work of indentation $W_{plastic}$ for the plastic deformation and the effective adhesive work $W_{adhesive}$. The colloidal probe technique is suitable for layers with an effective elastic modulus up to roughly 1 MPa. For harder surfaces, nanoindentation is more appropriate.

For a particular liquid-repellent surface, i.e. soot-templated superamphiphobic surfaces we balanced mechanical strength against wetting properties. The mechanical strength was tuned by varying the reaction parameters, i.e. duration of CVD and sintering temperature. Superamphiphobic surfaces with a 30 fold increased $E_{eff}$ were obtained compared to standard samples (750 kPa for 48 h CVD, 1000 °C compared to 25 kPa for 24 h CVD, 600 °C). A further increase of the sintering temperature to 1150 °C led to superhydrophobic surfaces which were tolerant to finger and pencil scratching (1H, $E_{eff}$ of about 1 GPa). To conclude, 48 h CVD and 1000 °C sintering led to superamphiphobic samples with greatly improved mechanical properties.

## 3.5 Experimental section

Tetraethylorthosilicate (TEOS, 98%), trichloro(1H,1H,2H,2H-perfluorooctyl)silane (PFOTS, 97%) and n-hexadecane (99%) were purchased from Sigma-Aldrich, Germany, toluene and acetone from Fischer Scientific, UK, ammonium hydroxide aqueous solution Normapur (28%) and absolute ethanol from VWR Chemicals,

France. Water was purified by a Sartorius Arium 611. Paraffin candles were obtained from the local supermarket. Silicon wafers were purchased from Si-Mat, Germany. All reagents were used as received.

Superamphiphobic surfaces were prepared according to Deng et al.[31] Si-wafers were super sonicated in toluene, acetone and ethanol for at least 5 min each and activated by oxygen plasma for 5 min at 300 W (Femto BL, Diener, Germany, chamber reactor, f=2.45 GHz, P=300 W, $O_2$-flow=7 scc/min). Wafers were coated with TEOS deposited from the gas phase to promote adhesion of the superamphiphobic surface. Therefore the wafers were placed in a desiccator together with 2 vials containing 3 ml of TEOS and 3 ml aqueous ammonia solution each. After 24 h the precoated wafers were covered with soot collected from a paraffin candle about 1 cm above the wick for 40 s (wick height 0.7 cm, total flame height about 4.5 cm).[51] The carbon template was coated with silica by exposure to TEOS as stated above for different time periods of CVD, namely 24 h, 48 h and 72 h. TEOS and aqueous ammonia solution were renewed every 24 h. The total thickness of the silica shell deposited on a smooth surface was determined by ellispometry (Nanofilm surface analysis EP3, 532 nm, 50 mW) and was found to be 35±1 nm, 71±2 nm and 100±2 nm for 24 h, 48 h and 72 h CVD, respectively. On the rough soot-templated silica surfaces the average silica shell thickness was 20±5 nm, 35±5 nm and 60±5 nm for 24 h, 48 h and 72 h CVD, respectively (determined by TEM).[31] The soot template remained part of the sample (coated soot) or samples were sintered at 600, 800, 1000 or 1150 °C (soot-templated silica) for 3 h in air, respectively, exclusive heat up time at maximum heat up speed (15 °C/min). For mechanical tests, the samples were not hydrophobized, i.e. they remained hydrophilic. The samples were hydrophobized to measure contact angles. Therefore, samples were placed in a desiccator, next to a 20 ml vial containing 100 µl PFOTS for 3 h at 25 mbar

Top view scanning electron microscopy (SEM) images were acquired at a voltage of 1 kV and cross-sectional images at 0.7 kV (InLens detector, LEO 1530 Gemini). To enhance the image quality samples were sputtered with 6 nm Pt (BalTec MED 020 Modular High Vacuum Coating System, Argon at $2\times10^{-2}$ mbar and 60 mA). A Tecnai F20 DEI, 200 kV, brightfield was used for TEM measurements.

Receding contact angles and roll-off angles were measured using a goniometer (Dataphysics OCA 35, Data Physics Instrument GmbH, Germany). To measure the receding contact angle, an initial drop of 10 µl hexadecane was deposited on a surface and inflated/deflated by adding/removing 20 µl hexadecane, respectively. Receding contact angles were determined by manual ellipse fitting. To determine the roll-off angles drops of 6 µl water and hexadecane were deposited on the surfaces, respectively. The stage was tilted at a speed of 1.37 °/s. For both, receding contact angle and tilting angle measurements 3-4 different spots per sample and 2-5 samples were investigated for every combination of CVD and sintering temperature.

Pencil scratch tests were performed using a homebuilt pencil holder (Figure 2). 6H to 6B pencils (Faber-Castell, Germany) were sharpened with a standard pencil sharpener, mounted on the holder at an angle of 45° and fixed by a screw. Proper mounting was checked by a water level. The samples were fixed to the table by double sided tape and scratches for more than 1 cm length were obtained by manually pushing the holder forward. The weight of the entire holder was 225 g. The load acting on the tip was 100 g. All scratches were investigated by optical microscopy and samples of interest were further analyzed by SEM.

All AFM and colloidal probe experiments were conducted on a JPK Nanowizard 3. Nanoscale mechanical testing was performed with cantilevers having a nominal resonance frequency of f=70 kHz and a spring constant of k=2 N/m (OMCL-AC240TS rectangular cross-section, n-type doped silicon, Japan). The experimental spring constants were determined by the thermal tune method.[52] Force scans of 64×64 pixels on an area of 10×10 µm$^2$ were recorded. A set point of 30 nN was chosen.

Colloidal probes were prepared by gluing hollow glass microspheres (Cospheric, USA) to tipless cantilever (AppNano ACL-TL, USA (f=190 kHz)). The hollow glass microspheres had a diameter of 47 µm (measured by SEM), a mean density of about 0.22 g/cc and a crush strength of ≈2 MPa (according to supplier). The colloidal probes were hydrophobized for 30 min under the same conditions as stated above. The spring constants were measured by the thermal noise method and ranged from 44-71 N/m. Force maps of 3×3 pixels over an area of

150×150 $\mu m^2$ were measured. Approach and retraction speeds were 1 µm/s with an extension delay of 0.5 s. The first force-displacement curve of each force map was discarded due to the initial surface approach. Four measurement series with different colloidal probes were conducted. Each series started with indentation of the mechanically strongest surfaces (72 h CVD, 1000 °C) to the weakest surfaces (24 h CVD, 600 °C). A total of 5-9 force maps were recorded on at least 3 different samples leading to 40-72 force curves for each combination of CVD time and sintering temperature. Reference force curves on a silicon wafers were measured for each series of experiments. All force-displacement curves were analyzed using a self-written LabVIEW software. First, the reference force curves were used to determine the deflection sensitivity. Consecutively, this deflection sensitivity was used to convert deflection signals in volts to cantilever deflections in nanometers, which in turn were converted to force by multiplying with the spring constant. The Cantilever deflection was subtracted from the piezo position signal to obtain the displacement. Zero displacement was defined as the onset of repulsive force during approach. The effective elastic modulus $E_{eff}$ was determined by fitting the first 10% of the retract curve using the Hertz model after setting the minimum of the retract curve as zero indentation. In addition, we allowed for a force offset as an additional fitting parameter. This force offset turned out to be similar but always somewhat larger (up to 50%) than the measured adhesion force. Therefore, our fits effectively correspond to a DMT contact model[53] (having a Hertz contact pressure distribution but including adhesion). Fitting a mixed elastic/plastic indentation with an elastic contact model to obtain the elastic modulus can, of course, be questioned. However, the initial part of the retract curve should reflect the elastic recovery of the material during unloading, whereas the approach curve and the later part of the retract curve will contain mixed contributions of elastic and plastic deformation. The fact that the adhesion obtained as a fit parameter was not too different from the measured adhesion is an indication that the retracting part of the curves is in fact to a relatively large extent elastic and justifies our approach of using an elastic fit of the unloading curve. As additional quantities, the work of plastic deformation $W_{plastic}$, effective work of adhesion $W_{adhesive}$ and the maximum Force $F_{max}$ at maximum approach were analyzed as shown in Figure 5 and 6a. It should be

noted that the effective work of adhesion calculated here is not a defined thermodynamic quantity like the Dupré work of adhesion because the relaxation processes occurring during retraction are irreversible. However, as long as cantilevers with the same spring constant are used, this quantity can give relative information on the adhesiveness of the sample.

Nanoindentation measurements were performed with a standard-force MFP NanoIndenter (Asylum Research, Santa Barbara, CA, spring constant k=2390 N/m) equipped with a conical diamond tip (r=25 µm, opening angle=60°). Samples sintered at 1150 °C were indented in a displacement-controlled mode with maximum displacements of 50, 100, 200, 300 and 500 nm at a penetration rate in the range of 10-100 nm/s. Thermal drift was measured and corrected for each indentation. The thicknesses of the indented surfaces were verified by cross-sectional SEM images. The thicknesses ranged from 4, 6.5 and 8 µm for samples exposed to 24 h, 48 h and 72 h CVD, sintered at 1150 °C. For 24 h CVD, we found a substrate effect for indentation depth >100 nm. In this case, $E_{eff}$ was only averaged over 50 and 100 nm indentation depth. $E_{eff}$ was analyzed in analogy to colloidal probe indentation experiments and spherical contact geometry was assumed.

## 3.6 Acknowledgments

M.P. synthesized the candle-soot templated surfaces and characterized the samples by contact angle measurement and SEM. He performed the finger and pencil scratch test, as well as the indentation experiments using AFM and colloidal probe. R.F. carried out the nanoindentation measurements and analyzed the nanoindentation data. M.K. programmed the data analysis software. M.P. and M.K. analyzed the data from AFM and colloidal probe experiments. T.Y. and A. N. I. conducted ellipsometry measurements and contributed with valuable discussion. H.-J. B., D.V. and M.K. had the idea for the project and organized it. M.P., D.V., M.K. and H.-J. B. wrote the manuscript. All authors discussed the results and edited the manuscript.

The authors thank G. Glasser, G. Schäfer, K. Kirchhoff and W. Scholdei for technical support, and G. Auernhammer, S. Weber, R. Berger and J. Pham for stimulating discussions. H.-J. B. wishes to thank the ERC for the advanced grant 340391-SUPRO. Financial support from SPP 1420 (H.-J. B.), SPP1486 (D.V, R.F) is gratefully acknowledged.

## 3.7 References

[1] C. W. Extrand, Langmuir **2002**, 18, 7991.

[2] L. Gao, T. J. McCarthy, Langmuir **2007**, 23, 3762.

[3] X. J. Feng, L. Jiang, Adv. Mater. **2006**, 18, 3063.

[4] D. Quere, Annual Review of Materials Research **2008**, 38, 71.

[5] N. J. Shirtcliffe, G. McHale, S. Atherton, M. I. Newton, Advances in Colloid and Interface Science **2010**, 161, 124.

[6] Z. Chu, S. Seeger, Chemical Society Reviews, 2014, 43, 2784.

[7] W. Barthlott, C. Neinhuis, Planta **1997**, 202, 1.

[8] J. L. Wang, A. Raza, Y. Si, L. X. Cui, J. F. Ge, B. Ding, J. Y. Yu, Nanoscale **2012**, 4, 7549.

[9] M. Paven, P. Papadopoulos, S. Schöttler, X. Deng, V. Mailänder, D. Vollmer, H.-J. Butt, Nat. Commun. **2013**, 4, 2512.

[10] B. J. Privett, J. Youn, S. A. Hong, J. Lee, J. Han, J. H. Shin, M. H. Schoenfisch, Langmuir **2011**, 27, 9597.

[11] A. B. D. Cassie, S. Baxter, T Faraday Soc. **1944**, 40, 0546.

[12] J. Bico, C. Marzolin, D. Quéré, Europhys. Lett. **1999**, 47, 220.

[13] S. Herminghaus, Europhys. Lett. **2000**, 52, 165.

[14] A. Tuteja, W. Choi, M. L. Ma, J. M. Mabry, S. A. Mazzella, G. C. Rutledge, G. H. McKinley, R. E. Cohen, Science **2007**, 318, 1618.

[15] H. J. Butt, C. Semprebon, P. Papadopoulos, D. Vollmer, M. Brinkmann, M. Ciccotti, Soft Matter **2013**, 9, 418.

[16] J. A. Greenwood, J. B. P. Williamson, Proceedings of the Royal Society of London A: Mathematical, Physical and Engineering Sciences **1966**, 295, 300.

[17] T. Verho, C. Bower, P. Andrew, S. Franssila, O. Ikkala, R. H. A. Ras, Adv. Mater. **2011**, 23, 673.

[18] C.-H. Xue, J.-Z. Ma, Journal of Materials Chemistry A **2013**, 1, 4146.

[19] B. P. Dyett, A. H. Wu, R. N. Lamb, ACS Applied Materials & Interfaces **2014**, 6, 18380.

[20] Q. Xie, J. Xu, L. Feng, L. Jiang, W. Tang, X. Luo, C. C. Han, Adv. Mater. **2004**, 16, 302.

[21] X. M. Li, D. Reinhoudt, M. Crego-Calama, Chemical Society Reviews **2007**, 36, 1350.

[22] P. Roach, N. J. Shirtcliffe, M. I. Newton, Soft Matter **2008**, 4, 224.

[23] H. Wang, J. Fang, T. Cheng, J. Ding, L. Qu, L. Dai, X. Wang, T. Lin, Chemical Communications **2008**, 877.

[24] D. Xiong, G. J. Liu, L. Z. Hong, E. J. S. Duncan, Chem. Mater. 2011, 23, 4357.

[25] E. Yoshida, Colloid Polym. Sci. **2012**, 290, 525.

[26] L. Xiong, L. L. Kendrick, H. Heusser, J. C. Webb, B. J. Sparks, J. T. Goetz, W. Guo, C. M. Stafford, M. D. Blanton, S. Nazarenko, D. L. Patton, ACS Applied Materials & Interfaces **2014**, 6, 10763.

[27] N. Valipour Motlagh, R. Khani, S. Rahnama, Colloids and Surfaces A: Physicochemical and Engineering Aspects **2015**, 484, 528.

[28] A. Tricoli, M. Righettoni, S. E. Pratsinis, Langmuir **2009**, 25, 12578.

[29] M. Stepien, J. J. Saarinen, H. Teisala, M. Tuominen, M. Aromaa, J. Kuusipalo, J. M. Mäkelä, M. Toivakka, Applied Surface Science **2011**, 257, 1911.

[30] B. S. Haynes, H. G. Wagner, Progress in Energy and Combustion Science **1981**, 7, 229.

[31] X. Deng, L. Mammen, H. J. Butt, D. Vollmer, Science **2012**, 335, 67.

[32] C. Su, Y. Xu, F. Gong, F. Wang, C. Li, Soft Matter **2010**, 6, 6068.

[33] Y. Lu, S. Sathasivam, J. Song, C. R. Crick, C. J. Carmalt, I. P. Parkin, Science **2015**, 347, 1132.

[34] J. Groten, J. Rühe, Langmuir **2013**, 29, 3765.

[35] Y. C. Jung, B. Bhushan, ACS Nano **2009**, 3, 4155.

[36] I. Malavasi, I. Bernagozzi, C. Antonini, M. Marengo, Surface Innovations **2015**, 3, 49.

[37] G. Binnig, C. F. Quate, C. Gerber, Physical Review Letters **1986**, 56, 930.

[38] H.-J. Butt, B. Cappella, M. Kappl, Surface Science Reports **2005**, 59, 1.

[39] W. C. Oliver, G. M. Pharr, Journal of Materials Research **1992**, 7, 1564.

[40] W. A. Ducker, T. J. Senden, R. M. Pashley, Nature **1991**, 353, 239.

[41] M. Kappl, H.-J. Butt, Particle & Particle Systems Characterization **2002**, 19, 129.

[42] S. O. Schopf, S. Salameh, L. Madler, Nanoscale **2013**, 5, 3764.

[43] M. D. Sacks, T.-Y. Tseng, Journal of the American Ceramic Society **1984**, 67, 532.

[44] C. J. Brinker, G. W. Scherer, Sol-gel science: the physics and chemistry of sol-gel processing, Academic press, USA **1990**.

[45] J. Frenkel, Journal of Physics (Moscow) **1945**, 9, 385.

[46] H.-J. Butt, M. Kappl, in Surface and Interfacial Forces, Wiley-VCH, GER **2010**.

[47] J. N. Israelachvili, Intermolecular and surface forces: revised third edition, Academic press, USA **2011**.

[48] L. O. Heim, H. J. Butt, J. Blum, R. Schräpler, Granular Matter **2008**, 10, 89.

[49] L. Heim, H. Butt, R. Schräpler, J. Blum, Australian Journal of Chemistry **2005**, 58, 671.

[50] L. Zhang, M. D'Acunzi, M. Kappl, A. Imhof, A. v. Blaaderen, H.-J. Butt, R. Graf, D. Vollmer, Physical Chemistry Chemical Physics **2010**, 12, 15392.

[51] M. Paven, P. Papadopoulos, L. Mammen, X. Deng, H. Sachdev, D. Vollmer, H.-J. Butt, pac **2014**, 86, 87.

[52] J. L. Hutter, J. Bechhoefer, Review of Scientific Instruments 1993, 64, **1868**.

[53] Derjaguin, B. V.; Muller, V. M.; Toporov, Y. P. Effect of contact deformations on the adhesion of particles. Journal of Colloid and Interface Science **1975**, 53 (2), 314-326.

# 4 Spontaneous jumping and long-lasting bouncing of hydrogel drops from a superheated surface

*Jonathan T. Pham, Maxime Paven, Tadashi Kajiya,[±] Hans-Jürgen Butt, and Doris Vollmer*

Max Planck Institute for Polymer Research, Ackermannweg 10, 55128 Mainz, Germany.

[±]Present address: Analysis Technology Center, Fujifilm R&D, 210 Nakanuma, Minamiashigara, Kanagawa 250-0123, Japan.

*submitted* 2016

## 4.1 Abstract

The impact and rebound of liquid drops on solid surfaces is ubiquitous in nature for self-cleaning and is of practical importance in many industrial heat transfer processes, such as spray cooling. Colliding and bouncing solid spheres are also relevant for many processes, such as ball milling, and is commonly encountered in sporting events. Here, we combine features from both liquids and solids and investigate the interaction of hydrogel drops with a superheated surface. Using high speed video microscopy, we focus on two aspects of hydrogel drops: 1) spontaneous jumping induced by rapidly heating the surface and 2) impact dynamics during subsequent bouncing on the hot surface. We demonstrate that millimetric hydrogel drops can jump from a hydrophilic surface upon rapid heating and continue to bounce with increasing heights. The interplay between elastic and liquid-like properties results in intriguing dynamics, which is reflected in jumping, long-lasting bouncing, trampolining, and the shortest contact times ever observed for water-like systems.

## 4.2 Introduction

When water is splashed onto a hot pan, drops of water bead up and appear to smoothly glide along the surface (**Figure 1**a, Movie S1). This common kitchen observation arises from the so-called Leidenfrost effect, also known as film boiling, in which the drops are separated from the hot surface by a film of its own vapor.[1–5] A high temperature surface is necessary such that the water vaporizes sufficiently fast to form a stable vapor cushion below a drop. When above the boiling temperature but below the Leidenfrost temperature, drops make contact with the surface and quickly evaporate. For purposes of cooling (i.e., spray cooling), this contact is essential because it provides faster heat transfer than film boiling.[6–8] On the other hand, the Leidenfrost effect delivers adhesion-free drops, which enables long-lasting drop bouncing[2] or easy transportation of small solid objects hovering over a surface.[9] Vapor mediated bouncing is also observed on unheated superhydrophobic surfaces,[10] as well as on hydrophilic surfaces with a low impact velocity.[11,12] Recently, it was even demonstrated that water drops resting on a superhydrophobic surface spontaneously jump and start trampolining with a rapid reduction in the atmospheric pressure, driven by pressure buildup in the surface.[13] These experiments have in common that drop dynamics are governed by the surface tension, drop-size and natural frequencies of the drop. When releasing a drop onto a surface, the initial kinetic energy is converted to surface energy on impact, resulting in velocity dependent spreading. During the subsequent retraction, the surface energy is reconverted into kinetic energy and the drop rebounds from the surface.

In contrast to water drops, the impact of a soft ball on a smooth surface can be described by Hertz dynamics, under the assumption of a fully elastic collision. In this case, the kinetic energy is converted to elastic strain energy, and then reconverted into kinetic energy. However in reality, the much of the kinetic energy is lost due to friction, adhesion, or irreversible excitation of internal degrees of freedom. Thus after a couple bounces, a ball typically comes to rest. It is then surprising to find that when hydrogel beads are dropped onto a hot pan, they bounce for an intriguingly long time (Figure 1b, Movie S2).[14] A hydrogel is a soft, elastic, highly-water-filled polymer network in which the elasticity and the water content are tunable by the crosslinking density. Although hydrogels can be over

99% water,[15] they possess solid-like character and offer shape stability to prevent drop spreading. Hence, hydrogels are an ideal model system to investigate the interplay between liquid and solid aspects of jumping and bouncing dynamics.

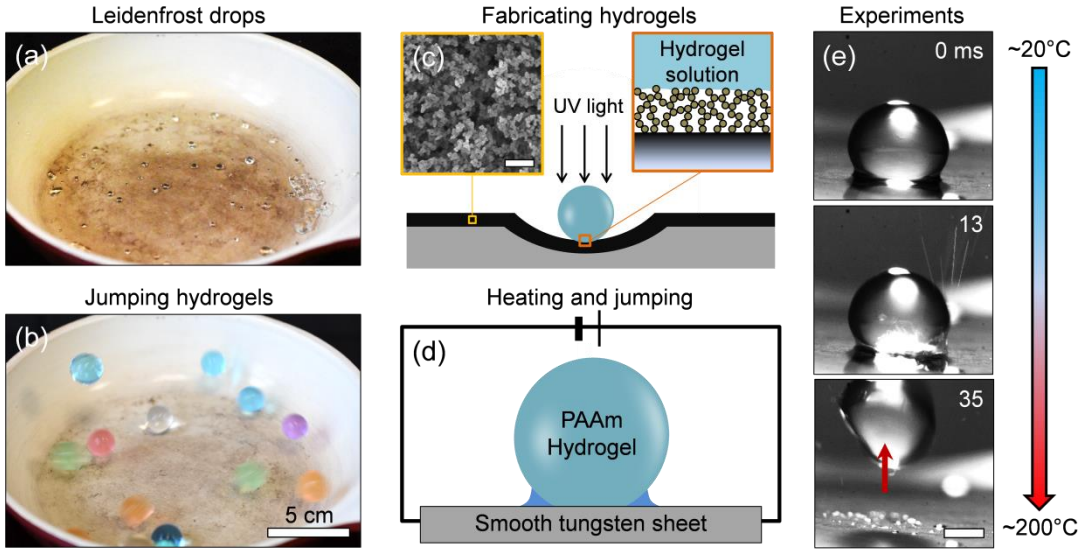


**Figure 1:** Jumping and bouncing hydrogel drops on a hot surface. a) Water drops on a hot pan gliding on the surface because of the Leidenfrost effect (see Movie S1). b) Hydrogel beads ($R$~8 mm) bouncing on the same hot pan (see Movie S2). c) Fabrication of millimetric hydrogel drops by using candle-soot surfaces. Inset scale bar: 1 µm (see Movie S3). d) Schematic of heating and jumping experimental setup where a hydrogel drop is placed on a tungsten sheet. A meniscus arises from the water. Heat is rapidly applied by an electrical current. e) Experimental observations of a hydrogel drop jumping from the surface upon heating. Bubbles are observed to burst from the side of the drop (13 ms) before a vapor explosion catapults the hydrogel upward (35 ms). The 0 ms frame is taken arbitrarily to illustrate the timescale of the event. Scale bar: 1 mm.

In this Communication, we show that the interplay between liquid and elastic character of *hydrogel drops* give rise to unique dynamics. We demonstrate that rapidly heating the underlying hydrophilic surface initiates jumping and long-lasting bouncing of a hydrogel drop, which is initially at rest. The hydrogels spontaneously jump from the surface and continue to bounce for several seconds with the lowest contact time ever observed for a water-like drop. Notably, we use a smooth substrate (RMS roughness ~15 nm, Figure S1).

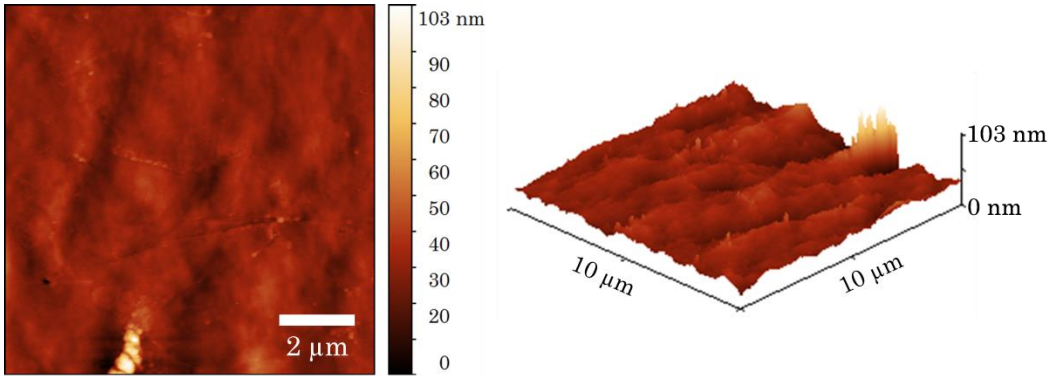


Figure S1: Examples of 2D and 3D AFM scans for measuring roughness. The RMS roughness averaged over three 100 µm$^2$ areas is measured as $15 \pm 5$ nm. The maximum roughness scale, which is taken as the maximum peak to the valley, is $195 \pm 89$ nm.

This renders the previously reported concept, based on vapor pressure buildup within the textured, superhydrophobic surface,[13,16] effectively impossible. By varying the elasticity of the drop, we illustrate when jumping, bouncing, or trampolining is a more favorable outcome.

## 4.3 Results

### 4.3.1 Preparation and characterization of millimetric hydrogel drops

Millimeter-scale hydrogel drops are fabricated by gently placing 10 microliters of an acrylamide/methylenebisacrylamide (AAm/BAAm) monomer/crosslinker solution on a superamphiphobic, candle-soot coated surface, as depicted in Figure 1c (see Movie S3).[17,18] This superamphiphobic surface provides a high contact angle of nearly all liquids, allowing for the fabrication of hydrogel drops upon polymerization of the starting solution. Since the reaction is oxygen sensitive, we utilize glucose and glucose oxidase as an oxygen scavenger to prevent oxygen inhibition during polymerization.[19] With the addition of a photoinitator, a solid hydrogel drop is prepared by UV-initiated crosslinking, affording a high contact angle, drop-like geometry with a drop radius of $R$~1.25 mm. The nearly spherical drops are then rinsed away from the candle-soot surface and stored in water for at least 48 hours before use.

To investigate the effect of elasticity on jumping and bouncing behavior of hydrogel drops, we created PAAm drops with elastic modulus values of

$E$~3, 30, and 200 kPa. The moduli for the 3 and 30 kPa gels were determined by impact experiments on low-adhesion surfaces, described below. Since the water content is not independent of the modulus in hydrogel materials, we measured the water fraction by weight, defined as $\%H_2O = (w_{wet} - w_{dry})/w_{wet}$, where $w_{wet}$ is the weight under equilibrium swelling and $w_{dry}$ is the weight when dry. These turn out to be $\%H_2O =$ 97, 94 and 72 for the soft (3 kPa), medium (30 kPa) and stiff hydrogels (200 kPa), respectively.

### 4.3.2 **Determining the modulus of soft hydrogel drops**

For soft gels, measuring the modulus that correctly reflects the drop is challenging because variations arise during the preparation and testing of macroscopic samples. In an ideal situation, measuring the modulus of the drop directly is more suitable. We introduce a unique approach to quantify the modulus that utilizes the impact mechanics of elastic spheres on solid surfaces. In principle, the modulus of hydrogel drops can then be extracted by dropping them onto a solid surface and measuring the deformation and velocity right before contact.

For an elastic collision, the kinetic energy equals the elastic energy stored in the deformed drop and is defined by Hertz. The force is given by $F = 16ER^{1/2}\delta^{3/2}/9$ where $\delta$ is the normal compression of the hydrogel. By integration, the elastic energy is given as

$$U_{Hertz} = \int F d\delta = \frac{32}{45} E R^{1/2} \delta^{5/2} \qquad \text{(eq. 4.1)}$$

Equating the kinetic energy, $U_{kin} = mv^2/2$, with the elastic energy leads to a calculation of the modulus as

$$E_{Hertz} = \frac{45mv^2}{64R^{1/2}\delta^{5/2}} \qquad \text{(eq. 4.2)}$$

where $m$ is the mass of the drop and $v$ is the velocity. Assuming the density $\rho$ of the hydrogel is that of water, the mass is given by the volume of the drop as $m = \rho V_{drop}$.

We release hydrogel drops onto flat, low-adhesion, candle-soot surfaces (**Figure 2**, Movie S4) and measure the deformation and impact velocity by high speed video microscopy. It is necessary to utilize these very low adhesion surfaces to minimize capillary adhesion. Even on a Teflon surface, the hydrogel drops are barely able to overcome capillary adhesion, if at all (Movie S5). By releasing hydrogel drops onto candle-soot surfaces, we observe large, nearly adhesionless rebounds. We consider these impacts as elastic, such that Hertz impact is suitable. With that assumption, we find the modulus to be $E{\sim}3$ kPa for the softest gel and $E{\sim}30$ kPa for the medium gel.

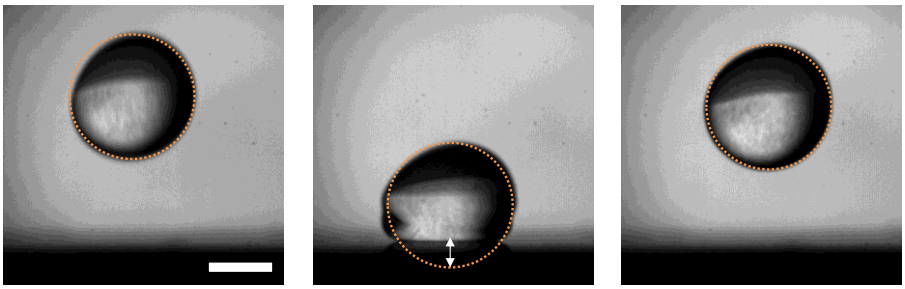

**Figure 2:** Determining modulus by hydrogel impacts. An example of a $\sim 3$ kPa hydrogel drop impacting an unheated, low-adhesion, candle-soot coated surface and rebounding. The white arrow denotes the deformation, $\delta \approx 620$ µm. See Movie S4. Scale bar: 1.5 mm.

As a test for the effect of surface tension, we add an additional surface term to the energy balance as $U_{kin} = U_{Hertz} + U_{surf}$ where $U_{surf} = 2\gamma\Delta A$. Here $A$ is the surface area of the drop and $\gamma$ is the surface tension, which we assume is constant and that of water (i.e., $\gamma = 0.072$ N/m). We approximate $A$ before contact by assuming a sphere and during contact by roughly fitting an ellipse. For the drop shown in Figure 2, the elastic energy is on the order of ~800 nJ while the surface energy is on the order of ~25 nJ. Since it is more than an order of magnitude lower, and is only about 3% of the total energy, we neglect it here. As a confirmation, we can include the surface term into the modulus determination as

$$E_{Hertz\_\gamma} = \frac{45(mv^2 - 2\gamma\Delta A)}{64R^{1/2}\delta^{5/2}} \qquad \text{(eq. 4.3)}$$

For the drop shown in Figure 2, $E_{Hertz} = 3.2$ kPa while $E_{Hertz\_\gamma} = 3.1$ kPa. In the drop where the change in area is largest, we also find marginal change with $E_{Hertz} = 3.3$ kPa and $E_{Hertz\_\gamma} = 3.0$ kPa.

### 4.3.3 **Heat-induced jumping and bouncing of 30 kPa hydrogels**

A hydrogel drop is placed on the surface of a smooth tungsten sheet (contact angle <10°) at room temperature and pressure (Figure 1d), which acquires a meniscus from the water that swells the gel. A current of 95 amps is applied across the metallic sheet, rapidly increasing the surface temperature (at ~170-200 °/s) to a maximum temperature of ~600 °C (Figure S2).

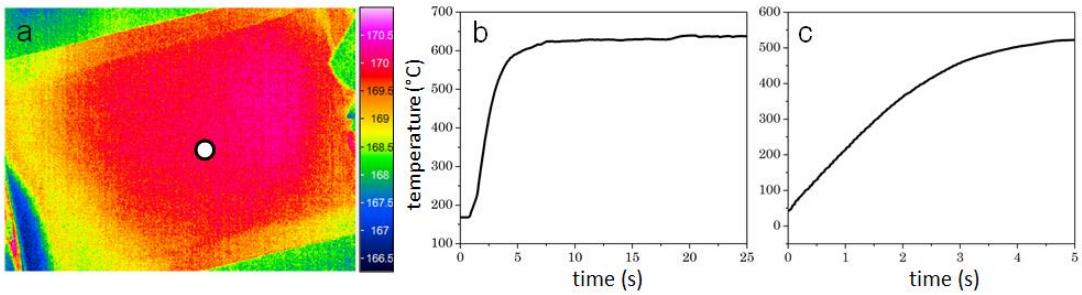


Figure S2: a) An image taken from the infrared camera approximately 1s after turning on the current. The white circle denotes the center position of the measurement, which is where the drops were positioned. b) A profile of the temperature as a function of time where the camera measurement range is 250-1200 °C. The temperature reaches a maximum at ~600 °C. c) A profile of the temperature as a function of time where the upper limit setting of the camera is 500 °C. We measure the heating rate in the linear portion to find a heating rate in the range of 170-200 °C/s. After about ~0.5 s, the temperature is above the water saturation temperature. The range is taken from both measurements since the camera settings do not cover the entire temperature range during one test.

In the range of ~170 to 200 °C, the droplet begins to vibrate on the surface while being held in place by capillarity (**Figure 3**a, 5 ms). This is associated with nucleate and transition boiling where small droplets are ejected from the contact zone. Bubbles are also observed to form and burst from the side (Figure 3a, 25-29 ms). Approximately 1s after the current is turned on, the drop jumps from the surface due to a rapid burst of the bubbles underneath the drop (Movie S6, Figure S3). The situation is reminiscent to vapor pocket formation in a leidenfrost

drop, which rises into a chimney until it reaches the top surface and releases into the air.[1,2]

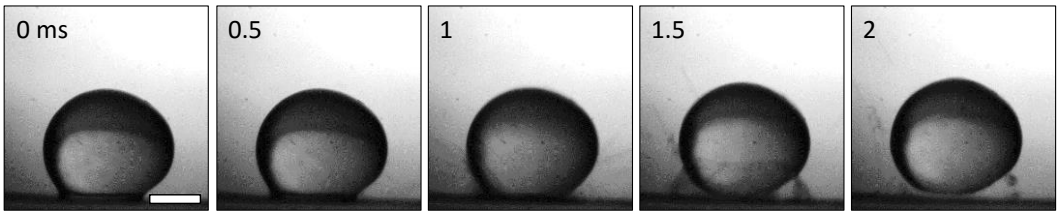


Figure S3: An example of a 30 kPa hydrogel drop jumping from the surface because of a rapid vapor explosion. The meniscus before jumping is on the order of 100 to 200 μm in height and is approximately the upper limit for a maximum bubble size. This is the size taken in the main text to calculate the jumping height. Scale bar: 1 mm.

In contrast to a water drop, however, hydrogel elasticity confines the bubble to the underside of the drop and prevents them from rising through the drop.

The initial jump ranges in height, likely because the size of the vapor bubble varies between different experiments. After the initial jump, the hydrogel bounces continuously (Figure 3b). Since we ramp the temperature from room temperature, the decreasing coefficient of restitution in the early stage of bouncing is likely due to the low temperature. The vapor explosion mechanism occurs at ~170 to 200 °C, which is below the dynamic Leidenfrost regime (300 to 600 °C) for water drops colliding on superheated surfaces.[4] At a temperature of ~340 to 400 °C, a trampolining effect is observed (Figure 3c) as the plate continues to ramp until it reaches 600 °C after ~4000 ms. We should mention that in some instances $e$ significantly decrease, at 3250 ms in Figure 2c, for example. Since our drops are not perfect spheres, some impacts are off-axis, leading to rotation and lower bouncing heights (Movie S7). Despite this fact, the general trend for increasing $e$ from ~2000-4500 ms is clear. To confirm gravity ($g$) is the only opposing force during bouncing, hang times are compared to a free-falling solid, defined as $t_{hang} \cong 2\sqrt{2h_2/g}$. Taking maximum bounce heights of 8 and 3 mm as examples, we measure hang times of ~80 and ~50 ms, respectively. Calculated values of 81 and 49 ms are in good agreement.

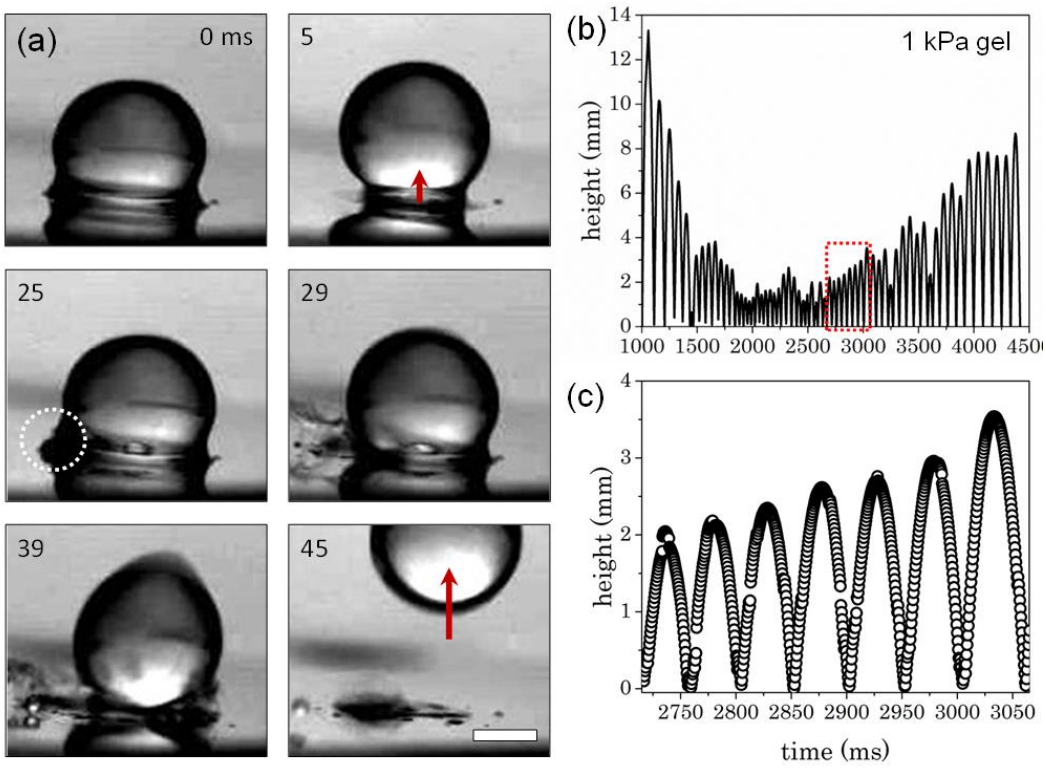


**Figure 3:** Jumping and continuous bouncing of millimetric, 30 kPa hydrogel drops. a) Upon heating, a hydrogel drop first starts to vibrate and makes small movements upward in the nucleate boiling regime, but is held down by the water meniscus (0-5 ms). Bubbles are then observed to form (dotted circle) and burst from the side of the drop (25-29 ms). Soon after, the hydrogel is observed to jump from the surface due to a vapor explosion underneath the drop (45 ms). The 0 ms frame is taken arbitrarily to illustrate the timescale of the entire event. Scale bar: 1 mm. b) Height vs. time for a 1 kPa hydrogel drop after the initial jump illustrating continuous bouncing and c) a zoom of the dotted red box in part b), showing a clear trampolining effect. The first jump is set to 1 second as an approximation of the time.

### 4.3.4 **Effect of elastic modulus on jumping and bouncing**

The elastic polymer network hinders bubble growth as well as their rise. Moreover, the elastic restoring force is the opposing force against drop spreading. Indeed, this is reflected in the hydrogel drop morphology and dynamics. For a stiff 200 kPa hydrogel, we find that the initial jumping mechanism is similar to that of the 30 kPa gel. However, the initial jump by vapor explosion is observed only on ~50% of the drops. In this case, capillary adhesion cannot deform the stiff drop, which keeps it spherical and lowers the contacting area.

This limits the drop's ability to capture and confine a vapor bubble underneath it and allows bubbles to escape and release energy on the side. When a jump is induced by a vapor explosion, the second bounce resembles that of a stiff ball impacting a solid surface (**Figure 4**a inset, Movie S8) and soon becomes stationary. Interestingly, upon reaching a temperature of ~400 °C, the stiff hydrogel drops can start to bounce erratically (Figure 4a) with varying heights and bounce as high as 8mm (Movie S8 and Movie S9).

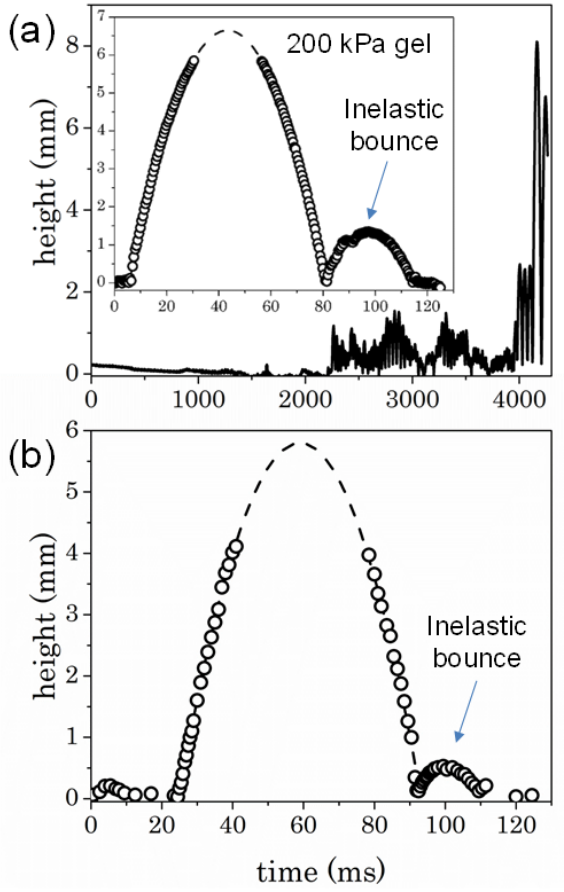


**Figure 4:** Jumping and inelastic bouncing of stiff 200 kPa hydrogel drops. a) Height vs. time plot of a 200 kPa hydrogel drop. This is an example of a drop that does not jump from a vapor bubble explosion. At ~400 °C, the drop spontaneously jumps and erratically bounces after. Inset: an example of a 200 kPa hydrogel drop jumping during a vapor explosion. The drop makes an inelastic collision with the surface afterwards. b) Height vs. time plot of a very stiff, unswollen acrylate drop (~GPa modulus) with a manually added water meniscus. The acrylate sphere can jump from the surface by vapor explosion and exhibits an inelastic collision afterwards. The x-axis time scale is taken from the first jump.

For a very soft 3 kPa hydrogel, a different jumping mechanism is observed. Initial jumping by vapor explosion is non-existent. Because the drop is very soft, it resembles a water drop on a hydrophilic surface (i.e., it spreads).

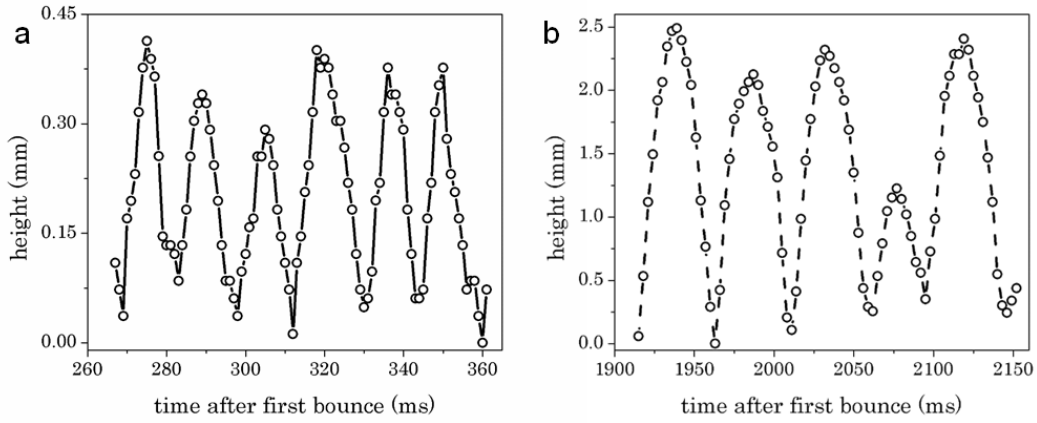


Figure S4: Bounce height of a soft hydrogel (3 kPa) after the drop is liberated from the surface by burning away the bottom of the drop (see Figure 4 from main text). a) Bouncing in the early stages after the drop detaches from the surface (associated with 1420 ms in Figure 4a from main text) and b) in the later stage after trampolining has occurred (associated with 3167 ms in Figure 4a of the main text). The bouncing heights are much higher in the later stage.

In this case, capillarity has a larger contribution and deforms the drop, leading to high adhesion. As with the other hydrogels, bubbles are observed underneath the drop upon heating. Since the elastic penalty for deforming such a soft gel is low, cavities and bubbles can expand within the drop (**Figure 5**a, Movie S10). Still, the elasticity hinders rising of the bubbles. Vapor explosions attempt to liberate the drop from the surface, however the formation of thin fibrils, or “bridges,” is observed between the drop and the surface (Figure 5a, 64 ms). This fibril formation, a common characteristic in debonding of soft adhesives,[20–22] keeps the drop adhered to the surface and inhibits jumping. As the water evaporates at the hydrogel-tungsten interface, the drop adheres to the surface and only rapid vibrations are observed (Figure 5a, 533-539 ms). After ~1.5 seconds, the polymeric components begin to thermally degrade, which is visualized in the smoke formation (Figure 5a, 1341-1420 ms). Finally, upon burning away the bottom of the drop at ~340-400 °C, consistent with thermal analysis in literature,[23] the drop is released from the surface and begins to bounce continuously (Figure 5a-5c, 3167 ms and Figure S4). The drop exhibits a

trampolining effect, similar to water drops on a superhydrophobic surface in reduced pressure.[24]

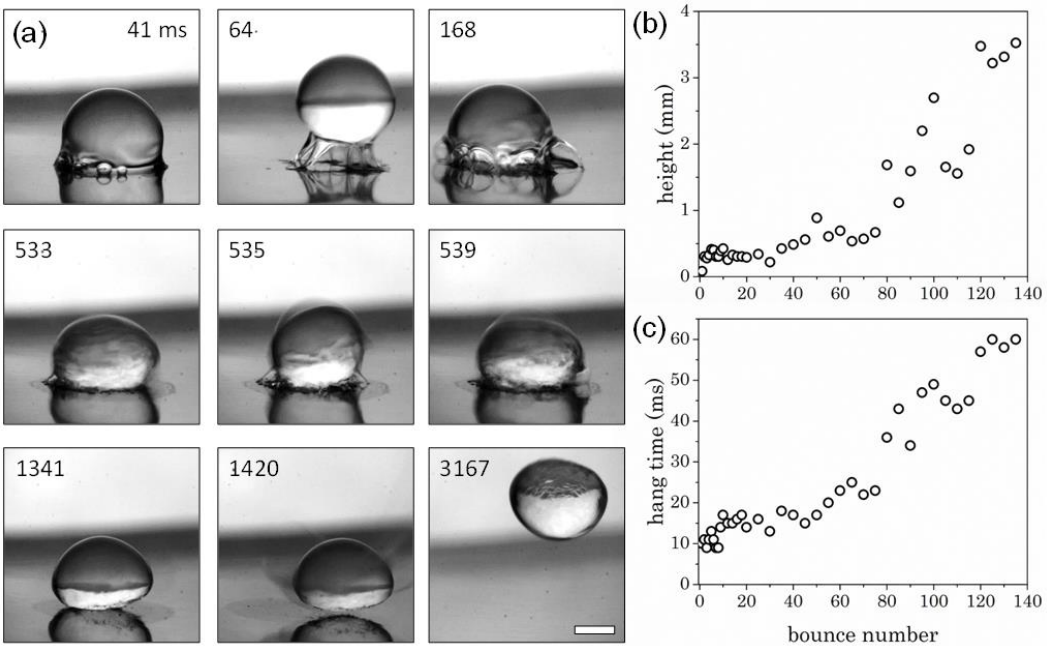


**Figure 5:** Jumping and bouncing soft 3 kPa hydrogel drops. a) Evolution of a soft hydrogel when heat is applied. Since adhesion is high and elasticity is low, bubbles first form underneath the drop. Vapor explosions lift the hydrogel drop (64 ms), but adhesion holds it back. The drop is then static on the surface and rapid vibrations are observed (533-539 ms). The hydrogel starts to burn away (1341 ms) and is then released from the surface (1420 ms). Finally bouncing and trampolining is observed (3167 ms). The first observation of a bubble is taken as the 0 ms time frame. b) Height and c) hang time vs. bounce number after the initial release the surface, illustrating a trampolining effect. Scale bar: 1 mm.

### 4.3.5 **Jumping mechanism**

To understand the jumping mechanism, the contributions of elasticity and evaporation of water need to be considered. For hydrogels, water in the material creates a meniscus under the drop where a bubble can form and explode. To test whether water in the meniscus is the key to the jumping mechanism, we replaced the hydrogel with a stiff acrylate sphere. The sphere is similarly fabricated on the candle-soot coated surfaces and contains no water;[25] no jumping or bouncing is observed. Upon manually adding a water meniscus, however, an initial jump is observed followed by an inelastic bounce (Figure 4b and Movie S11), similar to

the 200 kPa hydrogel in Figure 4a inset. This points to two effects that control heat-induced hydrogel jumping: (1) Bubble formation underneath the drop with subsequent bursting and (2) loss of the liquid meniscus.

At the hot surface, water evaporates and bubbles form. As a bubble grows, it is balanced by the hydrogel network elasticity, which provides an increasing resistance to further bubble growth. As a result, the pressure in the bubble increases until the hydrogel pushes the bubble to an interface where the bubble explodes. The energy released upon bursting can be calculated as $U_{burst} = (P - P_0)V$. Here $P$ is the maximum pressure in the bubble, which is the vapor pressure of water at elevated temperature, $P_0 =$ 101 kPa is the vapor pressure at boiling, and $V$ is the volume of the bubble; $P$ is 790 kPa at 170 °C and 1550 kPa at 200 °C.[26] Considering a bubble volume of $V_{bub} \sim 1 \times 10^{-12}$ m$^3$, which is approximated by the height of the meniscus directly before jumping (~100 µm, Figure S3), and taking $P - P_0 \approx 1$ MPa, the energy released is on the order of 1 µJ. Balanced by gravity, this is sufficient to propel a hydrogel drop of $R = 1.25$ mm and an assumed density $\rho = 1$ g/cm$^2$ to a height of $h = 3U_{burst}/4\pi R^3 \rho g \approx 12$ mm, if the pressure is fully converted into kinetic energy. We observe initial jump heights in the range of 5-15 mm, which is in good agreement with this approximation. For a hydrogel drop larger in size, such as the $R \sim 8$ mm commercial beads (Figure 1b), the calculated jump height is ~50 µm because gravity dominates. Consistent with this calculation, we are not able to resolve any jumping with such large beads.

The second effect reduces the adhesion of the hydrogel drop to the surface and thus allows it to be catapulted. The capillary force for a rigid sphere on a rigid substrate due to a water meniscus is $F_{cap} = 2\pi\gamma l - \pi l^2 \Delta P$. Here, $\Delta P = \gamma(1/l - 1/r)$ is the capillary pressure, $l$ and $r$ are the contact radius and meniscus radius of curvature, respectively, and $\gamma$ is the surface tension of water. The two radii of curvature have opposing signs since they have opposite concavities with respect to the liquid. The force simplifies to $F_{cap} = \pi\gamma l(1 + l/r)$, illustrating that as the meniscus size decreases, so does the capillary adhesion force. For soft spheres, such as hydrogel drops, such forces can be even stronger because of an increased $l$ due to deformation of the gel.[27,28] With increasing temperature, the meniscus evaporates and $l$ decreases, leading to a

decrease in the capillary force. Moreover, the surface tension is also reduced from 0.072 N/m at 25°C to 0.059 N/m at 100°C. Without this reduction of capillary adhesion, jumping of hydrogel drops would not by possible. Partially, this is observed in Figure 5a for the soft 3 kPa hydrogels.

### 4.3.6 **Observation of the contact time**

For bouncing hydrogel drops, we observed very short contact times, on the order of $t$~2 ms, for all modulus values studied (**Figure 6**). We first compare the contact time for an elastic ball defined by Hertzian impact, as described above. Reorganization of eq. 4.2 gives the elastic deformation as $\delta_{Hertz} = \left(45mv^2/64ER^{1/2}\right)^{2/5}$. The contact time is then described by the deformation and the incident velocity as $t_{Hertz} \approx 2.9(\delta_{Hertz}/v)$.[29,30] For 30 and 200 kPa hydrogel drops with a radius $R = 1.25$ mm colliding at a typical velocity of $v$~0.2 m/s, the calculated contact times are $t_{Hertz} \approx$ 2 and 1 ms, respectively, which is in good agreement with experimental results. Only for the softest, 3 kPa gel does $t_{Hertz} \approx$ 5 ms, which is about two times greater than the experimentally observed value. However, this overestimation may result from an increase in the elastic modulus during heating. Inhomogeneous evaporation and subsequent densification of the polymer network may lead to a stiff external shell, which effectively increases the modulus. For the contact to agree with Hertz, an increase in the effective modulus by a factor of 7-10x is needed.

An alternative approach is to consider the 3 kPa hydrogel, which is 97% water, as a water drop. In this case, inertia is balanced with capillarity, which leads to the contact time $t_{water} = \pi/\sqrt{2}\,(\rho R^3/\gamma)^{1/2}$.[31,32] The contact time is different from that of a solid sphere because for a water drop, kinetic energy is transformed into surface tension across the entire drop, as opposed to the localized elastic energy of a solid sphere. For a drop of $R = 1.25$ mm, this overestimates the contact time by approximately a factor of five at $t_{water} \approx 11$ ms. The large overestimation illustrates that the contact time is dominated by the elasticity of the hydrogel drop, which is consistent with our results from eq. 4.3.

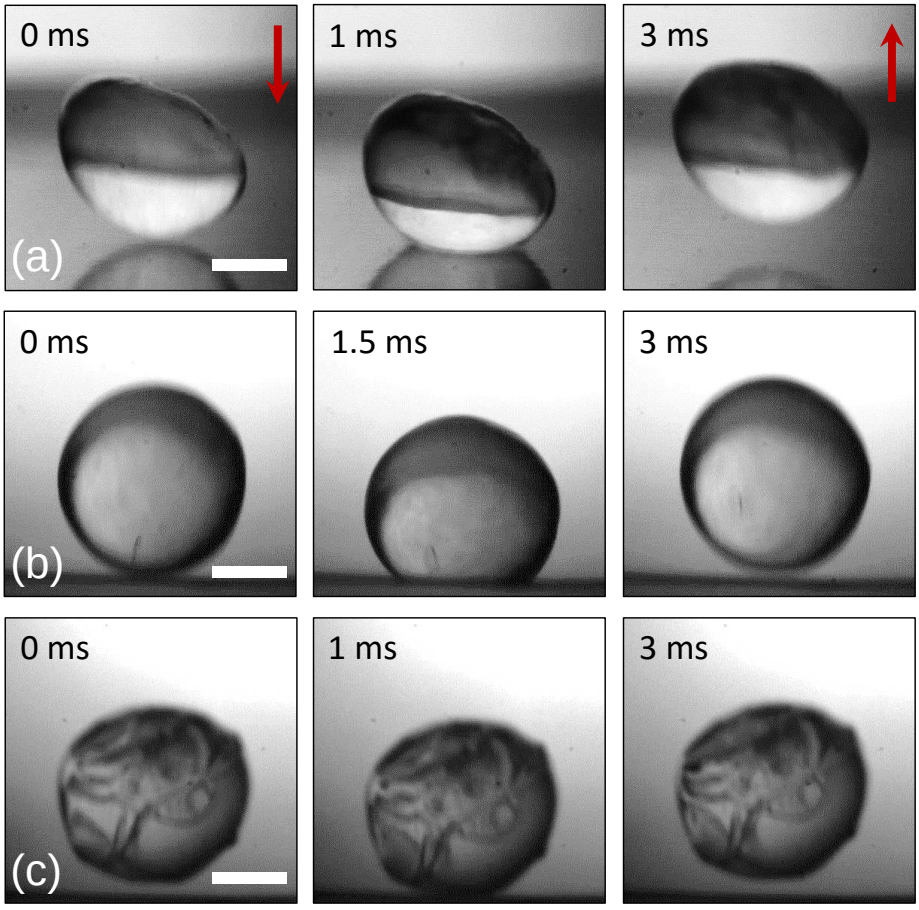


**Figure 6:** Contact time for different elasticity hydrogels. Optical images of the hydrogel drops before (left), during (middle) and after contact (right) with the superheated surface for the a) 3 kPa, b) 30 kPa, and c) 200 kPa hydrogel drops with incident velocities of a) 0.15, b) 0.25 and c) 0.15 m/s. In part a), the bottom of the drop has been degraded from heat (Figure 5a) and is therefore flattened on one side. In c), cracks are observed that likely arise from inhomogenous drying of the hydrogel.[33] A similar result is observed in commercial hydrogel beads after bouncing in a hot pan (Figure S5). The 0 ms time frame is taken as arbitrary to illustrate the timescale of the contact event. Scale bars: 1 mm.

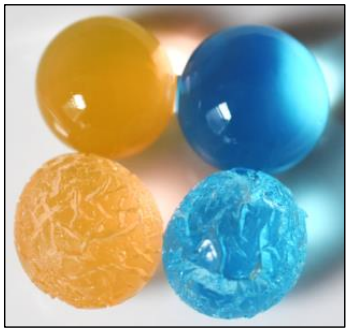


Figure S5: An image of commercial hydrogel beads before and after experiments in a hot pan. After the experiment, cracking is observed from inhomogeneous evaporation of the water from the hydrogel. This is similarly observed in the millimetric drops with a ~200 kPa modulus.

## 4.4 Discussion

Elasticity appears to play the dominating role in defining jumping and continuous bouncing of hydrogel drops from a superheated, metallic sheet. This is illustrated by i) the contact time following Hertzian impact dynamics and ii) the first jump behavior being affected by the gel modulus. However, we have also shown that bouncing does not occur without water. Moreover, hydrogel drops come to rest after a several bounces even on an unheated, candle-soot coated surface. This poses the question: What is the liquid contribution of the impact dynamics? First, it is clear that the water is needed to create the bubble burst for the initial jump. Second, rapid evaporation is necessary for long-lasting continuous bouncing and trampolining.

In particular, trampolining requires a gain in energy during impact, as opposed to the typical loss in energy. Since we only observe such results on hot surfaces, the upward force is attributed to evaporation of water from the bottom of the drop. This suggests that the vapor plays two important roles in the bouncing of hydrogel drops. The first is that it offers extra pressure from fast evaporation under the drop and second it provides a non-wetting situation where adhesionless contact is truly preserved.

To consider the extra pressure, we approximate the volume of vapor that evaporates during an impact event. We first consider the heat flux per unit area, given as

$$\Phi = \lambda(T_s - T_B)/h \qquad \text{(eq. 4.4)}$$

where $\lambda \approx 0.03$ Wm$^{-1}$K$^{-1}$ is the thermal conductivity of vapor, $h$ is the thickness of the vapor film, $T_S$ is the temperature of the substrate and $T_B = 100$°C is the boiling temperature. The rate of mass loss is then estimated as

$$\dot{m} \sim \Phi a^2/L \sim \frac{\lambda(T_s - T_B)}{Lh} a^2 \qquad \text{(eq. 4.5)}$$

where $L \approx 2 \times 10^6$ J/kg is the latent heat of vaporization and $a \approx 0.5$ mm is the contacting radius of the hydrogel drop. For static Leidenfrost drops, the thickness is of the order $h \sim 100$ µm.[2] However for impacting Leidenfrost drops, $h$ is more difficult to determine because dimples form and the thickness varies and because it is dependent on the Weber number. For hydrogels, the polymer network will also reduce dimple formation. For a water drop, $h$ has been shown to be ~3 µm for a Weber number of $We \sim 3$.[34] For comparison, the Weber number in our experiments is $We = \rho v R/\gamma \approx 1.5$, assuming a density and surface tension of water. Therefore as a rough estimate, we assume a height of $h \approx 10$ µm, resulting in $\dot{m} \approx 4 \times 10^{-8}$ kg/s at $T_S = 200$ °C and $\dot{m} \approx 2 \times 10^{-7}$ kg/s at $T_S = 600$ °C. Due to uncertainties in $h$, $a$ and $T_S$, this is considered as an order of magnitude approximation. It should be noted that a stable vapor layer can be formed instantly for an impacting drop in the Leidenfrost temperature regime.[35,36] Within the experimentally observed contact time of 2 ms, $8 \times 10^{-11}$ to $4 \times 10^{-10}$ kg of water evaporates. Accordingly, this produces a vapor volume under the drop of $V_{vap} = m/\rho_{vap} \approx 0.1$ mm$^3$, where $\rho_{vap} \approx 1$ kg/m$^3$ is the density of water vapor. For the estimated thickness of $h = 10$ µm and a contacting area of $\pi a^2 \sim 1$ mm$^2$, the vapor volume under the drop should be only ~0.01 mm$^3$. This difference is attributed to an extra pressure that aids in continuous bouncing with high restitution coefficients. Indeed a significant amount of this vapor will escape from the sides. However, for the vapor to play no role in the upward direction (i.e., when evaporated vapor volume equals ~0.01 mm$^3$ over 2 ms), it would need to escape radially with a velocity of $v_{vap} \approx \dot{m}/2\pi a h \rho_{vap} \approx 3$ m/s at 600 °C, which is unlikely. For Leidenfrost water drops, this is typically $v_{vap} \lesssim 100$ cm/s.[2] Moreover, if the contact area during successive bounces remains constant, the mass loss (and volume of the vapor film) increases with $\Delta T$ as given by eq. 4.4. An increase

in the vapor volume implies a higher pressure under the drop that leads to the trampolining effect observed with soft hydrogel drops.

Overall, we find an optimal modulus (~30 kPa) facilitates both jumping and bouncing. When the hydrogel is stiff (~200 kPa), it is able to jump from the surface by an explosion, but is followed by an inelastic collision. Our results suggest that the jumping mechanism is universal to any drop having a water meniscus, as long as it is not excessively soft.

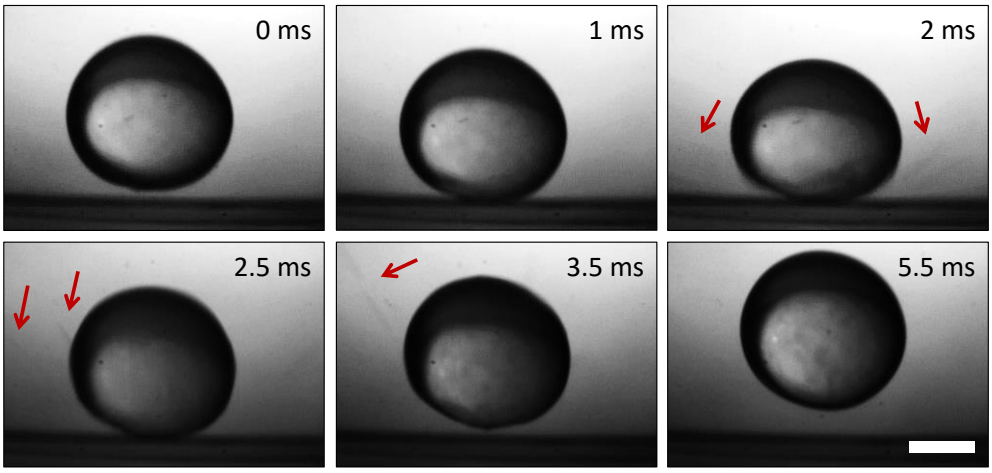


Figure S6: A 30 kPa hydrogel drop coming into contact with a superheated surface. Upon hydrogel drop contact, tiny droplets are observed to be rapidly ejected from the contact point, suggesting that the water may be coming into direct contact with the superheated surface. Examples of the ejected droplets are given by the red arrows. The 0 ms time frame is taken arbitrarily to illustrate the timescale of the event and the very fast speed of the small droplets. These droplets are only seen on contact and shortly after (2-3.5 ms for this drop). Scale bar: 1 mm.

When the hydrogel is very soft (~3 kPa), it sticks strongly to the surface and cannot be released without thermally degrading the polymer, at which point it continuously bounces. The drop must be sufficiently stiff that it does not spread and adhere strongly to the surface. Drops with high modulus do not start bouncing immediately after jumping, but require a substrate temperature of ~400°C to allow for sufficient vapor formation.

Unlike a purely solid ball, water from the hydrogel evaporates to form a vapor that provides additional pressure to the upward bounce of a drop. In addition, the water in the hydrogel may exhibit vigorous boiling if true contact is made with the surface (Figure S6).[5]

Our results demonstrate that jumping, long-lasting bouncing and trampolining require evaporation of water. However, the contact time of the drop is governed by the solid character of the hydrogels. Importantly, our experiments illustrate that hydrogel jumping and continuous bouncing is possible even without surface texture. We believe that hydrogel drops offer a new and unique route to spontaneous jumping and bouncing of solid-like drops that exhibit liquid-like aspects of the Leidenfrost effect.

## 4.5 Methods

**Chemicals and materials.** The following chemicals were purchased from Sigma-Aldrich: Tetraethyl orthosilicate (TEOS, 98%, Germany), trichloro(1H,1H,2H,2H-perfluorooctyl)silane (PFOTS, 97%, USA), Acrylamide (AAm, ≥99%, China), D-glucose (G, ≥99%, Germany), glucose oxidase from aspergillus (GOx, 10 KU, UK), 2-hydroxy-4'-hydroxyethoxy-2-methylpropiophenone (Irgacure 2959, 98%, USA), and absolute ethanol (Germany). N,N‘-methylenebis(acrylamide) (BAAm, ≥99%) was obtained from Alfa Aesar, Germany. Toluene (ACS grade) and ammonium hydroxide aqueous solution Normapur (28%) were obtained from VWR, France. Acetone (AR grade) was purchased from Fischer Scientific, UK. Water was purified by a Sartorius Arium 611. Paraffin candles were obtained from Real-Handels GmbH, Germany (TIP Haushaltskerzen, 100% paraffin, wick: 100% cotton). 3-well concavity slides (1.4-1.6 mm thick) are from ESCO–Erie Scientific Co., USA). Tungsten sheets (65x20x0.1 mm) were supplied from Umicore thin film products AG, Germany. All reagents were used as received.

**Preparation of superamphiphobic surfaces.** 3-well concavity slides were coated with a superamphiphobic, soot-templated coating as described below.[17,37] The slides were cleaned by sonication in toluene, acetone and ethanol for 5 min, respectively and were then activated by oxygen plasma (5 min, 300 W chamber reactor, f=2.45 GHz, P=300 W, O2-flow=7 scc/min, Femto BL, Diener, Germany). Afterwards, a layer of silica was deposited on the slides by chemical vapor deposition (CVD) of TEOS in the presence of ammonia. The slides were placed in a desiccator next to two 20 ml vials containing 3 ml TEOS and ammonia each (24 h at room temperature and ambient pressure). Such prepared slides were coated with candle soot collected from a paraffin candle approximately 1 cm

above the wick for 40 s (wick height about 0.7 cm, total flame height about 4.5 cm).[18] The candle-soot template was coated by a second CVD step of TEOS as described above followed by sintering of the slides at 550°C in air for 3 h (VKM-22, Linn High Therm GmbH, Germany). Finally, the slides were hydrophobized by CVD of a fluorosilane (PFOTS, 100 µl in a 20 ml vial). The slides and the vial were placed next to each other in a desiccator for 3 h at 25 mbar. Residual fluorosilane was removed at 80°C at 100 mbar for 3 h.

**Fabrication of millimetric hydrogel drops.** AAm, BAAm, Irgacure 2959, 500 mg/ml glucose in water and 200 µl $H_2O$ were mixed in an Eppendorf tube and sonicated for 5 min until the components were dissolved. To obtain different hydrogel modulus values, the following table gives the fraction of each of the components added.

**Table 1**: Fractions of each component in the solution for the different hydrogels. All values are given in mg/ml.

| | Acrylamide | BAAm | Irgacure 2959 | Glucose | GOx |
|---|---|---|---|---|---|
| stiff | 300 | 30 | 5 | 25 | 0.02 |
| medium | 60 | 5 | 5 | 25 | 0.02 |
| soft | 60 | 1 | 5 | 25 | 0.02 |

Glucose oxidase solution was added and 10 µl drops were immediately dispensed onto the superamphiphobic, 3-well concavity slides. The drops were crosslinked by UV irradiation for 10 min at a light intensity of 3-10 mW/cm$^2$ (UV-A LQ 400, Dr. Gröbel UV-Elektronik GmbH, Germany). The crosslinked drops were rinsed off the slides and stored in excess water for at least 48 hours before heating experiments. Arcylate drops were prepared as described in a prior publication.[25]

**Determination of water fractions.** Six drops of each type were measured individually by placing swollen drops in separate vial caps and weighed. The drops were dried under vacuum for 48 hours at room temperature and then

reweighed to calculate the water content as $\%H_2O = 97.4 \pm 0.2, 93.8 \pm 0.2,$ and $72.4 \pm 1.2$ for the soft, medium and stiff hydrogels, respectively.

**Heat-induced jumping and bouncing.** Tungsten sheets were clamped between two electrodes connected to a transformer, providing direct current at low voltage. The current applied to the sheet was measured and controlled. An applied current of ~95 A was chosen. Individual hydrogel drops were placed on the sheet at room temperature. After an equilibration time of ~30 s, the power was turned on. Hydrogel drops were observed by a high-speed camera (Photron) at 2000 frames per second equipped with a 2x objective. Time-temperature profiles of the tungsten sheets were recorded perpendicular with respect to the sheets using an IR-camera to determine the temperature-time profile (VarioCAM HD head, Infratec GmbH, Germany).

**Tensile testing.** The modulus values were determined directly on hydrogel drops by impact experiments on low adhesion surfaces. For the stiff hydrogels, where deformations were small and difficult to measure optically, we measured the modulus by tensile testing. Samples were prepared in a polystyrene petri dish with a thickness of 0.7 mm. Tensile test specimens were stamped with a gauge length and width of 20 mm and 4 mm, respectively. Uniaxial tensile testing was conducted on a Zwick/Roell Z005 materials testing machine equipped with a 50 N load cell at a rate of 10 mm/min. The modulus was determined by a linear fit of the stress-strain curve in the low strain regime.

**Roughness characterization of tungsten sheets.** The roughness of the tungsten sheets were measured by atomic force microscopy (Figure S2). The RMS roughness is ~15 nm and the maximum roughness scale is ~195 nm, measured over 300 $\mu m^2$. The measurements were made in tapping mode using a JPK Nanowizard atomic force microscope in air mounted with an Olympus silicon cantilever (model OMCL-AC240TS-R3, 70 kHz frequency, 2 N/m stiffness).

## 4.6 Acknowledgements

M.P. prepared the candle soot-templated surfaces, synthesized the hydrogel balls and performed the roughness measurement of the tungsten sheets. M.P.

and J. T. P. conducted the heat-induced jumping and bouncing experiments. T.K. and J. T. P. analyzed the high-seed videos. M.P. and J. T. P. performed the tensile testing test. H.-J. B., D.V. and J. T. P. had the idea for the project and organized it. J. T. P. and D.V. wrote the manuscript. All authors discussed the results and edited the manuscript. The authors thank Doroto Truszkowska for help with the infrared camera and Frank Schellenberger for the video of commercial hydrogels jumping in a pan. J.T.P. acknowledges support from an Alexander von Humboldt Postdoctoral Fellowship and H.J.B. acknowledges financial support by the ERC Advanced grant SUPRO 340391.

## 4.7 Further supporting information

**Supporting movies** will be published with the online version:

Movie S1: Leidenfrost drops on a hot kitchen pan

Movie S2: Commercial hydrogel beads (R~8 mm) in a hot kitchen pan

Movie S3: Fabrication of hydrogel drops by shaking

Movie S4: 3 kPa gel on an unheated, candle-soot coated surface

Movie S5: 3 kPa gel on an unheated, Teflon surface

Movie S6: 30 kPa gel jumping and bouncing

Movie S7: 30 kPa gel with high rotation upon contact

Movie S8: 200 kPa gel jumping by vapor explosion followed by inelastic bounce

Movie S9: 200 kPa gel jumping and bouncing at very high temperature

Movie S10: 3 kPa gel adhesion, bubble formation, burning and bouncing

Movie S11: Acrylate jumping by vapor explosion followed by inelastic bounce

## 4.8 References

[1] Biance, A. L., Clanet, C. & Quéré, D. Leidenfrost drops. *Phys. Fluids* **15,** 1632–1637 (2003).

[2] Quéré, D. Leidenfrost Dynamics. *Annu. Rev. Fluid Mech.* **45,** 197–215 (2013).

[3] Gottfried, B. S., Lee, C. J. & Bell, K. J. The leidenfrost phenomenon: film boiling of liquid droplets on a flat plate. *Int. J. Heat Mass Transf.* **9,** 1167–1188 (1966).

4] Tran, T., Staat, H. J. J., Prosperetti, A., Sun, C. & Lohse, D. Drop impact on superheated surfaces. *Phys. Rev. Lett.* **108,** 36101 (2012).

[5] Adera, S., Raj, R., Enright, R. & Wang, E. N. Non-wetting droplets on hot superhydrophilic surfaces. *Nat. Commun.* **4,** 2518 (2013).

[6] Kim, J. Spray cooling heat transfer: The state of the art. *Int. J. Heat Fluid Flow* **28,** 753–767 (2007).

7] Zhang, N. & Yang, W. J. Evaporation and explosion of liquid drops on a heated surface. *Exp. Fluids* **1,** 101–111 (1983).

[8] Weickgenannt, C. M. *et al.* Inverse-Leidenfrost phenomenon on nanofiber mats on hot surfaces. *Phys. Rev. E* **84,** 36310 (2011).

9] Hashmi, A. *et al.* Leidenfrost levitation: beyond droplets. *Sci. Rep.* **2,** 797 (2012).

[10] Antonini, C., Bernagozzi, I., Jung, S., Poulikakos, D. & Marengo, M. Water drops dancing on ice: How sublimation leads to drop rebound. *Phys. Rev. Lett.* **111,** 14501 (2013).

[11] Ruiter, J. De, Lagraauw, R., Ende, D. Van Den & Mugele, F. Wettability-independent bouncing on flat surfaces mediated by thin air films. *Nat. Phys.* **11,** 48–53 (2014).

[12] Kolinski, J. M., Mahadevan, L. & Rubinstein, S. M. Drops can bounce from perfectly hydrophilic surfaces. *Europhys. Lett.* **108,** 24001 (2014).

[13] Schutzius, T. M. *et al.* Spontaneous droplet trampolining on rigid superhydrophobic surfaces. *Nature* **527,** 82–85 (2015).

[14] Панч, Д. Гидрогель на сковороде / Hydrogel Beads in a Frying Pan. at <https://www.youtube.com/watch?v=OfcCsP-T1pc>

[15] Appel, E. A. *et al.* Ultrahigh-water-content supramolecular hydrogels exhibiting multistimuli responsiveness. *J. Am. Chem. Soc.* **134,** 11767–11773 (2012).

[16] Lee, D. J. & Song, Y. S. Anomalous water drop bouncing on a nanotextured surface by the Leidenfrost levitation. *Appl. Phys. Lett.* **108,** 201604 (2016).

[17] Deng, X., Mammen, L., Butt, H. J. & Vollmer, D. Candle Soot as a Template for a Transparent Robust Superamphiphobic Coating. *Science (80-. ).* **335,** 67–70 (2012).

[18] Paven, M. *et al.* Optimization of superamphiphobic layers based on candle soot. *Pure Appl. Chem.* **86,** 87–96 (2014).

[19] Oytun, F., Kahveci, M. U. & Yagci, Y. Sugar overcomes oxygen inhibition in photoinitiated free radical polymerization. *J. Polym. Sci. Part A Polym. Chem.* **51,** 1685–1689 (2013).

[20] Davis, C. S. *et al.* Debonding mechanisms of soft materials at short contact times. *Langmuir* **30,** 10626–10636 (2014).

[21] Ghatak, A. & Chaudhury, M. K. Adhesion-induced instability patterns in thin confined elastic film. *Langmuir* **19,** 2621–2631 (2003).

[22] Webber, R. E., Shull, K. R., Roos, A. & Creton, C. Effects of geometric confinement on the adhesive debonding of soft elastic solids. *Phys. Rev. E* **68,** 21805 (2003).

[23] Fortenberry, D. I. & Pojman, J. A. Solvent-free synthesis of polyacrylamide by frontal polymerization. *Polymer (Guildf).* **38,** 1129–1135 (2000).

[24] Vourdas, N., Pashos, G., Kokkoris, G., Boudouvis, A. G. & Stathopoulos, V. N. Droplet mobility manipulation on porous media using backpressure. *Langmuir* **32,** 5250–5258 (2016).

[25] Deng, X. *et al.* Solvent-free synthesis of microparticles on superamphiphobic surfaces. *Angew. Chemie Int. Ed.* **52,** 11286–11289 (2013).

[26] Wagner, W. & Pruss, A. International equations for the saturation properties of ordinary water substance. Revised according to the international temperature scale of 1990. Addendum to J. Phys. Chem. Ref. Data 16, 893 (1987). *J. Phys. Chem. Ref. Data* **22,** 783–787 (1993).

[27] Butt, H.-J., Barnes, W. J. P., del Campo, A., Kappl, M. & Schönfeld, F. Capillary forces between soft, elastic spheres. *Soft Matter* **6,** 5930–5936 (2010).

[28] Sokoloff, J. B. Effects of Capillary Forces on a Hydrogel Sphere Pressed against a Surface. *Langmuir* **32,** 135–139 (2016).

[29] Gugan, D. Inelastic collision and the Hertz theory of impact. *Am. J. Phys.* **68,** 920 (2000).

[30] He, A. & Wettlaufer, J. S. Hertz beyond belief. *Soft Matter* **10,** 2264–9 (2014).

[31]. Richard, D., Clanet, C. & Quéré, D. Contact time of a bouncing drop. *Nature* **417,** 811 (2002).

[32] Deng, X., Schellenberger, F., Papadopoulos, P., Vollmer, D. & Butt, H. J. Liquid drops impacting superamphiphobic coatings. *Langmuir* **29,** 7847–7856 (2013).

[33] Chung, J. Y., Regev, I. & Mahadevan, L. Spontaneous exfoliation of a drying gel. *Soft Matter* **12,** 7855–7862 (2016).

[34] Tran, T. *et al.* Droplet impact on superheated micro-structured surfaces. *Soft Matter* **9,** 3272 (2013).

[35] Shirota, M., Van Limbeek, M. A. J., Sun, C., Prosperetti, A. & Lohse, D. Dynamic Leidenfrost Effect: Relevant Time and Length Scales. *Phys. Rev. Lett.* **116,** 64501 (2016).

[36] Myers, T. G. & Charpin, J. P. F. A mathematical model of the Leidenfrost effect on an axisymmetric droplet. *Phys. Fluids* **21,** 63101 (2009).

[37] Paven, M. *et al.* Mechanical Properties of Highly Porous Super Liquid-Repellent Surfaces. *Adv. Funct. Mater.* **26,** 4914–4922 (2016).

# 5 Light-driven delivery and release of materials using liquid marbles

*Maxime Paven[a], Hiroyuki Mayama[b]*, Takafumi Sekido[c], Hans-Jürgen Butt[a], Yoshinobu Nakamura[c-e], and Syuji Fujii[d]**

[a] M. Paven, Prof. Dr. H.-J. Butt, Physics at Interfaces, Max Planck Institute for Polymer Research, Ackermannweg 10, D-55128 Mainz, Germany

[b] Dr. H. Mayama, Department of Chemistry, Asahikawa Medical University, 2-1-1-1 Midorigaoka-Higashi, Asahikawa 078-8510, Japan. E-mail: mayama@asahikawa-med.ac.jp

[c] T. Sekido, Prof. Dr. Y. Nakamura, Division of Applied Chemistry, Graduate School of Engineering, Osaka Institute of Technology, 5-16-1 Omiya, Asahi-ku, Osaka, 535-8585, Japan.

[d] Dr. S. Fujii, Prof. Dr. Y. Nakamura, Department of Applied Chemistry, Faculty of Engineering, Osaka Institute of Technology 5-16-1 Omiya, Asahi-ku, Osaka, 535-8585, Japan. E-mail: syuji.fujii@oit.ac.jp

[e] Prof. Dr. Y. Nakamura, Nanomaterials Microdevices Research Center Osaka Institute of Technology, 5-16-1 Omiya, Asahi-ku, Osaka 535-8585, Japan.

Reprinted with permission from Adv. Funct. Mater. **2016**; 26 (19): 3199-3206.


Keywords: Polypyrrole, nanoparticles, autonomous movement, miniature reactors, water particles, droplet, motors, motion, nanomachines, nanomotors

## 5.1 Abstract

Remote control of the locomotion of small objects is a challenge in itself and may also allow for the stimuli control of entire systems. Here, it is described how encapsulated liquids, referred to as liquid marbles, can be moved on a water surface with a simple near-infrared laser or sunlight. Using light rather than pH or temperature as an external stimulus allows for the control of the position, area, timing, direction and velocity of delivery. This approach makes it possible to not only transport the materials encapsulated within the liquid marble but also to release them at a specific place and time, as controlled by external stimuli. Furthermore, it is shown that liquid marbles can work as light-driven towing engines to push or pull objects. Being able to remotely transport and push/pull the small objects by light and control the release of active substances on demand should open up a wide field of conceivable applications.

## 5.2 Introduction

Controlling and powering the locomotion of small objects on the micrometer to millimeter scale is a fascinating topic of research[1] with possible applications in microfluidics and drug delivery. Interfacial chemistry, e.g., chemical reactions, dissolution and gradients in surface tension, and external stimuli play a crucial role in powering the movement of small objects. For example, the catalytic decomposition of hydrogen peroxide is widely used as a driving force to move colloidal particles.[2] This interest stimulated the development of a new research area, namely, active soft matter. Additionally, small objects can be moved and manipulated by external electric[3] and magnetic[4] fields. In particular, Marangoni flow, generated due to a surface tension gradient, can lead to the powerful propulsion of objects.[5] In nature, beetles of genus Stenus use Marangoni propulsion to move on air-water interfaces.[6] Similarly, camphor crystals,[7] soap boats,[8] depolymerizable plastics[9] and organic solvent-loaded objects[10] experience locomotion due to Marangoni propulsion: the dissolution of chemicals creates a surface tension gradient at the air-water interface, which induces motion. Recently, light-induced surface tension gradients have been proven to

produce powerful propulsion forces to move small objects.[11] The main goal of this philosophy is to bring together transport and the on-demand release of materials.

Liquid marbles (LMs)[12] are typically millimeter-sized liquid drops in air that are stabilized by solid powders adsorbed at the air-liquid interface. The liquid droplets can be stabilized by various hydrophobic and even hydrophilic powders as long as the powders repel the liquid.[13]

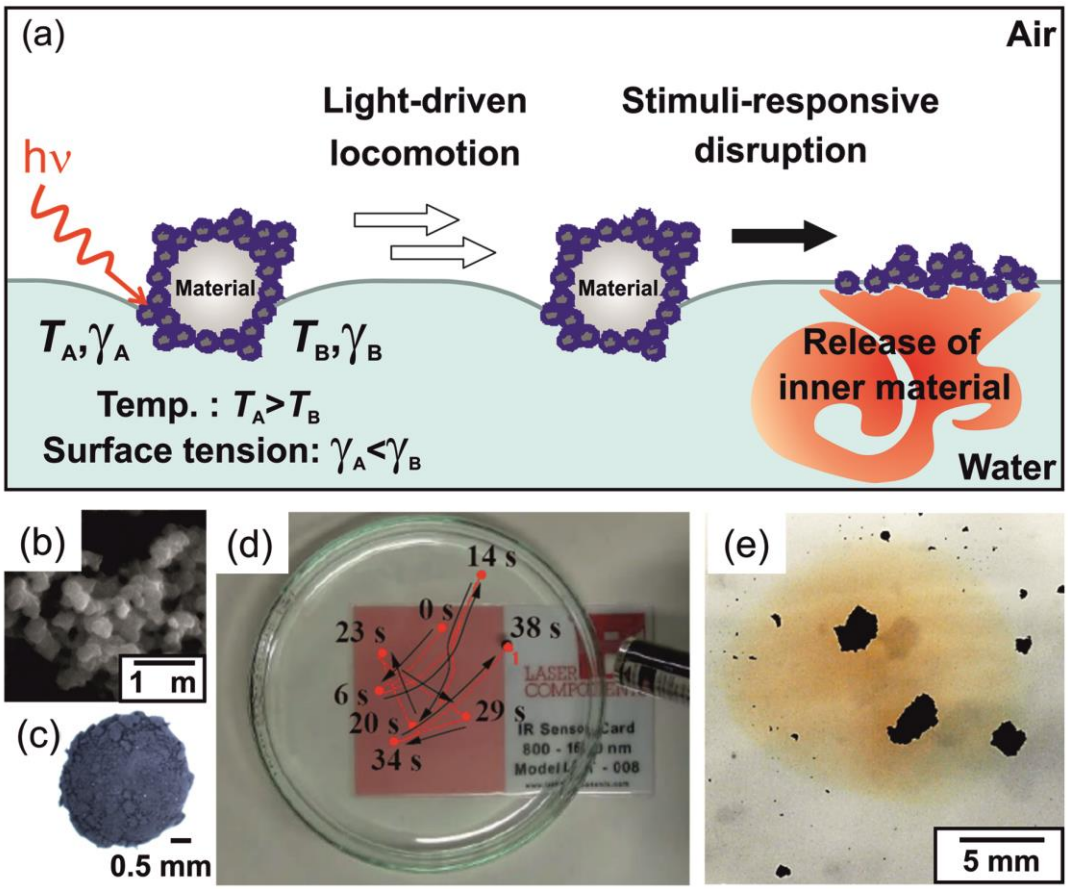


**Figure 1:** a) Scheme illustrating the light-driven delivery of material using liquid marbles (LMs). LMs can be moved on the planar air-water interface and a stimuli-induced disruption of the LM releases its inner material. NIR laser irradiation of LMs stabilized with black powder converts light into heat, generating a thermal surface tension gradient. This results in locomotion of the LM on the air-water interface. b) Scanning electron microscopy image of hydrophobic PPy powder. c) Stereomicrograph images of a PPy-stabilized LM (10 µl) placed on a glass substrate. Digital images illustrating d) locomotion of a PPy-stabilized LM on the air-water interface and (e) its on-demand disruption of a LM by external stimulus.

Many liquids and dispersions can be encapsulated to form liquid marbles which can hence be treated as non-wetting materials. Some aphids fabricate LMs using wax particles, allowing them to readily manipulate liquids that would otherwise be

sticky.[14] Thanks to their non-wetting nature, liquid marbles can easily move on various substrates.[15] Recently, LMs have attracted considerable attention in view of their potential applications in cosmetics,[16] transport and microfluidics,[17] miniature reactors,[18] personal and health care products,[19] sensors,[20] accelerometers,[21] gas storage[22] and pressure-sensitive adhesives[23] because of their ability to encapsulate functional materials.

Here, we describe the light-driven delivery of materials using LMs. Our approach allows for not only the transport of the materials encapsulated within the LM but also their release at a specific place and at a time determined by external stimuli (**Figure 1**a). In addition, LMs were shown to work as light-driven towing engines. For this purpose, LMs were docked to small floating objects by capillary forces. Irradiation of docked LMs allowed for the pushing or pulling of these objects over the air-water interface. Being able to remotely transport and push/pull the small objects by light and control the release of active substances on demand should open up a wide field of conceivable applications. This ability is particularly relevant in confined, restricted and/or dangerous areas where direct access is not possible, e.g., in microfluidics for the delivery of analytes or in polluted districts.

## 5.3 Results and discussion

To introduce the light-driven delivery ability to LMs, we used two different powders, namely, polypyrrole (PPy) and carbon black (CB), as LM stabilizers. Both powders are known to have photo-thermal properties.[24] PPy was rendered hydrophobic with octadecanoic acid as a surface modifier.

Octadecanoic acid adsorbed to the PPy powder surface via an electrostatic interaction between the carboxylic acid and cationic PPy. The PPy powder consisted of randomly shaped aggregates of primary particles with diameters of ≈350 nm (Figures 1b, S1).

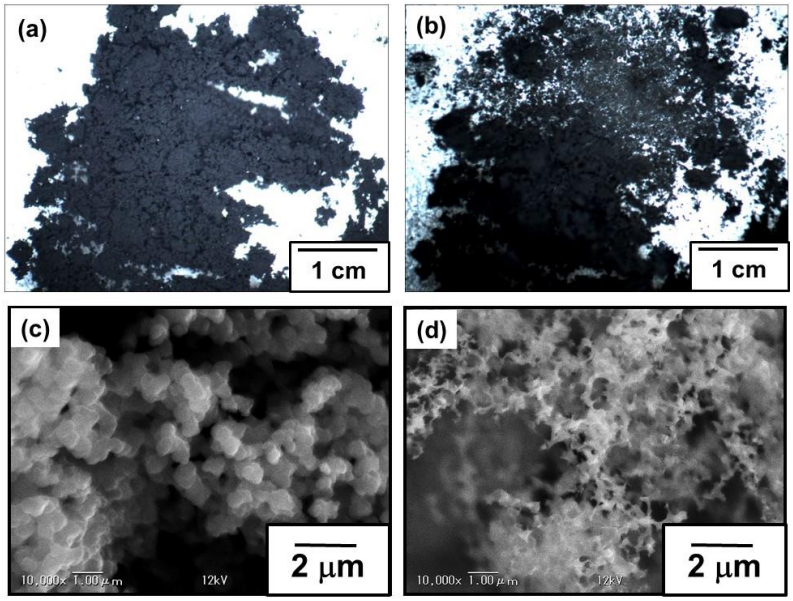


Figure S1: (a, b) Photographs and (c, d) SEM images of PPy bulk powder before (a, c) and after (b, d) being irradiated by a NIR laser (808 nm, 200 mW).

The utilized CB powder was intrinsically hydrophobic and consisted of submillimeter- to millimeter-sized flocs of undefined shape. These flocs were composed of primary particles with diameters of ≈100 nm (Figure S2).

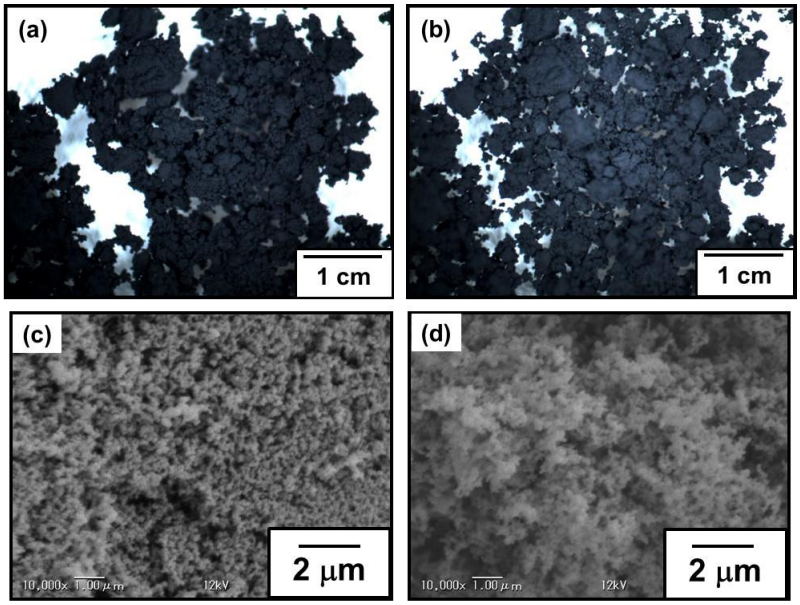


Figure S2: (a, b) Photographs and (c, d) SEM images of CB bulk powder before (a, c) and after (b, d) being irradiated by a NIR laser (808 nm, 200 mW).

Static contact angles of water drops (10 µl) on the PPy and CB powders were measured to be 124±2° and 139±1°, respectively, proving the powders' hydrophobicity.

To confirm their photo-thermal properties, PPy and CB bulk powders were exposed to near-infrared (NIR) laser irradiation (808 nm; spot diameter, 1 mm×5 mm; output power, ~200 mW), and the temperature as function of time was analyzed thermographically. When the bulk powder was irradiated, the temperature of the PPy and CB bulk powders rapidly exceeded 1,000 °C and then gradually decreased to settle to constant temperatures of approximately 350 and 600 °C for PPy and CB, respectively (Figure S3).

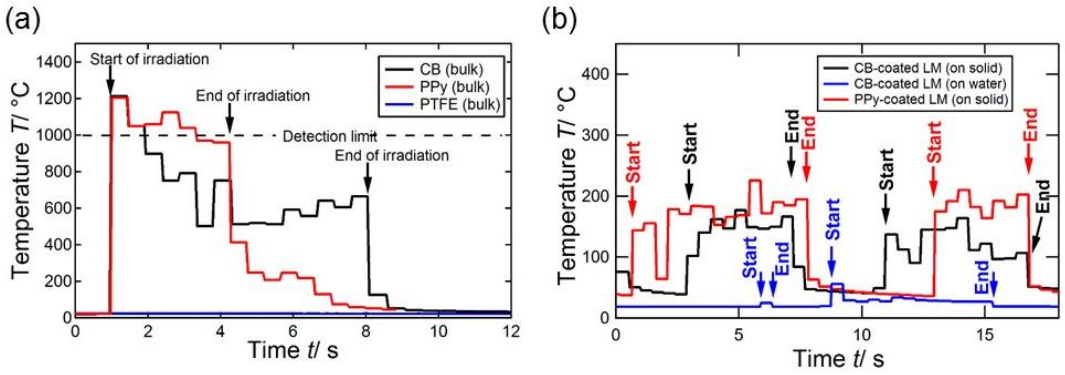


Figure S3: Typical hotspot temperature profile of samples being irradiated with a NIR laser (808 nm, 200 mW) as a function of irradiation time. The start and end of irradiation are marked by arrows. a) Bulk materials: CB, PPy and PTFE and b) liquid marbles on a glass substrate and on water. The initial strong increase of temperature observed for the CB and PPy bulk materials is due to effective conversion from light to heat. The temperature was successively reduced since the material properties should change upon irradiation. CB and PPy were decomposed and partially combusted leading to a decrease of their photo-thermal response. The fluctuation of temperature arises from microscopic shifts of the laser position during irradiation using hand. The surface temperatures of the LMs deposited on a glass substrate increased up to approximately 200 °C and 175 °C when irradiated with a NIR laser for PPy and CB LMs, respectively. The maximum temperatures were lower than those measured for the bulk black powders, likely due to the increased heat capacity of the water-filled marbles. Stopping the laser irradiation led to a rapid decrease of the temperature to 50 °C in less than 1 s and to less than 35 °C within 5 s.

Thus, the black powders convert the NIR laser energy into heat efficiently. The energy conversion efficiency from light to heat was calculated to be approximately 7% for both PPy and CB powders (Supporting Information). As a reference, bulk polytetrafluoroethylene (PTFE) powder was exposed to NIR laser irradiation under the same conditions. In contrast to the black powders, the temperature of the PTFE powder remained almost constant at 22°C independent

of the NIR irradiation time, indicating that PTFE does not have photo-thermal properties. Individual LMs were prepared by rolling a 10 µl (= 2.7 mm diameter) aqueous drop over the black powders. Both PPy and CB powders immediately coated the water drops and rendered them hydrophobic and non-wetting (Figure 1c and Figure S4).

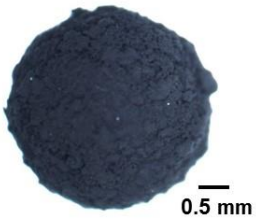


Figure S4: Stereomicrograph images of a CB-stabilized liquid marble (10 µl) placed on a glass substrate

The weight ratio of powder/water was gravimetrically measured to be 1/99 for both the PPy and CB systems. Once transferred to the planar air-water interface of a water bath, the LMs remained intact for more than 10 h. This stability at the air-water interface indicates that the water drops inside the LMs are well shielded by the hydrophobic powder and a vapor gap. They do not come into direct liquid contact with the water in the bath. To make the LMs move on the air-water interface on demand, the contact line formed by the LM resting on at the air-water interface was manually irradiated by the NIR laser at an angle of ~45°. The LMs immediately moved forward on the air-water interface, away from the point of irradiation. The exposure time was in the order of a few hundreds of millisecond. In Figure 1d, a PPy-coated LM was placed in a Petri dish filled with water. The marble was irradiated and its motion was traced (highlighted with red lines, whereas the black arrows indicate the direction, see also Supporting Information Movie 1). For a more in-depth understanding of the locomotion process, the heat distribution upon irradiation was studied by thermography.

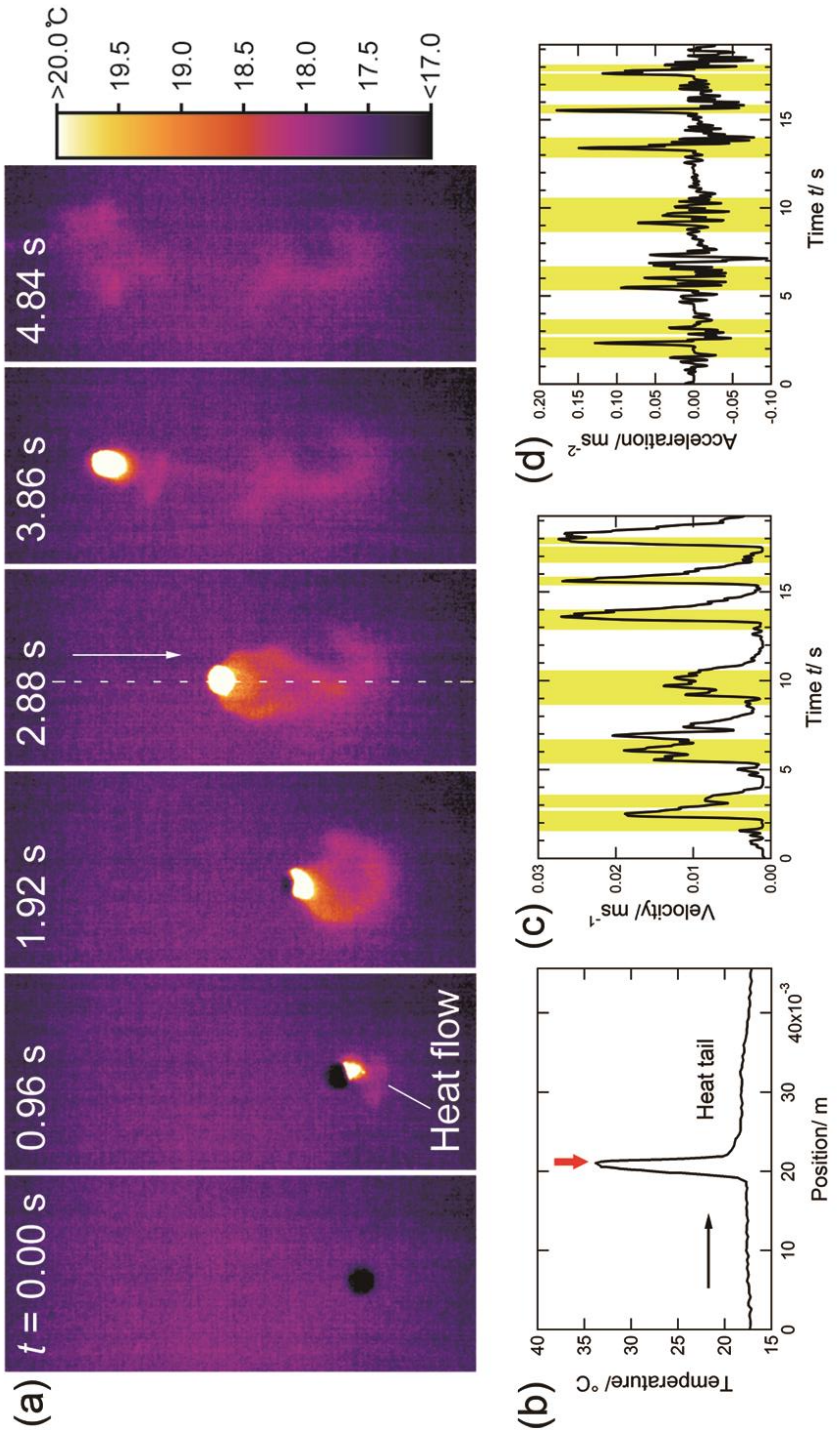


**Figure 2:** a) Snapshots of the light-driven locomotion of a CB-stabilized LM (1.8 mm in diameter) observed by thermography. At t=0, the LM was in thermal equilibrium. NIR irradiation caused a strong heating and locomotion of the LM (t=0.96-4.86 s). b) Temperature profile obtained from a), following the white dotted line at t=2.88 s in the direction of the arrow. The red arrow is the position of the laser irradiated liquid marble. c) Velocity and d) acceleration profiles of the locomotion of a PPy-stabilized LM on the air-water interface observed in Figure 1d. The yellow shaded areas correspond to the time period when the laser was triggered.

**Figure 2**a shows typical thermography snapshots of the light-driven locomotion of a CB-coated LM at the air-water interface. At t=0 s, the LM is in thermal equilibrium with the surrounding water. Upon NIR laser irradiation (snapshots at t=0.96 and t=1.92 s), the hottest spot is the center of irradiation, which is simultaneously the center of anisotropic heat flow. The heat profile, i.e., temperature vs. position, was recorded along the path of locomotion (white dotted line in snapshot t=2.88 s and Figure 2b). Figure 2b suggests that the temperature of the NIR laser-irradiated LM was > 35-40 °C (see also Supporting Information) and a heat tail could be identified. In contrast to the bulk water (T= 18 °C), water near the LM had a temperature of approximately 30 °C (Figure 2b). This temperature difference leads to a surface tension difference $\Delta\gamma$ of ≈2 mN/m at the irradiated side of the LM with a surface entropy of $s = -\frac{d\gamma}{dT} = -0.16\ \mathrm{mN/Km}$. This surface tension difference drives the locomotion of the LM.

Next, we try to determine the generated force and the work done by the LM. First, the equation of motion is described as in Equation (1)

$$\frac{md^2x}{dt^2} = \Delta\gamma w - \zeta v \qquad \text{(eq. 5.1)}$$

where $m$, $\Delta\gamma$, $w$, $\zeta$ and $v$ are the mass of the LM, the surface tension difference, the width of irradiated area, the friction coefficient between water and the LM, and the velocity of the LM, respectively. The first term on the right side represents the propulsion of the LM by the temperature-induced surface tension gradient produced by NIR laser irradiation. The second term corresponds to the friction between the LM and water. As shown in Figure 1d, changing the direction of NIR laser irradiation also rapidly changes the direction of locomotion of the LM. Figure S5 reflects this behavior, as the time dependence of the trace length changed in a stepwise manner. As shown in Figures 2c,d, the velocity and acceleration of the locomotion are obtained by the time differentiation of the length and velocity, respectively. As a result, the maximum velocity and acceleration are ≈2.7×10$^{-2}$ m/s and 0.17 m/s$^2$, respectively, and the generated force is ≈1.8 μN (the mass of LMs is 9×10$^{-6}$ kg) (Figure S6, Supporting Information).

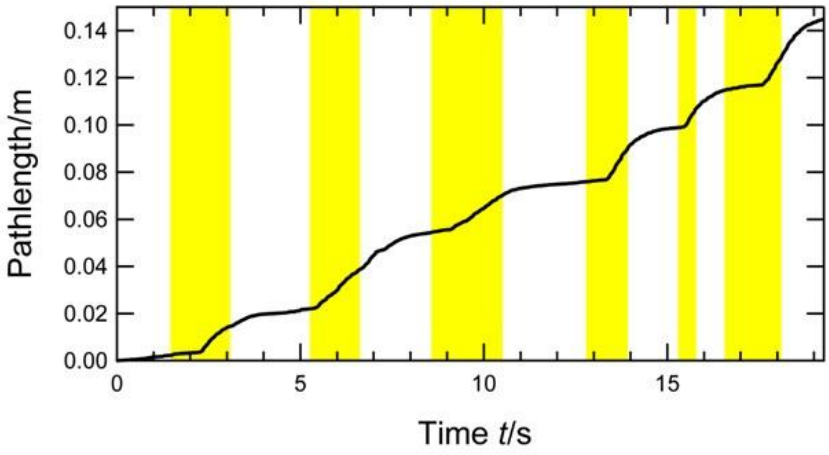


Figure S5: Analysis of Figure 1 d: Pathlength vs. time of the locomotion of a PPy-stabilized LM on the air-water interface observed in Figure 1d irradiated by a NIR laser (808 nm, 200 mW). The yellow shaded areas correspond to the time period when the laser was irradiated.

This calculated force agrees with an estimate of the maximal Marangoni force. Variations in the maximum velocity and acceleration of locomotion were found for individual laser shots. The difference should occur due to the variations in the positioning of the NIR laser and the thickness of the black powder layer on the LM. Also, variations might arise from fluctuations of the water surface temperature generated around the LM due to repeated irradiations.

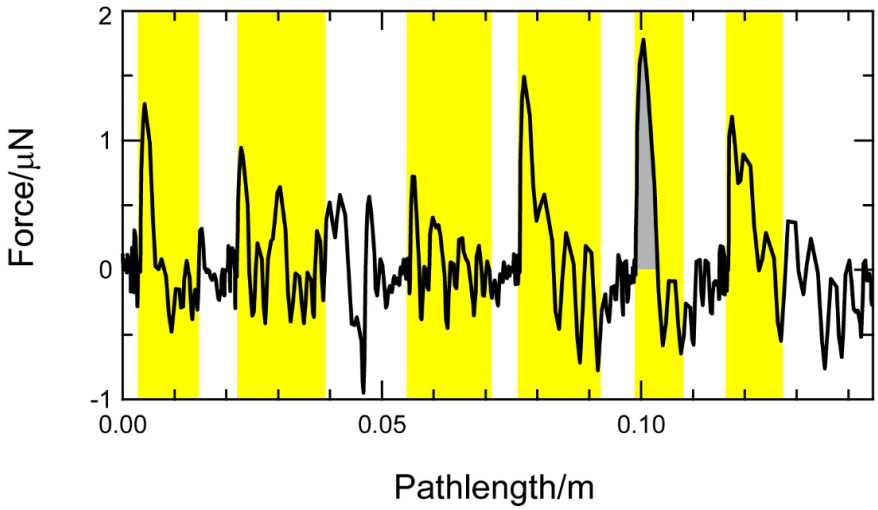


Figure S6: Analysis of Figure 1d: Force vs. pathlength of a PPy-stabilized LM irradiated with a NIR laser (808 nm, 200 mW) observed in Figure 1d. The yellow shaded areas correspond to the time period when the laser was irradiated. The area of the grayish peak corresponds to 4.9 nJ.

Assuming that we have a surface tension on one side of the LM that is $\Delta\gamma = 2\,\mathrm{mN/m}$ higher than that on the other side, the capillary force can be

estimated to be $\approx 2R\Delta\gamma$. With a radius of the LM of R=1.2 mm, this force is ≈5 μN. The maximum work was estimated to be 4.9 nJ in the plots of force vs. pathlength (Figure S6). The obtained force and work are quite larger than the generative force and work produced by a kinesin (5 pN and $4\times10^{-20}$ J).[25] A control experiment based on LMs stabilized with PTFE powder was conducted to prove that LMs need to be stabilized with powders having photo-thermal properties to achieve locomotion. Upon irradiation, no significant temperature gradient was observed around the PTFE stabilized LMs by thermography. No light-driven locomotion of the PTFE-stabilized LM occurred.

Transportation and targeted release of small amounts of analytes and reagents is of great interest. LMs are suitable candidates for transporting and releasing such agents. The moment of disruption can be well controlled by using external stimuli, such as organic solvents,[20a] pH,[26] temperature,[27] light[26d,28] and magnetic fields[29], and the suitable stimulus can be chosen depending on the situation. Here, we show that the concepts of light-driven locomotion and on-demand disruption can be combined. To prove this, photo-thermally active black LMs were disrupted on-demand by three external stimuli, namely, pH, isopropanol fumes and successive laser ablation. To obtain pH-responsive black LMs, a water drop was covered by a blend of CB and polystyrene latex particles carrying poly[2-(diethylamino)ethyl methacrylate] hair (PS-PDEA). Such LMs were stable and could be moved by irradiation on a neutral/basic planar air-water interface. When the water became acidic, the PS-PDEA particles became hydrophilic because of the protonation and hydration of the PDEA hairs and detached from the LM surface.[26a] As a result, water inside the LM contacted the water in the bath, and the LM was immediately disrupted (Supporting Information Movie 2). Additionally, black LMs were disrupted when selectively exposed to isopropanol fumes (Supporting Information Movie 3). The absorption of isopropanol fumes into the inner water drop caused a decrease in the surface tension, which led to reduced stability of the LM. Black LMs can also be moved and selectively disrupted by controlling the exposure time of the LMs to laser irradiation. As shown before, irradiation of the three-phase contact line at an angle of ≈45° caused locomotion of the LM; the exposure time was typically less than 1 s. By choosing an irradiation angle of 90°, i.e. from the top or when statically trapping the marble locomotion, the same

surface area of the LM could be continuously irradiated and ablated (several tens of seconds). During this time, the flocs of the powder were removed until the LMs became unstable and disrupted, as shown in **Figure 3** (Supporting Information Movie 4).

As one example, the on-demand and on-site disruption of LMs can be utilized for heavy ion detection in liquids. LMs containing 0.5 M $KSCN_{(aq)}$ were prepared and transferred to the interface of a 0.01 M $FeCl_{3(aq)}$ solution. The LM was directed to the proximity of a PTFE pin with a flat top by laser irradiation (Figure 3a). Here, the liquid level was chosen to be slightly higher than the height of the PTFE pin, and a finite contact angle formed due to its hydrophobicity. Thus, the top face of the pin was exposed to air, and the air-water interface was distorted. Once the LM was sufficiently close to the pin (approximately 1-1.5 cm), the lateral capillary forces between both effectively attracted the LM, and the LM moved to and landed on the PTFE pin without any irradiation (Figures 3a-c).[30] In this case, the LM is mainly on the solid substrate and cannot be moved any further by irradiation. When the trapped LM is constantly irradiated, PPy flocs are partially removed from its surface or smoothed, and vapor or smoke is visible due to the thermal decomposition of PPy and the evaporation of water (Figures 3d,e). Within 20 s, the LM broke and blood red $FeSCN_3$ immediately became visible, confirming the presence of $Fe^{3+}_{(aq)}$ near the place of interest, i.e., the PTFE pin (Figures 3f,g). We anticipate that using a laser with tunable powers could even facilitate the locomotion/disruption process by using low powers for locomotion and high powers for a quick on-demand disruption.

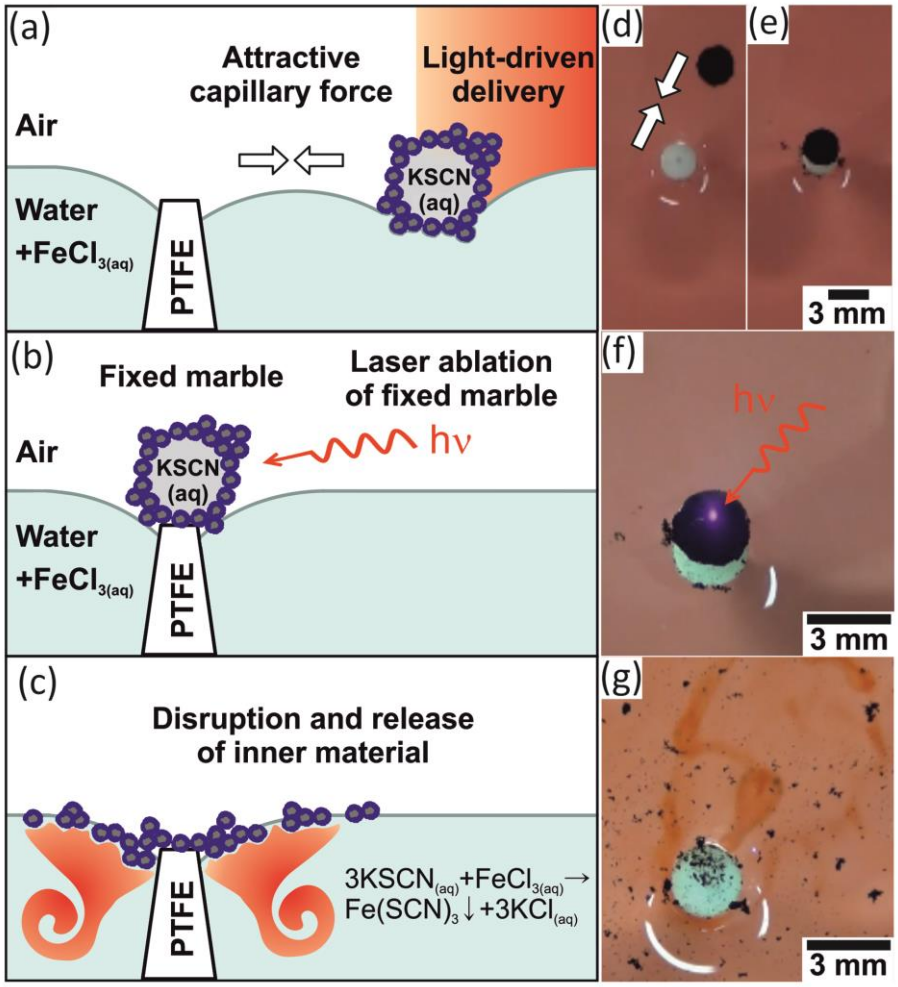


**Figure 3:** Scheme illustrating a) delivery, b) fixing and c) on-demand disruption of LM and release of the material at the air-water interface. (Data obtained using PPy-stabilized LM is shown.) Fixing of a LM at the air-water interface can be achieved by introducing inhomogeneities in the water film (e.g. a solid object, such as a PTFE pin). LMs in the proximity are attracted due to lateral capillary forces. Photographs illustrate the process of trapping and breaking on demand. d) The LM brought into the proximity of a PTFE pin by NIR laser irradiation was attracted to the pin due to lateral capillary forces. e) LM bound to the pin. f, g) Breaking on demand: f) the LM was ablated by NIR laser irradiation (18 s). g) The LM broke and released 0.5 M $KSCN_{(aq)}$. The water contained $Fe^{3+}_{(aq)}$, and the water close to the site of LM disruption immediately turned blood red due to the formation of $FeSCN_3$.

Black LMs were used as versatile light-driven towing engines for the pushing or pulling of objects (**Figure 4** and Supporting Information Movie 5). Plastic boats with different shapes for pushing (Figures 4a, 4b) and pulling (Figure 4c) were loaded with cargo to demonstrate their ability to tow objects. Single LMs were directed close to the boats by light. Lateral capillary forces allowed docking to the

boat. We showed that a boat driven by a black LM can pull multiple marbles over the air-water interface (Figures 4a,b).

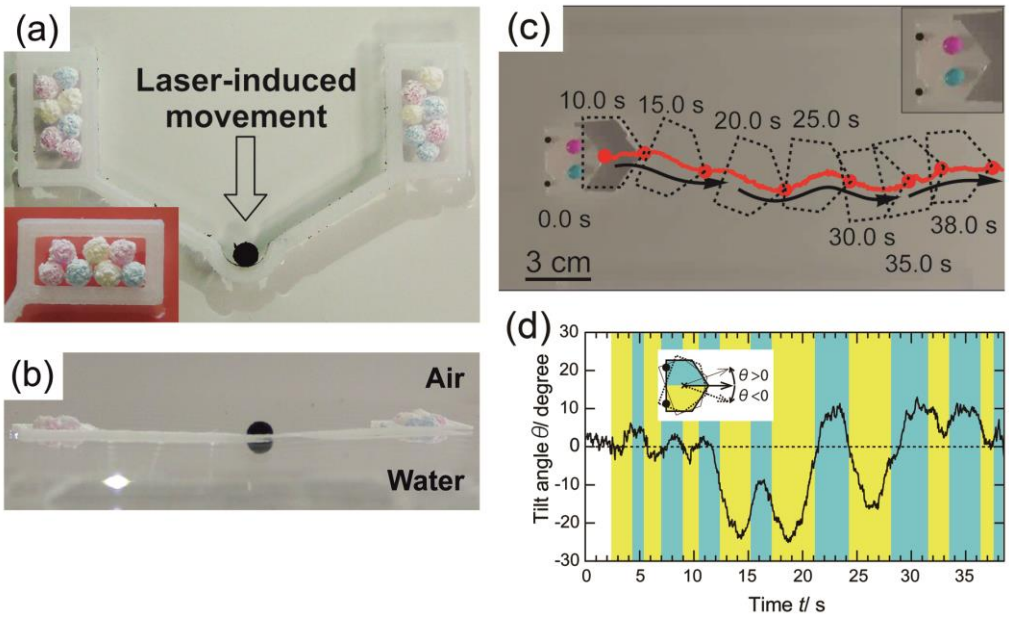


**Figure 4:** Delivery of materials and objects by the irradiation of LMs with a NIR laser or sunlight. Liquid marbles were readily bound to objects (boats) due to lateral capillary forces. a) Laser-driven boat containing 14 PTFE LMs. Laser irradiation of the PPy-stabilized LM led to a linear locomotion of the boat. Inset: magnification of a frame. PTFE-stabilized LMs were filled with dyed water. b) Side view of the boat. The LMs were in direct contact with the air-water interface and could potentially probe it. c) Sunlight-driven movement of a boat. Inset: magnification of the boat carrying 2×60 µl of dyed water droplets. Data obtained using CB-stabilized LMs is shown. Using multiple LMs, a non-linear locomotion could be attained. d) The relationship between the tilt angle of the boat based on the horizontal axis and the time depending on the application of focused sunlight on each LM. Application of sunlight on the left LM (with respect to the traveling direction) made the boat tilt to the right and vice versa.

The boat, which had two side frames holding 7 PTFE LMs filled with dyed water, moved linearly by laser irradiation of a black LM located in the center part of the boat. Loads of more than 1.4 g could be moved by irradiation of a single black LM, which corresponds to more than 150 times its own weight. The maximum velocity and acceleration of the plastic boat carrying multiple LMs were determined to be approximately $1.57\times10^{-2}$ m/s and $2.9\times10^{-2}$ m/s$^2$, respectively. These values were smaller than those of an isolated LM. The maximum force was calculated to be ≈12.3 µN (Figure S7), which was comparable to that of a single LM.

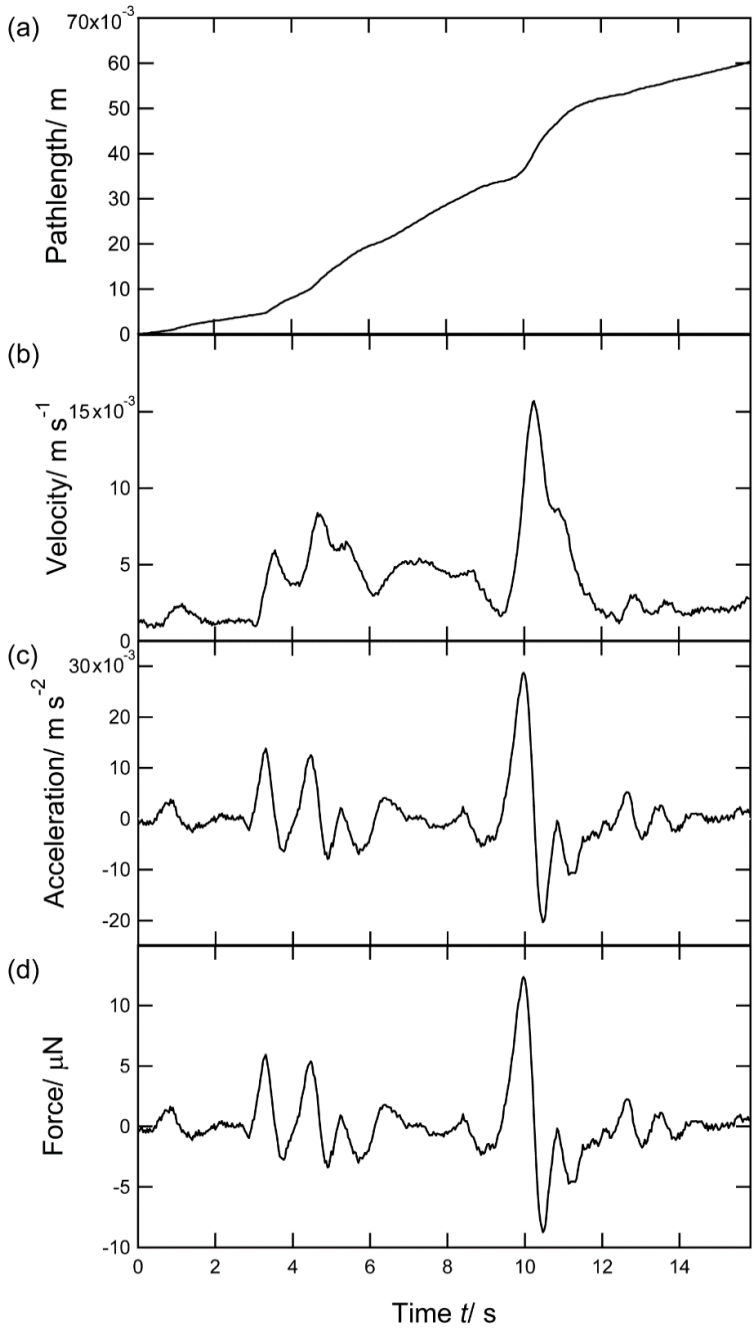


Figure S7: Analysis of the moving boat containing 14 PTFE liquid marbles (Supporting Movie 5). a) Pathlength vs. time, b) velocity, c) acceleration and d) force profiles of the boat. The PPy-stabilized LM was irradiated using a NIR laser (808 nm, 200 mW).

The smaller acceleration value is due to the larger mass of the boat considering the similar force value. The maximum work was estimated to be ≈55 nJ (Figure S8). Environmental conditions at the air-water interface can efficiently be probed by LMs: they can be designed to be gas,[20a] pH,[26] temperature,[27] light,[26d,28] magneto[29] and sound[31] responsive and can thus offer a quick low-cost technique

to probe the air-water interface. Typically, LMs cannot probe multiple properties at once; thus, different types of LMs need to be successively investigated.

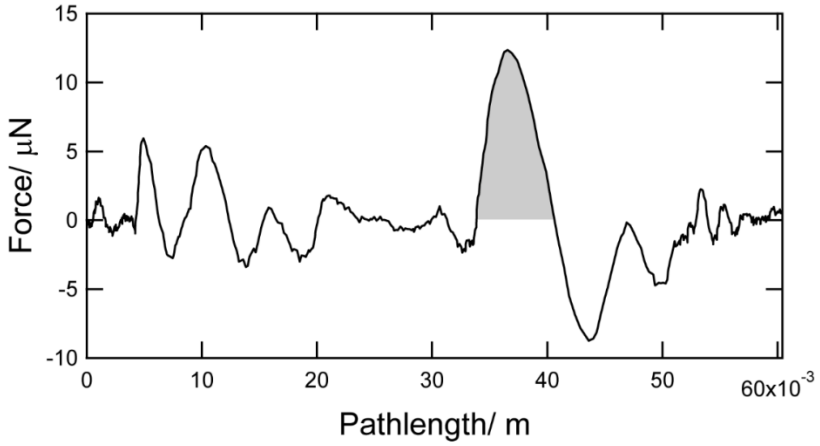


Figure S8: Force vs. path length of the moving boat containing 14 PTFE liquid marbles (Supporting Movie 5). The area of the grayish peak corresponds to 55 nJ.

We envision that gradients in the physico-chemical properties of the air-water interface on the scale of centimeter to meter distances can be detected by moving this boat over the air-water interface. This sensing can be particularly useful for confined, restricted and/or dangerous areas where no direct access by people is possible.

The broad absorption spectrum of black LMs allows for the variation of the excitation wavelengths. Sunlight provides free, affordable, inexhaustible and clean energy,[32] and sunlight focused with a magnifying glass can be used as alternative light source and provide efficient and environmentally friendly movement of black LMs. Figure 4a and Movie 6 (Supporting Information) show two CB LMs pushing a boat with exemplary reagents. The boat was loaded with 2 × 60 µl of dyed water and had a total weight of 0.39 g. Focused sunlight was applied alternately to each LM, which resulted in an on-demand meandering motion of the boat. Figure 4b shows the relationship between the tilt angle of the boat based on the horizontal axis and time depending on the application of focused sunlight on each LM. Application of sunlight on the left LM based on traveling direction led the boat bow to tilt to the right and vice versa. There was a lag (≈2 s) between the time when the sunlight started to irradiate the LM and that when the angle of boat bow changed due to Newton's first law of motion, the law of inertia.

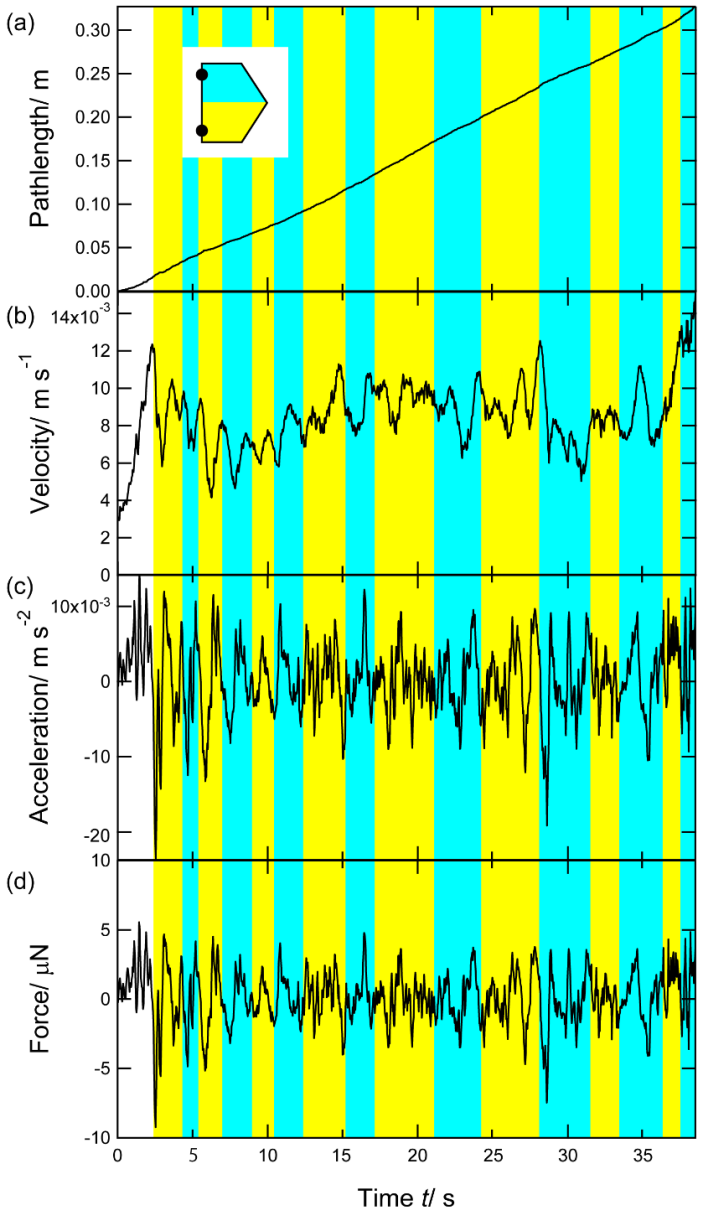


Figure S9: Analysis of the sun light-driven boat carrying 2×60 µl of dyed water droplets (Supporting Movie 6). a) Pathlength vs. time, b) velocity, c) acceleration and d) force profiles of the boat. The CB-stabilized LMs were irradiated using sunlight. The yellow and cyan shaded areas correspond to the irradiation period when the laser was irradiated to the upper and lower parts of the boats shown in the inset.

It takes time to change the direction of the boat in motion by the application of an external unbalanced force. Analyses of the movie indicated that the maximum velocity and acceleration of the plastic boat were ≈$1.2\times10^{-2}$ m/s and $1.4\times10^{-2}$ m/s$^2$, respectively, and the maximum force was calculated to be ≈5 µN

(Figure S9), which was comparable to those of the single LM and the plastic boat carrying multiple LMs.

The results demonstrate the conversion of sunlight directly into work through thermal surface tension gradients without energy collection and storage, which are compulsory for photovoltaic systems.[33]

## 5.4 Conclusions

We have described the light-driven transportation of LMs and the on-demand and on-site disruption of the LMs by an external stimulus to release the inner materials. Furthermore, the LM can be used as a light-driven towing engine to carry loads. The LM stabilizer building blocks are not limited to PPy and CB. A variety of other types of building blocks, including carbon nanotubes, graphene, fullerenes and conducting polymers, can be utilized; their size, shape and bulk and surface morphology are well designed and controlled. The versatility of light sources presents an advantage over other optical techniques, such as optical trapping. The simplicity and variety of these LM stabilizers and light sources will enable in-depth synergistic experimental and theoretical investigations geared toward the understanding and utilization of a new class of delivery and release system. In the future, a wide variety of applications can be explored, including light-controlled microfluidics and drug delivery systems.

## 5.5 Experimental section

**Materials:** Pyrrole (Py), octanoic acid and aluminum oxide activated, basic, Brockmann I (~#150 mesh, pore size: 58 Å, surface area: 155 $m^2$/kg) were purchased from Sigma-Aldrich (St. Louis, MO, USA). Iron(III) chloride hexahydrate was obtained from Wako Pure Chemical Industries Ltd. (Osaka, Japan). Carbon Black (CB, acetylene, 50% compressed, 99.9+%, S.A.: 75 $m^2$/g, bulk density: 80-120 g/L) was obtained from Alfa Aesar (Lancashire, UK). Deionized water (<0.06 µS $cm^{-1}$) was prepared using a deionized water-producing apparatus (MFS RFD240NA: GA25A-0715, Advantec Co. Ltd., CA, USA). Pyrrole was passed through activated aluminum oxide for purification.

Dyes (Brilliant Blue FCF, Sunset Yellow FCF and acid red) were kindly donated from San-Ei Gen F.F.I., Inc., and used as received. All other chemicals were used as received. A laser with a nominal wavelength of 808 nm and an output power of less than 200 mW (GLP-808-200 mW 13067032) was purchased from Changchun New Industries Optoelectronics Tech., Co. Ltd. (Changchun, China). A magnifying glass (f=10 cm) was used for sunlight-driven movement studies.

**Synthesis of PPy:** All reactions were conducted under ambient conditions. First, Py (3.00 ml, 43.4 mmol) was dissolved in 100 ml of $H_2O$ in a 500 ml round bottom flask under continuous stirring at 500 rpm using a magnetic stirrer bar. The monomer fully dissolved within 2 h. In parallel, iron (III) chloride hexahydrate (27.38 g, 101.3 mmol) was dissolved in 66 ml of water. The stirring speed of the Py solution was adjusted to 250 rpm, and the $FeCl_3$ aqueous solution was added within less than 1 min. Immediately, the Py reaction mixtures turned from transparent to dark green and then to black. The polymerization was conducted for 15 h. For purification, the suspension was centrifuged in $H_2O$ five times at 4,800 rpm for 20 min. The wet product was freeze-dried for 4 days. Finally, the dry powder was pulverized for 10 min using a mortar and pestle.

**Hydrophobization of PPy:** The hydrophilic PPy was hydrophobized by anion exchange of chloride against the octanoic acid anion. For this purpose, PPy (0.56 g) was suspended in 50 ml of $H_2O$. In parallel, octanoic acid (1.05 g, 7.3 mmol) and NaOH (0.29 g, 7.3 mmol) were dissolved in 88 ml of $H_2O$ within less than 1 h. The dissolved, neutralized acid was added to the suspended PPy, and the reaction mixture was mixed for 5 min at 2,000 rpm and subsequently defoamed for 10 min at 2,200 rpm using a planetary centrifugal Mixer ARE-310 (Thinky, Tokyo, Japan). Finally, the suspension was centrifuged three times at 4,800 rpm for 20 min in $H_2O$. The wet product was freeze dried for three days. After drying, the powder was hydrophobic. The dry powder was ground with a mortar with a pestle for 10 min.

**Contact angle measurement:** CB and PPy powder samples were prepared by finger-tight pressing of the respective powder between two glass slides. Static contact angles of water droplets (10 µl) were determined 10 s after deposition on the samples using an Excimer SImage02 apparatus at 25 ˚C.

**Preparation of LMs:** CB and hydrophobic PPy powder were slightly compacted in glass Petri dishes, and 10 µl water drops were rolled on the powder for 1 min. The hydrophobic powder adsorbed at the air-water interface of the drop to create a LM. Finally, the LM was carefully placed at the air-water interface. Depending on the experiment, Petri dishes, boats of 42×44×8 $cm^3$ (IR measurements) and 10×75×60 $cm^3$ (sun light induced boat movement) or water films on poly(methyl methacrylate) glass were used as containers.

**Light-controlled movement:** The light was manually directed sideways onto the LMs, aiming for three-phase contact. The angle of irradiation played a crucial role. An angle of up to 45° was most efficient at propelling the marble. At 90°, i.e., vertical irradiation, the LM typically remained stationary. Accurate laser positioning on the three-phase contact was difficult using hands, which should cause fluctuation of velocity and acceleration of LM locomotion. To simplify aiming at the LM, an NIR laser detection sheet was placed underneath the Petri dishes and acrylic glass (IR sensor card 800-1600 nm, LDT-008, Laser Components GmbH, Olching, Germany). (Note that the visible laser dot stems from the laser detection sheet which was underneath the water bath. Whenever the laser light did not hit the LM to be converted in heat it was converted to visible light by hitting the laser detection sheet. The shift in perspective of the visible laser dot and the liquid marble results from the upper back side illumination of the LM and the height difference between the LM floating on the water bath and the laser detection sheet.) A digital video camera (Sony Handycam HDR-CX270 V; 30x optical zoom lens, Sony Co., Tokyo, Japan) was used to record movies and photographic images of the LMs, and their locomotion was recorded using a digital camera (Ricoh G700SE; 5.0x optical zoom lens, Ricoh, Tokyo, Japan).

**Software:** The movies were analyzed using a commercial software (Keyence VW-9000 MotionAnalyzer, Keyence, Osaka, Japan) to obtain velocity, acceleration and applied force. Using this software, we first determined the position of the center of mass of the objects every frame, $r(t)$ Next, we obtained the finite difference of the position (displacement), $\Delta r(t)$ from the time course of $r(t)$, and the velocity $v(t) = \Delta r(t)/\Delta t$ where $\Delta t$ is the video rate (1/30 s). From the finite difference of $v(t)$ we obtained $\Delta v(t)$, the acceleration $a(t) = \Delta v(t)/\Delta t$, and the force $F(t) = ma(t)$, where $m$ is the mass of the object. We thus

evaluated the velocity, acceleration and force. The magnitude of $F(t)$was obtained from the $F(t)$ vs. $t$ plot. Furthermore, we determined the work applied on the object, $W$ from the $F(t)$ vs. $r(t)$ plot. Particularly, $W$ was evaluated from the area of a peak in the plot.

## 5.6 Acknowledgment

We thank Dr. Doris Vollmer and Dr. Michael Kappl for discussion. M.P. carried out the experiments with respect to the synthesis of the hydrophobic PPy powder, photo-thermal character analysis of the powder and liquid marbles, and light-driven liquid marble locomotion experiments. T.S. carried out the morphology characterization of the powders and contact angle measurements. H.M. conducted dynamic image analysis and characterized locomotion of the liquid marbles. S.F. organized the project and had the idea for the light-driven locomotion of the LMs. S.F., M.P. and H.M. wrote the manuscript. All authors discussed the results and edited the manuscript. This work was partially supported by JSPS-DAAD Bilateral Joint Research Projects and by a Grant-in-Aid for Scientific Research on Innovative Areas “Engineering Neo-Biomimetics (No. 15H01602)”, “New Polymeric Materials Based on Element-Blocks (No. 15H00767)”, “Molecular Robotics (No. 15H00791)” and “Molecular Soft Interface Science (No. 23106720)” from the Ministry of Education, Culture, Sports, Science, and Technology of Japan. H.J.B. wishes to thank the ERC for the advanced grant 340391-SUPRO.

## 5.7 References

[1] a) G. A. Ozin, I. Manners, S. Fournier-Bidoz, A. Arsenault, Adv. Mater. **2005**, 17, 3011-3018; b) J. Wang, ACS Nano **2009**, 3, 4-9; c) T. Mirkovic, N. S. Zacharia, G. D. Scholes, G. A. Ozin, ACS Nano **2010**, 4, 1782-1789; d) D. Yamamoto, A. Shioi, KONA Powder Particle J. **2015**, 32, 2-22; e) H. Wang, M. Pumera, Chem. Rev. **2015**, 115, 8704-8735; f) S. Sánchez, L. Soler, J. Katuri, Angew. Chem. Int. Ed. **2015**, 54, 1414-1444; Angew. Chem. **2015**, 127, 1432-1464.

[2] a) R. F. Ismagilov, A. Schwartz, N. Bowden, G. M. Whitesides, Angew. Chem. Int. Ed. **2002**, 41, 652-654; Angew. Chem. **2002**, 114, 674-676; b) S. Fournier-Bidoz, A. C. Arsenault, I. Manners, G. A. Ozin, Chem. Commun. **2005**, 441-443;

c) T. R. Kline, W. F. Paxton, T. E. Mallouk, A. Sen, Angew. Chem., Int. Ed. **2005**, 44, 744-746; Angew. Chem. **2005**, 117, 754-756

[3] S. T. Chang, V. N. Paunov, D. N. Petsev, O. D. Velev, Nat. Mater. **2007**, 6, 235-240.

[4] K. Ishiyama, M. Sendoh, A. Yamazaki, K. I. Arai, Sensors Actuat. A **2001**, 91, 141-144.

[5] a) A. Würger, J. Fluid Mech. **2014**, 752, 589-601; b) D. E. Lucchetta, F. Simoni, L. Nucara, R. Castagna, AIP Adv. **2015**, 5, 077147-1-5.

[6] G. Billard, C. C. Bruyant, R. Soc. Biol. **1905**, 59, 102-103.

[7] S. Nakata, J. Kirisaka, Y. Arima, T. Ishii, J. Phys. Chem. B **2006**, 110, 21131-21134.

[8] C. Vivian, Soap boats. In Science experiments & amusement for children, Dover publications Inc., New York, USA **1963**.

[9] H. Zhang, W. Duan, L. Liu, A. Sen, J. Am. Chem. Soc. **2013**, 135, 15734-15737.

[10] a) H. Jin, A. Marmur, O. Ikkala, R. H. A. Ras, Chem. Sci. **2012**, 3, 2526-2529; b) G. Zhao, T. H. Seah, M. Pumera, Chem. Eur. J. **2011**, 17, 12020-12026.

[11] a) D. Okawa, S. J. Pastine, A. Zettl, J. M. J. Fréchet, J. Am. Chem. Soc. **2009**, 131, 5396-5398; b) A. Diguet, R.-M. Guillermic, N. Magome, A. Saint-Jalmes, Y. Chen, K. Yoshikawa, D. Baigl, Angew. Chem. Int. Ed. **2009**, 48, 9281-9284; Angew. Chem. **2009**, 121, 9445-9448; c) M. Xiao, C. Jiang, F. Shi, NPG Asia Mater. **2014**, 6, e128.

[12] a) P. Aussillous, D. Quéré, Proc. R. Soc. A **2006**, 462, 973-999; b) L. C. Gao, T. J. McCarthy, Langmuir **2007**, 23, 10445-10447; c) S. Fujii, R. Murakami, KONA Powder Particle J. **2008**, 26, 153-166; d) E. Bormashenko, Curr. Opin. Colloid Interface Sci. **2011**, 16, 266-271; e) D. Matsukuma, H. Watanabe, H. Yamaguchi, A. Takahara, Langmuir **2011**, 27, 1269-1274; (f) G. McHale, M. I. Newton, Soft Matter **2015**, 11, 2530-2546.

[13] a) M. Dandan, H. Y. Erbil, Langmuir **2009**, 25, 8362-8367; b) E. Bormashenko, R. Pogreb, A. Musin, R. Balter, G. Whyman, D. Aurbach, Powder Technol. **2010**, 203, 529-533; c) M. D. Doganci, B. U. Sesli, H. Y. Erbil, B. P. Binks, I. E. Salama, Colloids Surfaces A **2011**, 384, 417-426.

[14] N. Pike, D. Richard, W. Foster, L. Mahadevan, Proc. R. Soc. B **2002**, 269, 1211-1215.

[15] a) P. Aussilious, D. Quéré, Nature **2001**, 411, 924-947; b) E. Bormashenko, Y. Bormashenko, R. Grynyov, H. Aharoni, G. Whyman, B. P. Binks, J. Phys. Chem. C **2015**, 119, 9910-9915; c) C. H. Ooi, A. van Nguyen, G. M. Evans, O. Gendelman, E. Bormashenko, N.-T. Nguyen, RSC Adv. **2015**, 5, 101006-101012.

[16] a) C. Dampeirou, WO Patent. 2005, 034917; b) K. M. Lahanas, U.S. Patent. **2001**, 6290941.

[17] a) E. Bormashenko, R. Pogreb, Y. Bormashenko, A. Musin, T. Stein, Langmuir **2008**, 24, 12119-12122; b) J. R. Dorvee, M. J. Sailor, G. M. Miskelly, Dalton Trans. **2008**, 6, 721-730.

[18] a) Y. Xue, H. Wang, Y. Zhao, L. Dai, L. Feng, X. Wang, T. Lin, Adv. Mater. **2010**, 22, 4814-4818; b) T. Arbatan, A. Al-Abboodi, F. Sarvi, P. P. Y. Chan, W. Shen, Adv. Health. Mater. **2012**, 1, 467-469; c) Y.-E Miao, H. K. Lee, W. S. Chew, I. Y. Phang, T. Liu, X. Y. Ling, Chem. Commun. **2014**, 50, 5923-5926; d) Y. Chu, Z. Wang, Q. Pan, ACS Appl. Mater. Interfaces **2014**, 6, 8378−8386; e) Y. Zhao, Z.

Xu, H. Niu, X. Wang, T. Lin, Adv. Funct. Mater. **2015**, 25, 437-444; f) Y. Sheng, G. Sun, J. Wu, G. Ma, T. Ngai, Angew. Chem. Int. Ed. **2015**, 54, 7012-7017; Angew. Chem. **2015**, 127, 7118-7123; g) W. Gao, H. K. Lee, J. Hobley, T. Liu, I. Y. Phang, X. Y. Ling, Angew. Chem. Int. Ed. **2015**, 54, 3993–3996; Angew. Chem. **2015**, 127, 4065-4068.

[19] T. Arbatan, L. Li, J. Tian, W. Shen, Adv. Health. Mater. **2012**, 1, 80-83.

[20] a) E. Bormashenko, A. Musin, Appl. Surf. Sci. **2009**, 255, 6429-6431; b) J. Tian, T. Arbatan, X. Li, W. Shen, Chem. Commun. **2010**, 46, 4734-4736; c) V. Sivan, T. Shi-Yang, P. A. O'Mullane, P. Petersen, N. Eshtiaghi, K. Kalantar-zadeh, A. Mitchell, Adv. Funct. Mater. **2013**, 23, 144-152; d) K. Ueno, G. Bournival, E. J. Wanless, S. Nakayama, E. C. Giakoumatos, Y. Nakamura, S. Fujii, Soft Matter **2015**, 11, 7728-7738.

[21] H. Zeng, Y. Zhao, Appl. Phys. Lett. **2010**, 96, 114104.

[22] W. Wang, C. L. Bray, D. J. Adams, A. I. Cooper, J. Am. Chem. Soc. **2008**, 130, 11608-11609.

[23] S. Fujii, S. Sawada, S. Nakayama, M. Kappl, K. Ueno, K. Shitajima, H.-J. Butt, Y. Nakamura, Mater. Horiz. **2016**, 3, 47-52.

[24] a) F. Li, M. A. Winnik, A. Matvienko, A. Mandelis, J. Mater. Chem. **2007**, 17, 4309-4315; b) K. M. Au, M. Chen, S. P. Armes, N. Zheng, Chem. Commun. **2013**, 49, 10525; (c) J. E. Minardi, H. N. Chuang, Sol. Energy **1975**, 17, 179-183

[25] L. Liu, E. Tüzel, J. L. Ross, J. Phys. Cond. Mat. **2011**, 23, 374104

[26] a) D. Dupin, S. P. Armes, S. Fujii, J. Am. Chem. Soc. **2009**, 131, 5386-5387; b) S. Fujii, S. Kameyama, D. Dupin, S. P. Armes, M. Suzaki, Y. Nakamura, Soft Matter **2010**, 6, 635-640; c) L. Zhang, D. Cha, P. Wang, Adv. Mater. **2012**, 24, 4756-4760; d) Z. Xu, Y. Zhao, L. Dai, T. Lin, Part. Part. Syst. Charact. **2014**, 31, 839-842.

[27] S. Yusa, M. Morihara, K. Nakai, S. Fujii, Y. Nakamura, A. Maruyama, N. Shimada, Polym. J. 2014, 46, 145-148.

[28] K. Nakai, S. Fujii, Y. Nakamura, S. Yusa, Chem. Lett. **2013**, 42, 586-588.

[29] Y. Zhao, J. Fang, H. Wang, X. Wang, T. Lin, Adv. Mater. **2009**, 21, 1-4.

[30] P. A. Kralchevsky, K. Nagayama, Adv. Colloid Interface Sci. **2000**, 85, 145-192.

[31] D. Zang, J. Li, Z. Chen, Z. Zhai, X. Geng, B. P. Binks, Langmuir **2015**, 31, 11502-11507.

[32] T. Seba, Solar trillions: 7 Market and investment opportunities in the emerging clean-energy infrastructure, Tony Seba, CA, USA **2010**.

[33] A. Hagfeldt, M. Gratzel, Acc. Chem. Res. **2000**, 5, 269-277.

## 5.8 Further supporting information

**Supporting Videos** can be downloaded from:

http://onlinelibrary.wiley.com/doi/10.1002/adfm.201600034/epdf

**SEM studies** (Keyence VE-8800, 12 kV) were conducted with Au sputter-coated (Elionix SC-701 Quick Coater) dried samples.

**Calculation of the energy conversion efficiency from light to heat:**

1. Energy of a photon $E_{photon}$

$$E_{photon} = h\nu = \frac{hc}{\lambda} \qquad \text{(eq. 5.1)}$$

where $h$ is the Planck constant, $c$ is the velocity of light and $\lambda$ is wavelength. Now, $\lambda$ = 808 nm.

$$E_{photon} = \frac{hc}{\lambda} = \frac{6.626 \times 10^{-34}\ \mathrm{J \cdot s} \times 2.998 \times 10^{8}\ \mathrm{m/s}}{808 \times 10^{-9}\ \mathrm{m}} = 2.46 \times 10^{-19}\ \mathrm{J}$$

2. Temperature increase per photon

The theoretical temperature increase *T* per photon is

$$T = \frac{E_{photon}}{k_B} = \frac{2.46 \times 10^{-19}\ \mathrm{J}}{1.38 \times 10^{-23}\ \mathrm{J/K}} = 1.78 \times 10^{4}\ \mathrm{K} \qquad \text{(eq. 5.2)}$$

3. Conversion efficiency from light to heat $\eta$

When irradiated, the maximum temperature of bulk CB and PPy were about 1200 K. The efficiency $\eta$ is

$$\eta = \frac{1200}{17800} = 0.067$$

Therefore, $\eta$ is 6.7 %.

**Plastic boat:**

The plastic boats for dragging pulling experiments were fabricated using dimension bst768 (Stratasys, USA) 3D printer and FDM ABS-P400$^{TM}$ Model (white) cartridge (Stratasys, USA) with the aid of CatalystEX software. The shapes of the boats were designed using Creo 2.0 3D CAD software (PTC Inc.).

**Thermographic analysis:**

Thermographic analysis was conducted with a thermal imager 890-2 from Testo (Lenzkirch, Germany).

**Analysis, equation and mechanism of locomotion:**

The difference in surface tension between the laser irradiation side and its opposite side works as a driving force for liquid marbles to move on the air-water interface. Once a liquid marble moves, friction occurs between the liquid marble and the fluid because of the fluid's viscosity. Considering the driving and the friction forces, it is possible to understand the locomotion of the small object (liquid marble and boat). In the following discussion, we mention the driving force, the friction force and the equation of locomotion step by step.

The driving force $F_{driving}$ is

$$F_{driving} = (\gamma_{lowT} - \gamma_{highT})w = \Delta\gamma w \qquad \text{(eq. 5.3)}$$

where $\gamma_{highT}$ and $\gamma_{lowT}$ are the surface tensions of air-water interface of laser irradiation side (relatively high temperature) and its opposite side (relatively low temperature), respectively, $\Delta\gamma = \gamma_{lowT} - \gamma_{highT}$ and $\gamma_{lowT} > \gamma_{highT}$. From $\Delta\gamma$ and the diameter of liquid marble ($w =$ 2.67 mm), it is possible to estimate the magnitude of $F_{driving}$. Since the force generated from the surface tension gradient is the product of surface tension difference and width of the laser-irradiated spot because surface tension is force by length (P.-G. de Gennes, F. Brochard-Wyart, D. Quéré, Capillary and Wetting Phenomena –Drops, Bubbles, Pearls, Waves-, Springer, **2003**, p. 5), $F_{driving}$ is calculated to be in the order of $10^{-6}$ N.

On the other hand, the friction force $F_{friction}$ is described by Newton's law of viscosity.

$$F_{friction} = \zeta v = \frac{\eta S v}{h} \qquad \text{(eq. 5.4)}$$

where $\eta$ is the viscosity of fluid, $S$ is the contact area between fluid and the object, $h$ is the thickness of fluid and $\zeta$ is the decay constant. The decay constant $\zeta$ is

$$\zeta = \frac{\eta S}{h} \qquad \text{(eq. 5.5)}$$

Considering $F_{driving}$ and $F_{friction}$, we get the equation of locomotion as

$$m\frac{d^2x}{dt^2} = F_{driving} - F_{friction} \qquad \text{(eq. 5.6)}$$

where $m$ is the mass of the small object.

**Temperature of liquid marbles at the air-water interface:**

Temperature analysis was conducted thermographically. In our setup, we were restricted to top-view analysis. Hence, precise thermographical analysis of the three-phase contact line of the irradiated LMs was not possible. The temperature of an irradiated liquid marble was traced as a function of the irradiation/propulsion time. Typically, temperatures in the range of 35-50 °C were measured. Seldom, peak values of *ca.* 100-150 °C were observed. On one hand, the real temperature at the three-phase contact might be higher than the observed range of 35-50 °C since the point of irradiation is shielded to thermography by most of the liquid marble. On the other hand, we assume the temperature at the three-phase contact line must be smaller than the observed peak values arising when the liquid marble is accidently irradiated from the top by human misplacement of the laser beam. This is conclusive since irradiation at or below the three-phase contact line allows the heat to efficiently dissipate into the bulk water as observed by thermography (Figure 2). This dissipated heat finally is the source of the observed Marangoni propulsion.

# 6 Conclusion

This thesis deals with three approaches, i.e. super liquid-repellent surfaces, the Leidenfrost effect and liquid marbles, to fabricate and manipulate non-wetting surfaces and drops. The key concept to obtain non-wettability in all three approaches is based on the entrapment of air pockets between the substrate and the drops. Four contributions are presented, which address recent developments in the mechanical refinement of super liquid-repellent surfaces and demonstrate new strategies for the manipulation of drops using the Leidenfrost effect and liquid marbles.

i) A technique based on a colloidal indenter mounted to a scanning probe microscope was successfully used to mechanically test candle soot-based super liquid-repellent surfaces. Quantitative values, like the effective elastic modulus, were obtained and compared to wetting measurements. In this specific case, the indentation technique allowed the careful balance of mechanical strength against wetting properties based on the reaction parameters of the surface. The study also shows that this technique and the analysis of the data is rather work intensive and not straight forward. Anyhow, the test proved to be valuable to refine the preparation process in the presented study and exposed the influence of the different reaction parameters on the mechanical strength. This technique might also be adaptable and helpful to differentiate surfaces of comparable mechanical strength, porosity and coating thickness, what still needs to be confirmed.

ii) Watery, drop shaped particles jumped from a smooth substrate if the temperature of the substrate was quickly ramped up. This was attributed to the violent boiling and splashing of the water meniscus around the objects at elevated temperatures. If the object was a highly water loaded hydrogel, it could repeatedly bounce thereafter. This is especially true if the hydrogel possessed a certain elasticity. In this case, the hydrogel even jumped at increasingly higher heights. Too soft hydrogels behaved more like liquid drops, whereas too stiff particles behaved like inelastic solids upon bouncing. Repeated bouncing was attributed to evaporation of water from the hydrogel, similarly to the Leidenfrost effect, which led to an upward force when the gel contacted the surface.

iii) Finally, photo-thermally responsive liquid marbles were prepared and successfully propelled over the water-air interface. A beam of light shot at the liquid marbles was converted to heat by the powder shell and dissipated into the liquid. This caused a heat-based Marangoni flow on the water surface close to the liquid marble and led to efficient propulsion of the liquid marble. This way, a light beam can be indirectly used to determine the movement of liquid marbles in space and time. Furthermore, the inner content was on-demand released by an external trigger, e.g. light or pH. This was used to detect iron ions dissolved in the water underneath the liquid marble by releasing a KSCN solution: When the liquid marble was broken, blood red precipitate formed under it due to the formation of $Fe(SCN)_3$. In a different application, light-driven liquid marbles were used to push millimetric objects floating at the air-water interface, similar to a towing engine. In this sense, light-driven liquid marbles proved to be very efficient to propel µl sized drops and millimetric objects over the air-water interface. Implementation of the presented concept into a practical application is yet to be shown.

Overall, super liquid-repellent surfaces, the Leidenfrost effect and liquid marbles are three efficient approaches to yield low adhesion, mobile drops based on entrapped air cushions between substrate and drop. The presented work contributed to current demands and needs. It is certain that these research fields have much more fascinating details and applications for us to come in the future.

# 7 Appendix

## 7.1 Supplement information to chapter 1.2.9: Brief overview of contact mechanics to analyse force-sensitive measurements

Data obtained from force-displacement experiments can be interpreted in different ways, depending on the characteristics of the surface.[110, 111] In an ideal case, the interaction between the two objects is purely elastic. In this case the approach and retract curve overlap. This was described by Hertz for two spheres which are being pressed together.[112] He related the force ($F_H$) acting on the spheres, the indentation depth $h_{max,\ Hertz}$, the contact radius $a$ and the radius $R$ of the spheres to the effective elastic modulus $E_{eff}$ :

$$F_H = \frac{4E^* a^3}{3R} \qquad \text{(eq. 7.1)}$$

And the indentation depth $h_{max,\ Hertz}$ is

$$h_{max,\ Hertz} = \frac{a^2}{R} \qquad \text{(eq. 7.2)}$$

Combining eq. 7.1 and eq. 7.2 leads to a relationship between $E_{eff}$, $F$ and $h$. Using this equation, the effective elastic modulus can be measured by deformation of the spheres when the applied load is known.

$$F = \frac{4\sqrt{R}}{3} \cdot h^{\frac{3}{2}} \cdot E_{eff} \qquad \text{(eq. 7.3)}$$

Equally, $E_{eff}$ is obtained from the slope S of the retract curve in Figure 21, which corresponds to the derivative $\frac{dF}{dh}$.

$$S = \frac{dF}{dh} = \frac{2}{\sqrt{\pi}} E_{eff} \sqrt{A} \qquad \text{(eq. 7.4)}$$

The effective elastic modulus $E_{eff}$ is a mixed value of both bodies interacting. It depends on the Poisson's ratios, $\nu_1$ and $\nu_2$ and the elastic moduli $E_1$ and $E_2$ of the respective bodies:

$$\frac{1}{E_{eff}} = \frac{(1-\nu_1^2)}{E_1} + \frac{(1-\nu_2^2)}{E_2} \qquad \text{(eq. 7.5)}$$

Often, the contact is not purely elastic and non-negligible adhesive forces are involved. Adhesive contact can lead to the formation of a “neck” when a sphere is retracted from a plane surface. Based on the Hertzian equation two theories to describe adhesive contact were developed. The first is the JKR theory, named after Johnson, Kendall and Roberts and the second is the DMT theory, named after Dejarguin, Müller and Toporov.

The JKR theory extends the Hertz theory by adding an additional term for the balance between stored elastic energy and the corresponding loss in surface energy $\gamma$ when the sphere is retracted.[113] The theory considers the effect of contact pressure and adhesion within the contact area and it applies for relatively soft materials were strong, short-ranged interaction forces are present.

The force $F_{JKR}$ is related to the indentation depth and contact radius as:

$$F_{JKR} = \frac{4E_{eff}\, a^3}{3R} - \sqrt{8\pi a^3 E_{eff}\, \gamma} \qquad \text{(eq. 7.6)}$$

The indentation $h_{JKR}$ is:

$$h_{max,\ JKR} = \frac{a^2}{R} - \sqrt{\frac{2\pi\gamma}{E_{eff}}} \qquad \text{(eq. 7.7)}$$

Rearrangement of eq. 7.6 leads to the contact radius

$$a^3 = \frac{3R}{4E_{eff}}\left(F_{JKR} + 3\pi\gamma R + \left(6\pi\gamma R F_{JKR} + (3\pi\gamma R)^2\right)^{1/2}\right) \qquad \text{(eq. 7.8)}$$

The DMT theory applies for relatively stiff materials and it assumes a weak interaction between sphere and material.[114, 115] Unlike the JKR theory, the DMT theory considers attractive interaction not inside but in the close proximity outside of the contact area.

In this case, the force $F_{DMT}$ is given as:

$$F_{DMT} = \frac{4E_{eff}\, a^3}{3R} - 2\pi\gamma R \qquad \text{(eq. 7.9)}$$

And the indentation $h_{max,\ DMT}$ is equal to $h_{max,\ Hertz}$. This finally relates to the contact radius as:

$$a^3 = \frac{3R}{4E_{eff}}\left(F_{DMT} + 2\pi\gamma R\right) \qquad \text{(eq. 7.10)}$$

Whereas mechanical testing of continuous materials such as braking systems or train wheels contacting rails is rather well established and understood, mechanical testing of very rough surfaces remains a challenge. Especially, the analysis of force sensitive measurements is not trivial. The real contact area $A$ is much smaller if a rough surface is indented compared to the nominal contact area $A_0$ of perfectly smooth surfaces interacting.

Greenwood and Williamson approximated this problem by considering a surface which is randomly rough on one length scale.[116] Upon making the assumption that the height $x$ of the asperities follows a Gaussian distribution $P_x$, that the asperities are not too close to each other and that their contact is purely elastic, it is possible to treat every asperity contact as an individual Hertz contact. Provided that the surface roughness is well characterized and the height profile is known, the nominal squeezing stress $\sigma_0$, which is the nominal Force $F_N$ divided by the nominal area $A_0$, is given as:[110, 116]

$$\sigma_0 = \frac{F_N}{A_0} = \frac{4E}{3(1-\nu_1^2)} n_0 \int_\delta^\infty dx(x-h)^{3/2} \sqrt{R} P_x \qquad \text{(eq. 7.11)}$$

Where $n_0$ is the number of asperities per unit area. In this form and for simplicity, it is assumed, that the top part of the asperities are spherically shaped and have a constant radius $R$. Asperities which have a height of $x > h$ will then make contact at an indentation depth $h$.

Thereafter, Fuller and Tabor incorporated adhesive interaction between probe and surface asperities by replacing Hertz contact mechanics against JKR contact mechanics.[117]

Bush, Gibson and Thomas refined the Greenwood and Williamson model by considering roughness to occur on different length scales.[118, 119] As long as the real contact area $A$ is much smaller than the nominal contact area $A_0$, the stress distribution at the interface is constant. This means that the real contact area $A$ increases with increasing load $F_N$ for the case that $A$ is much smaller than $A_0$. The mathematical treatment and assumptions are similar to the Greenwood and Williamson theory but the asperities are assumed to have a parabolic shape. Perrson accounted for the opposite case, when a firm contact between probe and rough surface is established, i.e. when $A$ is close to $A_0$.[110]

The above-mentioned cases consider that the interaction between probe and surface is elastic, i.e. reversible. In reality, many materials deform plastically, i.e. they yield, once a critical yield stress $\sigma_Y$ is exceeded.[110, 120]

One quantity to characterize surfaces, which deform elastically and plastically, is the hardness $H$. $H$ is given as:[67]

$$H = \frac{F_{max}}{A_{res}} \qquad \text{(eq. 7.12)}$$

Here, $A_{res}$ is the residual area after the indentation process due to plastic deformation of the surface. $H$ is practical to classify a material as long as the indent is large enough and the surface smooth enough to clearly determined $A_{res}$. This becomes non-trivial if $A_{res}$ becomes small and/or the surface roughness becomes high, especially in the case of rough surfaces.

Following the concepts from above, the asperities of a rough surface first respond elastically to an imposed force and then yield once the yield stress $\sigma_Y$ is exceeded. The load is then carried by a mixed contact area, which is partially elastically and plastically deformed. The normal force acting on the elastically deformed contact area $F_{el}(\zeta)$ is given by: [110, 120]

$$F_{el}(\zeta) = A_0 \int_0^{\sigma_Y} d\sigma \; \sigma \; P(\sigma, \zeta) \qquad \text{(eq. 7.13)}$$

Whereas $P(\sigma, \zeta)$ is the stress distribution at the interface. $\zeta = L/\lambda$ is the so-called magnification. $L$ is the diameter of the nominal contact area between the two bodies and $\lambda$ is the shortest surface roughness feature which can be resolved at magnification $\zeta$.

Overall, force sensitive measurements on not too rough surfaces are practical to understand and classify material properties. Rough surfaces can also be included if the surface texture is well characterized and the asperities respond elastically. The work and effort to analyze force sensitive data strongly increase if the texture cannot be well-described and the asperities break at low yield stress. This is also why no standardized protocol and technique is found for such surfaces. If the specimen is isotropic and thick enough an averaged mechanical response can be obtained by choosing high indentation depths. This way, the influence of the roughness on the averaged mechanical response can be reduced.

# 8 List of publication

## 8.1 Original paper

1. Butt H.-J., **Paven M.**, Steffen W., Vollmer D. Warum der Tropfen nicht hält. Nachrichten aus der Chemie **2016**, 64, 10, 945-951.

2. Schmüser L., Encinas N., **Paven M.**, Graham D. J., Castner, D. G., Vollmer D., Butt H.-J., Weidner T. Candle soot-based super-amphiphobic coatings resist protein adsorption. Biointerphases **2016**, 11 (3), 031007.

3. **Paven M.**, Fuchs R., Yakabe T., Vollmer D., Kappl M., Itakura A. N., Butt H.-J. Mechanical properties of highly porous super liquid-repellent surfaces. Adv. Funct. Mater. **2016**, 4914-4922.

4. Harrold V. C., **Paven M.**, Vollmer D., Sharp J. S. Rheological properties of viscoelastic drops on superamphiphobic substrates. Langmuir **2016**, 32 (16), 4071-4076.

5. **Paven M.**, Mayama H., Sekido T.; Butt H.-J., Nakamura Y., Fujii S. Light-driven delivery and release of materials using liquid marbles. Adv. Funct. Mater. **2016**, 26 (19), 3199-3206.

6. Wooh S., Huesmann H., Tahir M. N., **Paven M.**, Wichmann K., Vollmer D., Tremel W., Papadopoulos P., Butt H.-J. Synthesis of mesoporous supraparticles on superamphiphobic surfaces. Adv Mater **2015**, 27 (45), 7338-7343.

7. Shi C., Cui X., Zhang X., Tchoukov P., Liu Q.; Encinas N., **Paven M.,** Geyer F., Vollmer D., Xu Z., Butt H.-J., Zeng, H. Interaction between air bubbles and superhydrophobic surfaces in aqueous solutions. Langmuir. **2015**, 31 (26), 7317-7327.

8. **Paven M.**, Papadopoulos P., Mammen L., Deng X., Sachdev H., Vollmer D., Butt H.-J. Optimization of superamphiphobic layers based on candle soot. Iupac. **2014**, 86 (2), 87-96.

9. **Paven M.**, Papadopoulos P., Schöttler S., Deng X., Mailänder V., Vollmer D., Butt H.-J. Super liquid-repellent gas membranes for carbon dioxide capture and heart–lung machines. Nat Commun. **2013**, 4.

10. Deng X., **Paven M.**, Papadopoulos P., Ye M., Wu S., Schuster T., Klapper M., Vollmer D., Butt H.-J. Solvent-free synthesis of microparticles on superamphiphobic surfaces. Angew Chem Int Edit. **2013,** 52 (43), 11286-11289.

**In preparation:**

Pham J., **Paven M.**, Kajiya T., Vollmer D., Butt H.-J., Spontaneous jumping and long-lasting bouncing of hydrogel drops from a superheated surface.

Mayama H., **Paven M.,** Butt H.-J., Nakamura Y., Fujii S. Friction in locomotion of liquid marble on air-water and air-solid interfaces.

## 8.2 Books

1. **Paven, M.**; Mammen, L.; Vollmer, D. CHAPTER 8 Challenges and opportunities of superhydrophobic/superamphiphobic coatings in real applications. In “Smart Materials for Advanced Environmental Applications”; the Royal Society of Chemistry, **2016**, pp 209-243.

## 8.3 Patent applications

1. Butt H.-J., Vollmer D., **Paven M.**, Deng X., Papadopoulos P. *Method and device for transferring gas molecules from a gaseous medium into a liquid medium of low surface tension* (12008422.3).

2. Butt H.-J., Vollmer D., Deng X., Klapper M., **Paven M.**, Schuster T., Papadopoulos P. *Process and device for particle synthesis on a superamphiphobic surface* (13000764.4).

# 9 Acknowledgment

[n.a. in online version]

# 10 Curriculum Vitae

[n.a. in online version]

## 10.1 Conference contributions

### 10.1.1 **Oral contributions**

[n.a. in online version]

### 10.1.2 **Poster contributions**

[n.a. in online version]

## 10.2 Awards

[n.a. in online version]